From Luminescent Lanthanide Complexes to Color Reproduction and Optical Document Security with Invisible Luminescent Inks

PAR

Julien ANDRÈS

EPFL

ÉCOLE POLYTECHNIQUE
FÉDÉRALE DE LAUSANNE

Suisse
2012

J'aurais pu m'éloigner de ces fourches caudines,
Mais j'y voulus passer pour les briser du front.

Alfred de Vigny (1838)

Acknowledgements

Remerciements

J'aimerais remercier par ces modestes lignes
Tous ceux qui s'estimeraient dignes de l'être.
J'espère combler de la sorte tout oubli fâcheux
Qui se serait glissé dans ces quelques lettres,
Et qui pourrait blesser l'essence d'un être digne
Ou irriter les sens d'un lecteur moins chanceux.

Je note toutefois quelques personnes méritantes
Qui malgré ce préambule doivent être nommées.

Je remercie tout d'abord, Anne-Sophie qui a su me superviser tout en me donnant la possibilité de m'exprimer librement. Merci pour sa disponibilité, sa patience, et sa bienveillance, pour avoir partagé sa chimie avec moi, pour m'avoir soutenu dans les heures sombres, et pour avoir enduré une situation parfois délicate de par sa position.

Ensuite Roger, qui de sa manière plus ferme a su co-superviser la partie colorée de cette thèse. Merci pour m'avoir financé pendant ces quelques années, pour m'avoir poussé à chercher plus en avant afin d'accorder les humeurs de la chimie à celle de la reproduction couleur.

Il convient également de remercier le jury de cette thèse, soit David Parker, Jacques-Edouard Moser et Patrick Emmel, ainsi que Lothar Helm pour sa présidence.

Je tiens dans un second temps à remercier les personnes qui m'ont accueilli. Pour commencer Jean-Claude Bünzli qui a bien voulu que j'utilise les ressources de son laboratoire, dont Anne-Sophie, pour ma première année. Mon seul regret est que le laboratoire dût fermer si vite. Pour les années restantes de ma thèse, je remercie Jacques-Edouard Moser pour son hospitalité dans ses murs et pour m'avoir permis d'utiliser son équipement laser pour mes expériences. Sans cela, toute une partie de mon travail n'aurait pas été la même. Je le remercie également pour m'avoir donné goût à la lumière et ses interactions avec la matière, et pour avoir permis que je rencontre Roger au travers de mon travail de Master.

Il y eut durant ces années quelques personnes compétentes que je tiens aussi à remercier particulièrement. En premier, Frédéric Gumy dit Fred, qui m'a aidé au début à apprivoiser les lanthanides et surtout le matériel utilisé pour caractériser

Julien Andres

Summary

Summary of the thesis

The present thesis deals with luminescent compounds based on lanthanide complexes that are suitable for color reproduction and optical document security with invisible luminescent inks. This thesis is divided in two distinct fields: chemistry, which produces luminescent lanthanide complexes, and color science, which was required to characterize luminescent colors and use them for color reproduction and optical document security.

Concerning luminescent lanthanide complexes, the investigation is focused on the derivatization of dipicolinic acid. A modification of the carboxylate coordinating moiety of the ligand is first undertaken in order to synthesize phosphorylated ligands, which often show interesting variations of the properties of the complexes among related structures. On another hand, a derivatization of the ligand by grafting a polyoxyethylene side chain with a terminal chromophore at the *para* position on the pyridine core of dipicolinic acid is carried out. The ability of this chromophore to act as a sensitizer for the distant lanthanide ion coordinated on the dipicolinate moiety is investigated. A series of coumarin fluorophores are tested as sensitizers and the best coumarin is then used to further examine the mechanisms of the sensitization of the lanthanide ion, for example by shortening the polyoxyethylene pendent and thus modifying the distance between the sensitizer and the lanthanide ion.

The parent europium and terbium dipicolinate complexes are then used as red emitting and green emitting luminescent dyes in invisible luminescent inks together with a blue luminescent ink. An ink spreading enhanced spectral Neugebauer prediction model is used to predict the spectral radiant emittance of any combination of the luminescent inks. The good prediction accuracy of the model is then related to the photophysical properties of the luminescent inks, which are shown to be unquenched by superposition with the other inks. This trichromic system is finally used to reproduce luminescent color halftone images visible under UV light by relying on a gamut mapping algorithm and on the spectral prediction model.

In a final part, a new spectral prediction model for transmittances and reflectances is developed. It is then used for building a backlighting model where the backlight source is a luminescent emission under UV light from printed luminescent inks, and where the backlit colors are obtained by the transmission of the backlight source through color halftones printed with classical cyan, magenta and yellow inks on the

other side of the same substrate. Luminescent backlit color images can then be created, which produces a new security feature for optical document security combining recto classical images under normal light, with verso luminescent images and recto luminescent backlit images under UV excitation.

Résumé de la thèse

Cette thèse traîte de composés luminescents à base de complexes de lanthanide utilisables pour la fabrication d'encres invisibles luminescentes. L'emploi d'encres invisibles luminescentes est ensuite étudié comme un moyen de reproduction de couleurs par luminescence et comme une source de techniques optiques contre la contrefaçon de documents. Cette thèse se divise donc en deux parties distinctes : Une partie dite chimique qui s'occupe de la production de complexes de lanthanide, et une partie dite de science de la couleur qui est nécessaire pour caractériser des couleurs luminescentes et les utiliser dans un cadre de reproduction de couleurs et de techniques optiques contre la contrefaçon de documents.

En ce qui concerne les complexes de lanthanide, l'étude s'est concentrée sur la dérivatisation de l'acide dipicolinique. Une modification du groupe fonctionel coordinant carboxylate sur le ligand est d'abord entreprise. Une série de ligands phosphorylés, qui ont souvent montré d'intéressentes variations de leurs propriétés parmi des structures similaires, est synthétisée à cette attention. Dans un second temps, une dérivatisation de l'acide dipicolinique par couplage en position *para* sur le cycle pyridine d'une chaîne polyoxyethylénique portant un chromophore terminal est engagée. La capacité de ce chromophore à sensibiliser un ion lanthanide coordiné à la partie dipicolinate, et donc espacé par rapport à celui-ci, est étudiée. Une série de fluorophores appartenant à la famille des coumarines est testée comme sensibilisateurs, et la coumarine donnant les meilleurs résultats est ensuite examinée plus en détails afin de déterminer les mécanismes impliqués dans la sensibilisation de l'ion lanthanide. Dans cette optique, la chaîne polyoxyethylénique est par exemple raccourcie afin de faire varier la distance entre le sensibilisateur et l'ion lanthanide.

Les complexes trisdipicoliniques d'europium et de terbium sont ensuite utilisés comme colorants liminescents émettant dans le rouge et dans le vert pour la fabrication d'encres luminescentes invisibles. Complétés par une encre luminescente émettant dans le bleu, un modèle de prédiction spécrale selon Neugebauer et prenant en compte l'étalement des encres est utilisé afin de prédire l'émission de n'importe quelle combinaison des encres luminescentes imprimées sur un papier non-fluorescent. La bonne précision de la prédiction du modèle est subséquemment reliée aux propriétés photophysiques des encres luminescentes qui ne sont pas altérées par la superposition avec les autres encres. Ce système trichromatique est finalement utilisé pour reproduire des images luminescentes

tramées en demi-tons et en couleur. Ceci est accompli par l'emploi d'un algorithme de mise en correspondance de la gamme des couleurs et par l'utilisation du modèle de prédiction spéctrale.

Dans la partie finale de cette these, un nouveau modèle de prédiction spéctrale pour les transmittances et les réfléctances est développé. Il est utilisé pour construire un modèle de rétro-éclairage dans lequel la source de rétro-éclairage provient de l'émission luminescente sous irradiation UV d'une couche imprimée d'encres luminescentes, et où les couleurs rétro-éclairées sont obtenues par transmission de la source de rétro-éclairage à travers des trames colorées de demi-tons imprimées avec des encres classiques cyan, magenta et jaune sur l'autre face du même substrat. Des images luminescentes rétro-éclairées en couleur peuvent donc être créées, ce qui constitue un nouveau moyen de sécurisation optique contre la contrefaçon de documents. Cette méthode combine des images classiques sous lumière blanche avec des images luminescentes et des images luminescentes rétro-éclairées sous irradiation UV.

Mots clefs: Lanthanide, luminescence, reproduction de couleurs, sensibilisation, acide dipicolinique, europium, terbium, coumarine, polyoxyéthylène, rétro-éclairage, transmittance, émittance monochromatique, sécurité de documents, encre invisible, modèle de prédiction spéctrale, colorimétrie

Table of contents

Table of contents

Glossary

List of abbreviations

%w   Weight percent

$^{(2S+1)}\Gamma_J$ Spectroscopic level with a total spin quantum number S and total angular momentum quantum number J from the spectroscopic term $^{(2S+1)}\Gamma$, where Γ represents the orbital angular momentum L.

3D   Three dimension

6ppa   6-phosphorylpicolinic acid

a_f Surface coverage of the luminescent colorant f

a_j Surface coverage of the colorant j

a_{KWlum} Surface coverage of the UV-absorbing black ink

Anal.   Analysis

Avg.   Average

CIE   Commission Internationale de l'Éclairage

CIELAB   Color space with lightness coordinates L^*, and chroma coordinates a^*, b^*

CIELCH   Cylindrical representation of the CIELAB color space with lightness coordinates L^*, chroma radial coordinates C_{ab}^* and hue angle coordinates h_{ab}.

CIE-xyY   Color space with chroma coordinates x and y and relative luminance coordinates Y

CIE-XYZ   Color space with tristimulus values X, Y and Z

Calcd.   Calculated

CMY   Cyan, Magenta and Yellow

CMYK	Cyan, Magenta, Yellow and blacK
CRT	Cathod Ray Tube
D65	Standard daylight illuminant with a correlated color temperature of approximately 6500 K.
DCM	Dichloromethane
Δ (in synthesis)	heat
ΔE_{94}	Color difference metric. The smaller the value, the smaller the color difference.
deppa	Diethoxyphosphorylpicolinic acid
dhppa	Dihydroxyphosphorylpicolinic acid
DIAD	Diisopropylazodicarboxylate
DMF	Dimethylformamide
do3a	1,4,7,10-tetraazacyclododecane-1,4,7-triacetic acid
dota	1,4,7,10-tetraazacyclododecane-1,4,7,10-tetraacetic acid
dp3R	Dipicolinate-*para*-R-trioxyethylenated ligands
dpa	Dipicolinic acid
dpi	Dot per inch
dpxCy	Dipicolinate-*para*-chromophore -polyoxyethylenated ligands
$E(\lambda)$	Relative spectral radiant emittance
e.g.	*Exempli gratia* (for the sake of an example)
$E^{\ominus}_{red}$	Standard reduction potential

$E_{bl}(\lambda)$	Relative spectral radiant emittance of the luminescent backlight
ED transition	Electric Dipole transition
$E_f(\lambda)$	Relative spectral radiant emittance of the luminescent colorant f
$E_{KWlum}(\lambda)$	Relative spectral radiant emittance of the white luminescent layer attenuated by a UV-absorbing halftone
EPFL	École Polytechnique Fédérale de Lausanne
ESI-MS	Electrospray Ionization Mass Spectrometry
ET	Energy Transfer
η_{et}	Efficiency of the energy transfer
η_{isc}	Efficiency of the intersystem crossing
η_{sens}	Efficiency of the sensitization
$E_{Wlum}(\lambda)$	Relative spectral radiant emittance of the unattenuated white luminescent layer
free L	Free ligand
G_{bp}	Luminescent backlit gamut on the Bio Top paper
G_{sRGB}	sRGB gamut
G_{tp}	Luminescent backlit gamut on the tracing paper
HOMO	Highest Occupied Molecular Orbital
HPLC	High-Performance Liquid Chromatography
IC	Internal Conversion
i.e.	*Id est* (that is)

IR	Infrared
ISA	Ink spreading enhanced Spectral Absorption model
ISC	Intersystem Crossing
IS-CYNSN	Ink Spreading enhanced Cellular Yule-Nielsen Spectral Neugebauer model
IS-SN	Ink Spreading enhanced Spectral Neugebauer model
IS-YNSN	Ink Spreading enhanced Yule-Nielsen Spectral Neugebauer model
$\kappa(\lambda)$	Spectral attenuation factor due to the presence of a UV-absorbing halftone on top of the luminescent layer
k_{abs}	Absorption rate constant
k_f	Radiative fluorescence deactivation rate constant
k_p	Radiative phosphorescence deactivation rate constant
k_{nr}	Non-radiative deactivation rate constant
k_{obs}	Observed deactivation rate constant
k_q	Quenching rate constant
k_{rad}	Radiative deactivation rate constant
k_{sq}	Self-quenching rate constant
L^*_{high}	High lightness focal point of the multiple foci gamut mapping algorithm
L^*_{low}	Low lightness focal point of the multiple foci gamut mapping algorithm
L^*_{min}	Minimum lightness of the gamut
λ	Wavelength
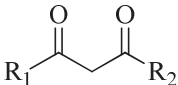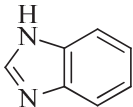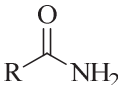
L   Ligand

LCD   Liquid Crystal Display

Ln   Lanthanide

Logβ Logarithm base 10 of the stability constant β

lpi   Line per inch

LUMO   Lowest Unoccupied Molecular Orbital

LUT   Lookup table

m-CPBA   *meta*-Chloroperoxybenzoic acid

MD   Magnetic Dipole transition
transition

meppa   Monoethoxyphosphorylpicolinic acid

MO   Molecular Orbital

mpxCy   Methyl-polyoxyethylenated-chromophore

NIR   Near Infrared

NMR   Nuclear Magnetic Resonance

nom   Nominal surface coverage

OBA   Optical Brightening Agent

Φ_L^{Ln} Sensitized quantum yield of the lanthanide emission

Φ_{Ln}^{Ln} Intrinsic quantum yield of the lanthanide emission

POE   Polyoxyethylene

PS-PPh$_3$ Polymer supported triphenylphosphine

q	Number of water molecules in the first coordination sphere of the lanthanide ion (hydration number)
$Q_{95\%}$	95 % quantile
$R(\lambda)$	Reflectance
S_n	N^{th} singlet energy level
sRGB	Standard color space for display devices
$T(\lambda)$	Transmittance
$T_{HTcolor}(\lambda)$	Transmittance of the color halftone
$T_j(\lambda)$	Transmittance of the colorant j
τ_f	Fluorescence radiative lifetime
τ_{obs}	Observed lifetime
τ_p	Phosphorescence radiative lifetime
τ_r or τ_{rad}	Radiative lifetime
TMSI	Trimethylsilyl iodide
T_n	N^{th} triplet energy level
Tris	Tris(hydroxymethyl)aminomethane
Ts	Tosyl group (4-toluenesulfonyl)
$T_{sub}(\lambda)$	Transmittance of the substrate
UV	Ultraviolet
UV-Vis	Ultraviolet and Visible
vs.	*versus*
Xe light	Xenon light

Glossary of terms

Antennæ	Chromophore capable of transferring part of the absorbed energy onto a lanthanide ion.
Backlighting	Illumination that comes from behind the observed object from the point of view of the observer.
Bandpass filter	Optical filter that transmits specific bands of wavelengths.
β-diketones	

Beer Lambert's law	Law of absorption: the absorbance $A(\lambda) = \varepsilon(\lambda) \cdot c \cdot \ell$, where ℓ is the optical pathlength, c the concentration of the absorbing compound and $\varepsilon(\lambda)$ the molar decadic extinction coefficient of the absorbing compound at the wavelength λ.
Benzimidazole	

bis species	Species of a complex with two ligands per metal ion
Carbamoyl	

Chelate	Chelate complexes are formed by chelating polydentate ligands that binds to metal ions with more than one bond (coordination site).
Chroma	Radial component in the CIELCH color space cylindrical representation of CIELAB.

Chromaticity   Color characteristic regardless of the luminance and specified by x and y coordinates in the CIE-xyY color space.

Chromophore   Compound or parts of a compound that absorb UV or visible light.

Classical inks   Color inks typically used for printing color images (CMY or CMYK)

Clicked dpa   Dpa derivative formed by grafting a *para* substituent using Click chemistry.
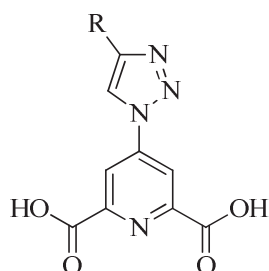
Colorant   Fulltone color used as a color primary in spectral prediction models.

Color matching   Set of spectral sensitivities of a standard observer
functions   describing its chromatic response.

Color primaries   Set of colors that can be combined to produce the other colors.

Complex   Molecular assembly formed by the coordination of metal centers with ligands.

Contrast   Difference in luminance and/or color that enables distinguishing elements of a scene, e.g. of an image.
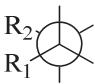
Coumarin   Molecules with a core composed of 1-benzopyran-2-one.

Demichel's equations   Set of equations describing the surface coverages of each colorant in a color halftone.

Derivatization   Modification of a molecule (framework) by replacing functional groups or adding substituents.

Diffuser   Device that diffuses transmitted light (opal diffusing glass or opal glass diffuser)

Dot gain   Difference between the effective surface coverage and the nominal surface coverage of an ink. Accounts for ink spreading and lateral propagation of light in prints

Electrophotography   Also known as xerography or laser printing. Printing technology that uses a photoconductor to generate an electrostatic latent image upon exposure to an image. The electrostatic latent image is developed by fixing toner particles on the charges of the latent image by electrostatic interactions. The toner image is finally electrostatically transferred on paper and permanently fixed by heat of pressure, which melts the toner particles into the printed substrate.

Equivalent (number of)   An equivalent is the number of moles required to match the number of moles of another compound taken as reference. Equivalents higher than 1.0 indicate an excess relative to the reference compound.

Excitation   Promotion of an electron to a higher unstable energy level. The electronic transition can be induced by light (photoexcitation).

Fluorescence   Radiative relaxation (emission) from an excited state without any change of the electron spin between the initial state and the final state.

Fluorophore   Compound or parts of a compound that emit light by fluorescence.

Gamut   Color range reproducible with a specific device.

gauche conformation

Halftone   Binary tone made of printed dots that looks like a continuous tone.

Helicate   Ligand that wraps around metal ions in a helical way.

Hypersensitive transition   Transition that is particularly sensitive to the chemical environment (e.g. the $^5D_0 \rightarrow ^7F_2$ f-f transition of Eu^{3+}).

Ink spreading   Diffusion of ink in the paper bulk causing dot gain. Ink spreading enhanced models are spectral prediction models that account for dot gain.

Ink-jet printing   Printing technology that prints by ejecting the ink on paper "on-demand" at the desired location.

Longpass filter   Optical filter that absorbs wavelengths shorter than a specific cutoff wavelength and transmits wavelengths larger than the specific cutoff wavelength.

Lookup table   Table or matrix setting correspondences between input values and output values.

Luminescence   General word for the radiative relaxation (emission) from an excited state. Includes fluorescence and phosphorescence phenomena.

Macrocycle   Cyclic molecule with at least three donor atoms capable of binding metal ions.

Neugebauer   The Neugebauer approach models color halftones by summing the spectra of the Neugebauer primaries (i.e. of the colorants) and weighting each colorant by its surface coverage in the halftone.

n-factor

Also known as Yule-Nielsen factor. Exponent raising the spectra of the colorants in spectral prediction models based on the Yule-Nielsen approach.

Offset printing

Printing technology that uses an offset cylinder (blanket cylinder) as a contact cylinder that transfers the inks onto paper. This cylinder is inked by the printing plate cylinder and the transfer occurs when an impression cylinder presses the paper on the offset cylinder.

Opal glass

Piece of glass with a white opal coating that diffuses light homogeneously (near Lambertian).

para
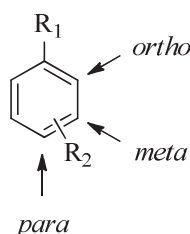
Phosphonate
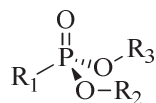
Phosphorescence

Radiative relaxation (emission) from an excited state with a change of the electron spin between the initial state and the final state.

Phosphoryl
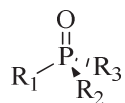
Photobleaching

Photochemical destruction of a luminescent compound that reduces its luminescence intensity.

Photophysics

Study of the laws and processes arising from the interaction of light with matter.

Pyrazolyl
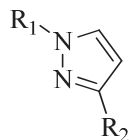
Pyridine

Quenching   Non-radiative deactivation of an excited chromophore by energy transfer to a quencher molecule.

Quinolinone
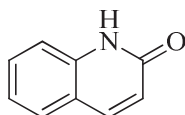
Racemization   Conversion of an enantiomerically pure compound into a mixture of enantiomers. When the enantiomers are present in equal quantities, the mixture is called racemic.

Recto/verso   Front and back sides of a sheet of paper.

Saturation (color)   In CIELAB, the saturation of a color is defined as the ratio of its chroma $C_{ab}*$ divided by its lightness $L*$.

Security feature   Anti-counterfeiting technique used in optical document security.

Sensitizer   Also known as photosensitizer. Chromophore that can transfer the absorbed energy to another compound that would not absorb that light without the sensitizer.

Shortpass filter   Optical filter that absorbs wavelengths longer than a specific cutoff wavelength and transmits wavelengths shorter than the specific cutoff wavelength.

Singlet   Zero electronic quantum spin state of a compound.

Spectral prediction model   Model used to predict a spectral characteristic of a print (e.g. the reflectance).

Spectral radiant emittance	Radiometric quantity describing the power emitted from a surface per wavelength ($W \cdot m^{-2} \cdot nm^{-1}$).
Surface coverage	Area covered by a specific ink or colorant.
trans conformation	Also known as anti, or antiperiplanar conformation:
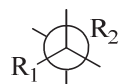
Transition	Modification of the energy level of an electron, e.g., resulting from absorption or emission of light.
Triazolyl	
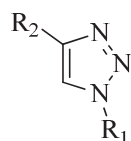
Triplet	Set of electronic quantum spin state of a compound with a total spin of one.
tris species	Species of a complex with three ligands per metal ion.
Tristimulus values	Color coordinates usually in CIE-XYZ.
UV-absorbing (ink)	Ink that absorbs part of the UV light.
Yule-Nielsen	The Yule-Nielsen approach models color halftones by summing the n-factor exponent raised spectra of the Neugebauer primaries (i.e. of the colorants), weighting each colorant by its surface coverage in the halftone, and raising the sum by the inverse of the n-factor. The n-factor is introduced to account for lateral propagation of light.

Chapter 1

Introduction

Concerning lanthanide ions and color science

1.1   General considerations

The present thesis deals with luminescent compounds suitable for color reproduction and document security. A new range of luminescent compounds is synthesized and characterized. The compounds are water soluble to ensure an optimal applicability as luminescent inks for ink-jet printing. The photophysical properties of the luminescent dyes are investigated and suitable candidates are further tested as luminescent inks. A novel approach to embody luminescence as a document security feature is developed from available luminescent inks and non-luminescent inks. The method is based on color spectral prediction models and gamut mapping.

1.1.1   Motivations

The general idea behind this work was to design new luminescent compounds that should possess photophysical properties that are interesting for color reproduction and document security. Two distinct fields of research were therefore explored: In one hand, chemistry, which focused on producing luminescent compounds, studying them and by doing so, further contribute to the understanding of the fundamentals of luminescence; and on the other hand, color science, which was necessary to characterize luminescent colors and utilize them in order to reproduce color images and security features for document security.

Because luminescent colors behave additively, the chemistry main attention was focused on producing red-emitting, green-emitting and blue-emitting compounds. Lanthanide complexes with their sharp transitions were found to be very attractive therefore. The red emission of europium(III) and the green emission of terbium(III) are particularly suited for color reproduction. Less emissive lanthanide ions such as dysprosium(III) and samarium(III) might also be useful for security applications. Near infrared emitters such as erbium(III), ytterbium(III) or neodymium(III) are more difficult to sensitize. Their application towards security features, even though very attractive, is thus limited by their very low emission efficiency. In this thesis, the emissive lanthanide ions investigated are Eu^{3+} and Tb^{3+}.

On the color reproduction side, one of the interests was to be able to print the luminescent materials with the ink-jet technology. Since this technology is using nearly exclusively water based inks, and in order to simplify the formulation of

luminescent inks, it was decided from the beginning that the luminescent lanthanide complexes ought to be water soluble, so that they could easily be used as luminescent dyes in an ink-jet formula.

1.1.2   Overview

1.1.2.1 Introduction

As a starting point of this thesis, a brief description of the lanthanide chemistry and photophysics will be undertaken. The particular case of lanthanide luminescence will be explained and will encompass the special phenomenon of photosensitization. Since the present thesis is interested in water soluble luminescent lanthanide complexes, the state of the art will be restricted to water soluble luminescent lanthanide complexes. In particular, the trisdipicolinato lanthanide complexes will be discussed as an example of the coordination and luminescence of lanthanide compounds. The different derivatization approaches that can be carried out on the dipicolinate framework will then be presented.

In order to understand most of the aspect of color reproduction and document security, which are unfamiliar to most chemists, the color science section will first introduce basic concepts about colorimetry, printing, halftoning and image formation. These prime notions will then be extended towards color prediction models and spectral prediction models applied to reflectances, transmittances and relative spectral radiant emittances. It will be shown how to use these prediction models to build gamuts and how to map the colors from one gamut into another one in order to preserve the relative appearance of colors viewed on different media or under different conditions.

1.1.2.2 Achievements

After this necessary introduction to the lanthanide ions, photophysics and color reproduction, the results obtained during this thesis will be presented as follows. The dipicolinate complexes will be the starting point. The modification of its coordination site will be studied by replacing one of the carboxylate by phosphoryl derivatives. After that, a new method to extend the absorption range of the dpa framework will be investigated. It consists in the grafting at the *para* position on the pyridine ring of a polyoxyethylene linker with a chromophore at the end of it. Different coumarin chromophores (or fluorophores) will be tested thereof with a fixed trioxyethylene side chain as a linker. The length of this side chain will eventually be shortened and will allow the investigation of the energy transfer

mechanisms involved in such architectures. Both the synthesis and photophysical characterization of all the complexes will be presented.

Finally, the color reproduction section will start with an application of the dipicolinate complexes for reproducing images under UV excitation. A novel strategy to embody document security features using luminescence as a backlight source will then be described in detail, which will also enable the presentation of the new spectral prediction models that were developed during this thesis.

1.2   Chemistry of the lanthanide ions

Lanthanides (Ln) or lanthanoids are elements from lanthanum ($Z = 51$, La) to lutetium ($Z = 71$, Lu). The progression along the series adds one proton, one electron and some neutrons. Since these electrons are added into 4f orbitals, filling the 4f electron shell, lanthanides are also called 4f-elements or f-block elements. Lanthanides are rare-earths or rare-earth elements, but rare-earths are not only lanthanides. Rare-earths also include scandium ($Z = 21$, Sc) and yttrium ($Z = 39$, Y), because of their chemically similar properties compared to lanthanides. The chemical similarities within the lanthanide series were also responsible for the long period over which they were discovered (from 1794 to 1907).

In this work, lanthanide coordination complexes formed by cationic lanthanide centers coordinated to organic ligands are investigated. This section gives a quick overview of the different notions and parameters required to understand the formation and the stability of such complexes. The next section will explore the luminescence of the lanthanide complexes. Most of what is reported here can be found in textbooks.[1, 2]

1.2.1   Coordination of the lanthanide ions

In order to understand the coordination of the lanthanide ions, two fundamental notions about the electronic properties of 4f elements are needed, first about the oxidation state of the lanthanide ions, and then about the electronic structure of those ions.

Lanthanide ions are almost entirely encountered as trivalent ions (oxidation state +3). The removal of three electrons from the f-elements is taking place in the 6s subshell (two electrons), and the remaining one in the 5d subshell or 4f subshell

when no 5d electron is present in the electronic structure of the lanthanide. The fourth ionization energy of the lanthanides that would form the tetravalent ions is always higher than the sum of the first, second and third ionization energy of the same 4f-element, so that the formation of lanthanides(IV) by the release of chemical bond energy is almost never achieved. Considering lower oxidation states, only europium(II) might be stable in water. The reduction from the trivalent ion: $Eu^{3+}(aq) + e^- \rightarrow Eu^{2+}(aq)$ has a standard reduction potential $E^{\ominus}_{red} = -0.35$ V. Since the balance of the oxidation of Eu^{2+} with the reduction of water ($2\,H_2O + 2\,e^- \rightarrow H_2 + 2\,OH^-$, $E^{\ominus}_{red} = -0.83$ V) yields a potential lower than zero, Eu^{2+} is stable in water under the standard conditions. Eu^{3+} is nevertheless more stable in water. Its reduction is not sufficient to oxidize water ($2\,H_2O \rightarrow O_2 + 4\,H^+ + 4\,e^-$, $E^{\ominus}_{ox} = -1.23$ V). This particular stabilization of Eu^{2+} comes from its half-filled subshell ($4f^7$).

From lanthanum(III) to lutetium(III), the progression along the lanthanide series fills the 4f subshell. La^{3+} has no electron in the 4f subshell, whereas Lu^{3+} has all its 4f orbitals filled with electrons (fourteen electrons maximum for the seven 4f orbitals). The subshell is half-filled with Gd^{3+}.

The remarkable property of the lanthanides is that their 4f electrons are inner electrons, shielded by the electrons in the more extended fifth shell (i.e. in the 5s and 5p subshells). Inversely, the outer electrons are shielded from the nucleus by the 4f electrons. Consequently, the effective charge of the nucleus at the outer shells is decreased by the 4f electrons. This shielding is however weaker and weaker as the inner 4f subshell is filled, because the effective charge of the nucleus increases more and more along the lanthanide series. Since the effective charge of the nucleus experienced by the outer electrons thus increases, the outer electrons are more attracted towards the nucleus. The resulting contraction of the outer electrons decreases the ionic radii along the lanthanide series. This phenomenon is called the lanthanide contraction. The difference between the larger La^{3+} and the smaller Lu^{3+} is 0.18 Å in nine coordinated ions.

Because the 4f electrons are inner electrons, the coordination bonds in a complex with a trivalent lanthanide ion are first and foremost ionic (no covalent bonds with 4f orbitals). The lanthanide contraction induces one major difference between the coordination with early lanthanides or late lanthanides, which is a preferred coordination number in solution of nine for the early ones, and a preferred coordination number in solution of eight for the late ones. The middle of the series is either nine or eight. In solid state, the coordination number is usually nine across the whole series.

In an aqueous solution, the hydration energies of the lanthanide ions are high. As a result, the release of the solvation sphere demands that the formation of the new coordination sphere (the formation of the coordination bonds) liberates as much energy as possible (strong ligand-metal interactions) and that entropy favors the reaction. Therefore a minimum number of ligand should release as much water molecule as possible to ensure that the reaction is driven by entropy. Multidentate ligands or chelates are thus preferred in aqueous solutions to guarantee a good coordination. Because lanthanide ions are hard Lewis acids that bond through ionic interactions, some hard electron-donating coordination functional groups are required in the ligand, preferentially negatively charged oxygen containing groups or nitrogen containing groups with a lone electron pair.

The geometry of the coordination sphere depends on the coordination number and on the steric hindrance of the ligands. Usually, a complex with a coordination number of nine will exhibit a tricapped trigonal prism symmetry (D_3).

1.2.2   Stability in aqueous solutions

Prior to any detailed photophysical characterization of a lanthanide complex, its stability has to be determined. The stability of the complexes in aqueous solution depends on four factors: The redox stability of the metal ion, which is not problematic for lanthanide ions as seen earlier; the thermodynamics of the complexation process, which requires properly designed ligands as also seen earlier, the acid/base equilibria of the complex which depends on the protonation constants of the ligands and the hydroxide association constant of the metal ion, and finally, the ionic strength of the solution,[3] ions being susceptible to interact with charged complexes and free ligands and thus disrupt the equilibria.

The equilibria and corresponding formula used for the calculation of the stability constants are presented in the appendices. In this work, the stabilities of the lanthanide complexes will be quantitatively assessed by the logβ values. The formation of the different species in solution (e.g. 1:3, 1:2 and 1:1 Ln:L complexes for a tridentate ligand) are therefore characterized each by a logβ value. The Ln:L notation defines the soichiometry of the complex. For example, the 1:3 Ln:L complex has one lanthanide ion Ln and three ligands L: the species 1:3 then corresponds to the complex [LnL$_3$].

The stability constants can be measured by complexometry. A titration of the ligand with increasing amounts of metal ions and the measurement of a property

that allows calculating the concentration of the species in solution at each metal/ligand ratio enables calculating the stability constants as well as the distribution diagram of those species as a function of the stoichiometry under defined conditions. Potentiometry and UV-Vis absorption spectrophotometry are the two major techniques used in complexometry. Spectrofluorimetry is sometimes used as well, but it requires all species but one to be sufficiently luminescent, which is not always true. Alternatively, stability constants can be determined from NMR spectra if the species are in rapid exchange relative to the NMR time-scale and if the chemical shift of a suitable nucleus is altered upon formation of the complex species. The preferred technique in the micro- to millimolar concentration range is absorption spectrophotometry. Potentiometry usually needs higher concentrations.

These complexometric experiments are conducted at a defined pH value, usually neutral (pH 7.4 using a Tris 0.1 M buffer solution). Under basic conditions, the formation of lanthanide hydroxides is favored and can at least partly disrupt the metal-ligand complex. Under acidic conditions, the protonation of the ligand is favored. Since most of the ligands in aqueous solutions are coordinated through oxygen or nitrogen atoms that are susceptible to protonation, when occurring, the protonation also partly disrupts the complex. Furthermore, a constant ionic strength is required to avoid any effect of the ionic strength on the complexation equilibria.

1.2.3 Concluding remarks

An extensive part of this thesis deals with luminescent lanthanide complexes. The understanding of the basic chemistry of lanthanide(III) ion, and particularly their coordination ability towards organic ligands is therefore necessary. The stability of the complex is an essential piece of information, which should always be determined before any conclusions on photophysical properties can be confidently assessed. The determination of the stability constants is not the only way to evaluate the stability of a complex though. Qualitative assessements can be undertaken by probing or measuring several properties. Some photophysical properties such as the emission intensity of the observed lifetime are for example very usuful for determining the relative stability of a luminescent lanthanide complex under different conditions. More details will be encountered in the Chapters 2 and 3 when actually investigating new lanthanide complexes.

The next section of this introduction deals with the luminescence of the lanthanide ions. Several important concepts that are relevant for deducing the stability of lanthanide complexes will be presented.

1.3   Luminescence of the lanthanide ions

All the lanthanide ions, except lanthanum and lutetium, which have an empty and a full 4f configuration respectively, are luminescent by f-f transitions. Such a transition corresponds to a rearrangement of the 4f subshell. It is a forbidden transition because of Laporte's selection rules and have therefore a very low extinction coefficient in absorption, and very low radiative rate constants (long radiative lifetimes) in emission.

In coordination complexes, the organic ligand often acts as a sensitizer of the lanthanide ion. The photosensitization process will now be briefly explained. The luminescence of the lanthanide ions will then be rationalized and the notation for the characterization of the f-f transitions, which is followed in this work, will be presented. Finally, the different parameters measured or calculated from experimental data and used to describe the luminescence of the lanthanide ion and the sensitization process (i.e., quantum yields, lifetimes and sensitization efficiency) will be detailed. The special case of the europium ion, which is extensively investigated in this thesis, will conclude this section.

The present section represents a short version of a more extensive work to be published by the end of the year 2012 in "The Rare Earth Elements: Fundamentals and Applications" (chapters "Lanthanide: Luminescence" and "Lanthanide: Luminescence Applications"), and for which the author of this thesis has contributed.[4, 5] Other textbooks such as "Lanthanides and Actinides" by Simon Cotton, "Rare-Earth Coordination Chemistry" edited by Chun-Hui Huang, "Lanthanide Luminescence" edited by Pekka Hänninen and Harri Härmä, and the reference textbook on fluorescence "Molecular Fluorescence" by Bernard Valeur also provide further information.[1, 2, 6, 7]

1.3.1   Photosensitization

Because of their very low extinction coefficient, in order to activate the luminescence of the lanthanide ions, a photosensitizer is needed. The photosensitization, (or simply sensitization) is a photophysical or photochemical process that excites or reduces/oxidizes a non-absorbing material through an energy or electron transfer respectively via the absorption of light by a distinct compound

called the sensitizer. In the case of the lanthanide luminescence, an organic ligand with a high extinction coefficient may be used as a photosensitizer.

The photosensitization of lanthanide ions is, most of the time, not a photochemical process because it involves no electron transfer (because of the high reduction/oxidation potentials of the trivalent lanthanide ions). The mechanism is purely photophysical. The excitation of the sensitizer is transferred onto the lanthanide ion, which becomes excited, and the excitation may then be deactivated by emission from the lanthanide ion. The term excitation energy transfer is sometimes encountered to specify that the sensitization transfers the excitation energy.

1.3.2   Electronic structure of the lanthanide ions

The luminescence of a sensitized lanthanide ion depends on the electronic structure of this ion. The configuration of the 4f subshell is usually described by the Russel-Saunders coupling scheme. In this scheme, the 4f configuration is first split into spectroscopic terms $^{(2S+1)}\Gamma$ due to the electronic repulsion, and each spectroscopic term is then split into spectroscopic levels $^{(2S+1)}\Gamma_J$ by the spin-orbit coupling. A $^{(2S+1)}\Gamma_J$ spectroscopic level has a spin multiplicity of $(2S+1)$, where S is the total spin angular momentum quantum number of the electronic state, has an orbital anular momentum quantum number L, which corresponds to the Γ letter $(L = 0 \rightarrow \Gamma = S, L = 1 \rightarrow \Gamma = P, L = 2 \rightarrow \Gamma = D, L = 3 \rightarrow \Gamma = F, …)$, and has a total angular momentum quantum number, or spin-orbit quantum number J that can spand from |L-S| up to L+S by steps of 1. A particular J value has a multiplicity of 2J+1, which is therefore the multiplicity of a spectroscopic level. When the lanthanide ion is coordinated to ligands, a ligand field further splits each spectroscopic level in several spectroscopic sub-levels according to the symmetry of the coordination sphere (i.e., breaks part of the 2J+1 degeneracy). However, the ligand field is very weak for a lanthanide ion because the 4f electrons are inner electrons. The f-f transitions are therefore fairly constant in energy and are usually described by the associated spectroscopic levels. To completely break the 2J+1 multiplicity, an external magnetic field in one direction is required.

The ground state of each lanthanide ion can then be determined according to Hund's rules. It states that the lowest energy configuration has a maximal spin angular momentum and orbital angular momentum (first and second Hund's rules) and that the spin-orbit coupling stabilizes the minimum total angular momentum when the subshell is less than half filled and maximum total angular momentum

when it is more than half filled. It then corresponds to a configuration with quantum numbers S_{max}, L_{max} and J_{min} (< half filled) or J_{max} (> half filled). For further details, see [5].

1.3.3   Brief overview of the possibilities of the luminescence of the lanthanide ions

Among the lanthanide ions, gadolinium has the highest energy gap between its ground spectroscopic level ($^8S_{7/2}$) and its first excited spectroscopic level ($^6P_{7/2}$). The difference of 32,000 cm^{-1} corresponds to a wavelength in the UV-B. Practically, the sensitization of gadolinium cannot be achieved under conventional conditions. It is therefore often used as a non-luminescent lanthanide ion in the investigations of the ligand-centered photophysical properties. It is preferred to the non-luminescent lanthanum and lutetium when studying europium and terbium complexes because gadolinium has a closer electronic structure and ionic radius.

The other high energy gap lanthanide ions are terbium with its typical green emission, and europium with its red emission. Those two lanthanide ions are the most efficient emitters in the visible spectrum because they do not have any spectroscopic level in between the ground state and the luminescent spectroscopic level that may favor nonradiative deactivations. Thulium and dysprosium have for example transitions that can occur in the blue, but several levels are also present in between so that the efficiency of the high energy transition is usually low. Dysprosium is yet interesting because of its yellow emission. The efficiency might be compared to that of samarium and its orange emission. Considering the remaining lanthanide ions, they mainly exhibit NIR emissions. The major NIR emitters are ytterbium, neodymium, praseodymium erbium and holmium. For further details, see [5] and [4]. Because of the motivations of this thesis, only the visible emitting lanthanide ions will be considered afterwards for the metal-centered photophysical properties. Gadolinium(III) will be used for the determination ligand-centered photophysical properties, whereas the diamagnetic non-luminescent lanthanide ions (La^{3+} and Lu^{3+}) will be used in NMR spectroscopy studies.

1.3.4   Quantum yields, lifetimes and sensitization efficiencies

The efficiency of the luminescence from a lanthanide ion are usually rationalized by two parameters: the quantum yield Φ_L^{Ln}, which is defined as the number photons emitted by the lanthanide ion divided by the number of photons absorbed by the

sensitizer, and the observed lifetime τ_{obs} which corresponds to the decay rate of the luminescence. Those two parameters are easily measured for all the luminescent lanthanide ions. In addition, the intrinsic quantum yield $\Phi_{Ln}{}^{Ln}$, which corresponds to the number of photons emitted from the lanthanide ion per number of lanthanide ions excited, is rarely directly measured because of the difficulty to determine the number of excited lanthanide ion. Practically, the measurement of the intrinsic quantum yield requires exciting directly the lanthanide ion via one of its very weak f-f transition, and measuring the number of absorbed photon as well as the resulting emitted photons.

The intrinsic quantum yield is related to the observed lifetime (inverse of the sum of all the deactivation rate constants) and to the radiative lifetime τ_{rad} like any "conventional" quantum yield (Equation 1).

$$\Phi_{Ln}^{Ln} = \frac{k_{rad}}{k_{rad} + \sum k_{nr}} = \frac{\tau_{obs}}{\tau_{rad}} \qquad (1)$$

The sensitized quantum yield $\Phi_{L}{}^{Ln}$ is linked to the intrinsic quantum yields by the sensitization efficiency η_{sens}, which defines the percentage of the number of absorbed photons that yield an excited lanthanide ion (Equation 2).

$$\Phi_{L}^{Ln} = \eta_{sens} \cdot \Phi_{Ln}^{Ln} \qquad (2)$$

The sensitization of the lanthanide ions can occur via different pathways. Usually, the triplet pathway is predominant. It means that in most cases, the energy is first absorbed by the sensitizer, which is then in its singlet excited state, afterwards the sensitizer relaxes down to its excited triplet state via intersystem crossing (isc) before transferring the energy onto the lanthanide ion, which goes from its ground spectroscopic level to a higher one. The energy transfer (et) mechanism is either a Förster type transfer by dipole-dipole couplings[8], or a Dexter type transfer by an electron exchange[9]. Nevertheless, the triplet pathway is not mandatory. It has been shown that when the intersystem crossing rate is slow enough ($<10^{11}$ s^{-1}), the singlet pathway is consistent with the experimental data.[10]

Usually, in a triplet pathway energy transfer mechanism, the sensitization efficiency is split into two contributions: an intersystem crossing and an energy transfer term. But in a more general approach, the sensitization efficiency should contain the contribution from the singlet state η_{et}^{S}, as well as the contribution from

the triplet state η^T_{et}. The sensitisation efficiency should thus be approximated as in Equation 3.

$$\eta_{sens} = \eta^S_{et} + \eta^T_{et} \cdot \eta_{isc} \tag{3}$$

Each of those parameters can be expressed in terms of rate constants as the ratio of the considered process relative to all the deactivations of the associated excited state as shown in Equation 4.

$$\eta_{isc} = \frac{k_{isc}}{k^S_{obs}}, \quad \eta^S_{et} = \frac{k^S_{et}}{k^S_{obs}}, \quad \eta^T_{et} = \frac{k^T_{et}}{k^T_{obs}} \tag{4}$$

The sum of all the deactivations of the associated excited state k_{obs} can be approximated as in Equation 5, where k_f is the fluorescence radiative rate constant, k_p the phosphorescence radiative rate constant and k_{nr} the sum of all the non-radiative deactivations of the excited state.

$$k^S_{obs} = k_f + k_{isc} + k^S_{et} + k^S_{nr}$$
$$k^T_{obs} = k_p + k^T_{et} + k^T_{nr} \tag{5}$$

1.3.5   Number of water molecules in the first coordination sphere

The number of water molecules in the first coordination sphere can be obtained from the difference between the observed lifetime (decay of the luminescence intensity) in water and in deuterated water according to Equation 6 proposed by Supkowski and Horrocks.[11]

$$q = A \cdot [\tau^{-1}_{obs}(H_2O) - \tau^{-1}_{obs}(D_2O) - k_{XH}]$$
$$k_{XH} = \alpha + \beta \cdot n_{OH} + \gamma \cdot n_{NH} + \delta \cdot n_{O=CNH} \tag{6}$$

Where $\tau_{obs}(H_2O)$ is the lifetime in water, $\tau_{obs}(D_2O)$ the lifetime in deuterated water and n_{XH} the number of XH oscillators in the first coordination sphere, α the contribution of the water molecules in the outer coordination sphere, β the contribution of an OH oscillator in the first coordination sphere, γ the contribution of a NH oscillator in the first coordination sphere and δ the contribution of a O=CNH oscillator in the first coordination sphere.

This equation was calibrated from the difference in observed lifetime as a function of the number of water molecule in the first coordination sphere of various complexes of known q numbers. The difference in observed lifetime between the water solution and the deuterated water solution comes from the different deactivation of the lanthanide ion by O-H or by O-D oscillators. The heavier isotope lowers the oscillation frequency of the chemical bond. Therefore, more oscillations from the chemical bond with the heavier isotope are needed to deactivate a lanthanide ion with a fixed energy gap between its excited and ground state. Since the probability to transfer energy to several oscillator at the same time in order to relax the lanthanide ion is defined by the probability to transfer the energy to one oscillator power the number of oscillators required to achieve a complete relaxation, the more oscillators, the lower the probability of the relaxation. It means then that the rate constant of a non-radiative deactivation by transfer to a chemical bond vibration depends on the number of vibrations needed for the deactivation (i.e., on the ratio of the vibration energy divided by the deactivation energy). By suppressing part of this non-radiative deactivation, the observed lifetime is expected to increase. Lifetimes in deuterated water are therefore higher than the lifetimes in water.

1.3.6   Europium as a versatile luminescent probe

Europium is certainly the most versatile lanthanide. Besides the characteristic red emission from its trivalent oxidation state, the divalent europium ion can be used to reproduce blue ($BaMgAl_{10}O_{17}$:Eu^{2+}) or green ($SrGa_2S_4$:Eu^{2+}) in inorganic phosphors.

Regarding the luminescence of the trivalent ion, the visible emission spectrum from Eu^{3+} is composed of the $^5D_0 \rightarrow {}^7F_J$ transitions. Three transitions are particularly useful: the $^5D_0 \rightarrow {}^7F_2$, $^5D_0 \rightarrow {}^7F_1$, and $^5D_0 \leftarrow {}^7F_0$.

The so-called hypersensitive transition ($^5D_0 \rightarrow {}^7F_2$) found around 615 nm enables detecting changes in the coordination sphere. This perturbation can be caused by the addition of another molecule (a competitive ligand for example), by a variation of the ionic strength of the solution (addition of a salt), by a variation of the polarity of the solvent (addition of another solvent), or by a variation of the pH value of the solution (addition of an acid or a base) when working in aqueous solutions.

The purely magnetic dipole transition ($^5D_0 \rightarrow {}^7F_1$) has an intensity that is practically independent of the chemical environment and that provides an estimate of the radiative lifetime of the europium ion.[12] The calculation of the radiative

lifetime of Eu^{3+} only requires its emission spectrum (corrected to take into account the sensitivity function of the detector as a function of the wavelength) and uses the ratio of the total intensity of the lanthanide emission over the intensity of the MD transition, as well as the refractive index of the medium n, and a parameter $A_{MD,0}$ that defines the strength of the MD transition. For Eu^{3+}, $A_{MD,0} = 14.65$ s^{-1} (see Equation 7).

$$\frac{1}{\tau_{rad}} = k_{rad} = A_{MD,0} \cdot n^3 \cdot \left(\frac{I_{tot}}{I_{MD}} \right) \qquad (7)$$

Finally, the $^5D_0 \leftarrow {}^7F_0$ transition is unsplit by the ligand field due to the multiplicity of one (2J+1 = 1) of both the final the initial state. This transition is usually measured by scanning at low temperature the excitation wavelength with a laser source and recording of the emission intensity of the $^5D_0 \rightarrow {}^7F_2$ transition. Since any splitting of the 0-0 transition is due to a different europium environment because a single europium species has only one peak, the number of peaks in the 0-0 transition shown in the excitation spectrum indicates the number of differently coordinated luminescent europium species.

1.3.7   Concluding remarks

Most of the photophysics of the lanthanide(III) ions was covered in this section. However, several aspects of the ligand-centered emission properties are not discussed in this introduction in details. More information can be found in the two chapters of "The Rare Earth Elements: Fundamentals and Applications" for which the author of this thesis has contributed.[4, 5]

Chapter 2 will present a typicall photophysical investigation of a new luminescent lanthanide complex. On the other hand, Chapters 3-5 will focus in more details to the particular sensitization processes that occur in the new complex design presented there. The next section will introduce the lanthanide complexes developed in this thesis and place them in their context.

1.4 Dipicolinic acid as a versatile ligand for lanthanide ions

The lanthanide complexes studied in this work are all derivatives of dipicolinic acid. This section therefore starts by presenting the parent dipicolinic acid ligand. Its properties with lanthanide ions, and particularly, the structure of the complex and its stability constant, as defined in Section 1.2.2 and in the appendices, are first introduced. In a next part, its photophysical properties, such as the quantum yields and lifetimes with europium and terbium ions, are explored. Finally, the different derivatization strategies that can be undertaken on the ligand backbone will be presented with selected examples from the literature, which will eventually lead to the introduction of the ligands investigated in this thesis.

1.4.1 Lanthanide dipicolinate complexes

There are numerous ligands that form interesting complexes with lanthanide ions. Some of those ligands are entirely artificial and were designed for a precise purpose, while others are simply natural products that are suited for coordinating lanthanide ions. In both domains, the ligands can span over a large range of complexity. However, the understanding of small and simple ligands is very important in order to comprehend and design more complex structures.

From all the simple chelates coordinating lanthanide ions, tridentate ligands are particularly suited to form nine-filled coordination sphere with three ligands coordinated to a lanthanide ion. It is therefore not surprising that one of the most remarkable simple ligand in lanthanide coordination complexes, dipicolinic acid, is tridentate. The structure of dipicolinic acid (H_2dpa) is presented in Scheme 1 together with key values associated to the ligand and to the europium and terbium complexes. This dicarboxylic acid on a pyridine core is a natural compound present in bacteria and spores. Their europium and terbium complexes were even used as an analytical way to detect such organisms by luminescence.[13]

$pK_{a1} = 0.5$

$pK_{a2} = 2.0$

$pK_{a3} = 4.5$

Eu:L

$\log\beta_{1:1} = 8.7$

$\log\beta_{1:2} = 16.8$

$\log\beta_{1:3} = 22.4$

H$_2$dpa

$[Eu(dpa)_3]^{3-}$ $\Phi_L^{Eu} = 24\%$ $\tau_{obs} = 1.6$ ms

$[Tb(dpa)_3]^{3-}$ $\Phi_L^{Tb} = 22\%$ $\tau_{obs} = 2.1$ ms
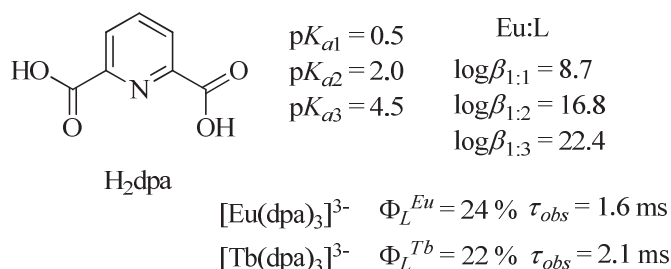
Scheme 1. Dipicolinic acid: structure, pK_a values of the ligand stability constants of its europium and terbium complex, quantum yields and lifetimes in Tris-buffered solution pH 7.4, 0.1 mM in complex. Values taken from Chauvin et al.[14] and Gassner et al.[15]

1.4.1.1 Structure

The tris(dipicolinato) lanthanide complexes, also known as trisdipicolinate lanthanide complexes, are water soluble. They crystallize at high concentrations and were investigated by X-Ray crystallography.[16, 17] They display a tricapped trigonal prism structure typical of nine-coordinated ions. The plane formed by each ligand can be oriented either in a left handed screw or in a right handed screw relative to the C$_3$ rotation axis. There are then two isomers of the complex, the Λ enantiomer and the Δ enantiomer, that crystallize as a racemic mixture. It was shown however that racemization occurs in solution.[18]
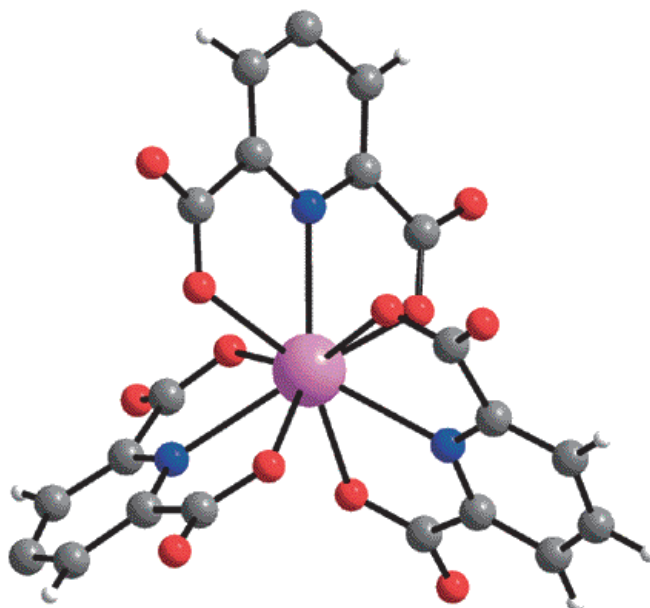
Figure 1. Structure of the lanthanide tris-dipicolinate architecture (from Chauvin et al.[14])

The tris structure is nonetheless retained in aqueous solution at neutral pH. This was proved, for example, from the lanthanide induced shifts,[19, 20] and by calculating the number of water molecules in the first coordination sphere from the observed lifetime in water and in deuterated water according to Equation 6. With $\alpha = 0.31$ ms^{-1}, $A = 1.11$ ms, and zero XH oscillators in the first coordination sphere, no water molecule is found. This parameter is important because it usually allows good photophysical properties of the luminescent lanthanide complexes. One of the major problems in aqueous solution is indeed the deactivation of the lanthanide ion by quenching with high energy vibrations such as O-H stretchings, the presence of such oscillators in direct contact with the lanthanide ion is thus highly deactivating.

1.4.1.2 *Stability of the lanthanide complexes*

The other issue in aqueous solution is the stability of the complex. The competition with the hydrated species requires strongly coordinating functional groups on the coordination site of the ligand. Dipicolinic acid coordinates as a dipicolinate, and the stability of carboxylate complexes is known to be among the best in aqueous solution. The stability constants of the dipicolinate species were calculated from spectrophotometric data at pH 7.45. $\text{Log}\beta_1 = 8.7$, $\log\beta_2 = 16.8$, $\log\beta_3 = 22.4$.[14] Those values are presented in Scheme 1. Such stability constants are in good agreement with those calculated by Grenthe from potentiometric data.[21] Grenthe also showed that this stability depends on the lanthanide ion and particularly, that the early lanthanide ions from La^{3+} up to Nd^{3+} have a lower stability than the other lanthanide ion from Sm^{3+} to Lu^{3+}. He then investigated the thermodynamics of the complexation of the lanthanide ions with dipicolinic acid and demonstrated that the entropy, enthalpy and free energy are not monotonic functions of the ionic radius, but are complicated by solvation and coordination effects.[22]

From the stability constants, one can calculate the percentage of each species in solution, i.e. tris 1:3, bis 1:2, mono 1:1 and free ligand L. This percentage depends on the pH and on the total concentration. At neutral pH, for example in Tris 0.1 M pH 7.4, and at concentrations higher than 0.1 mM, it was determined that the tris species forms predominantly with more than 85 % and that only the bis species is also present in solution (less than 15 % of bis species). If the pH is changed, the stability is also disrupted because competitive processes such as ligand protonations under acidic conditions and hydroxide formation under basic conditions are favored. For the dipicolinate complexes, it was shown by monitoring the sensitized quantum yield of the luminescence of the europium emission and of the terbium
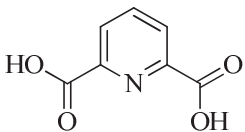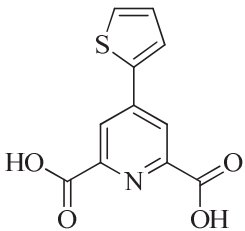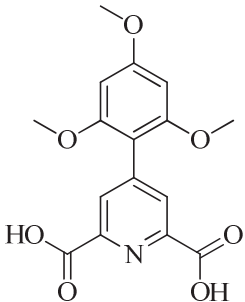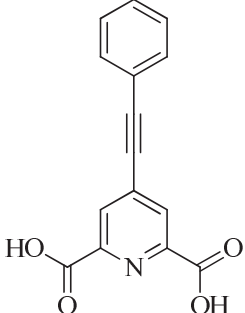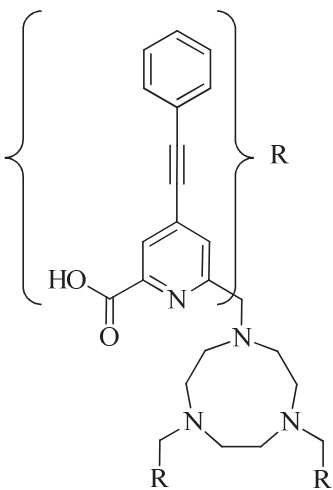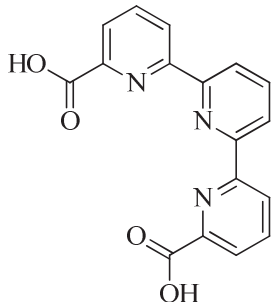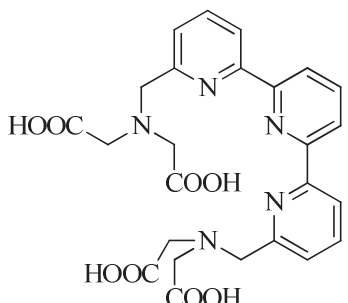
emission in their respective complexes, that the complex seems stable (no change in the quantum yield) from pH values from 4 up to 10.[23] Similarly, it was demonstrated by changing the concentration that no self-quenching phenomena are occurring in solution, the quantum yield even increasing over the whole tested concentration range because of the diminution of the bis species ratio.
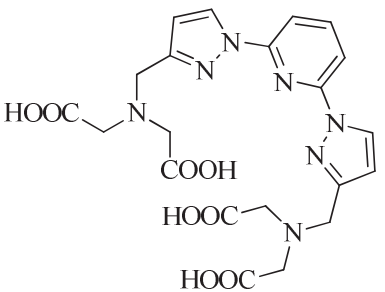
1.4.1.3 Photophysical properties

In the work by Latva et al.[24], the quantum yield in aqueous solution of the tris(dipicolinate) europium and terbium complexes is among the highest values within this family of ligand. A selection of the highest quantum yields of this works is shown in Table 1. The reason for this selection will be explained in the following section (1.4.2).

Table 1. Selection of ligands from the work of Latva et al.[24] with high quantum yields. The quantum yield values in this table have been corrected to match the standard quantum yields of the dipicolinate complexes displayed in Scheme 1

	Structure of the ligand	Φ_L^{Eu}	τ_{obs}^{Eu} / ms	Φ_L^{Tb}	τ_{obs}^{Tb} / ms
H$_2$dpa		0.24	1.65	0.22	2.25
H$_2$**L2**		0.50	1.16	~0	n.d.
H$_2$**L3**		0.09	1.23	0.50	1.26

	Structure of the ligand	Φ_L^{Eu}	τ_{obs}^{Eu} / ms	Φ_L^{Tb}	τ_{obs}^{Tb} / ms
H$_2$**L4**		0.77	1.15	0.02	0.02
H$_3$**L5**		0.44	0.85	0.01	0.07
H$_2$**L6**		0.22	0.82	0.09	2.16
H$_4$**L7**		0.35	1.31	0.30	1.1

	Structure of the ligand	Φ_L^{Eu}	τ_{obs}^{Eu} / ms	Φ_L^{Tb}	τ_{obs}^{Tb} / ms
H$_4$**L8**		0.06	1.3	0.61	2.75

Dipicolinic acid has also the unusual property to display a similar quantum yield for the terbium and for the europium emission. Most of the complexes typically exhibit a high quantum yield for one of the two lanthanide ions and a lower one for the other one. The only other ligand in Table 1, which has a similar quantum yield for both the europium and the terbium complex, is H$_4$**L7**, with its terpyridine structure bearing polyaminocarboxylates instead of simple carboxylate coordinating moieties. This particular behavior and the availability of dipicolinic acid (CHF 637.- per kg) make this ligand very good as a standard for quantum yield measurement.[14] Furthermore, as it will be shown in Chapter 6, these properties make trisdipicolinate complexes very attractive for color reproduction. The values of the quantum yields of the europium and terbium trisdipicolinate complexes in aqueous solution and in the proper pH range (around 7.4) are, after corrections, 24 % for europium and 22 % for terbium at a concentration of 0.1 mM.[23] At higher concentrations, when the tris species is nearly quantitatively present in solution (i.e. above 10 mM), the quantum yield is around 29 % ± 2 % for the europium complex. Those values were measured by an absolute method in an integrating sphere.[23] They can be used as a standard for the determination of other lanthanide quantum yields providing that the absorption is corrected to take into account the different amount of absorbed quanta (Equation 8, Φ_{sample} is the quantum yield of the sample, I^{em}_{sample} is the emitted intensity of the sample, I^{abs}_{sample} is the absorbed intensity of the sample, I_0 is the incident intensity, T_{sample} is the transmittance of the sample, T_{ref} is the transfmittance of a reference, I^{em}_{ref} is the emitted intensity of the reference and Φ_{ref} is the quantum yield of the reference).

$$
\begin{aligned}
\Phi_{sample} &= \frac{\int I^{em}_{sample}(\lambda) \cdot d\lambda}{\int I^{abs}_{sample} \cdot d\lambda} \\[2ex]
&= \frac{\int I^{em}_{sample}(\lambda) \cdot d\lambda}{\int I_0(\lambda) \cdot \left(1 - T_{sample}(\lambda)\right) \cdot d\lambda} \\[2ex]
&= \frac{\int I^{em}_{sample}(\lambda) \cdot d\lambda}{\int I^{em}_{ref}(\lambda) \cdot d\lambda} \cdot \frac{\int I_0(\lambda) \cdot \left(1 - T_{ref}(\lambda)\right) \cdot d\lambda}{\int I_0(\lambda) \cdot \left(1 - T_{sample}(\lambda)\right) \cdot d\lambda} \cdot \Phi_{ref}
\end{aligned}
\tag{8}
$$

The absorption range of dipicolinate is however quite restricted, since it absorbs only below 300 nm and with modest extinction coefficients compared to other organic chromophores. The absorption range is increased in solid state up to 350 nm. Furthermore, the f-f absorption bands are also much stronger, and particularly those around the $^5L_6 \leftarrow {}^7F_0$ transition (around 400 nm). In solid state, the microcrystalline samples exhibit also higher quantum yields. The europium emission is 58 % and the terbium one 30 %. This difference points to an easier deactivation of europium, which can gain more than terbium once the deactivations are limited. On the other hand, terbium is easier to efficiently sensitize and can reach with some sensitizers nearly quantitative quantum yields even in aqueous solution (Scheme 5, page 26).[25]

Besides europium and terbium, dipicolinic acid also forms luminescent complexes with dysprosium and samarium, as well as with NIR-emitters.[23, 26-28]

1.4.2   Derivatizing dipicolinic acid

Dipicolinic acid is a quite unique sensitizer of the luminescent lanthanide ion. Because of these exceptional properties, the dipicolinate chromophore was extensively derivatized. Most of these derivatizations focus on extending the limited absorption range (below 300 nm) of the chromophore by grafting aromatic extensions or auxochromic functional groups on the pyridine ring. The 3, 4 and 5 positions on the pyridine are therefore often modified, and particularly, the 4 position (*para* position).

1.4.2.1 Modification of the dpa framework at the para position

The *para* modification often takes place from chelidamic acid (4-hydroxydipicolinic acid, see Scheme 2) as a starting material. An important number of such derivatizations can be found in the work by Latva et al. about the investigation of a correlation between the triplet state location of the ligands and the efficiency of the lanthanide emission.[24] The best improvements considering the efficiency of the lanthanide emission (i.e. the quantum yield) was observed for the addition of a phenylethynyl group for europium (ligand H$_2$**L4** in Table 1) and a trimethoxyphenyl for terbium (ligand H$_2$**L3** in Table 1). However, the solubility should be greatly affected by those substitutions. Another advantage yet is that the excitation wavelength was extended up to 320 nm and that the extinction coefficient was also increased, particularly for the *para*-phenylethynyl (H$_2$**L4**) derivative.

chelidamic acid
(enol form)   (keto form)
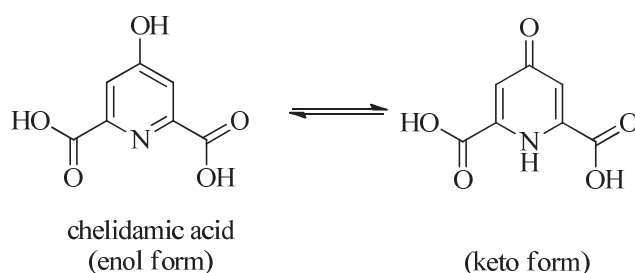
Scheme 2. Chemilamic acid and its tautomer

Para-ethynyl derivatives of dipicolinic acid were comprehensively investigated by Maury and coworkers for their attractive ability towards multi-photon absorption.[29] The presence of an electron donor amino-phenyl group at the end of the triple bond was shown to be particularly effective for improving the two-photon absorption cross section, while the presence of polyoxyethylene (POE) side chains on the amino group ensure that the complexes are water soluble.[30]

The idea to use polyoxyethylene (POE) pendent arms as solubilizing groups has been used and extended to add the possibility to couple the dpa complexes to biological materials by grafting a series of POE side chains at the *para* position on the pyridine ring.[15] The influence of the terminal functional group was demonstrated to remarkably tune the sensitization efficiency of the dpa chromophore towards the luminescent lanthanide complexes, yet mostly keeping the lifetime (both radiative and observed lifetime) and intrinsic quantum yields unaltered.

R = OMe $\Phi_L^{Eu} = 26.6\,\%$ $\Phi_L^{Tb} = 12.7\,\%$
R = OH $\Phi_L^{Eu} = 11.8\,\%$ $\Phi_L^{Tb} = 17.8\,\%$
R = NH$_2$ $\Phi_L^{Eu} = 28.9\,\%$ $\Phi_L^{Tb} = 15.3\,\%$
R = Phthalimide $\Phi_L^{Eu} = 18.3\,\%$ $\Phi_L^{Tb} = 10.8\,\%$
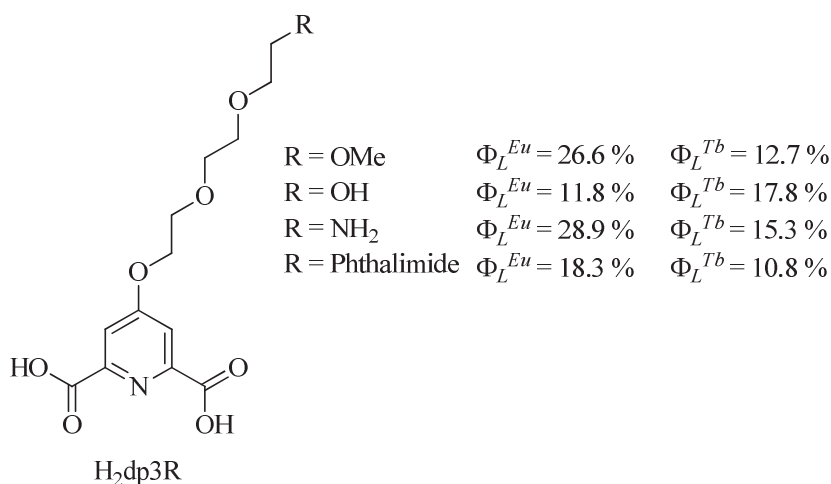
Scheme 3. R-substituted-*para*-trioxyethylenated dipicolinate ligands (dp3R) and the corresponding quantum yields for the europium and terbium complexes

Regarding the length of the polyoxyethylene side chains, Gassner et al. did not investigate its influence on the properties of the complexes. However, Deiters et al. reported that the length of a solubilizing POE side chain on helicate architectures (with ligands H$_2$L^{C2} and H$_2$L$^{C2'}$ in Figure 2, page 28) has little impact on the stability and luminescence properties of the lanthanide complexes.[31]

Fernández-Moreira et al. with ligand H$_2$L$^{C2(CO2H)}$ (also depicted in Figure 2, page 28) grafted helicate complexes with biological material and used them for the lab-on-a-chip detection of cancer biomarkers.[32] The POE side chain then acted as a linker between the luminescent complex and the labeled biological material. However, no occurance of POE linkers between a sensitizer and a lanthanide ion was found.

POE side chains may not be ideal as linkers between a coordinated lanthanide ion and a sensitizer because of its flexibility. It is nonetheless difficult to have a rigid linker without any conjugated linker, which would alter the photophysical properties of the terminal sensitizer and coordinating dpa moiety. A solution would be to rely on peptide linkers, since peptide bonds should adopt preferentially a trans conformation. This solution was used by Parker and coworkers who showed that the incorporation of a valine linker between a dota coordination site and a phenanthridine sensitizer decreased the quantum yield of the complex (see Scheme 4).[33]

Estimated separation
Eu-phen
2.55 Å

$\Phi_L^{Eu} = 6.3\ \%$
$\tau_{obs} = 0.64$ ms

Estimated separation
Eu-phen
5.2 Å

$\Phi_L^{Eu} = 1.4\ \%$
$\tau_{obs} = 0.68$ ms

$\Phi_L^{Eu} = 0.4\ \%$
$\tau_{obs} = 0.61$ ms

Estimated separation
Eu-phen
8.2 Å
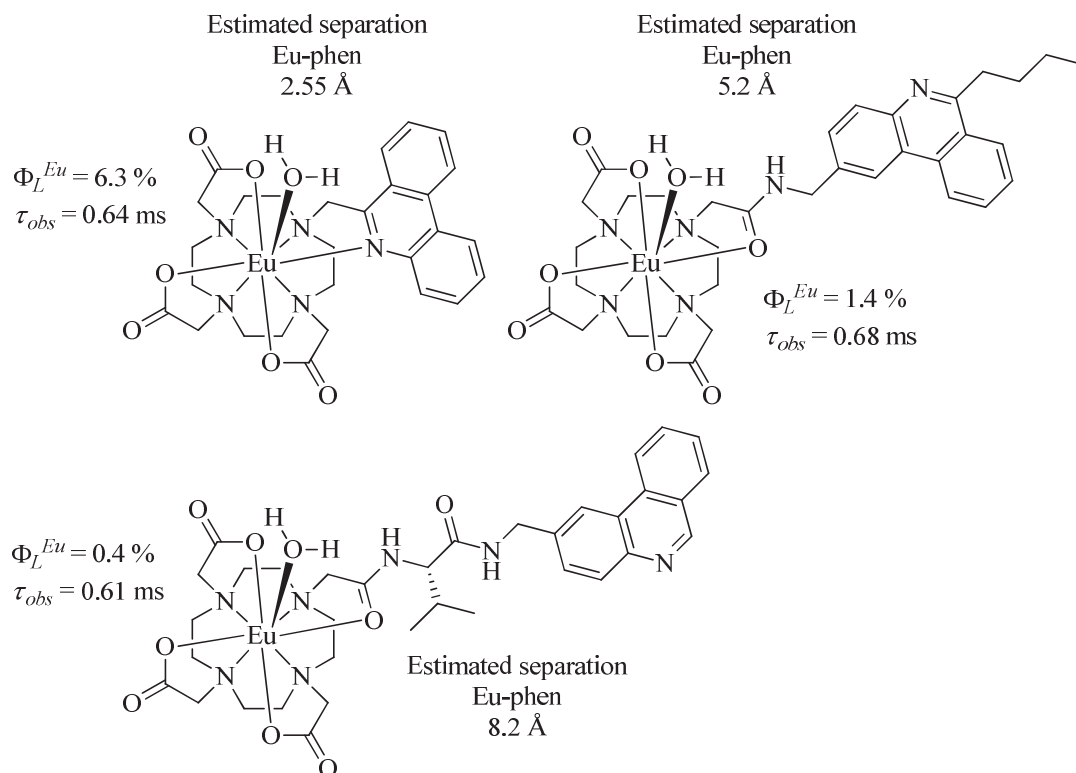
Scheme 4. Sensitization of europium by phenanthridyl groups located at different distances from the europium ion coordinated to a dota moiety (taken from Clarkson et al.[33])

In solid states, the POE side chains usually adopts a trans-gauche-trans conformation at each -CH$_2$CH$_2$O- unit, which forms helical structures.[34] In solution, the movement (diffusion) of polymer pendent arms grafted on a surface generally describes mushroom structures at room temperature when the density of the polymer pendent arms is low and brush structures at high density.[35]

With similar potential applications than the dp3R ligands, clicked dipicolinate ligands (*para*-triazolyl dipicolinate) proved to be interesting dpa derivatives.[36] Multiple photons excitation properties were demonstrated with the *para*-triazolyl-dipicolinate antennae. They were also successfully derivatized to be grafted on a glass surface.

1.4.2.2 *Modification of the dpa framework on the coordinating groups*

The remaining positions suitable for a derivatization of the dipicolinate framework are the coordinating carboxylate functional groups. Here again, a large number of structures were developed over the years. In the quite comprehensive

work by Latva et al., the replacement of the tridentate coordinating moieties by polyaminocarboxylates that add six coordination sites was found to yield interesting improvements. The best results for europium and terbium are respectively a terpyridine derivative (H_4**L7** in Table 1) and a bis(N-pyrazolyl)pyridine derivative (H_4**L8** in Table 1).

Such modifications change completely the coordination of the lanthanide ion since they alter the coordination site. The complexes have now a 1:1 stoichiometry (one ligand per lanthanide ion) and are mononegatively charged. The extension of the absorption range increases up to 330 nm for both ligands, even though the extinction coefficient remains quite low. A derivatization of H_4**L8** with a carbamoyl substituent at the *para* position of the pyridine ring yielding H_4**L9** resulted in the most efficient terbium complex with a near unity quantum yield.[25]

$$[TbL]^-$$
$$\Phi_L^{Tb} = 95\ \%$$
$$\tau_{obs} = 2.65\ ms$$

H_4**L9**
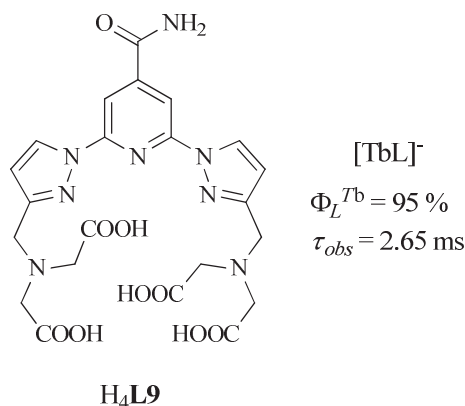
Scheme 5. Polycarboxylate-bearing dipyrazolylpyridine ligand with a near-unity quantum yield of the terbium complex (taken from Brunet et al.[25])

From the dipicolinic structure, only the pyridine core remains in those architectures since the modification is performed on both carboxylates symmetrically. In some other chromophores, only one half of the dipicolinate core is altered, thus resulting in picolinate structures, for examples in the macrocyclic architecture of H_3**L5** in Table 1.

A nice illustration of this kind of modification is helicates [Ln_2L_3] based on 6-benzimidazolylpicolinic acid. Helicates are ligands that wrap around the metal ions and form a helical shape. The first occurrence of such architectures with lanthanide ions is a self-assembled triple helical dinuclear complex obtained by Piguet and

coworkers.[37] This complex was however not water soluble. Later on, together with Bünzli and coworkers, they presented similar complexes with the 6-benzimidazolylpicolinate coordination site ([Ln$_2$L$^C_3$], which is stable in water, yet slightly soluble. Water solubility was increased by grafting polyoxyethylene pendent arms on the H$_2$L^C ligand.[31, 38-40] It was found that the *para* position on the pyridine ring was a better solution than the N-benzimidazole location because of its superior luminescence. Figure 2 shows all the different derivatizations of this family of ligands. For more information, see [41].

The 6-benzimidazolylpicolinate chromophore turned out to be an efficient sensitizer, particularly for europium. The development of europium tris(6-benzimidazolylpicolinate) complexes by Shavaleev et al. led to very high quantum yields for the europium emission in solid state samples.[42] Besides the very good photophysical properties of these complexes, a series of derivatization also yield to a nice correlation between the location of the triplet excited state of the ligand and the quantum yield of the corresponding sensitized europium emission with triplet state locations between the $^5D_2$ and $^5D_1$ spectroscopic levels of europium(III).

		[EuL$_3$]
H**L10**	R = H	Φ_L^{Eu} = 71 %, τ_{obs} = 2.95 ms
H**L10F**	R = F	Φ_L^{Eu} = 68 %, τ_{obs} = 3.00 ms
H**L10Cl**	R = Cl	Φ_L^{Eu} = 71 %, τ_{obs} = 2.94 ms
H**L10Br**	R = Br	Φ_L^{Eu} = 54 %, τ_{obs} = 2.51 ms
H**L10Me**	R = CH$_3$	Φ_L^{Eu} = 68 %, τ_{obs} = 2.69 ms
H**L10O8**	R = OC$_8$H$_{17}$	Φ_L^{Eu} = 52 %, τ_{obs} = 2.45 ms
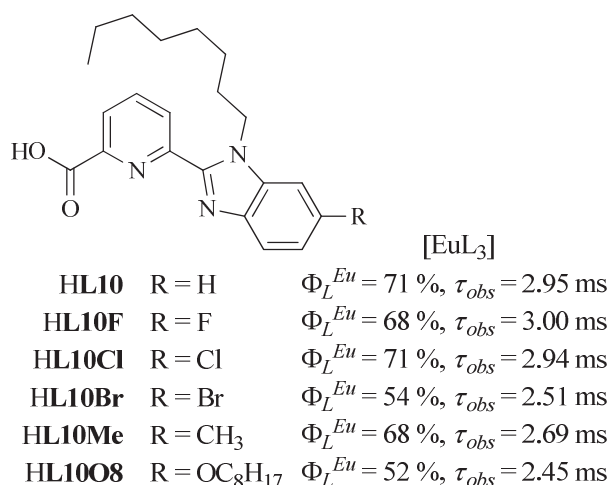
Scheme 6. Tridentate ligands based on a 6-benzimidazolylpicolinic acid structure and the corresponding quantum yields and lifetimes of the europium complexes in solid state (taken from Shavaleev et al.[42])
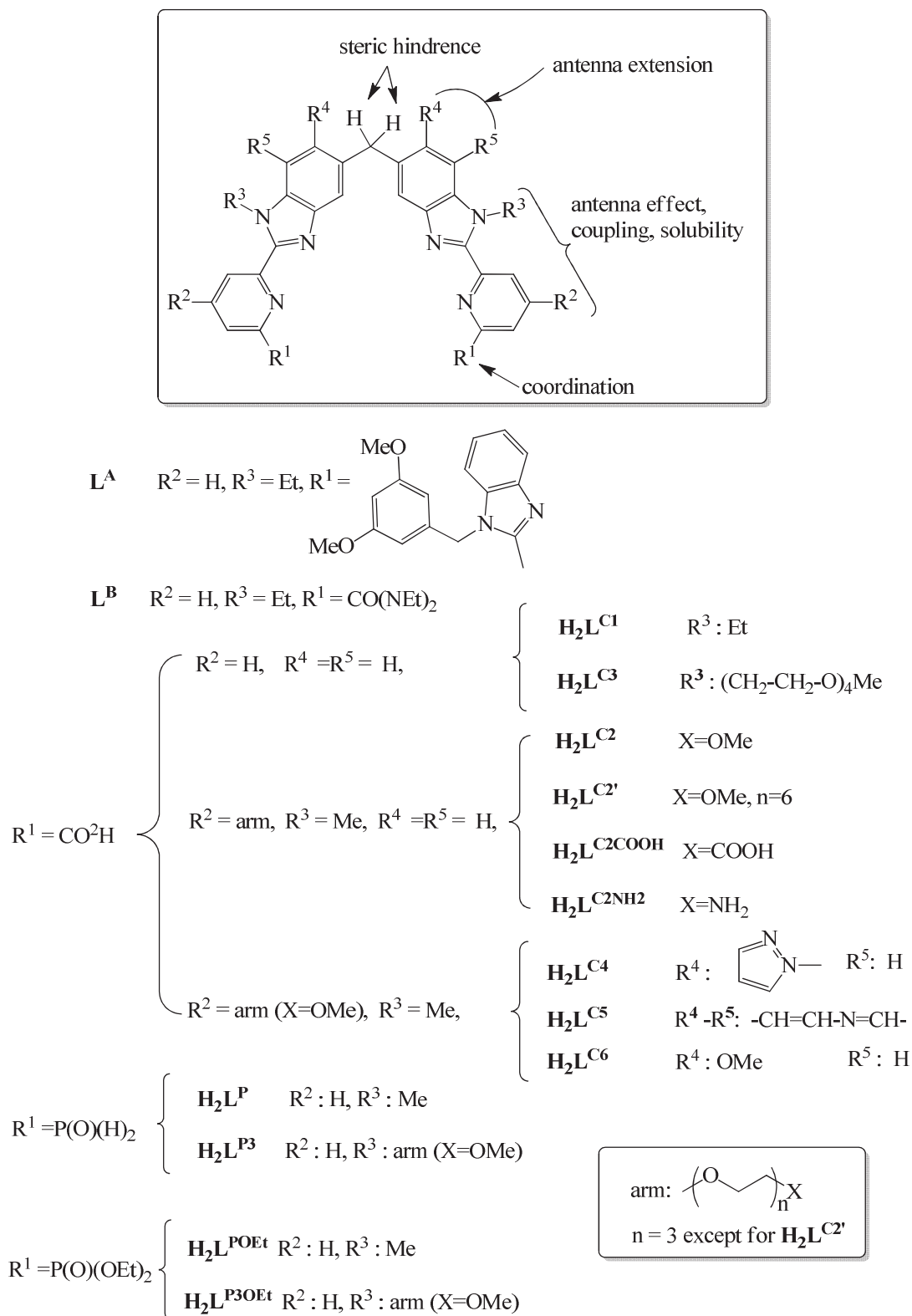
Figure 2. Ditopic ligands able to form 2:3 Ln:L helicates (taken from Chauvin[41]).

Among the numerous variations of the helicate ligands, the modification of the coordination site was of course investigated. Other groups than the carboxylate, which guarantee a good stability in aqueous solution, were tested, and phosphoryl derivatives were found to be valuable to further increase the stability of the lanthanide complexes.

Similar effects were observed on simpler structures: In macrocyclic architectures, for instance when comparing H_3do3a (1,4,7,10-tetraazacyclododecane-1,4,7-triacetic acid, see Scheme 7), H_4dota (1,4,7,10-tetraazacyclododecane-1,4,7,10-tetraacetic acid, , see Scheme 7), and H_4dota-like ligands with their phosphonate analogs, the stability of the phosphorylated ligands was enhanced, yet conserving the coordination mode, compared to the carboxylate analog.[43, 44] The same trend was observed in complexes with pyridine based ligands, for example with bis(N-pyrazolyl)pyridine ligands[45] and bipyridine ligands[46].
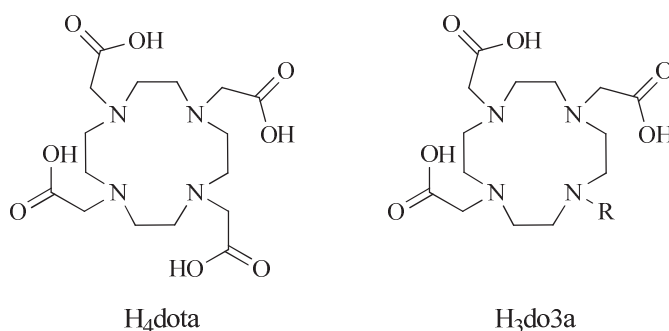
Scheme 7. Dota and do3a structures

1.4.3   From dipicolinic acid to 6-phosphorylpicolinic acids

Concerning the effect of a phosphoryl coordinating group versus a carboxylate one on the luminescence properties of the lanthanide complexes, little documentation are found.[45-48] It seems however, that the replacement of a carboxylate with a phosphonate sometimes enhances the luminescence quantum yield and/or the observed lifetime.[45, 46, 48] For example, the terbium complex of bis(N-pyrazoyl)pyridine polyaminocarboxylate $L8^{4-}$ (see Table 1) exhibits a quantum yield of 61 % and a lifetime of 2.75 ms whereas the phosphonate analog has a lower quantum yield of 37 % but a higher lifetime of 3.28 ms.[45] In helicate

structures, the phosphorylated analogs $[\text{Tb}_2(\text{L}^{\text{POEt}})_3]$ and $[\text{Tb}_2(\text{L}^{\text{P}})_3]$ (see Figure 2) have a quantum yields twice as large as the carboxylate analog $[\text{Tb}_2(\text{L}^{\text{C1}})_3]$ (1.2 %), although quite modest with values of 2.5 % and 2.7 % respectively. Compared to the europium complexes with the same ligands, the quantum yields are always lower with the phosphorylated ligands than with the carboxylate ones.[48] An advantage of phosphoester groups as in the LPOEt ligand seems yet to be an improvement of the water solubility, whereas phosphonates tends to form precipitates. Therefore, phosphoesters might also be an interesting and easier way to enhance the water solubility of some lanthanide complexes.

Motivated by the possibility to improve the photophysical properties of the already efficient dipicolinate sensitizer and even possibly increase the stability of the lanthanide complexes, one of the carboxylate of the dipicolinate ligand will be replaced by a series of three phosphoryl derivatives. 6-Diethoxyphosphorylpicolinic acid (H**deppa**), 6-monoethoxyphosphoryl-picolinic acid (H$_2$**meppa**) and 6-dihydroxyphosphorylpicolinic acid (H$_3$**dhppa**) will be investigated during this thesis (structures presented in Scheme 8). Their acid/base properties, the stability constants of the different species of their lanthanide complexes and the photophysical properties of the most stable species, which should be the tris species if the coordination mode is similar to the dipicolinate ligand, will be determined in aqueous solution. This study takes place as an investigation of the importance of the coordination site, and as a possible derivatization of the dipicolinate framework that is simpler than on a complicated architecture such as helicates, and that should alter neither the water-solubility, nor the stability of the complexes.
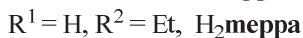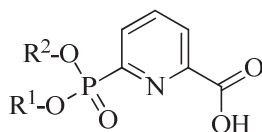
$$R^1 = R^2 = Et, \quad H\textbf{deppa}$$
$$R^1 = H, R^2 = Et, \quad H_2\textbf{meppa}$$
$$R^1 = R^2 = H, \quad H_3\textbf{dhppa}$$

Scheme 8. Diethoxyphosphoryl picolinic acid (H**deppa**), monoethoxyphosphoryl picolinic acid (H$_2$**meppa**), and dihydroxyphosphoryl picolinic acid (H$_3$**dhppa**).

1.4.4   Terminal chromophores on *para*-polyoxyethylene dipicolinic acid

The possibility to graft something else than biological materials at the end of *para*-polyoxyethylenated dpa (R position on Scheme 3, page 24) was not mentioned in the original work on such complexes.[15] This framework seems however versatile enough to accommodate materials such as nanoparticles or smaller compounds such as chromophores. Therefore, *para*-POE-dpa complexes could be interesting to probe surfaces or investigate the delicate relationship between a sensitizer and the luminescence of the lanthanide ion, because of the possibility to have terminal distant compounds which seem not to affect the coordination sphere of the lanthanide ion.

In the present thesis, we are interested in increasing the absorption range of lanthanide trisdipicolinate complexes, because it would be more convenient to excite the complexes under longer wavelength UV light (e.g., with a 366 nm light source instead of the 254 nm one). The addition of a terminal distant chromophore on the *para*-POE-dpa architecture could be an interesting way to achieve this purpose if the distant chromophore can act as a sensitizer for the lanthanide ion coordinated on the dpa moiety. Furthermore, such a system would allow investigating the effect of the sensitizer on the sensitization efficiency without disrupting the coordination, and thus keeping the environment of the lanthanide ion unchanged, which is something that was little investigated yet.

One of the major problems when comparing different sensitizers is indeed that the coordination sphere and therefore the ligand field around the lanthanide ion often depends on the nature of the backbone of the sensitizer. It is hence delicate to conclude whether an improved emission of the luminescent lanthanide ion is due to the coordination, to the structure of the ligand, its photophysical properties or to a combination of those contributions. It has been proven for example that the radiative lifetime of the lanthanide excited states mainly depends on the refractive index of the medium and on the coordination environment of the lanthanide ion.[49]
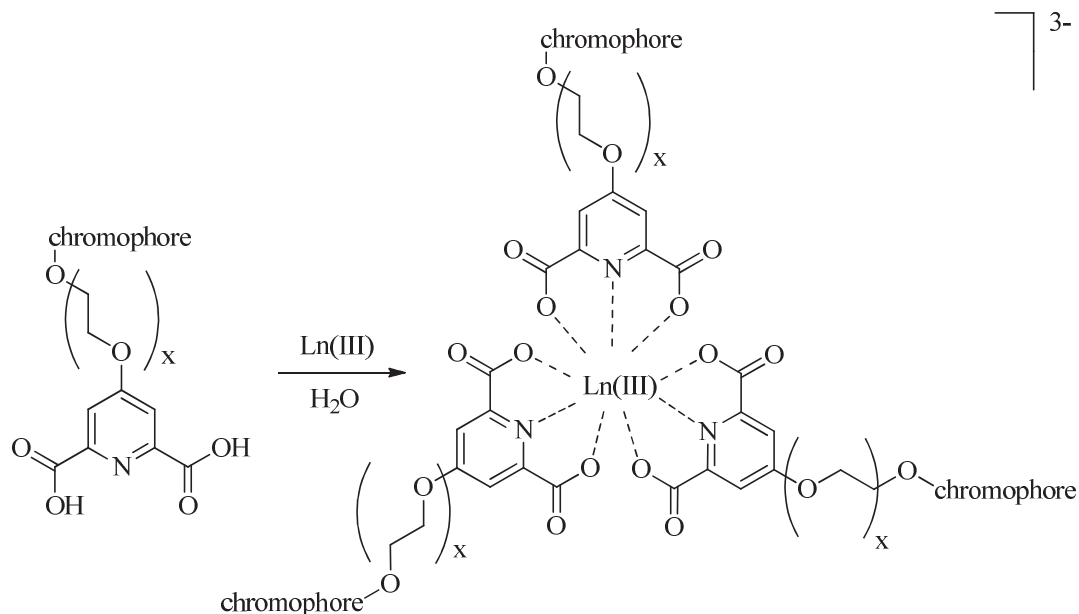
Scheme 9. Ligand design forming tris complexes with lanthanide ions and allowing the variation of the distant chromophore and of the length (x = 1-3) of the polyoxyethylene (POE) side chain
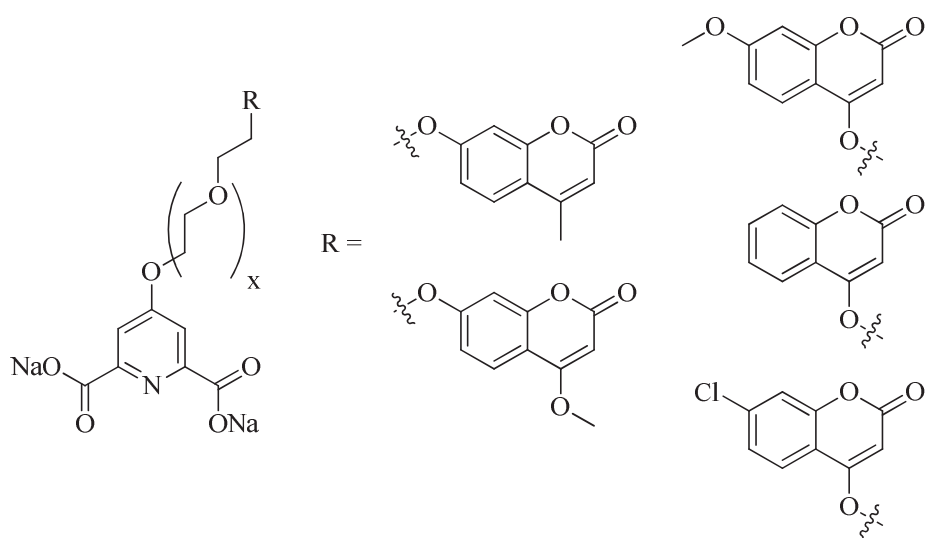
Scheme 10. Series of coumarins tested as chromophore

The general structures of the ligands and corresponding complexes are depicted in Scheme 9. In a first step, a series of coumarin fluorophores (shown in Scheme 10) will be tested in order to prove that such a system can sensitize lanthanide ions. Different coumarins will be used so as to study the influence of the structure of the

sensitizer on the sensitization efficiency, and particularly the effect of the location of their excited states. With the best candidate, the sensitization pathways will be further investigated. The POE linker will be shortened in a second step (x = 1-3). The purpose is to prove that by having a sensitizer closer to the lanthanide ion, the sensitization efficiency is increased as predicted by energy transfer theories.

Regarding the length of the linker, polyoxyethylene side chains may not be ideal to look for a distance relationship, because of its flexibility, as already explained previously. The position of the sensitizer at the end of the side chain relative to the lanthanide ion is hence certainly not well defined; nevertheless, the sensitizer is clearly not in direct contact with the lanthanide ion because of the three dpa moieties that already fulfil the coordination sphere.

There are a few examples of coumarin-sensitized lanthanide luminescence in the literature, most of which involving macrocyclic crown ethers, or the direct coordination of a coumarin.[50-55] Their photophysical properties, with absorption typically in the 300-450 nm range and emission in the 350-550 nm range, are yet quite attractive for the sensitization of lanthanide ions. In addition, the substitution effects are well-documented.[56, 57] The simpler coumarins are also easily synthesised,[58] and some coumarins, particularly 4-methylumbelliferone (aka 4-methly-7-hydroxycoumarin), are commercially available and inexpensive. The incorporation of coumarins as sensitizer in polyaminocarboxylate complexes were demonstrated by Féau et al.[59] Recently, an analyte responsive luminescent probe based on an analyte-triggered formation of a coumarin sensitizer was also developed.[60] The system is based on a dota macrocycle coordinating europium or terbium, and on a protected coumarin precursor that can undergo a cyclization to form the sensitizing coumarin in presence of the proper deprotecting analyte. For all these reasons, the coumarin family was the first choice to test terminal sensitizers. Finally, the work of Selvin and co-workers on quinolinones as sensitizers should also be mentioned here.[61-64] The structure of quinolinone is close to the one of coumarins, the endocyclic oxygen atom of coumarins being replaced by an amine in quinolinones.

The motivation of this study is to prove that such an architecture can sensitize lanthanide ion, and to develop a synthesis in order to easily vary the sensitizer and eventually control its photophysical properties. The second motivation is the ability to change the linker, and particularly, easily modify its length, thus resulting in a versatile ligand design, which could be used to investigate many fundamentals of the sensitization of the lanthanide ions with a simple framework. Finally, the

possibility to extend the absorption range of dpa based ligands and the opportunity to have a fluorescent emission from the distant chromophore together with the long lived lanthanide luminescence is attractive for color reproduction and optical document security.

This study also takes place as an investigation of the *para* derivatization of the dipicolinate framework that is a logical continuation of the state of the art about such modifications.

1.4.5   Concluding remarks

Up to now, this chapter has presented purely chemical or photophysical related topics. The ligands and the corresponding lanthanide complexes that will be investigated in the next chapters have just been introduced, and the motivations for their study have been explained. However, this thesis is also interested in using luminescence, and particularly luminescent lanthanide complexes for color reproduction. Some basic notions about colorimetry and color reproduction are therefore required. They will now be presented.

1.5   Colorimetry

This section opens the introduction about color science. Basic concepts required to understand the color reproduction part of this thesis will be presented hereafter, starting with colorimetry. More information can be found in the book by Wyszecki and Stiles.[65]

Colorimetry is the science that measures and characterizes the color perception of the human visual system. It associates the perceptual colors to photophysical spectral properties and formulates them mathematically. The spectral characteristics that are related to colors are spectrophotometric or spectroradiometric properties such as the reflectance, the transmittance, and the spectral radiant emittance. They define respectively the amount of light reflected on an object, transmitted through it and emitted from it, for example by luminescence. Because the human retina of the eye is composed of three types of photoreceptor cells (cone cells) that are responsible for color vision, the human visual system is trichromic.[66] It means that any cone response produced by a stimulus can be reproduced by balancing the

intensity of three primary light sources capable of activating the cones with different levels. Grassmann's law states thereof that any luminous stimulus can be expressed as a weighted sum of three primaries, and that this equalization is constant over a wide range of illumination level.

Early experiments were performed by the CIE (commission internationale de l'éclairage) in order to define the relative combination of a red (r), a green (g) and a blue (b) spot light (projector) that would yield an identical color as a defined sample. In order to be able to define the relative intensity of the r, g and b projector without performing the experiment, they equalized each monochromatic color along the wavelength range of the visible spectrum. This yielded three color matching functions $\overline{r}(\lambda)$, $\overline{g}(\lambda)$, and $\overline{b}(\lambda)$ giving the intensities of each primary red, green, and blue spot light. The color matching functions determine how sensitive the human visual system is to red, green and blue light. They also allow to equalize any color as a linear combination of these three color matching functions. Any color is thus defined as a tri-stimulus value R, G and B according to Equation 9.

$$R = \int_{\lambda_{vis}} \overline{r}(\lambda) \cdot S(\lambda) \cdot d\lambda$$

$$G = \int_{\lambda_{vis}} \overline{g}(\lambda) \cdot S(\lambda) \cdot d\lambda \qquad (9)$$

$$B = \int_{\lambda_{vis}} \overline{b}(\lambda) \cdot S(\lambda) \cdot d\lambda$$

They however noticed that the chosen primaries result in a negative color matching function of the red primary from 430 up to 550 nm. To facilitate the calculation of colors, a new set of primaries was defined later based on the RGB system. The requirement was that the color matching functions should be positive over the whole visible spectral range, that one of the color matching function corresponds to the photopic luminous efficiency function V(λ), which determines the sensitivity of the human visual system under daylight, and that a constant energy white illumination should yield equivalent tristimulus values (normalized values of 1/3 each). The new color matching functions were called $\overline{x}(\lambda)$, $\overline{y}(\lambda)$, and $\overline{z}(\lambda)$. They are displayed in Figure 3. The colors represented as XYZ tri-stimulus values can be represented in a 3D color space called the CIE-XYZ color space, which is the basic space in colorimetry.[67, 68]
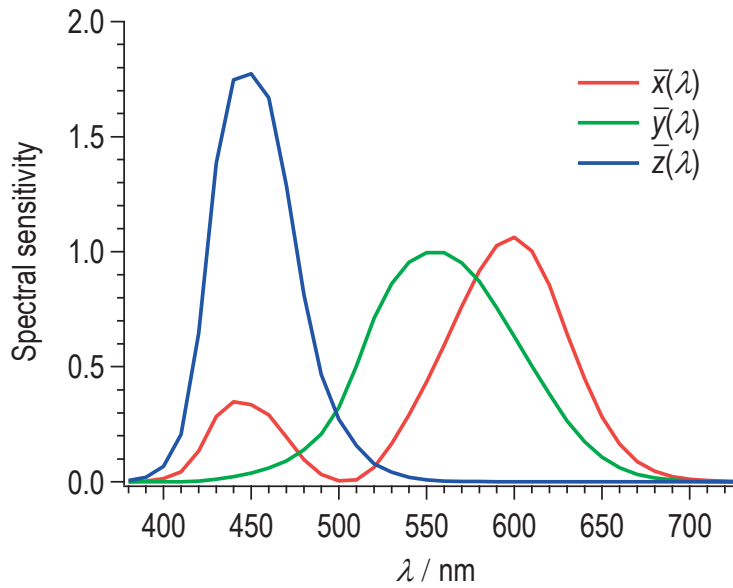
Figure 3. Color matching functions of the CIE-XYZ color space

The projection of the XYZ coordinates onto the X + Y + Z = 1 plane yields the x, y and z chromaticity values. Since they are defined by two of the three values, only x and y are usually kept together with the Y value, which corresponds to the relative luminance. The xyY color space is widely used. The xy coordinates provide the chromaticity of the stimulus. They are typically displayed in the chromaticity diagram shown in Figure 4.
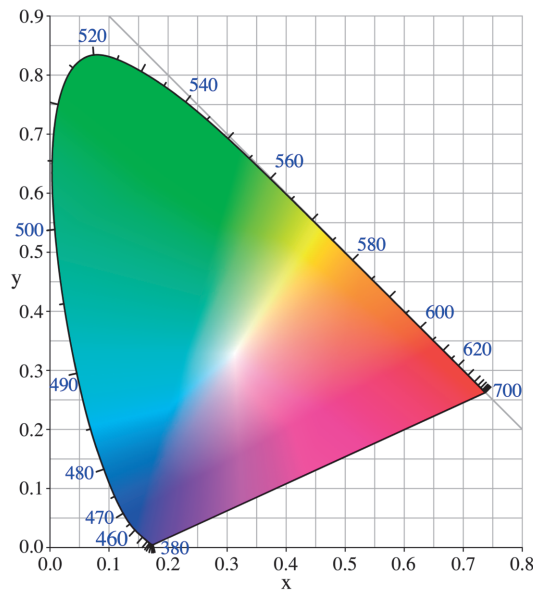
Figure 4. CIE-xyY chromaticity diagram of the human visual system (Y = 100)

The XYZ tri-stimulus values are calculated from the irradiance of a stimulus $S(\lambda)$ similar to the RGB values. A scaling factor K constrains the range of Y values up to 100. The Y = 100 value then represents the maximal luminance of the considered system. This maximal luminance is usually defined as the brightest white. A reference stimulus $S_{ref}(\lambda)$ will be used hereafter to set the scaling factor K, according to Equation 10.

$$X = K \cdot \int_{\lambda_{vis}} \overline{x}(\lambda) \cdot S(\lambda) \cdot d\lambda$$

$$Y = K \cdot \int_{\lambda_{vis}} \overline{y}(\lambda) \cdot S(\lambda) \cdot d\lambda$$

$$Z = K \cdot \int_{\lambda_{vis}} \overline{z}(\lambda) \cdot S(\lambda) \cdot d\lambda \qquad (10)$$

$$K = \frac{1}{\int_{\lambda_{vis}} \overline{y}(\lambda) \cdot S_{ref}(\lambda) \cdot d\lambda}$$

For colors formed by reflected or transmitted light, the reference stimulus $S_{ref}(\lambda)$ is most of the time the illuminant or the whitest color achievable by reflection or transmission of this illuminant on or through an object. For a color formed by reflection of light (reflectance mode), the stimulus $S(\lambda)$ would be an illuminant $I(\lambda)$ reflected on the surface of an object with a reflectance $R(\lambda)$, thus resulting in the stimulus $S(\lambda) = R(\lambda) \cdot I(\lambda)$. Similarly, for a color formed by transmission of light (transmittance mode), the stimulus $S(\lambda)$ resulting from an illuminant $I(\lambda)$ transmitted through an object with a transmittance $T(\lambda)$ is $S(\lambda) = T(\lambda) \cdot I(\lambda)$. If on the other hand, the color is formed by the emission of light from a surface or from an object (emission mode), the stimulus $S(\lambda)$ is directly a spectral radiant emittance (hereafter simply called emittance) $E(\lambda)$ coming out of the sample, for example from a luminescent material. In that case, the reference stimulus $S_{ref}(\lambda)$ should be the whitest and brightest emission that can be generated by emitting material, or an arbitrary white reference such as a D65 illuminant or E illuminant.

The chromaticity coordinates xyY are obtained by dividing each tri-stimulus values by the sum of the tri-stimulus values (Equation 11).

$$x = \frac{X}{X+Y+Z}$$

$$y = \frac{Y}{X+Y+Z} \qquad (11)$$

$$z = 1 - x - y$$

The CIE-XYZ is the fundamental color space in colorimetry. However, color differences are not perceptually uniform across this space, as demonstrated with the so-called MacAdam's ellipses.[69] It means that a color difference (i.e., two colors located at a defined distance from each other in the color space) in the green is very dissimilar from the same color difference in the blue for example. Therefore, perceptually significant color differences cannot be specified in the CIE-XYZ color space.

The CIELAB color space, which is a non-linear transformation of the CIE-XYZ color space as defined in Equation 13, is a perceptually nearly uniform color space. It encloses L^*, a^* and b^* coordinates that represent the lightness axis, green to magenta axis and blue to yellow axis respectively. Such a representation hence separates the lightness of a color from its chroma and hue represented by the a^* and b^* values. The chroma or chrominance is defined in the CIELAB space as the Euclidean distance from the lightness axis. The hue is the azimuth angle between the reference hue, which is magenta ($h_{ab} = 0°$), and the line of the projection of the color point coordinate on the a^*b^* plane (Equation 12). The CIELCH is then a cylindrical representation of the CIELAB color space.

$$C_{ab}^* = \sqrt{a^{*2} + b^{*2}}$$

$$h_{ab} = \text{atan} 2\left(\frac{b^*}{a^*}\right) \qquad (12)$$

The CIELAB coordinates are calculated from the CIE-XYZ tri-stimulus values, providing a reference tri-stimulus value (X_n; Y_n; Z_n) that represent the white point of the color space, i.e. the (L^*; a^*; b^*) = (100; 0; 0) coordinate. A simple lightness and chromatic adaptation is then performed in the calculation of the CIELAB colors. Note that the scaling factor K from Equation 10 should be the same in the calculation of the CIE-XYZ of the sample (X; Y; Z) and of the white reference (X_n; Y_n; Z_n).

$$L^* = 116 \cdot f\left(\frac{Y}{Y_n}\right) - 16$$

$$a^* = 500 \cdot \left[f\left(\frac{X}{X_n}\right) - f\left(\frac{Y}{Y_n}\right) \right]$$

$$b^* = 200 \cdot \left[f\left(\frac{Y}{Y_n}\right) - f\left(\frac{Z}{Z_n}\right) \right] \qquad\qquad (13)$$

$$f(t) = \begin{cases} t^{\frac{1}{3}} & \text{if } t > \left(\frac{6}{29}\right)^3 \\ \frac{1}{3} \cdot \left(\frac{29}{6}\right)^2 \cdot t + \frac{4}{29} & \text{otherwise} \end{cases}$$

The colors of digital pictures are usually defined in the sRGB color space. The sRGB color space is a standard color space developed for display devices. It consists in an additive color synthesis of a red, a green and a blue color primary typical of red green and blue phosphors. The sRGB values are raised by a gamma power function, usually 2.2, that corresponds to the non-linear relationship between the CRT voltage and the displayed intensity. The chromaticities of the primaries and of the white point are defined. The white point should match a D65 illuminant. The luminance level and ambient illuminantion are also parameters of the sRGB specification. To convert sRGB values into CIE-XYZ, the gamma transfer function is applied first so that the RGB values add linearly. A transformation matrix is then applied on the linear sRGB values in order to obtain the corresponding CIE-XYZ tristimulus values.

1.6   Color reproduction

The human visual system can differentiate up to about 10 million colors, but when it comes to color reproduction, most devices can only reproduce part of the perceivable colors. When represented in a color space, the sub-space that encloses all the colors reproducible by a device or method is called a gamut. For example, when printing an image, all the colors that can be printed out of a specific printer with a defined set of inks and on a defined substrate form the print gamut. The same applies for display devices, which can only display colors by additive combinations of primaries (from phosphors in cathod ray tube CRT and plasma displays, or from

RGB filtered white emission in liquid crystal displays LCD). The gamut is usually represented by its boundary. Outside the domain delimited by the boundary, the colors cannot be reproduced.

Because of its good uniformity, CIELAB is the preferred color space to visualize gamuts. The extent of the gamuts can therefore be compared together, with minimal color difference issues due to the non-uniformity of the color space. This also enables the definition of color difference metrics that allow comparing two colors together. Such color differences are often estimated by the ΔE and its improved version, the ΔE^*_{94} and the ΔE^*_{00}. The ΔE^*_{94} is preferred here because of its simpler implementation yet accurate enough metric. It is defined according to Equation 14.

$$
\begin{aligned}
\Delta L^* &= L_1^* - L_2^* \\
\Delta a^* &= a_1^* - a_2^* \\
\Delta b^* &= b_1^* - b_2^* \\
\Delta E_{ab}^* &= \sqrt{\Delta L^{*2} + \Delta a^{*2} + \Delta b^{*2}} \\
\Delta C_{ab}^* &= C_1^* - C_2^* \\
\Delta H_{ab}^* &= \sqrt{\Delta E_{ab}^{*\,2} - \Delta L^{*2} + \Delta C_{ab}^{*\,2}} \\
\Delta E_{94}^* &= \sqrt{\Delta L^{*2} + \left(\frac{\Delta C_{ab}^*}{1 + 0.045 \cdot C_1^*}\right)^2 + \left(\frac{\Delta H_{ab}^*}{1 + 0.015 \cdot C_1^*}\right)^2}
\end{aligned}
\tag{14}
$$

1.6.1   From color images to halftoned color prints

One way to reproduce colors is to print them on a substrate, typically paper. The printing process creates a printed image from a displayed image. Printing is a mechanical process. The oldest printing technology relies on the transfer of a latent image, formed or carved on a solid substrate, onto a substrate. The word "print" actually comes from the old French "preindre" meaning to press. Nowadays, there are two main types of printing: those formed by pressing a latent image on a substrate, and those formed by mechanically painting the substrate directly. Offset and intaglio printing are examples of the first category, whereas ink-jet printing is an example of the second.

In every printing process, the printable colors are limited by two factors: the color of the inks, which is mostly determined by their absorption spectra, and the number

of different inks (i.e., the number of different colors). This limitation comes from the binary nature of the printing method. An ink dot can be either printed or not printed at a defined location. Therefore, the number of colors is determinded by the number of combinations of the inks. For three inks, there are eight different combinations, which yield eight different colors. The colors generated by superposition of the inks are called hereafter colorants. In order to overcome this binary limitation, and particularly, to introduce variable intensity colors, a mean of printing different surface coverages of the inks is required. This process is called halftoning. Halftoning is a process that transforms a continuous tone into a binary tone made of printed dots. If the size of the halftone (of the dots) is small enough, or if the viewing distance is large enough, the halftone looks like it was continuous.

Historically, halftones come from photography. In order to engrave an object on a photosensitive plate without introducing large etched areas that are detrimental for intaglio printing, William Henry Fox Talbot used in the mid 18th century a screen of gauze to develop a regular pattern throughout the whole plate first, and then expose the object. Thereby, the plate was fully exposed where the object did not block the light, and the screen pattern was present where light was blocked. If the pattern was fine enough, the resulting printed pattern was quite invisible but looked like a mid-tone. The fundamental principle of halftoning is to convert variable intensity images or tones into dot like patterns by means of a screen.

dpi (dot per inch) = Ink pixel resolution
lpi (line per inch) = Halftone screen frequency
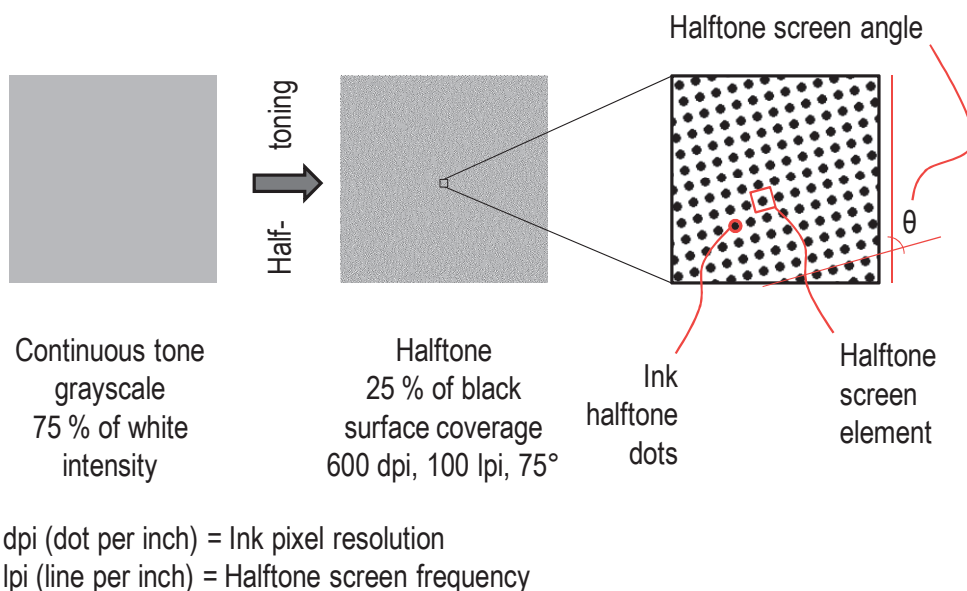
Figure 5. Halftoning principle with a classical rotated screen

Modern halftones are classified in two distinct types: amplitude modulated halftones are halftones where the tones are reproduced by increasing the size of inked areas repeated at a fixed frequency, and frequency modulated halftones are halftones where the size of the inked areas is fixed but where the frequency of the inked areas is increased to achieve darker tones. Classical rotated screen halftones are examples of amplitude modulated halftones because a periodic halftone screen element is repeated at a defined frequency but more or less pronounced depending on the desired surface coverage of the color (see Figure 5). Ink halftone dots compose the halftone screen elements. The size of the inked areas in the halftone screen element (i.e., the surface coverage of the ink) is increased by printing more ink pixels. The way the ink halftone dots grow when increasing the surface coverage defines the shape of the halftone screen. On the other hand, error diffusion halftoning algorithms generate frequency modulated halftones. In this thesis, only classical rotated screen halftones were used.

Nowadays, most of the prints are performed from digital images. To achieve the conversion of a digital image defined by its pixel count (e.g. 1000×1000 pixels = 1 MegaPixel), into a printable halftoned image, several steps have to be carried out.

First of all, the colors of the input image that are usually defined in the sRGB color space have to be converted in a device independent color space such as CIELAB. From the sRGB gamut of the display device (device dependent input gamut), the colors have to be mapped into the output print gamut by a gamut mapping algorithm. This transformation of the CIELAB colors ensures that all the colors can be printed. There are several gamut mapping techniques, which can correspond to different reproduction intents. There is for example an absolute reproduction intent that just clips the colors that are out of the destination print gamut without altering the other colors. This intent guarantees the closest match between the input and output colors, however, if many regions of the input image have out of print gamut colors, the resulting print may not be pleasant. Usually, a perceptual reproduction intent is favoured. With this intent, the colors are mapped so that all colors are inside the destination print gamut, and so that the perceptual relationships between the colors of the image are retained. Other different strategies exist, but the best solution is highly dependent on the input image, and on the observer preferences. More details about gamut mapping can be found in the book by J. Morovic.[70] The gamut mapping algorithm used in this thesis will be presented in Section 1.6.3.2.

In order to perform a gamut mapping, the gamut of both the input device (display device) and the output device (printer) have to be known. The method for computing gamuts is presented in Section 1.6.3.1.

A typicall display device is defined by its sRGB gamut which is the standard color space for display devices, scanners and digital cameras. The sRGB gamut does not enclose all the colors that can be perceived by the human visual system though. Therefore, certain colors cannot be displayed on a monitor.

Concerning the gamut of a printer, it depends on several parameters and particularly on the printing technology (ink-jet, electrophotography, off-set, flexography, intaglio, etc.), the inks, the number of inks in the printer and their densities, as well as on the substrate (paper, plastic sheet, textile, etc.) on which the image is printed. For example, an ink-jet printer with a fixed number of inks (at least cyan, magenta, yellow and black inks), and matt photo paper typically has a smaller gamut than sRGB, meaning that some colors displayed on a monitor are not printable.

The next step after gamut mapping is to transform the continuous tone mapped CIELAB color image to a halftoned image. A halftoning algorithm is thus chosen. First, the CIELAB colors are converted to surface coverages of the inks. In this work, the relationship between the surface coverages of the inks and the resulting printed colors for the chosen halftone are deduced from spectral prediction models. This transformation will be explained in details in Section 1.6.2 and 1.6.3. Once the ink color separation was performed, the surface coverages of each ink are known for each mapped CIELAB colors of the input image. The ink layers can finally be interpolated to match the output print size and resolution, and halftoned with the chosen halftone algorithm to yield the halftone ink separation layers. By performing this color management, the printed halftoned colors are ensured to correspond to the desired mapped CIELAB colors.

1.6.2   Spectral color prediction models

Color gamut mapping is an essential part to preserve the overall color perception. However, the gamuts of both the source device and the destination medium must be known. This means that all the colors achievable on both devices have to be known. For this purpose, a huge number of colors could be printed and measured. In order to reduce the number of measurements to a minimum, color prediction models may be used. The purpose of such prediction models is to calculate the displayed colors

according to a defined model, based on a set of measured calibration samples. Color prediction models are particularly suited for printing because of the important variations depending on the printer type, printed substrate, ink sets, halftones, etc. Under specific conditions, the model predicts for any input surface coverages of the inks, the color that is actually printed. By gradient descent, a color prediction model can also be inverted, so that the surface coverages of the inks for any desired printed reproducible color can be retrieved. Therefore, color prediction models are particularly usueful for color reproduction.

Nowadays, color prediction models are generally spectral prediction models that predict for a given input surface coverages of the inks, the reflectance of the printed sample.

One of the earliest color prediction models was developed by Neugebauer in 1937 and yielded to what is known nowadays as the Neugebauer spectral color prediction model.[71] The approach of Neugebauer was to simply sum all the color contribution from all the halftone elements within a halftone screen element (Equation 15).

$$R(\lambda) = \sum_i a_i \cdot R_i(\lambda) \tag{15}$$

In the Neugebauer model, the surface coverages of the inks are used to determine the surface coverages of all the colorants generated by the superposition of the inks. For example, when printing with cyan, magenta and yellow inks, the colors that can be generated by the eight superpositions of these three inks are cyan, magenta, yellow, blue (cyan + magenta), green (cyan + yellow), red (magenta + yellow), chromatic black (cyan + magenta + yellow) and white (no ink on a white substrate). This color synthesis is known as subtractive because the colors are formed by subtraction of color components from a white illumination. For independently laid out halftones, the surface coverages of the colorants a_i can be determined from the effective surface coverages of the three inks ($c_{eff}, m_{eff}, y_{eff}$) by the so-called Demichel equations (Equation 16).

$$
\begin{aligned}
a_w &= (1 - c_{eff}) \cdot (1 - m_{eff}) \cdot (1 - y_{eff}) & a_r &= m_{eff} \cdot y_{eff} \cdot (1 - c_{eff}) \\
a_c &= c_{eff} \cdot (1 - m_{eff}) \cdot (1 - y_{eff}) & a_g &= c_{eff} \cdot y_{eff} \cdot (1 - m_{eff}) \\
a_m &= m_{eff} \cdot (1 - c_{eff}) \cdot (1 - y_{eff}) & a_b &= c_{eff} \cdot m_{eff} \cdot (1 - y_{eff}) \\
a_y &= y_{eff} \cdot (1 - c_{eff}) \cdot (1 - m_{eff}) & a_k &= c_{eff} \cdot m_{eff} \cdot y_{eff}
\end{aligned}
\tag{16}
$$

The Neugebauer model is yet not very accurate for two reasons. First, when printing, the expected nominal surface coverage is not exactly achieved. The ink typically spreads resulting in a physical dot gain. Secondly, light does not travel only within a halftone element, but propagates laterally in the substrate due to scattering and due to reflections at the print-air interfaces. As a consequence, a light beam that enters one colorant might come out of the halftone from another colorant. These optical phenomena cause what is known as optical dot gain. Because of these two kinds of dot gains, the effective surface coverages of the colorants and inks are usually larger than expected. In order to take into account ink spreading, a correction needs to be undertaken. This correction is performed by calibrating the ink-speading behavior of the different inks on halftoned samples. The effective ink surface coverages are hence fitted in the model by minimizing the difference between predicted spectra and measured spectra.

Nonetheless, even when the ink spreading is taken into account, the Neugebauer model does not model the lateral propagation of light. Nowadays, one of the most versatile and widely used models in color reproduction is the Yule-Nielsen modified spectral Neugebauer model.[72-74] The Yule-Nielsen approach was improved by Viggiano who demonstrated that using narrow band measurements (with 10 nm or smaller bandwidths), instead of wide band densitometers, resulted in better prediction accuracies.[74] Finally, the model is further enhanced by using ink spreading calibrations that depends on the ink superposition conditions.[73]

The Yule-Nielsen model is an extension of the Neugebauer model, which works in a space where the spectrum of each colorant is raised by a power function $1/n$ (Equation 17). The n-factor, or Yule-Nielsen factor, is a parameter that needs to be fitted and varies depending on the printing conditions (printer type, substrate, inks, halftone frequency, dot profiles, etc). The n-factor can be empirically correlated with lateral propagation of light within halftones and ink thickness profiles of the halftone dots. For example, it has been shown that, by using blurred halftone functions, the more the halftones are blurred, which corresponds to a larger lateral propagation of light or to a variation of the ink thickness at the edge of the ink halftone dots, the larger the optimal n-factor.[75]

$$R(\lambda) = \left(\sum_i a_i \cdot R_i(\lambda)^{1/n} \right)^n \qquad\qquad (17)$$

The Yule-Nielsen model can be applied in different modes. Reflectances (R), transmittances (T) and emittances (E) are well predicted by the Yule-Nielsen approach.[76, 77]

In order to test the accuracy of prediction models, the ΔE_{94} metrics may be used. Test color samples are measured and their spectra converted to CIE-XYZ and then to CIELAB colors. These colors are compared with those obtained from the corresponding predicted spectra. The average color difference, 95 % quantile and maximum ΔE_{94} are good indicators of the accuracy of the prediction. Models with average ΔE_{94} and 95 % quantile values below 1.0 and 2.0 respectively are very good models, since ΔE_{94} values between 1 and 2 represent just noticeable color differences. But higher values (up to 3-5) might still be acceptable.

1.6.3   Toward a simple versatile color reproduction framework

In order to create color prints that have a desired appearance under a controlled illumination, two steps are required. First, the input colors of the images, for example, the sRGB colors of an input image viewed on an sRGB display device, need to be mapped into the gamut of the output device, for example, the gamut of the CMYK inks of a printer printed on a specific paper substrate. When the colors are mapped inside the destination gamut, all the mapped colors of the image can be reproduced with the output device. In a second step, the amount of each ink that yields the desired color needs to be determined. Therefore, a correspondence between the surface coverages of the inks and the resulting color is required. This correspondence can be found by relying on a spectral prediction model. In this thesis, different spectral prediction models were used to predict colors obtained for example by luminescence under UV light, or by transmittance through a halftone printed colored substrate. Spectral prediction models were used for two purposes:

a) The prediction of a high amount of reproducible colors for the computation of the boundary of the color gamut.

b) The construction of 3D lookup tables establishing the correspondances between the desired reproducible CIELAB colors and the correct surface coverages of the inks.

1.6.3.1 Computation of the boundary and volume of a color gamut

The boundary of the gamut volume is obtained from the set of predicted printable CIELAB colors. The set of colors should sample all the volume of the real gamut. From the CIELAB colors, by applying a Delaunay triangulation, a set of triangles representing the convex gamut volume is created. The boundary, or surface, of the volume is found by the ball-pivoting algorithm.[78] The resulting mesh of triangles forms the convex gamut boundary.

1.6.3.2 Gamut mapping

The first step to map the colors of an input sRGB device into a destination gamut is to set the correspondence between the input device sRGB lightness range and the lightness range of the destination color gamut. In this thesis, a linear compression was chosen, but nonlinear functions might possibly yield better looking images. For example, a sigmoid curve might enhance the contrast of the compressed image.[79]
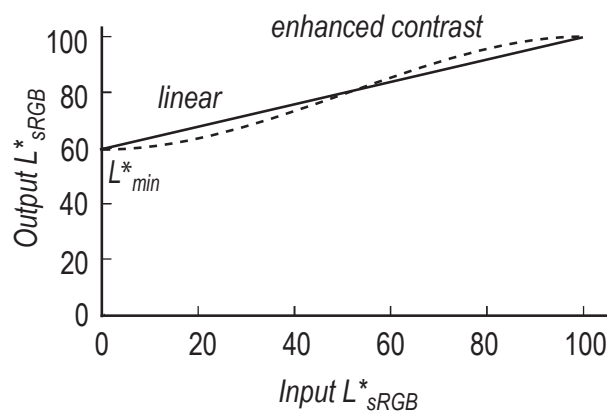
Figure 6. Examples of lightness compressions of the sRGB gamut
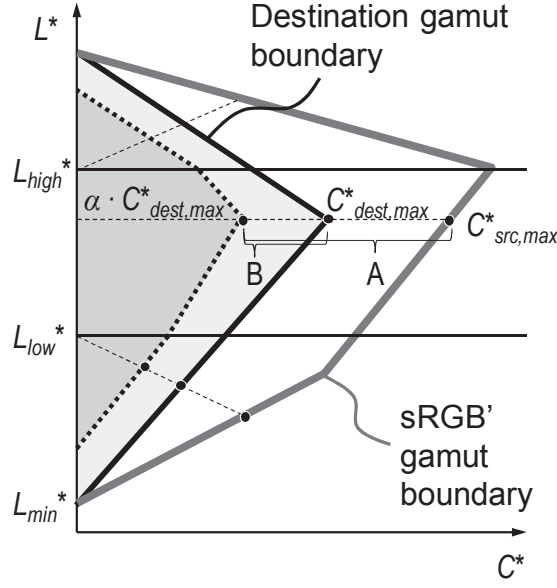
Figure 7. Multiple foci gamut mapping algorithm used to map the colors of source lightness compressed sRGB gamuts into destination gamuts

Once lightness compressed, the sRGB' gamut (G_{sRGB}') is mapped into the destination gamut according to the chosen gamut mapping algorithm. In this work, a multiple foci gamut mapping algorithm (Figure 7) was chosen.[80] This gamut mapping algorithm proved to be quite versatile and yielded nice results for a wide variety of input images and output gamuts. With this algorithm, the sRGB' CIELAB colors located in between two focal points $L_{low}*$ and $L_{high}*$ are linearly mapped at constant lightness from the interval A to the interval B, as shown in Figure 7. The distance $\alpha \cdot c*_{dest,max}$ is defined by a chroma reduction factor α. Hereafter, the α factor was usually set at 0, thus mapping the interval $[0, c*_{src,max}]$ into the interval $[0, c*_{dest,max}]$. Outside the constant lightness mapping region, a modification of the lightness is applied to avoid an excessive chroma reduction in the low and high lightness ranges. It is performed by mapping linearly the CIELAB points in this region on a line from each point to the corresponding focal point $L*_{low}$ or $L*_{high}$.

1.6.3.3 LookUp Table for mapping colors to surface coverages

For a given gamut mapped color, the surface coverages of the inks need to be deduced. If the gamut mapping is performed correctly, all the mapped colors can be reproduced by appropriate amounts of each ink. In order to be able to quickly

establish the relationship between the desired CIELAB color and the corresponding surface coverages of the inks, a 3D lookup table (3D LUT) setting up the correspondences is build. The 3D LUT is formed by a regular grid in CIELAB. At each point of the grid, the surface coverages of the inks are deduced from the spectral prediction model by minimizing the color difference between the desired color and the predicted color. At the image generation time, any desired gamut mapped CIELAB color can then be located in the mesh grid and the surface coverages of the inks interpolated from the neighbor vertices.

The ink layers are then halftoned according to the selected halftoning method, at the defined resolution, frequency and screen angle, and the layers are finally printed.

1.7   Luminescence in optical document security

In our society, counterfeiting is a serious issue. Counterfeited goods and values are not only detrimental to enterprises and governments, but they also often fund criminal organizations that do not care about quality or safety. Anti-counterfeiting techniques were introduced to check the authenticity of an item and ensure that a genuine object cannot be easily reproduced. Optical document security remains one of the most appreciated means to authenticate documents such as banknotes, diploma, packagings, certificates and other valuable documents. Such optical methods are valued for two reasons:

1. Their convenient authentication can incorporate elements visible by the naked eye, or readable by a specific apparatus.

2. Their visual appeal enables them to be easily incorporated in graphical designs.

Furthermore, they often include special printing methods or components such as security inks that are not easily available to counterfeiters.

The luminescent patterns that appear on most banknotes are one of the most famous security features.[81] In addition, luminescent filaments with several different emissive colors are often incorporated in security papers. Up-converting materials are also present in some cases and allow authenticating the document with a near infrared (NIR) laser pointer. NIR emitters can also be found, with a hidden pattern that can be revealed with an infrared (IR) camera. Characteristic emissions or

spectral fingerprints might also secure a document by mixing several luminescent compounds in defined ratios (lanthanide compounds are particularly useful in that case). Even lifetime analysis provides efficient anti-counterfeiting means. Easily visible features observable with the naked eye, a UV lamp, or special filters are yet very important because they enable a quick verification of the validity of the document or valuable item.

There are numerous patents and patent applications regarding luminescent materials as security features. Relevant examples include compositions of luminescent inks with lanthanide chelates (e.g. β-diketonates and dipicolinates), as well as detection methods and precise applications (e.g. lifetime comparison or printing of bar codes).[82-85]

Luminescent patterns as authentication features consist rarely of full color images. In some cases, several luminescent colors are achieved by using several different luminescent inks. The generation of full color images invisible under normal light and revealed upon UV excitation is not very common, even though they increase both the visual appeal and the security of the anti-counterfeiting technique. Such images can be reproduced by using three luminescent inks emitting in the blue, green and red region of the spectrum. An easily implemented technique is to replace the cyan, magenta and yellow inks of the printer by red, green and blue emitting inks, to take the negative of a CMY image and to print the negative C channel as red-emitting, negative M channel as green-emitting and negative Y channel as blue-emitting. A patent based on this technique was filed in 2004 by Coyle and Smith and accepted in 2010.[86] A more complex technique yielding more reliable results was developed at the EPFL.[77] The method uses juxtaposed halftoned luminescent inks with a yellow-emitting ink instead of the green-emitting one, and reproduces images via spectral prediction models, and gamut mapping algorithms as described in the previous section (1.6.1). This patented technique is used as a security feature on current EPFL diplomas.

Chapter 2

6-phosphoryl picolinic acids

Exploring the importance of the coordination moiety

2.1 Introduction

In this chapter, a series of 6-phosphorylated picolinic acids (6ppa) is investigated as ligands for lanthanide ions forming luminescent complexes. The ligands were presented in Scheme 8, page 30, Section 1.4.3. In order to ease the reading of this chapter, this scheme is redrawn at the bottom of this page. The synthesis and acid-base properties of ligands are first presented. The complexation of the ligands with lanthanide ions is then studied by several techniques in order to dertermine the stoichiometry of the complexes under specific conditions. The photophysical properties (energy of the singlet excited state and triplet excited state of the ligands, intrinsic and sensitized quantum yields, radiative and observed lifetimes) of these complexes are finally considered and more particularly, their luminescence is shown and rationalized under different conditions such as the pH value of the solution, or the presence of a salt. This study intends to demonstrate the effect of the variation of the 6-phosphorylated coordinating moiety on the stability and on the photophysical properties of the lanthanide complexes, and propose to contextualize the results with related structures found in the literature.
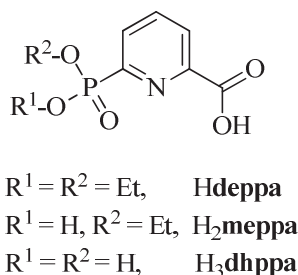
$$R^1 = R^2 = Et, \quad H\textbf{deppa}$$
$$R^1 = H, R^2 = Et, \quad H_2\textbf{meppa}$$
$$R^1 = R^2 = H, \quad H_3\textbf{dhppa}$$

Scheme 8. Diethoxyphosphoryl picolinic acid (H**deppa**), monoethoxyphosphoryl picolinic acid (H$_2$**meppa**), and dihydroxyphosphoryl picolinic acid (H$_3$**dhppa**).

2.2 Synthesis of the ligands

The synthesis of the three 6-phosphorylated picolinic acid (6ppa) ligands is based on a selective hydrolysis of the protective ethyl ester groups under controlled conditions. The ethyl ester carboxylate is removed in ethanol by slow addition at room temperature of 1.1 equivalents of sodium hydroxide. These conditions leave

the diethoxyphosphoryl moiety unreacted. In order to cleave one of the ethoxyphosphoryl group, the reaction has to be performed in water. In these conditions, only one of the two ethoxyphosphoryl group is removed at room temperature. The removal of the remaining one requires harsh conditions to be completed, since 10 equivalents of sodium hydroxide under reflux are needed thereof. The detailed procedure for the synthesis of the 6ppa ligands and their characterization is reported in the appendices.
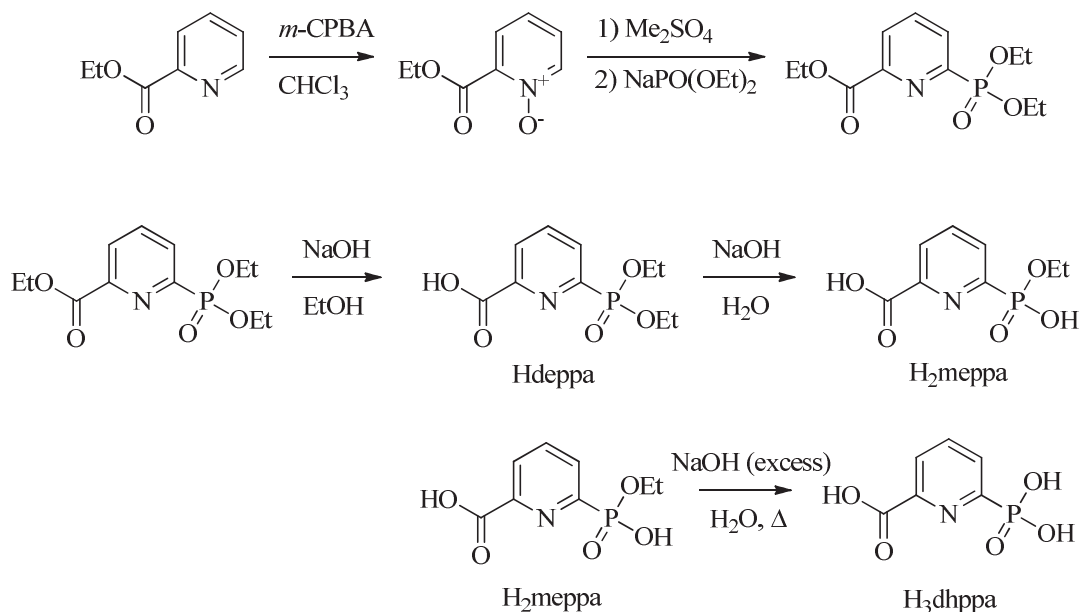
Scheme 11. Synthesis of the 6ppa ligands based on Chauvin et al.[48]

2.3   Acid/base properties of the ligands

The number of protonation sites of the phosphoryl ligands is not constant, but depends on the phosphoryl moiety. The dihydroxyphosphoryl (i.e. phosphonic acid) group has two protonation sites, the monoethoxyphosphoryl has only one protonation site, whereas the diethoxyphosphoryl does not possess any protonation site. The rest of the molecule (i.e. the picolinic acid moiety) is identical, with two additional protonation sites, either a pyridine that can be protonated to give a pyridinium or a carboxylate that can be protonated to give a carboxylic acid.

$$H_2deppa^+ + H_2O \xrightleftharpoons{K_{a1}} Hdeppa + H_3O^+$$

$$Hdeppa + H_2O \xrightleftharpoons{K_{a2}} deppa^- + H_3O^+$$

$$H_4dhppa^+ + H_2O \xrightleftharpoons{K_{a1}} H_3dhppa + H_3O^+$$

$$H_3meppa^+ + H_2O \xrightleftharpoons{K_{a1}} H_2meppa + H_3O^+$$

$$H_3dhppa + H_2O \xrightleftharpoons{K_{a2}} H_2dhppa^- + H_3O^+$$

$$H_2meppa + H_2O \xrightleftharpoons{K_{a2}} Hmeppa^- + H_3O^+$$

$$H_2dhppa^- + H_2O \xrightleftharpoons{K_{a3}} Hdhppa^{2-} + H_3O^+$$

$$Hmeppa^- + H_2O \xrightleftharpoons{K_{a3}} meppa^{2-} + H_3O^+$$

$$Hdhppa^{2-} + H_2O \xrightleftharpoons{K_{a4}} dhppa^{3-} + H_3O^+$$
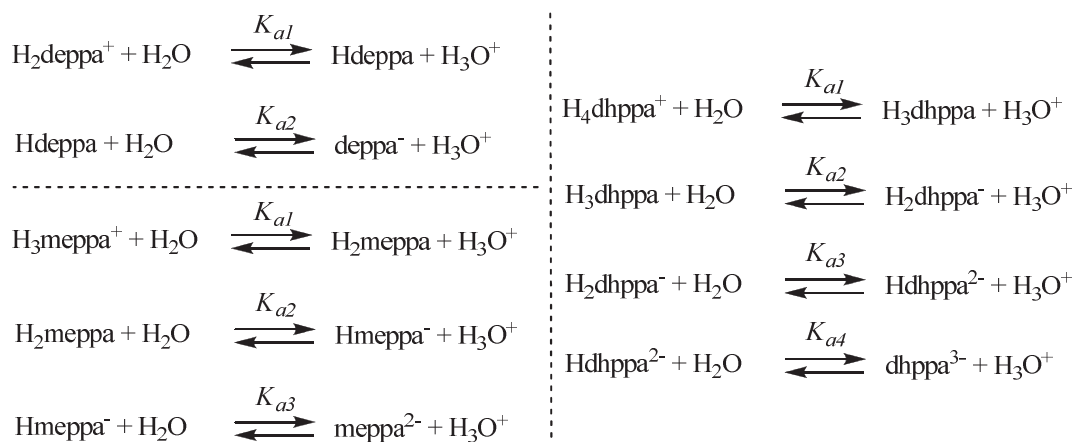
Scheme 12. Equilibria of protonation in water

In order to characterize the acidity of the ligands and the amount of the different species (with different protonation state) in solution as a function of the pH value, the absorption spectra of Hdeppa, H_2meppa and H_3dhppa were collected at different pH (Figure 8 – Figure 10) and these data were used to fit the pK_a values (Table 2) using SPECFIT. A protonation model with 2, 3, and 4 pK_a values respectively was used. The reconstructed distribution diagrams are shown together with the absorption spectra in Figure 8 – Figure 10.
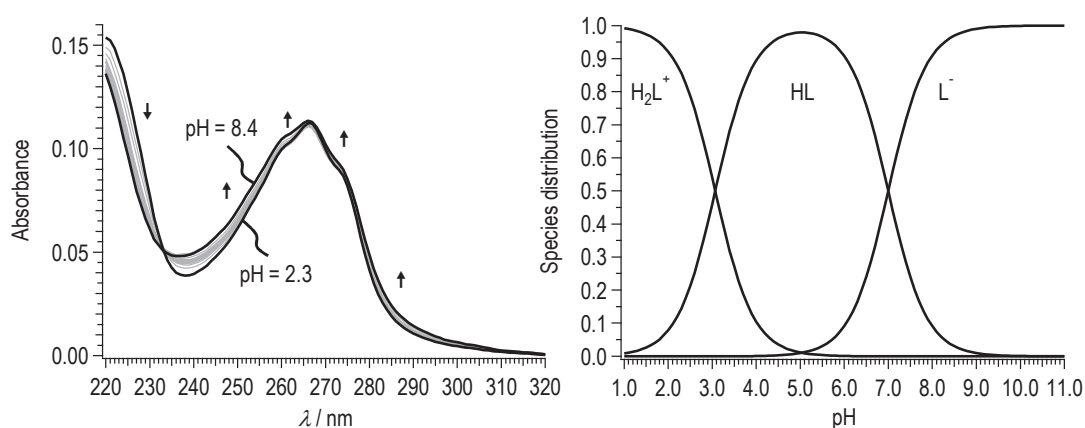
Figure 8. Absorption spectra at different pH values of Hdeppa and the resulting calculated species distribution diagram as a function of pH
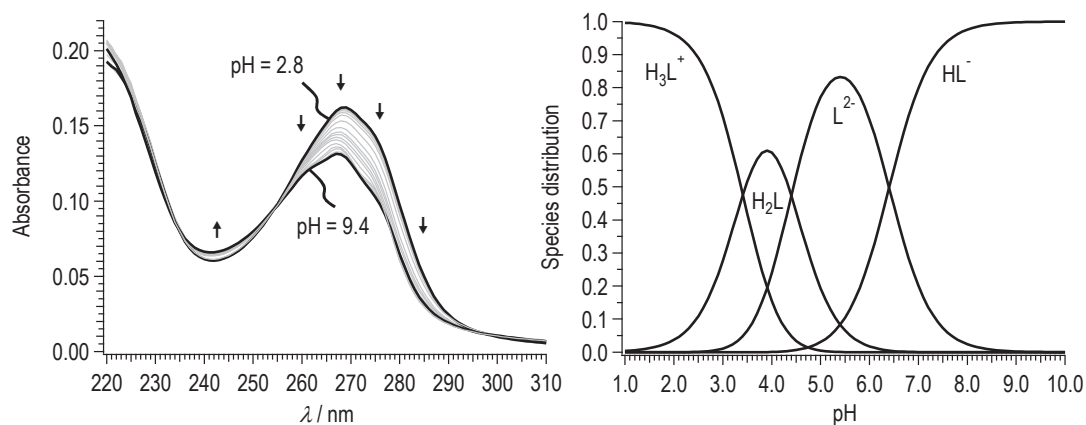
Figure 9. Absorption spectra at different pH values of H$_2$meppa and the resulting calculated species distribution diagram as a function of pH
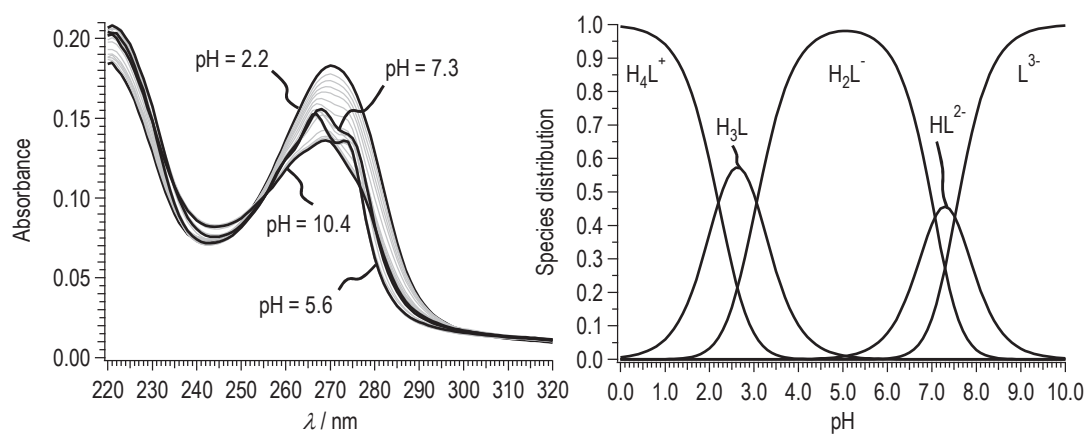
Figure 10. Absorption spectra at different pH values of H$_3$dhppa and the resulting calculated species distribution diagram as a function of pH

56

Table 2. Acid dissociation constants of the 6ppa ligands. In 0.1 M KCl aqueous solution at 25°C.

	H_2dpa^a	Hdeppa	H_2meppa	H_3dhppa
pK_{a1}	0.5(2)	3.07(4)	3.41(9)	2.2(3)
pK_{a2}	2.03(1)	7.0(1)	4.4(2)	3.06(9)
pK_{a3}	4.49(1)	/	6.4(2)	7.07(8)
pK_{a4}	/	/	/	7.53(9)

a) Taken from Gassner et al.[15]

The pK_a values, obtained from the UV-Vis absorption spectra are shown in Table 2. According to the acidic nature of the carboxylic acid and basic behavior of the pyridine, the two pK_a values found for Hdeppa are attributed to the deprotonation of the carboxylic acid concerning the pK_{a1} = 3.07 ($H_2deppa^+ \leftrightarrows$ Hdeppa) and to the deprotonation of the pyridinium nitrogen to form the pyridine for the pK_{a2} = 7.0 (Hdeppa $\leftrightarrows$ deppa$^-$). Similarly, the pK_{a1} value of H_2meppa (3.41), was attributed to the carboxylic acid ($H_3meppa^+ \leftrightarrows H_2meppa$), the pK_{a2} (4.4) to the monoethyl ether phosphonic acid ($H_2meppa \leftrightarrows$ Hmeppa$^-$), and the pK_{a3} (6.4) to the pyridine nitrogen (Hmeppa$^- \leftrightarrows$ meppa^{2-}). Concerning the four protonation sites of H_3dhppa, the attribution of the acidic pK_a values is intricate. Usually, phosphonic acids are more acidic than their carboxylic analogs.[87] Nevertheless, the ^{31}P-NMR chemical shifts of the ligand in 0.1 M D_2SO_4, D_2O or 0.1 M NaOD (see Table 3) show that the peak of the phosphorus nucleus is more shifted by the removal of a proton from H_3dhppa than by the removal of a proton from H_4dhppa^+. Such higher shifts of the ^{31}P-NMR chemical shift may be expected for the removal of phosphonic protons separated by only two chemical bonds from the phosphorus, whereas the removal of the far carboxylic proton should affect the chemical environment of the phosphorus to a lesser extent. For example, the ^{31}P-NMR chemical shift of Hdeppa is only shifted from 12.5 ppm to ± 0.7 ppm by the addition of the carboxylic proton or the removal of the pyridinium proton. On the other hand, the increased capability of H_2dhppa to form hydrogen bonds may also have a significant influence on the chemical shifts. Therefore, only the pK_{a3} value of 7.07 can be easily assigned to the pyridine core ($H_2dhppa^- \leftrightarrows$ Hdhppa^{2-}) and the pK_{a4} value of 7.53 to the second deprotonation of the phosphonic acid (Hdhppa$^{2-} \leftrightarrows$ dhppa^{3-}). The pK_{a1} and pK_{a2} values are tentatively assigned to the carboxylic acid and the phosphonic acid, respectively.

Table 3. ^{31}P-NMR chemical shifts in ppm of the three ligands protonated species measured in D_2O by addition of deuterated aqueous solutions of D_2SO_4 0.1 M and NaOD 0.1 M.

Species (charges omitted)	deppa	meppa	dhppa
L	13.2	9.20	6.94
HL	12.5	7.84	5.5 - 5.9
H₂L	11.94	2.9 - 3.06	3.7 (broad)
H₃L	/	+ 0.9	- 0.9
H₄L	/	/	+ 0.9

The pK_a values, obtained from the UV-Vis absorption spectra (Table 2), correlates to some extend with those obtained for other phosphonic acids within related structures. For example, a 2,2'-bipyridine substituted in the 6 position by a phosphonic acid has pK_a values for the deprotonation of the phosphonic acid of 3.1 and 7.1.[46] This is close to the values of 3.1 and 7.5 found for the H₃dhppa ligand and tentatively attributed to the phosphonic acid moiety. Helicates bearing phosphonic acid or phosphoester units instead of carboxylates also show some correlated results with those displayed in Table 2, especially concerning the monoethylphosohorylated ligands that have a pK_a value for the deprotonation of the monoethyl-phosphonic ester around 4.[48]

Consequently, the main influence of a phosphoryl coordinating moiety (diethoxy, monoethoxy or diethoxyphosphoryl) on the acido-basic properties of such ligands that can be safely stated is a much more basic pyridine in all the phosphoryl ligands compared to dipicolinic acid. A difference of at least two pK_a units is indeed observed between the pK_a of the pyridinium in dipicolinic acid and the one from the pyridinium in any of the 6-phosphorylpicolinic acid. As seen in Figure 8 – Figure 10, this has a dramatic effect on the distribution diagrams of the phosphoryl ligands, since the full deprotonation of dipicolinic acid needs a pH higher than 7.0, while the deprotonation of the pyridinium in all phosphoryl ligands needs a pH higher than 9.0. A similar increased basicity of the pyridine core was also observed in helicate structures (Figure 2, page 28) by Chauvin et al. when replacing carboxylates by phosphoryl derivatives.[48]

2.4 Stoichiometry and stability of the lanthanide 6ppa complexes

The formation of the lanthanide 6ppa complexes was observed by two methods: UV-Vis absorption, which enables calculating the stability constants of the different absorbing species in solution, and ^{31}P-NMR spectroscopy. In addition to these experiments performed with a titration of the ligands by a lanthanide ion (europium for spectrophotometry and lutetium for NMR spectroscopy), Mass spectrometry and luminescence measurements were undertaken at a fixed stoichiometry in order to illustrate the formation of the tris species under 1:3 metal to ligand ratio. Concerning the luminescence measurements, the luminescence intensity of the europium ion was measured as a function of pH in order to find the optimal pH values, i.e., which yield the most intense emissions.

2.4.1 Determination of the stability constants by spectrophotometry

To a $9.0 \cdot 10^{-5}$ M aqueous solution of ligand in KCl 0.1 M, increasing amounts of europium perchlorate were added up to more than 1 equivalent of europium ions. The pH of the solution was kept at 4.8 for Hdeppa and at 9.0 for meppa^{2-} by addition of HCl and NaOH solutions. These pH values will be shown to be optimal for luminescence in a next section (see Job plots in Figure 18, page 67).

The stability of a lanthanide complex in aqueous solution depends on the pH of the solution. The formation of the complex is indeed in competition with other equilibria such as the ligand protonation or deprotonation and the formation of lanthanide hydroxides. Ideally, the stability of the complexes should be determined as a function of pH, but this procedure is tedious. Instead of determining the stability constants as a function of pH, the luminescence of the complexes at a fixed stoichiometry was measured at several pH values and the stability constants determined at the optimal pH values.

Concerning H$_3$dhppa, the formation of a precipitate was observed upon addition of lanthanide salts. The stability constants are then undetermined for this ligand. Interestingly, all the ligands are water soluble, but only deppa$^-$ and meppa^{2-} form water soluble complexes. A highly charged ligand such as dhppa^{3-} is here

disadvantageous since a precipitation occurs in presence of lanthanide ions, whereas the uncharged [Ln(deppa)$_3$] complex is well soluble in water.

The absorptions of the ligands as a function of the amount of europium ion are shown in Figure 11 and Figure 12. A better definition of the absorption bands is observed for the two titrated ligands upon addition of europium ions. This behavior might come from the restricted vibrational modes of the ligand once coordinated.

The titration of Hdeppa shows a neat growth of its two absorption peaks at 273 and 266 nm, whereas the remaining shoulder at 260 nm decreases when the concentration of europium increases. Five isosbestic points have emerged at 275, 271, 268, 264 and 239 nm. They are shown in Figure 11 by dashed lines.

Concerning H$_2$meppa, the evolution of the absorption spectrum upon addition of the europium salt is more intricate. While a similar evolution as Hdeppa is observed up to 0.33 equivalent with a slight bathochromic shift of 1 nm upon europium addition, an increase of absorption at the local minimum between 240 and 250 nm, at the maxima at 275 and 268, as well as at the shoulder at 262 nm is observed up to 0.5 equivalent. The minimum then keeps growing, whereas the maxima decrease even below the absorption at 0.33 equivalent. One isosbestic point is defined at 280 nm, the other crossings being either poorly defined or only valid for part of the spectra. The isosbestic point is shown in Figure 12 by a dashed line.
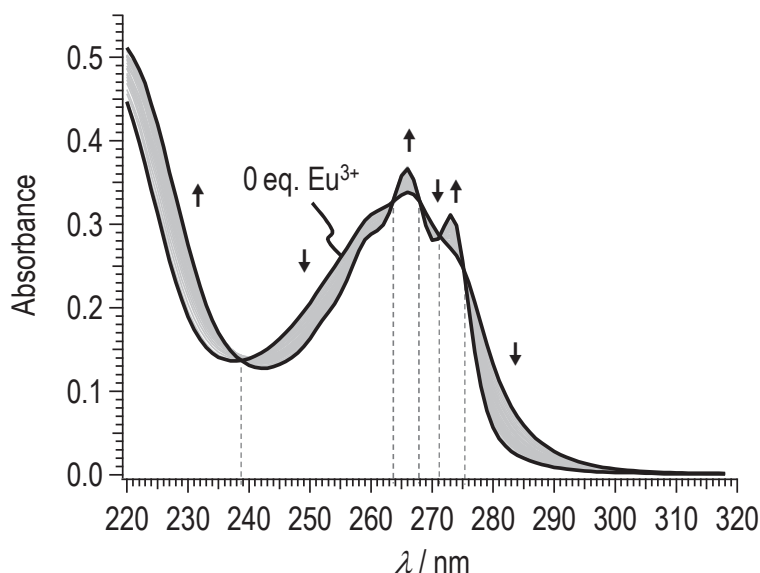
Figure 11. UV-vis spectrophotometric titration of a $9.0 \cdot 10^{-5}$ M aqueous solution of Hdeppa in KCl 0.1 M with Eu^{3+}, pH 4.8, 298 K. Arrows indicate the evolution upon addition of Eu^{3+}, dashed lines indicate isosbestic points.
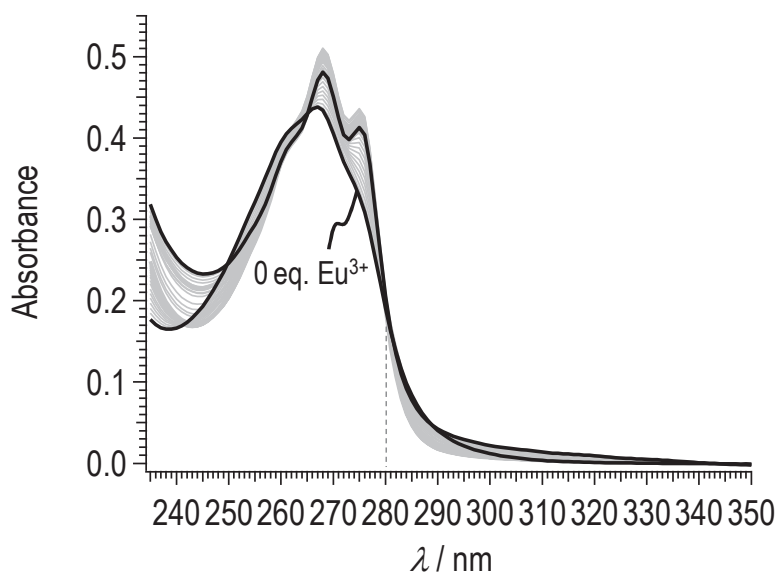
Figure 12. UV-vis spectrophotometric titration of a $9.0 \cdot 10^{-5}$ M aqueous solution of H_2meppa in KCl 0.1 M with Eu^{3+}, pH 4.8, 298 K. Dashed lines indicate isosbestic points.

The fitting with SPECFIT of the absorption spectra of both ligands gives the logβ values shown in Table 4. These values result in the species distribution diagrams presented in Figure 13 and Figure 14. The equilibria involved in the formation of the different species are shown in Scheme 13.

$$\text{Ln} + \text{L} \xrightleftharpoons{\beta_{[LnL]}} [\text{LnL}]$$

$$\text{Ln} + 2\,\text{L} \xrightleftharpoons{\beta_{[LnL_2]}} [\text{LnL}_2]$$

$$\text{Ln} + 3\,\text{L} \xrightleftharpoons{\beta_{[LnL_3]}} [\text{LnL}_3]$$
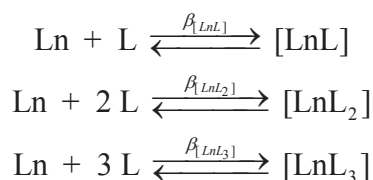
Scheme 13. Equilibria for the complex formation (charge omitted)

Table 4. Stability constants of the complexes in KCl 0.1 M, 298 K

L pH	H$_2$dpa[a] 7.4	Hdeppa 4.8	H$_2$meppa 9.0
Logβ$_{[EuL]}$	8.7(3)	8.0 fixed	8.2(4)
Logβ$_{[EuL2]}$	16.8(3)	16.2(2)	16.0(5)
Logβ$_{[EuL3]}$	22.4(3)	23.8(2)	24.3(4)

a) *Taken from Chauvin et al.[14]*
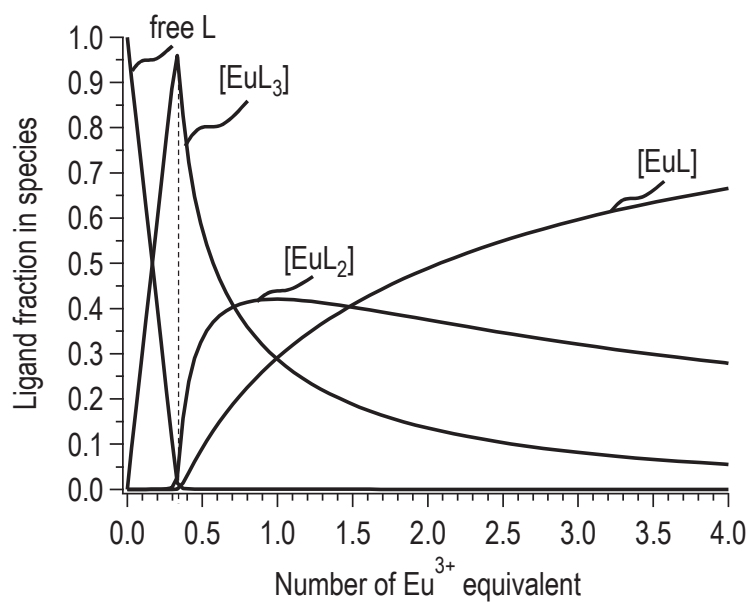
Figure 13. Distribution diagram of the species formed during the titration of Hdeppa by Eu^{3+} in KCl 0.1 M, pH 4.8, 298 K. Dashed line points at the maximum of 1:3 species at 0.33 eq.
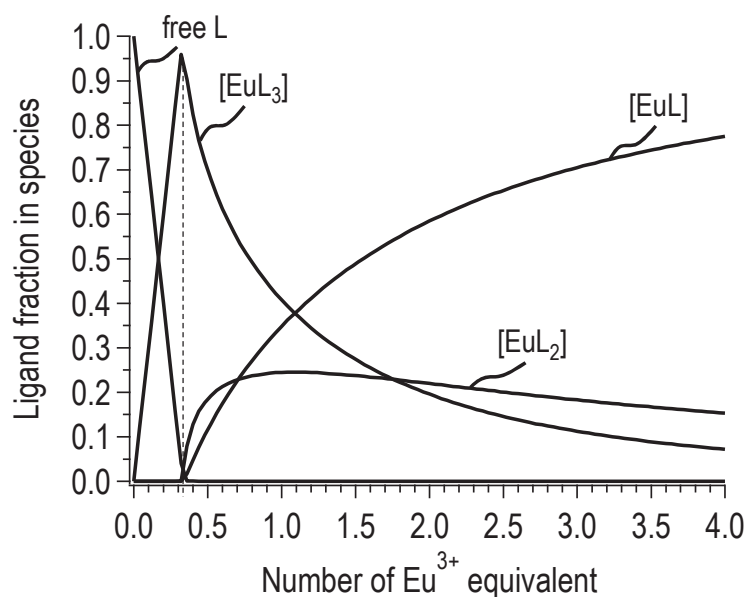
Figure 14. Species Distribution diagram of the species formed during the titration of H$_2$meppa by Eu^{3+} in KCl 0.1 M, pH 4.8, 298 K. Dashed line points at the maximum of 1:3 species at 0.33 eq.

The fit of the absoption spectra of the [Eu(deppa)$_n$]$^{3-n}$ species needed a fixed log$\beta_{[LnL]}$ value in order to converge towards reasonable reconstructed absorptivities. A value of 8.0 was found to give satisfactory results and seems rational by comparison with the stability constants of [Eu(dpa)$_n$]$^{3-2n}$ measured in comparable conditions with the same technique.[14] The fit of the absoption spectra of the [Eu(meppa)$_n$]$^{3-2n}$ species was not as good as the fitting for the [Eu(deppa)$_n$]$^{3-n}$ species. Even though the values presented in Table 4 yielded realistic reconstructed absorptivities for every species, the logβ values are to be taken cautiously.

Despite the limits of the fitting procedure, the similar stability constants (within experimental error) for all the [Eu(deppa)$_n$]$^{3-n}$ and the [Eu(meppa)$_n$]$^{3-2n}$ (n $\in$ [1,3]) stoichiometries suggest that the phosphoryl substituents (i.e. a PO(OEt)$_2$ versus a PO(OEt)OH) have no strong effect on the coordination strength or coordination mode. However, relative to the [Eu(dpa)$_n$]$^{3-2n}$ complexes, the 1:3 species of the phosphoryl analogs seem more stable than the parent carboxylate, similarly with what have already been observed with other phosphoryl based ligands.[46] The increased stability compared to [Ln(dpa)$_n$]$^{3-2n}$ complexes can be rationalized by the increased basicity of all the coordinating groups in the 6-phosphoryl picolinate series. A strong base is usually a good coordinating group because of its better electron donating ability (by definition, a base is an electron donor according to Lewis's definition of acids and bases). The larger bond lengths with a phosphorus

atom in 6ppa ligand compared to the carbon arom of dpa, as well as the larger angles between the coordinated lanthanide ion and the coordinating oxygens, could also explain the higher stabilities of the lanthanide complexes with phosphoryl based ligands.

2.4.2 ^{31}P-NMR chemical shift as a function of the Ln:L ratio

To further check the presence of a 1:3 complex, which should be the main species in solution, NMR experiments were conducted. The ligands were dissolved in D_2O and titrated by Lu^{3+}. ^{31}P-NMR spectroscopy was found to be really useful, exhibiting different signals for each species (both proton speciation of the ligands and complex species).

This is particularly true for the Hdeppa ligand that shows a defined peak at 0.33 equivalent of Lu^{3+} (Figure 15). During the titration of Hdeppa by Lu^{3+}, an evolution of the ligand single peak at 12.5 ppm is observed upon addition of the lanthanide salt. The ligand peak decreases in intensity as soon as lutetium is added. A new peak consistent with the appearance of $[Lu(deppa)_3]$ forms around 20 ppm and remains from 0.33 to 0.44 equivalent of lutetium. It then begins to decrease in agreement with the decrease of the 1:3 species concentration. A new broad peak appears then between 20 and 21 ppm before a defined peak emerges from the broad one and keeps growing as for the concentration of the $[Ln(deppa)]^{2+}$ species.
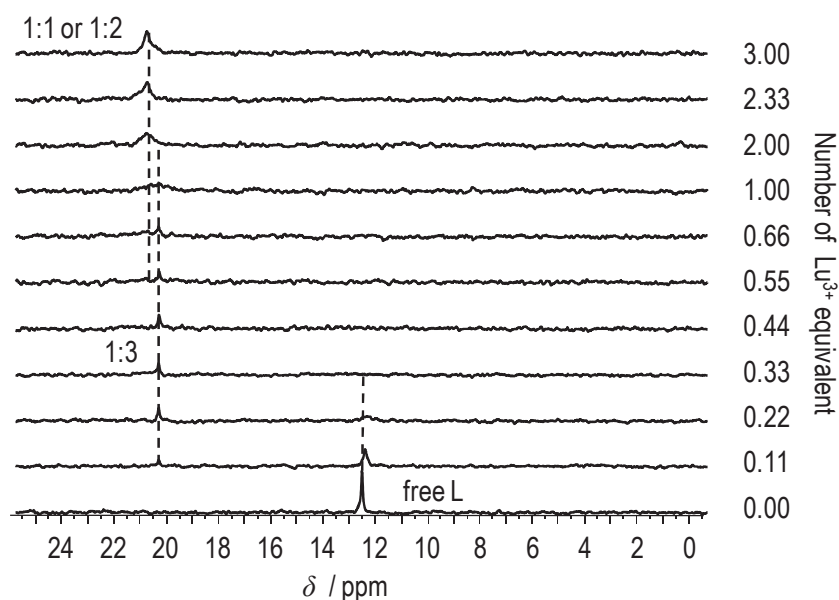
Figure 15. ^{31}P-NMR spectrum of Hdeppa $3 \cdot 10^{-3}$ M in D_2O titrated by Lu^{3+}, pD ~5.4.

The H$_2$meppa spectrum, on the other hand, is poorly defined at 0.33 equivalent (Figure 16). A peak at 15 ppm is observed at metal concentrations higher than 0.33 equivalent of lutetium, and a progressive decrease of the free ligand peaks at 3 ppm and 7.9 ppm (two protonated species are present at this pD) is encountered up to 0.33 equivalent of lutetium. This experiment did not directly enable visualizing the formation of a major [Lu(meppa)$_3$]$^{3-}$ species, but the evolution of the other species associated with the observed ^{31}P-NMR peaks suggests that a 1:3 complex form at 0.33 equivalent of lutetium similarly to [Lu(deppa)$_3$].
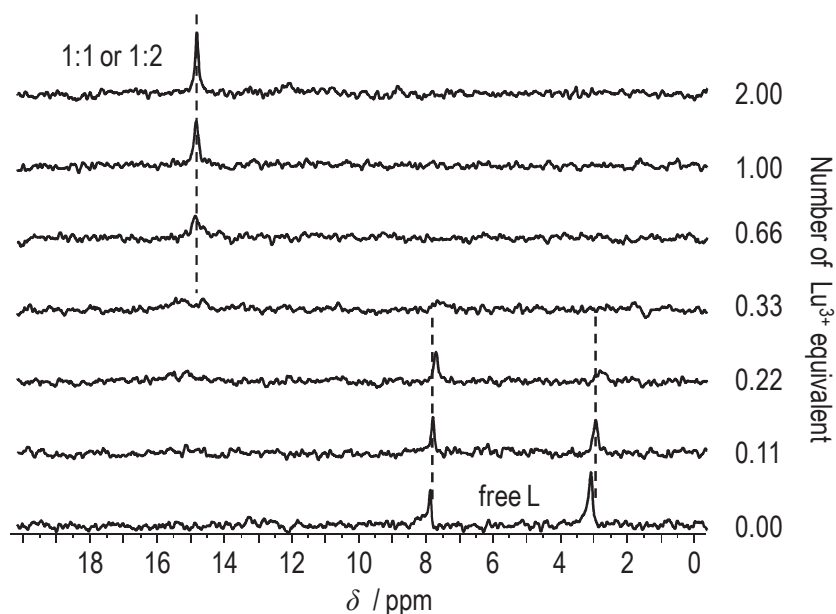
Figure 16. ^{31}P-NMR spectra of H$_2$meppa 3 · 10^{-3} M in D$_2$O titrated with Lu^{3+}, pD ~4.8.

2.4.3   Mass spectrometry of a 1:3 europium to ligand solution

The 1:3 stoichiometry was further tested by mass spectrometry. Some europium perchlorate and the appropriate amount of ligand were dissolved in distilled water, keeping a strict 1:3 concentration ratio, and the resulting solution was injected in an electrospray mass spectrometer within micromolar concentration range.

[Eu(deppa)$_3$] was detected as monoprotonated (Figure 17) and biprotonated tris species. The isotopic distributions of the measured species are in agreement with the calculated distributions expected for these complexes.
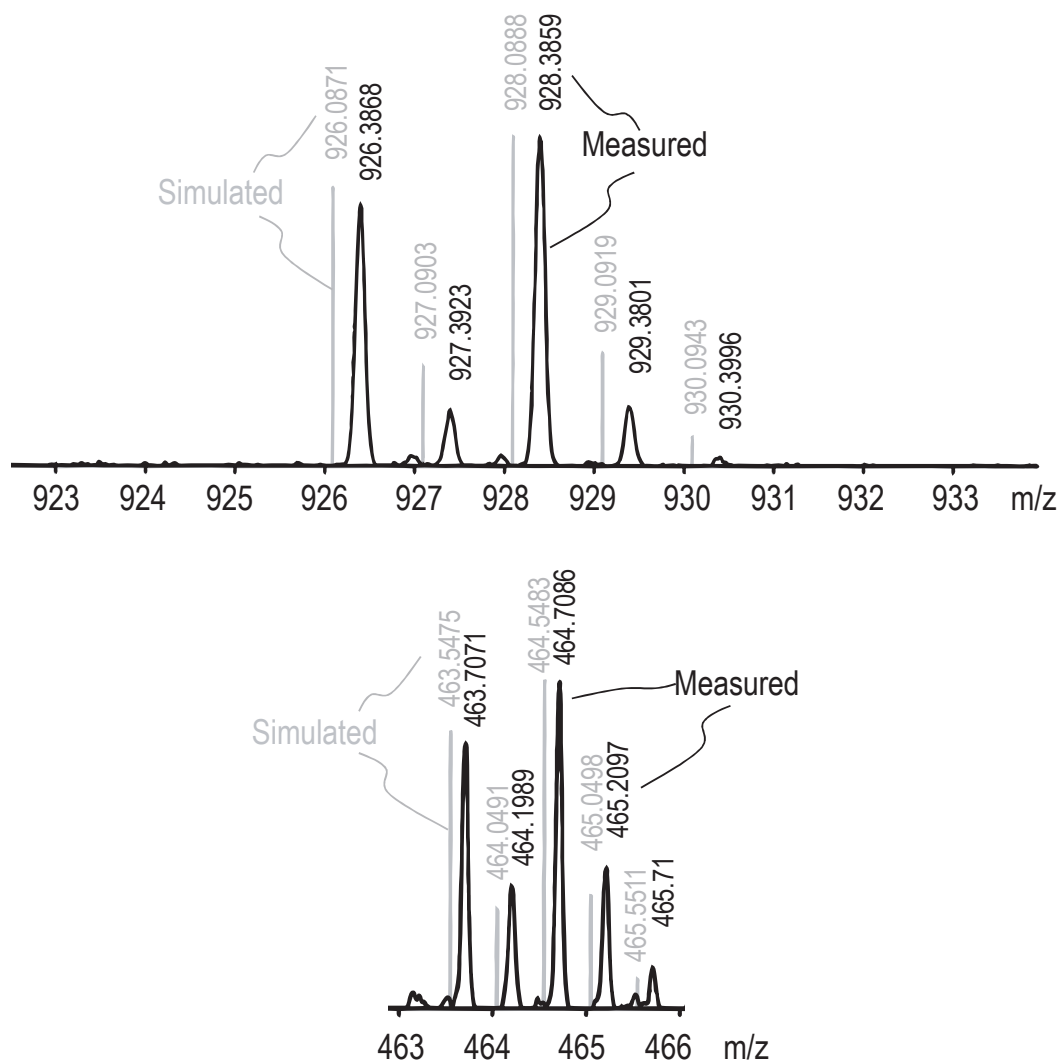
Figure 17. ESI-TOF-MS spectra of $[Eu(deppa)_3]$ (Top: $C_{30}H_{40}EuN_3O_{15}P_3^+$, bottom: $C_{30}H_{41}EuN_3O_{15}P_3^{2+}$) in water. Gray lines calculated, black peaks measured.

Peaks corresponding to $[Eu(meppa)_2]^-$ have been measured but no tris species was observed with this method. It may be due to the conditions required for mass spectrometry, i.e. the detection of complexes in negative mode being somewhat more difficult than in positive mode. But since luminescence based methods, presented in the photophysical properties section, will prove the formation of a non hydrated coordination sphere in meppa^{2-} complexes at pH 9.0 upon 1:3 metal:ligand ratio, the ligand filled coordination sphere that corresponds to the 1:3 species ought to be the major species.

2.5   Luminescence as a function of pH

The emission spectra of [Eu(deppa)$_3$] and [Eu(meppa)$_3$]$^{3-}$ were measured as a function of pH. The integration of the emission and the normalization relative to the maximal integrated intensity results in Figure 18. An optimum pH value at 4.8 is found for [Eu(deppa)$_3$], whereas [Eu(meppa)$_3$]$^{3-}$ is more luminescent at pH 9.0. This phosphoryl series then nicely complements the maximum luminescence of [Eu(dpa)$_3$]$^{3-}$ around pH 7.4.[14]
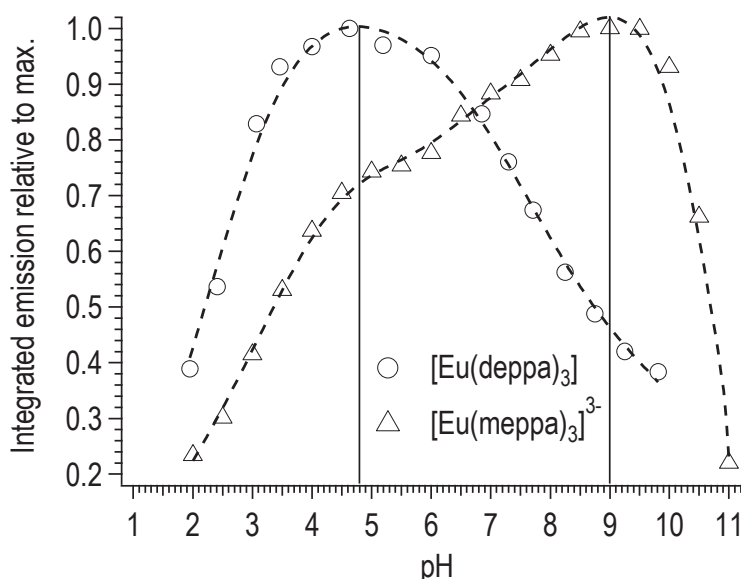
Figure 18. Normalized integrated emission intensity of (circles) [Eu(deppa)$_3$] and (triangles) [Eu(meppa)$_3$]$^{3-}$ as a function of pH. Concentration of the complex (either [Eu(deppa)$_3$] or [Eu(meppa)$_3$]$^{3-}$): $1 \cdot 10^{-4}$ M in KCl 0.1 M aqueous solution, 298 K. Solid lines point at the chosen pH values resulting in a maximal emission of the considered complex.

The competition between the formation of the complex and the protonation of the ligands usually prevents an acidic optimal luminescence, whereas on the other hand, the competition between the formation of the complex and the formation of lanthanide hydroxides generally precludes a basic optimal luminescence. Such difficulties are not encountered with [Eu(deppa)$_3$] that keeps 75 % of its maximal emission in the acidic range from pH 2.8 to 7.4, and with [Eu(meppa)$_3$]$^{3-}$ that still emits 75 % of its maximal emission in a range from pH 5.2 to a fairly basic value of 10.4.
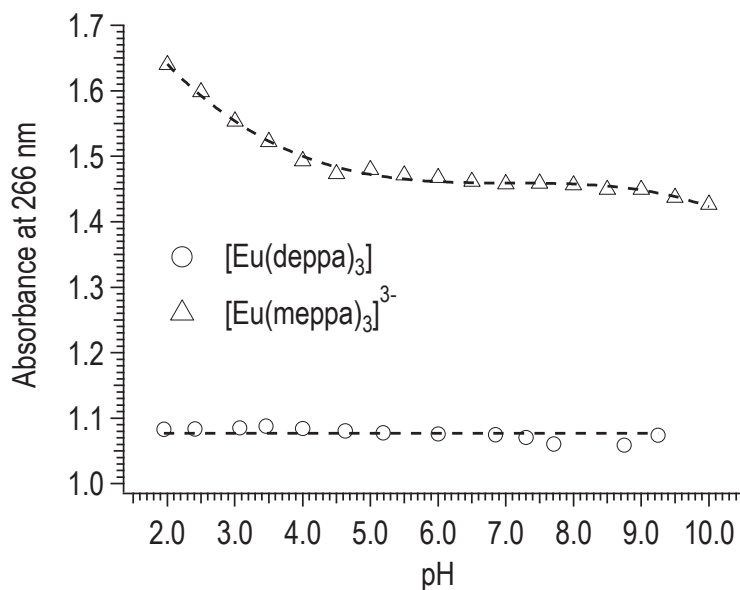
Figure 19. Absorption of the 6ppa europium complexes as a function of pH. Concentration of the complex (either [Eu(deppa)$_3$] or [Eu(meppa)$_3$]$^{3-}$): $1 \cdot 10^{-4}$ M in KCl 0.1 M aqueous solution.

The modifications of the absorptions of the complexes as a function of pH correlate well with the absorption of the free ligands as a function of pH. The absorbance of [Eu(deppa)$_3$] at 266 nm remains fairly constant over the whole pH scale, whereas, the absorbance of [Eu(meppa)$_3$]$^{3-}$ at 266 nm significantly changes (see Figure 19). The more acidic, the more [Eu(meppa)$_3$]$^{3-}$ absorbs, decreasing as the pH value increases. The absorption of [Eu(meppa)$_3$]$^{3-}$ thus behaves like the inverse of the emission. The obvious consequence of this behavior is that the quantum yield of [Eu(meppa)$_3$]$^{3-}$ benefits from both a better emission and a lower absorption at the optimal pH.

In addition, the integrated emission may be taken as an estimation of the quantum yield as a function of pH for [Eu(deppa)$_3$]. This is not the case for [Eu(meppa)$_3$]$^{3-}$, since its absorption considerably changes with pH; its quantum yield at low pH should decrease even more than the relative integrated emission of the luminescent lanthanide.

The effect of the pH under non-optimal conditions was further investigated by looking at the emission spectra of the $^5D_0 \rightarrow ^7F_2$ hypersensitive transition of europium and its decay rate. The emission spectra of the $^5D_0 \rightarrow ^7F_2$ hypersensitive transition of europium may indicate if the coordination is changing as a function of pH, whereas the lifetime analysis may point at the presence of more than one emitting species.

Concerning [Eu(deppa)₃], the hypersensitive transition seems not to be affected by the change of pH. The emission just increases or decreases, but the shape is identical. The lifetimes at pH 4.8 and at pH 7.4 are well fitted with a mono exponential decay. A double exponential did not improve the residuals of the fits. The lifetimes are presented in Table 5. The mono exponential decay of the europium emission is similar within experimental error at pH 4.8 and at pH 7.4. The observed lifetime of 1.9 ms seems thus independent of the pH. If the loss in emission intensity is due to some decomplexation or to the formation of other species, these species are practically non-luminescent so that only the decrease of the amount of the tris species is observed. If the loss in emission intensity were due to some quenching of the europium emission, the lifetime would be affected. The lifetime is in agreement with the hypersensitive transition. No structural change in the tris complex is observed.
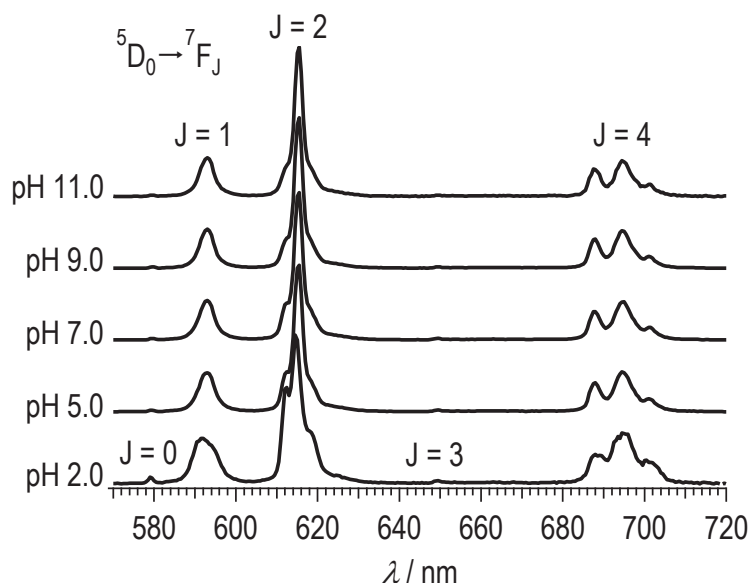
Figure 20. Emission spectra of [Eu(meppa)₃]³⁻ (λ_{ex} = 270 nm) as a function of pH. Conc. $1 \cdot 10^{-4}$ M in complex, solvent: KCl 0.1 M

For [Eu(meppa)₃]³⁻, the shape of the hypersensitive transition changes from the acidic pH values to the neutral and basic pH values (Figure 20). At pH 2, the transition is asymmetrically split, whereas at pH 11, the transition is symmetrical. The coordination of the europium ion to the meppa²⁻ ligands is then affected in acidic solutions, and the species formed in acidic solutions is luminescent, even if to a lesser extent than the species that is encountered at the optimal basic pH.

Table 5. Lifetimes evolution as a function of pH. λ_{ex} = 274 nm, λ_{em} = 615 nm (Eu), 545 nm (Tb). Experimental error and lifetime percentage in brackets (100% means mono exponential fit)

Lifetimes Conc. 0.1 mM		Eu^{3+} τ_{obs1} / ms τ_{obs2} / ms	Tb^{3+} τ_{obs1} / ms τ_{obs2} / ms
[Ln(deppa)$_3$]	pH 4.8	1.87(5) (100%)	2.38(5) (100%)
	pH 7.4	1.90(5) (100%)	n.d.
[Ln(meppa)$_3$]$^{3-}$	pH 9.0	2.04(5) (92%) 0.53(8) (8%)	1.37(5) (100%)
	pH 7.0	2.01(5) (89%) 0.37(5) (11%)	1.36(5) (100%)
	pH 5.0	2.00(5) (85%) 0.40(5) (15%)	1.41(5) (100%)

Let us call the species found at pH 9 as the optimal species, and the species formed in acidic solutions and exhibiting a disrupted inner coordination sphere as the acid induced species. The asymmetrical transition measured at pH 2 is then attributed to the acid induced species and the symmetrical transition measured at pH 11 is attributed to the optimal species. The amount of acid induced species at pH 5, 7 and 9 was estimated by fitting the normalized emission spectra of the europium hypersensitive transition at the considered pH by a linear combination of the normalized emission spectra at pH 2 and 11. This procedure might enable retrieving the percentage of acid induced species and optimal species present in the $^5D_0 \rightarrow {}^7F_2$ transitions at the intermediate pH values. Only 13 % of the acid induced species was fitted at pH 5, 8 % at pH 7, and none at pH 9. This suggests that no residual inefficient acid induced species remain at pH 9.

A lifetime analysis at pH 5, 7 and 9 was conducted similarly to [Eu(deppa)$_3$]. The decay was found here to be better fitted with double exponentials. A long lifetime of 2.0 ms and a shorter lifetime of 0.4 ms were found within the decay at all the measured pH values. The percentage of the long lifetime was found to decrease relative to the percentage of the short lifetime as the pH decreases (Table 5). This result is in reasonable agreement with the fit of the hypersensitive transition. The short lifetime species can thus be associated with the acid induced species. The

exact nature of this species is unknown, nevertheless, since the [Eu(deppa)$_3$] complex did not show any structural change in the $^5D_0 \rightarrow {}^7F_2$ transitions as a function of pH, the monoethoxyphosphoryl functional group is almost certainly involved in such a change.

The results obtained in this section further confirm the prevailing presence of the 1:3 (metal:ligand) species for both the deppa and meppa lanthanide complexes in aqueous solution and under the chosen conditions (i.e., 0.1 mM in complex, 0.1 M in KCl, pH 4.8 for the deppa complexes and pH 9.0 for the meppa complexes, room temperature).

2.6   Photophysical properties

The emission and excitation spectra of the ligands and their gadolinium, europium and terbium complexes were measured both at room temperature and at 77 K (Figure 22 and Figure 23). An aqueous KCl 0.1 M solution was used as a solvent and 10 % of glycerol was added for the low temperature measurements. The pH was set at the optimal value for luminescence by addition of HCl and NaOH 0.1 M (i.e., 4.8 for the deppa complexes and 9.0 for the meppa complexes as determined in the previous section with Figure 18).

2.6.1   Emission intensity as a function of the salt concentration

A KCl solution was used because it was beneficial for the luminescence of the lanthanide ion. As shown in Figure 21, the luminescence intensity depends on the concentration of an external salt for meppa^{2-} complexes. The influence of the ions was tested by measuring the luminescence in KCl, NaCl and NaClO$_4$ solutions. Each time, the intensity was increased compared to the unsalted solution. Furthermore, adding sodium perchlorate instead of sodium chloride does not seem to affect the improvement of the luminescence, so that the complex should be sensitive to cations rather than anions. A titration of the complex with increasing amounts of NaCl was then performed. Large amounts of salts are needed in order to significantly affect the emission intensity (100 equivalents). The evolution up to 1000 equivalents of sodium chloride was recorded, which corresponds to a concentration of 0.1 M at the fixed concentration of 0.1 mM in complex (Figure 21). The improvement of the luminescence intensity is not a linear function of the salt concentration, but seems to tend towards a saturated maximal intensity.
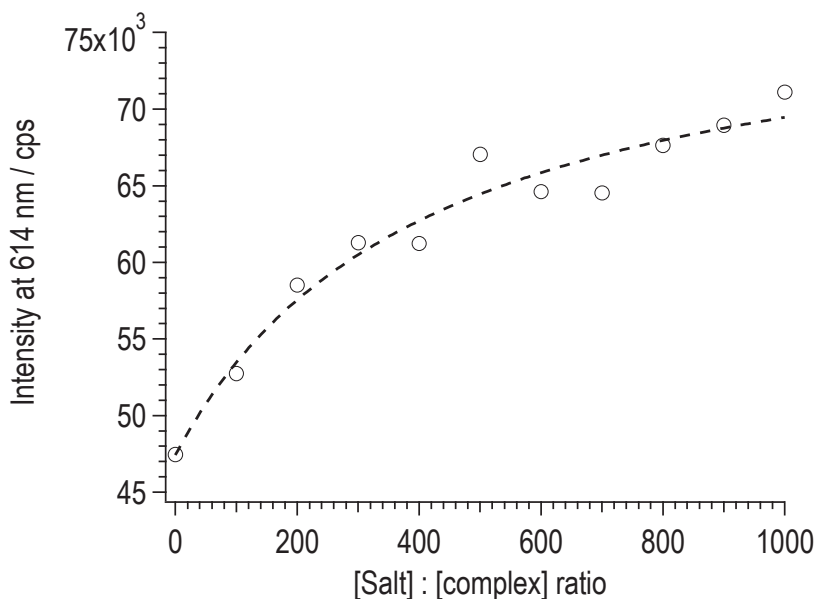
Figure 21. Luminescence increase upon addition of salt and the corresponding fit according to a Langmuir isotherm

This behavior might come from an affinity of the complex for cations, which somehow enhances the luminescence intensity. Its variation fits well with an intensity that depends on the association ratio of the complex with the cations according to a Langmuir equation: with θ the association ratio and K the association constant (see Equation 18)

$$M^+ + [LnL_3] \xrightleftharpoons{K} [M^+LnL_3]$$

$$K = \frac{\left[[M^+LnL_3]\right]}{[M^+] \cdot [[LnL_3]]} = \frac{\theta}{[M^+] \cdot (1-\theta)}$$

$$\theta = \frac{K \cdot [M^+]}{1 + K \cdot [M^+]}$$

$$I = (1-\theta) \cdot I_0 + \theta \cdot I_s$$

(18)

The improvement of the luminescence is then modeled as a combination of the free complex with intensity I_0 together with the higher emission intensity I_s from the associated complex-cation species. The association constant was here fitted at $K = 24 \pm 9$.

From the emission spectra, no change in the hypersensitive transition was observed upon variation of the salt concentration. The observed lifetime of the

lanthanide ion is slightly increased from 1.9 ms to 2.0 ms, thus suggesting a lower ratio of non-radiative deactivation. Since no change in the I_{tot}/I_{MD} ratio was found, and since this ratio defines mostly the radiative deactivation rate constant as shown by Werts et al.[12] with Equation 7 in Section 1.3.6, any increase of the radiative lifetime ought to be due to the small alteration of the refractive index when changing the salinity of the solution, which should be negligible compared to the experimental error. The association may thus decrease the non-radiative deactivation rate, for example due to the possible displacement of water molecules in the second coordination sphere in the cation-complex system.

The effect of KCl on the luminescence of the meppa complexes is similar to that of NaCl. Instead of the investigated NaCl salt and in order to match the conditions used in the determination of the stability constants, a KCl 0.1 M aqueous solution was then used as solvent for the meppa and deppa complexes.

2.6.2   Excitation and emission spectra

Concerning the ligand-centered and lanthanide-centered photophysical properties of the 6ppa complexes in a KCl 0.1 M aqueous solution with the optimal pH value, both ligands exhibit a broad triplet emission band at low temperature (77 K), 50 μs after the pulsed excitation at 274 nm (Figure 22 and Figure 23). This emission becomes slightly sharper upon coordination with a non emissive lanthanide ion, here gadolinium, and is strongly decreased when the energy can be transferred to a luminescent lanthanide ion (europium and terbium). A nearly complete disappearance is observed with deppa$^-$ complexes, and a faint remaining triplet emission is observed with the meppa^{2-} complexes. This already shows a better energy transfer from the deppa$^-$ triplet state to the lanthanide ion than from the meppa^{2-} to the same lanthanide ion.

The excitation spectra are all located on the absorption range of the ligands and have similar shapes as the absorption spectra, meaning that the energy is indeed absorbed by the ligands and transferred to the lanthanide (antenna effect).

A usual broadening of the emission peaks of the luminescent cations and a disappearance of the remaining emission from the triplet state is experienced between the emission spectra of the europium and terbium complexes measured at room temperature and at low temperature, but no other significant difference is observed.
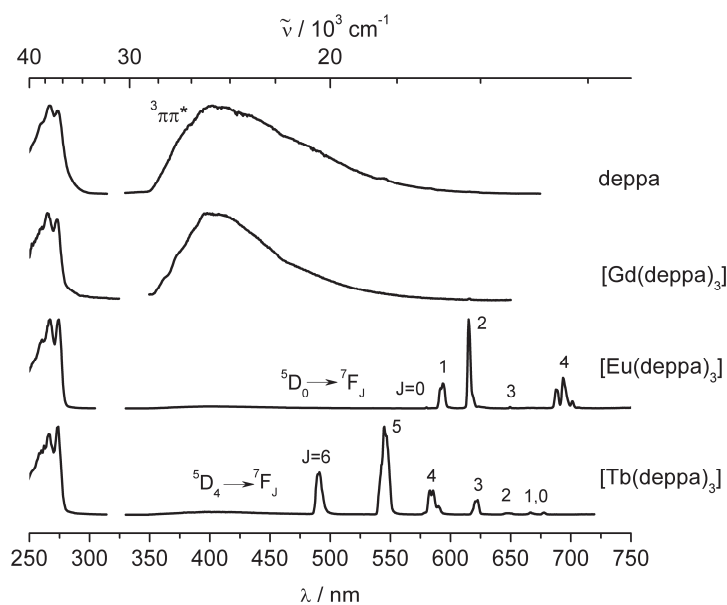
Figure 22. Excitation and emission spectra of deppa⁻ and its complexes at 77 K, 50 µs time delay, $1 \cdot 10^{-4}$ M, in KCl 0.1 M aqueous solution, pH 4.8, λ_{ex} = 274 nm, λ_{em} = λ_{max}.
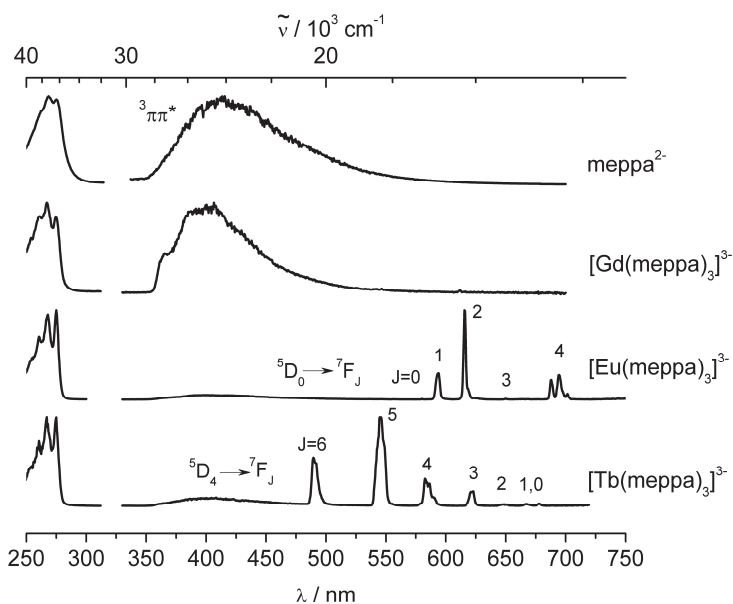
Figure 23. Excitation and emission spectra of meppa²⁻ and its complexes at 77 K, 50 µs time delay, $1 \cdot 10^{-4}$ M, in KCl 0.1 M aqueous solution, pH 9.0, λ_{ex} = 274 nm, λ_{em} = λ_{max}.

2.6.3   Lifetimes, Eu^{3+} $^5D_0 \leftarrow ^7F_0$ transition and quantum yields

The emissions of europium and terbium were characterized at room temperature by their lifetime analysis, as well as with the determination of their quantum yields.

The fit of the decay of the emission intensity of [Eu(deppa)₃] is monoexponential and that of [Eu(meppa)₃]³⁻ is a double exponential decay exhibiting a long and a short lifetime. The mono exponential lifetime and the long double exponential lifetime are in the millisecond range (Table 5). They are fairly similar with a value of 1.9 ms for [Eu(deppa)₃] and 2.0 ms for [Eu(meppa)₃]³⁻, which corresponds to the monoexponential values presented in Table 6 and Table 7. The shorter second lifetime of [Eu(meppa)₃]³⁻ found in Table 5 is 0.4 ms. These lifetimes are in good agreement with typical values for filled and hydrated coordination sphere. As a comparison, the standard [Eu(dpa)₃]³⁻ complex exhibits a long lifetime around 1.7 ms and a short lifetime around 0.3 ms that is attributed to the trishydrated [Eu(H₂O)₃(dpa)₂]⁻ species.[14]

When it comes to the terbium emission, [Tb(deppa)₃] exhibits a high lifetime of 2.4 ms, whereas [Tb(meppa)₃]³⁻ shows a lifetime of 1.4 ms (Table 7). In addition, the lifetime of [Tb(deppa)₃] remains unchanged upon cooling down to 77 K indicating that no significant vibrationally assisted back-transfer or deactivation is taking place between the terbium ion and the ligand. In comparison, [Eu(deppa)₃] has a higher lifetime of 2.3 ms at 77 K versus 1.9 ms at room temperature.

The number of water molecules in the first coordination sphere (q) was determined for the europium complexes by measuring the lifetimes both in H_2O and D_2O (Table 6). Using $\alpha = 0.31$ ms⁻¹, $A = 1.11$ ms, and zero XH oscillators in the first coordination sphere as parameters (see Equation 6, Section 1.3.5, page 13), no water molecules are found.

Table 6. Water molecules (q) in first coordination sphere obtained by Supkowski and Horrocks' formula providing lifetimes in H_2O and D_2O

	$\tau_{obs}(H_2O)$	$\tau_{obs}(D_2O)$	q
[Eu(deppa)₃]	1.87(5) ms	3.24(5) ms	-0.1(5)
[Eu(meppa)₃]³⁻	1.98(5) ms	3.00(5) ms	-0.2(5)

A high resolution excitation spectrum of the $^5D_0 \leftarrow {}^7F_0$ transition was performed for the europium tris(diethoxyphosphoryl picolinate). A $5 \cdot 10^{-3}$ M aqueous solution of [Eu(deppa)$_3$], pH 4.8 with 10 % glycerol added was frozen at 12 K and the high resolution excitation spectrum recorded for the emission of the $^5D_0 \rightarrow {}^7F_2$ transition.
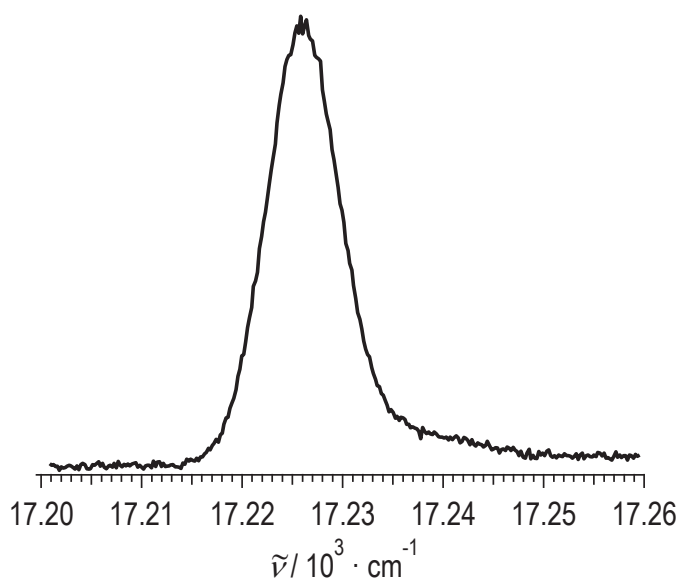
Figure 24. High resolution excitation spectrum of the $^5D_0 \leftarrow {}^7F_0$ transition for the emission at 615 nm. 12 K, $5 \cdot 10^{-3}$ M aqueous solution of [Eu(deppa)$_3$], pH 4.8 with 10 % glycerol. Maximum at 17226 cm^{-1} (580.53 nm), half-width of 8.4 cm^{-1}.

A single peak is clearly measured with a maximum at 17226 cm^{-1} and a half-width of 8.4 cm^{-1}. A very weak broad peak seems to be centered between 17,235 cm^{-1} and 17,240 cm^{-1} and could be attributed to the 1:2 species. Its feeble intensity could be due to the weak luminescence of the bis species as well as to the low population of this species. The presence of this peak is yet uncertain. Therefore, this experiment rather suggests that the emitting europium ion has only one defined luminescent coordination geometry. The 1:3 complex is hence the major luminescent species and exhibits only one geometry in the case of deppa$^-$ as ligand.

The quantum yields were finally calculated relative to the europium and terbium trisdipicolinate emission. The europium emission spectra were then used to calculate the radiative lifetimes, intrinsic quantum yields and sensitization efficiencies. These photophysical properties are presented in Table 7.

Table 7. Radiative and observed lifetimes, sensitized and intrinsic quantum yields and sensitization efficiencies. Conc. $1.0 \cdot 10^{-4}$ M, 298 K. under optimal conditions (see Sections 2.5 and 2.6.1), estimated errors 10%.

	τ_{obs} / ms	τ_r / ms	$\Phi_{L,Ln}$	$\Phi_{Ln,Ln}$	η_{sens}
$[Eu(dpa)_3]^{3-}$ [a]	1.7	4.4	0.24	0.39	0.61
$[Tb(dpa)_3]^{3-}$	2.1	n.d.	0.22	n.d.	n.d.
$[Eu(deppa)_3]$ [b]	1.9	6.2	0.15	0.31	0.49
$[Tb(deppa)_3]$ [b]	2.4	n.d.	0.40	n.d.	n.d.
$[Eu(meppa)_3]^{3-}$ [c]	2.0	5.2	0.08	0.38	0.21
$[Tb(meppa)_3]^{3-}$ [c]	1.4	n.d.	0.14	n.d.	n.d.

a) Taken from Gassner et al.[15], b) pH = 4.8, c) pH = 9.0

The deppa[-] sensitized emissions are always better than the meppa[2-] sensitized ones. The europium emission is more efficient in first $[Eu(dpa)_3]^{3-}$, then $[Eu(deppa)_3]$ and weaker in $[Eu(meppa)_3]^{3-}$. The decrease in quantum yield between the $[Eu(deppa)_3]$ and the $[Eu(meppa)_3]^{3-}$ sensitized europium emission is nearly by a factor two. When looking at the intrinsic quantum yields and sensitization efficiencies, the difference between $[Eu(deppa)_3]$ and $[Eu(meppa)_3]^{3-}$ is mainly due to the better sensitization efficiency of the deppa[-] ligand. Nearly half of the absorbed photons are transferred to the lanthanide with deppa[-], versus only 21 % with meppa[2-]. Additionally, the little increase in intrinsic quantum yields from $[Eu(deppa)_3]$ to $[Eu(meppa)_3]^{3-}$ is not sufficient to compensate for the lower sensitization of the meppa[2-] ligand.

Concerning the terbium emissions, a better efficiency is found in $[Tb(deppa)_3]$. A high quantum yield of 40 % is reached, almost twice that of the $[Tb(dpa)_3]^{3-}$ sensitized emission. $[Tb(meppa)_3]^{3-}$ is also better than the corresponding europium emission, with a fair 14 % quantum yield.

Very high terbium quantum yields up to 95 % have already been measured in aqueous solution with functionalized 2,6-bispyrazolyl-pyridine derivatives (e.g. H_4**L9** in Scheme 5, page 26).[25] Such ligands form 1:1 complexes with lanthanide ions. The replacement of the carboxylate coordinating groups in such 2,6-bispyrazolyl-pyridine derivatives with phosphonates was also undertaken and yielded lower quantum yields and higher lifetimes.[45] Despite the unique example of

carboxylate functionalized 2,6-bispyrazolyl-pyridine derivatives, quantum yields higher than the luminescent $[Ln(dpa)_3]^{3-}$ complexes in aqueous solutions are seldom encountered. A quantum yield of 40 % thus remains high compared to the average quantum yields in aqueous solutions.

Even though no simple calculation of the radiative lifetime of terbium luminescence is known, some reasonable assumptions considering the efficiency of the high $[Tb(deppa)_3]$ luminescence can be undertaken based on the previous discussion on lifetimes. Since cooling the sample seems to have no effect on the lifetime, the energy is lost by other means than back-transfer. Hence, the portion of the sensitization efficiency coming from the ligand to metal energy transfer efficiency should be rather high (higher than with usual values for which back-transfer is taking place). The limiting factor of this sensitization efficiency might then be the intersystem crossing of the ligand from singlet to triplet. Nevertheless, no indication considering the intrinsic quantum yield is available, so that it is difficult to discuss whether the high quantum yield is the result of a high sensitization and an average intrinsic quantum yield or an average sensitization with a good intrinsic quantum yield.

Rationalizing the lower quantum yield of the meppa^{2-} complexes compared to the corresponding deppa$^-$ ones should also be performed carefully, since very few data are available to confirm the assumptions. A similar observation was performed comparing helicate structures formed with monoethoxyphosphoryl or dihydroxyphosphoryl groups replacing the carboxylates (as shown in Figure 2, page 28).[48] There, the dihydroxy helicate complex usually had a lower quantum yield than the monoethoxy analog. The attempted explanation was a higher hydrophilicity of dihydroxy groups which could generate more H-bonding with proximate water molecules. However, a simple structure based discussion might yield to some further interesting considerations. The structural difference between the two ligands is the replacement of one ethoxy group on the phorphoryl with a hydroxyl group. Independently of any consideration on the coordination mode of the phosphoryl group, the removing of one ethoxy has two direct consequences. First it relaxes some steric hindrance in the complex, and furthermore introduces an additional negative charge which might allow a harder interaction between the phosphoryl and the cation and should thus shorten the distance between the ligand and the metal ion compared to the interaction with an uncharged coordination site. Therefore, the major difference between the two complexes ($[Ln(deppa)_3]$ or $[Ln(meppa)_3]^{3-}$) is probably a slightly different distance and tilt between the ligands and the lanthanide ion. Looking at the triplet state energies on Figure 22 and

Figure 23, the position is fairly similar, so that the energy gap between the triplet state and the excited levels of either europium or terbium should be similar for both ligands. In addition, as already partly proposed by Chauvin et al.[48], the negative charge might induce some other effects for example on the surrounding solvent, which might favor quenching and impact the transfer rate from the ligand toward the lanthanide ion, the deactivation of the excited state of the ligand and the different deactivations of the lanthanide ion. This statement might even be reinforced by the observed dependence of the luminescence intensity of the meppa^{2-} complexes on the salinity of the solution, which might counterbalance to some extent the effect of the negative charge, and thus disrupt the structure of the surrounding water molecules.

2.7 Conclusions

6-Diethoxyphosphoryl picolinic acid, 6-monoethoxyphosphoryl and 6-dihydroxyphosphoryl picolinic acid were synthesized and used as ligands for luminescent lanthanide complexes. All the three phosphoryl derivatives are water soluble and therefore suitable for a direct comparative study. The formation of lanthanide complexes was studied and showed comparable stabilities within the phosphoryl series, except for the dihydroxy ligand because of a prompt precipitation when a lanthanide cation is added. Similarly to the literature, the phosphoryl derivatives tend to increase the stability constants compared to a carboxylate analog. A nice complementary behavior was shown between dpa^{2-}, deppa$^-$ and meppa^{2-} complexes which have respective maximum emission intensities in neutral (pH 7.4), acidic (pH 4.8) and basic (pH 9.0) media. Hence, an uncommonly low pH of 3 still allows a good emission of europium tris deppa$^-$ complex, whereas an uncommonly high pH of 10 still allows a good emission of europium tris meppa^{2-} complex. This pH behavior was partly explained for [Eu(meppa)$_3$]$^{3-}$ by pointing at a change in the shape of the hypersensitive $^5D_0 \rightarrow {}^7F_2$ europium transition that indicates a change in the inner coordination sphere at low pH. The presence of a mixture of the disturbed, possibly protonated complex species, together with the more efficiently luminescent tris complex under acidic conditions up to neutral conditions was also confirmed by lifetime analysis.

The [Eu(meppa)$_3$]$^{3-}$ complex was also shown to be sensitive to the salinity of the aqueous solution. Up to salt to complex ratio of 200, the luminescence is linearly improved as the concentration of salt is increased. At higher concentrations, a

saturation of the improvement is observed. This behavior can be well fitted by assuming an association between the complex and a cation, which can be modeled by a Langmuir isotherm, and by combining the contribution of the free complex lower emission together with the higher emitting associated complex-cation system.

Concerning the photophysical properties in KCl 0.1 M and at the optimal pH value, for the europium tris deppa$^-$ complex, a fair quantum yield of 15 % was measured at pH 4.8. It was found to be much more important for terbium tris deppa$^-$, with a quantum yield of 40 %. On the other hand, europium and terbium tris meppa^{2-} complexes have lower quantum yields at pH 9.0, with 8% and 14% respectively. The lifetimes in deuterated water precluded the presence of water molecules in the first coordination sphere of deppa$^-$ and meppa^{2-} complexes. A high resolution excitation spectrum of the $^5D_0 \leftarrow ^7F_0$ transition at low temperature also demonstrated that the europium ion has a single luminescent geometry with deppa$^-$ as ligand. The estimations of the radiative lifetimes and intrinsic quantum yields of the europium complexes suggest a better emission efficiency of the europium in $[Eu(meppa)_3]^{3-}$ compared to $[Eu(deppa)_3]$, but the low sensitization efficiency significantly decreases the quantum yield so that $[Eu(deppa)_3]$ is a better emitter than $[Eu(meppa)_3]^{3-}$. This significant decrease in lanthanide quantum yield from the sensitization with a deppa$^-$ ligand to the sensitization with a meppa^{2-} ligand might be rationalized by plausible structural differences induced by the negative charge and the less hindered ligand as well as by possible increased solvent interactions in the charged and less hindered meppa^{2-} complex favoring non radiative deactivations.

Comparatively to the dipicolinic acid complexes, it is obvious that the 6-phosphoryl picolinic ligands are to some extent more intricate. This may favor the simpler dpa^{2-} as standards for quantum yields for example, but opens many perspectives for applications and investigations based on deppa$^-$ and meppa^{2-} structures.

Potential applications of this class of ligands towards sensors and probes or in color reproduction domains are certainly to retain due to their interesting pH complementarities, potential sensing abilities of the monoethoxyphosphoryl group, yet to explore, and high quantum yields of the terbium diethoxyphosphoryl complex.

Chapter 3

Dipicolinate trioxyethylenated coumarin architecture

Searching for an efficient sensitizer

3.1 Introduction

The forthcoming study investigates a novel way to derivatize the dipicolinate framework in order to form ligands capable of sensitizing lanthanide ions. The design comprises a dipicolinate coordination site grafted at its *para* position with a polyoxyethylenated chromophore. The polyoxyethylene (POE) side chain acts as a linker between the coordination site and the distant chromophore. The design of the ligands was carried out to allow investigating the influence of several chromophores as sensitizers without disrupting the coordination sphere around the lanthanide ion. The architecture of the lanthanide complexes is represented in Figure 25.
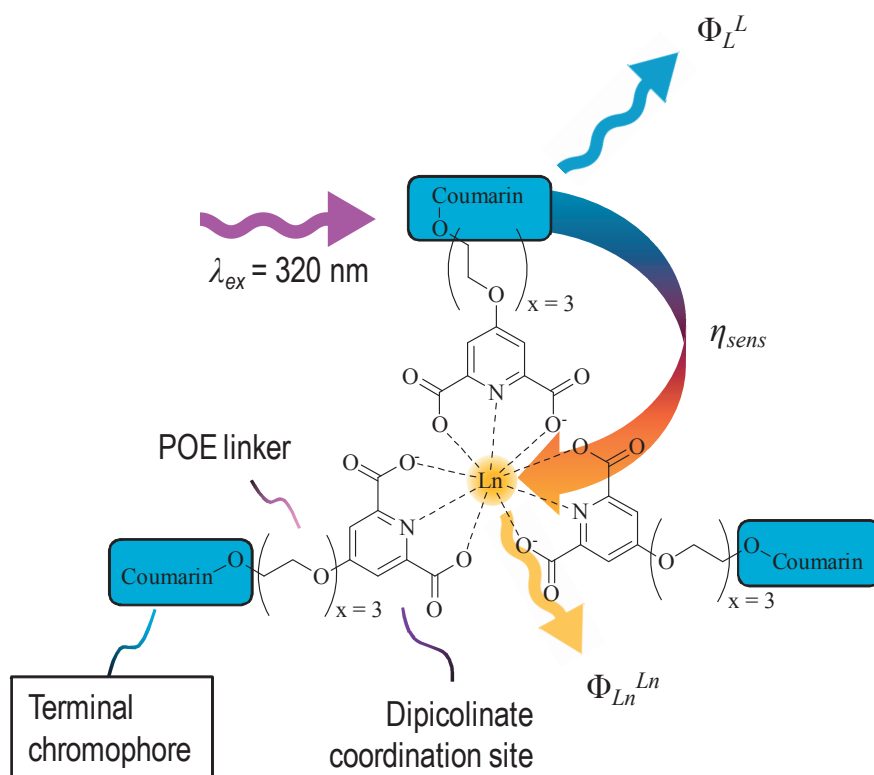
Figure 25. dp3Cy architecture and representation of the sensitization of lanthanide ions coordinated to the dipicolinate moieties by a series of terminal coumarin chromophores attached at the *para* position of the dipicolinate moiety by a trioxyethylene linker (POE, x = 3)

In this chapter, the linker is a trioxyethylene side chain (x = 3). The variation of the chromophore is investigated with a series of coumarins. The dipicolinate (dpa) framework acts as a coordination site for a lanthanide ion, forming 1:3 Ln:L complexes under stoichiometric conditions. Dpa also has a chromophore. The chromophore of the dpa framework is a classic example of a good sensitizer of several lanthanide ions, as extensively discussed in the first chapter (in Section 1.4, page 16-34). Nevertheless, its absorption is limited to short-wave UV light below 300 nm. A distant chromophore that would absorb higher than 300 nm would thus be exclusively excited, leaving the dpa moiety at its ground state. The wavy arrow pointing at a terminal chromophore in Figure 25 and representing its excitation by UV light at 320 nm symbolizes this exclusive excitation of the terminal chromophore.

Coumarins were chosen as chromophores absorbing above 300 nm, yet below 400 nm to ensure that the excited state is not too low (which would preclude any sensitization). A series of five coumarins will be investigated in this chapter. Each coumarin is grafted at the *para* position of the dipicolinate moiety, with a linker in between the dpa moiety and the coumarin. Trioxyethyene arms (POE, x = 3) were selected as linkers between the coumarin and the coordination site. This choice was motivated by its water-soluble compatibility, by the absence of conjugation with the dpa moiety or other chromophoric bridges, and by the characterization of lanthanide complexes based on similar structures (without the sensitizer at the end of the side chain).[15] This approach is therefore different from other designs involving dpa derivatives, for example as undertaken by Maury et al, who has developed highly conjugated systems with a Donor/Acceptor effect (based on the H_2**L4** from Table 1, page 19) for two photon microscopy.[88]

As a starting point for this chapter, a general procedure for the synthesis of the ligands is presented. The ability of the ligands to form stable lanthanide complexes will then be discussed, particularly, the stability of the tris complexes in aqueous solution and the stability at different pH values. Afterwards, the ligand-centered and metal-centered photophysical properties will be described. The sensitization of the europium and terbium ions will be demonstrated and the effect of the variation of the coumarin chromophore on the photophysical properties will be highlighted as an endeavor to relate the structure of the sensitizer to its sensitization efficiency.

3.2   General synthesis

Scheme 14. Synthesis of dp3Chrom ligands from a chromophore with an acidic –OH group (**1**), tosylated trioxyethylene monomethyl ether (**2**) and diethylester chelidamate (**5**).

The synthesis of the ligands is performed in four steps. The first step consists in the coupling of the chromophore (**1**) with the polyoxyethylene side chain. A nucleophilic functional group – an acidic hydroxyl at the seventh or fourth position on the coumarin core – reacts with a tosylated oligoethylene glycol monomethyl ether (**2**). The terminal monomethyl ether (**3**) is then cleaved by trimethylsilyl iodide (TMSI), thus forming the terminal alcohol (**4**). This alcohol is grafted on a chelidamic diester (**5**) through a Mitsunobu coupling. Because the coupled diester is hard to purify by chromatography without a massive loss of compounds, the Mitsunobu coupling has to be as clean as possible, in order to ensure that it can be

used directly in the next step. Therefore, polymer-supported triphenylphosphine (PS-TPP) was used instead of free triphenylphosphine. PS-TPP is a very convenient way to guarantee a minimal amount of impurities in the ligand diester precursor, since the polymer can be easily filtered out of the solution. The final step is the deprotection of the carboxylic esters (**6**) to form the carboxylates (Na$_2$dp3Chrom). The hydrolysis is carried out in ethanol upon addition of an aqueous solution of sodium hydroxide. The sodium salt of the ligand, which precipitates in ethanol, can then be further purified by a series of precipitations in ethanol. Five different coumarins were coupled to dpa by this way, using triethylene glycol as a side chain. The final ligands are shown in Scheme 15. Each ligand was characterised by NMR spectroscopy, and microanalysis. The detailed procedure as well as the characterization is reported in the appendices. The lanthanide complexes were directly prepared in aqueous solution by adding the stoichiometric amount of lanthanide ions (from a titrated solution of a lanthanide salt) to a Tris-buffered solution at pH 7.4 of diluted ligand.
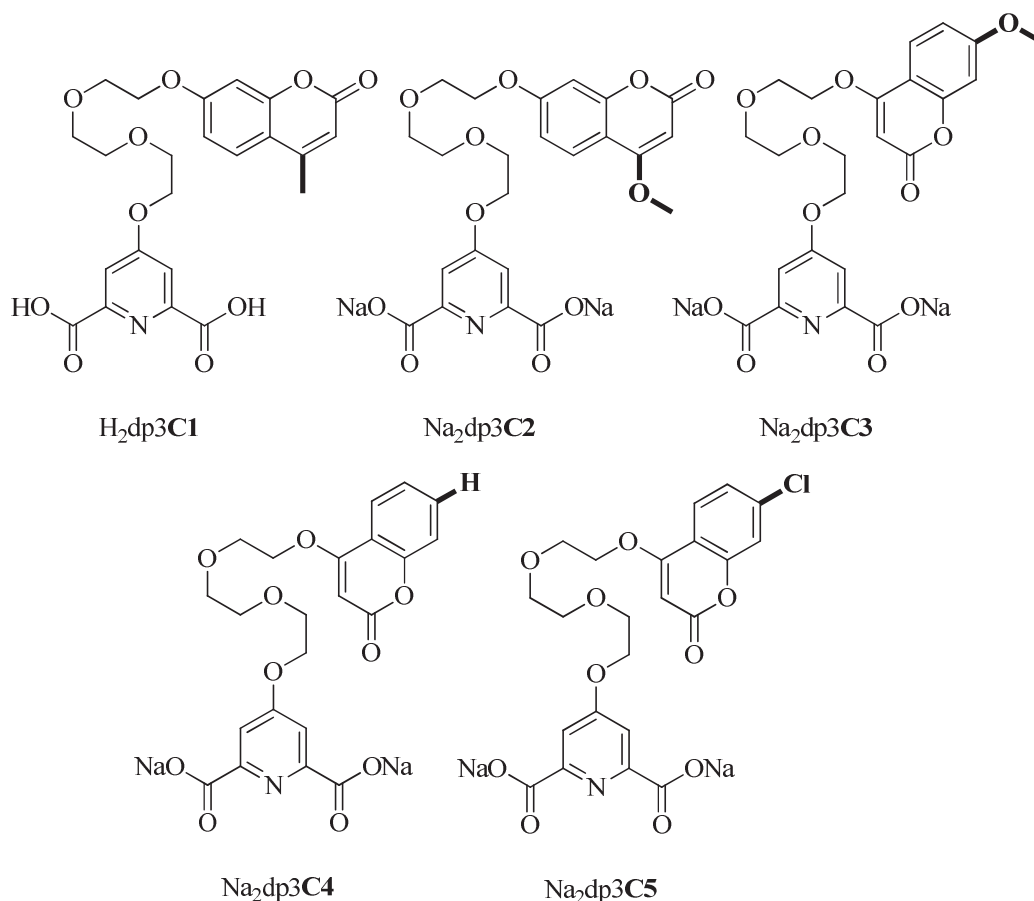
Scheme 15. Studied ligands with various coumarins as terminal chromophores

3.3   Stability in aqueous solution

The stabilities of the complexes in aqueous solution were probed in Tris-buffered aqueous solutions at pH 7.4. Such a pH value is typical for the investigations of dpa derivatives[14, 15] and will be demonstrated in the next section to be well suited for the luminescence of one of these complexes.

In order to confirm the predominant formation of the tris complex under 1:3 stoichiometry, one of the ligands was systematically submitted to several experiments. They include a Mass Spectrometry of the stoichiometric diluted solution, the measurement of the emission intensity of the ligand-centered and metal-centered luminescence as a function of the ligand to metal ratio, a lifetime analysis, the determination of the number of water molecule in the first coordination sphere and a high resolution spectrum of the $^5D_0 \leftarrow {}^7F_0$ transition of Eu^{3+} by monitoring the emission intensity of the $^5D_0 \rightarrow {}^7F_2$ transition upon excitation of the 0-0 transition. The stability of the other ligands was assessed by comparing their luminescence properties with those of the deeply studied ligand.

3.3.1   Mass spectrometry analysis of the 1:3 complex

The Mass Spectrometry analysis was carried out with an Electrospray Ionisation (ESI) in negative mode. The experiment shows series of peaks consistent with the 1:3 stoichiometry of the desired complex $[Eu(dp3C1)_3]^{3-}$: half the exact mass of the monoprotonated complex ($[Eu(dp3C1)_3]^{3-}$, m/z = 783.67), and half the exact mass of the monoprotonated complex with a water molecule ($[[Eu(dp3C1)_3]^{3-} + H_2O]$, m/z = 792.68).

3.3.2   Emission as a function of the [Eu³⁺] / [ligand] ratio

The stoichiometry of the complex is often critical for good luminescent properties. In the case of tridentate ligands such as dipicolinate derivatives, the 1:3 complexes has a coordination sphere filled by ligands. On the other hand, in aqueous solution, 1:2 and 1:1 species have water molecules in their first coordination sphere, which results in poor luminescence due to the quenching by close OH vibrations. The

apparition of these species at higher than 1:3 stoichiometries thus decreases the emission intensity of the luminescent lanthanide ion. Monitoring the intensity of the europium emission in solution as a function of the europium to ligand ratio hence allows observing the emergence and vanishing of the highest luminescent species (the 1:3 species). The excitation wavelength was chosen at the coumarin absorption maximum, i.e. 320 nm. This wavelength would also enable monitoring the emission intensity of the coumarin moiety as a function of the ligand to europium ratio. A titration of a $3 \cdot 10^{-4}$ M solution of the ligand with increasing amount of europium perchlorate was undertaken. The pH value of the solution was set at 7.4 with a Tris buffer, similarly to other studies with dipicolinate complexes. Figure 26 shows the emission intensity of the coumarin and europium sensitized emission upon addition of europium perchlorate. The emission of europium exhibits a Bell-shaped curve with a maximum in presence of 0.3 equivalent of Eu^{3+}. On the other hand, the coumarin emission resembles a sigmoid with a constant emission from 0.33 equivalent of europium ions. These results are then consistent with the formation of a luminescent 1:3 complex under stoichiometric conditions.
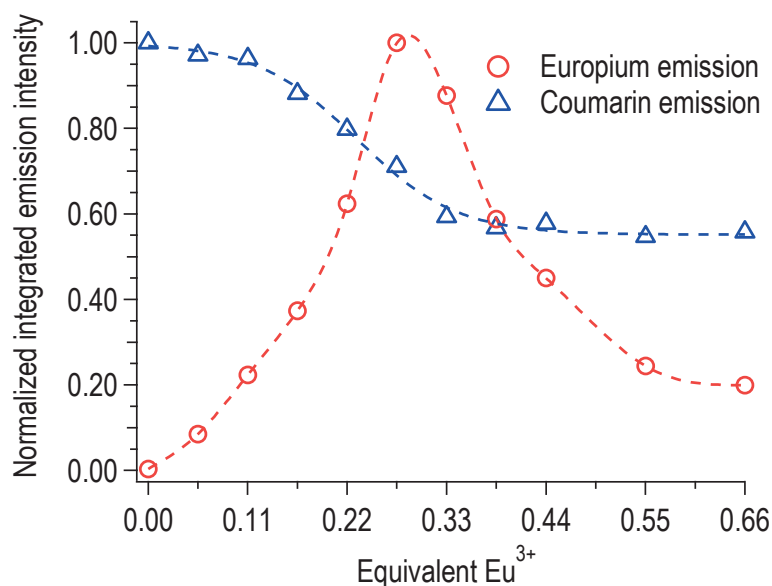
Figure 26: Normalized integrated emission of the europium (red circles) and coumarin (blue triangles) emission upon 320 nm excitation and upon addition of europium perchlorate to a $3 \cdot 10^{-4}$ M solution of $(dp3C1)^{2-}$ in Tris 0.1 M, pH 7.4, 298 K

3.3.3   Absorption as a function of the [Eu³⁺] / [ligand] ratio

The absorption of the ligand was also monitored as a function of the amount of Eu^{3+} (Figure 27), but precipitation did occur above 0.66 equivalent Eu^{3+}, so that no stability constant could be extracted from these experiments and no correlation could be established with the dpa ligand. However, according to previous results for dipicolinate *para*-polyoxyethylene ligands (shown in Scheme 3, page 24),[15] it was established that stability constants of the Eu^{3+} complexes were close to that of dpa. It seems then reasonable to consider that the dp3C1 ligand has a comparable ability towards lanthanide complexation.
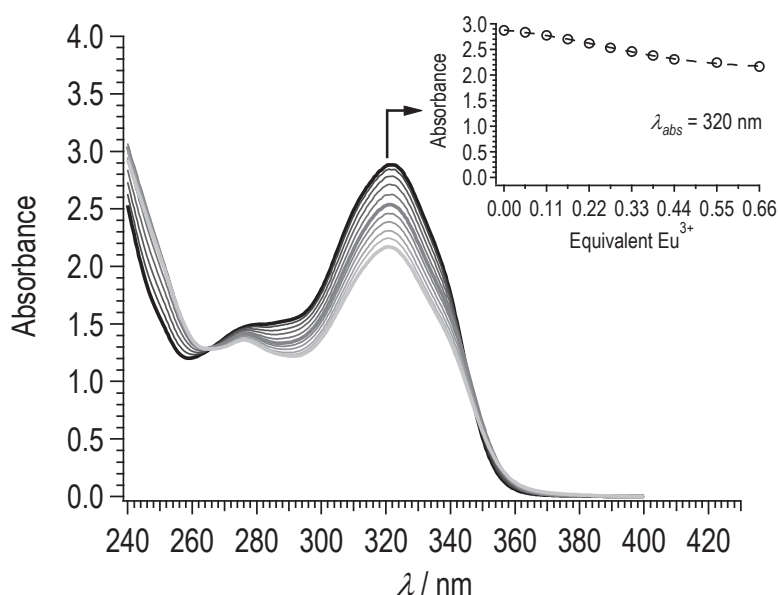
Figure 27. Absorption of dp3C1 $3 \cdot 10^{-4}$ M in Tris 0.1 M, pH 7.4, upon addition of europium perchlorate

3.3.4   Photophysical properties of the 1:3 stoichiometry

In Figure 28 the emission spectrum of $[Eu(dp3C1)_3]^{3-}$ is compared with the emission spectra of $[Eu(dp3OMe)_3]^{3-}$ and of $[Eu(dpa)_3]^{3-}$. The emission spectrum of the $[Eu(dp3C1)_3]^{3-}$ complex has the same shape as other *para*-polyoxyethylenated dipicolinate complexes $[Ln(dp3R)_3]^{3-}$ where the substituent R is OH, NH_2, OMe or Phthalimide instead of the coumarin.[15] Therefore, the coordination spheres around the europium cation must be equivalent for all these dipicolinate ligands. It also

indicates that the presence of the coumarin moiety does not interfere with the coordination sphere.
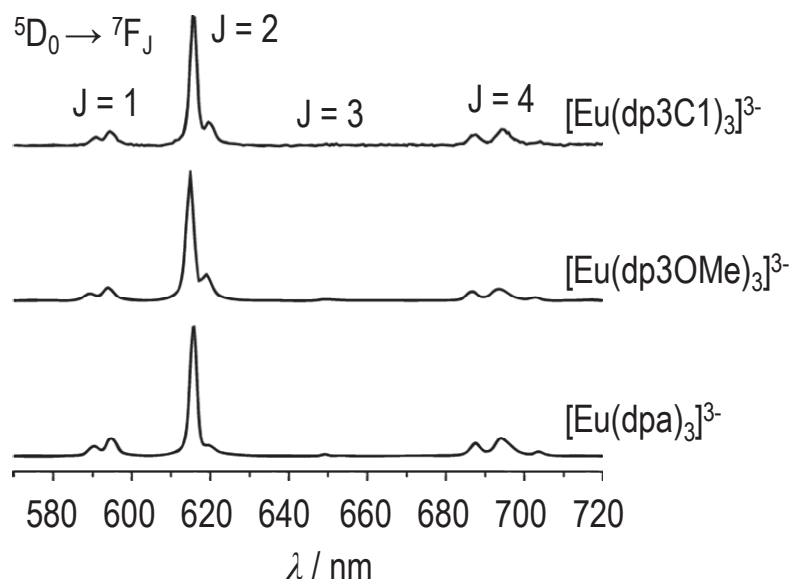
Figure 28. Characteristic emission from Eu^{3+} in a series of europium trisdipicolinate complexes

In addition, lifetime measurements both in water, $\tau_{obs}(H_2O) = 1.4 \pm 0.1$ ms, and in deuterated water, $\tau_{obs}(D_2O) = 2.6 \pm 0.1$ ms, lead to the conclusion that no water molecule is in the first coordination sphere ($q = 0.02$), using Horrocks phenomenological equation (Equation 6, Section 1.3.5, page 13) with $\alpha = 0.31$ ms^{-1}, $A = 1.11$ ms, and zero XH oscillators in first coordination sphere. This last result confirms that the coordination sphere of the europium ion is filled by the three tridentate dipicolinate entities. Besides, the lifetime is close to those previously obtained within the dipicolinate series.

A high resolution excitation spectrum was measured on the powder solid sample at 12 K by direct excitation of the $^5D_0 \leftarrow {}^7F_0$ transition (Figure 29). The emission intensity of the $^5D_0 \rightarrow {}^7F_2$ transition at 615 nm has been monitored thereof as a function of the excitation wavelength. The resulting spectrum shows a single peak located at 17223 cm^{-1} (580.61 nm) with a half-width of 17.9 cm^{-1}. Hence, only one luminescent europium geometry is present in the solid state sample, in all probability similar to that of $Cs_3[Eu(dpa)_3]$ (D_3 symmetry). All these results are in agreement with the hypothesis of a similar coordination of the europium ion to dp3C1 ligands compared with the coordination to dp3R or dpa ligands.
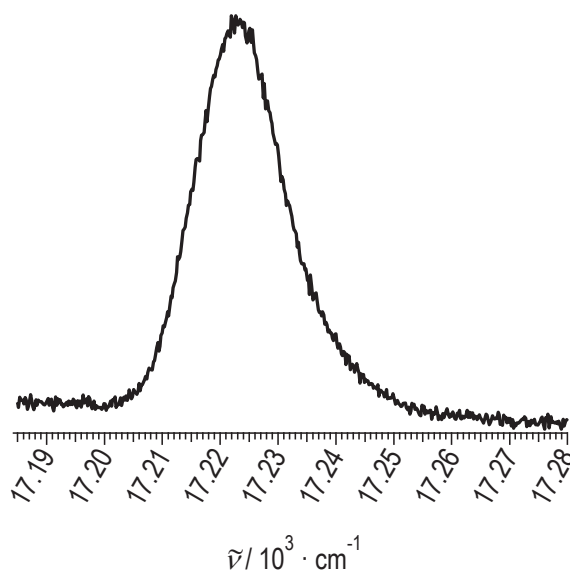
Figure 29. High resolution excitation spectrum of the $^5D_0 \leftarrow ^7F_0$ transition for the emission at 615 nm. 12 K solid state sample. Maximum at 17223 cm^{-1} (580.61 nm), half-width of 17.9 cm^{-1}.

3.3.5   Emission as a function of the [Eu^{3+}] / [ligand] ratio upon variation of the terminal coumarin

From the experiments performed with the dp3C1 ligand, it seems clear that the distant coumarin does not affect the predominant formation of the luminescent tris complex in aqueous solution. No evidence for a disruption of the character expected for a stable tris complex under stoichiometric conditions was highlighted.

In order to confirm that this behavior persists with the other ligands bearing different coumarins at the end of the trioxyethylene linker, the formation of the complexes in solution was verified by monitoring the emission of the lanthanide ion upon titration of the dp3Cy ligands with Eu^{3+} (Figure 30). In each case, a maximum of the emission is reached at a ligand to lanthanide ratio (Ln:L) of 1:3. Furthermore, the lifetimes from the emissions at a Eu:L ratio of 1:3 are all around 1.4 ms ± 0.1 ms, which are, as already seen, typical of the relaxation of europium through f-f transitions in dpa complexes without water molecules in the first coordination sphere. The parent dpa ligand exhibits for example a lifetime of 1.6 ms for its tris species and 0.3 ms for its tris-hydrated bis species.[11, 14] With the dp3Cy containing complexes, the lifetimes at 1.4 ms are well fitted by monoexponential decays; the [LnL$_3$] species are then the major luminescent species in aqueous solution under those conditions.
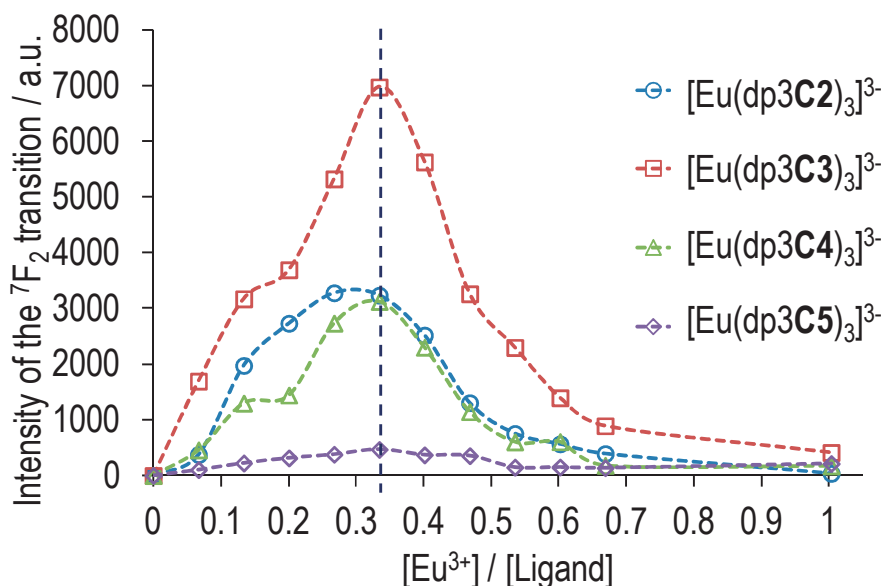
Figure 30. Intensity of the $^5D_0 \rightarrow {}^7F_2$ transition of europium(III) upon titration of $3 \cdot 10^{-4}$ M aqueous solutions (Tris-buffered, pH 7.4) of each dp3**Cy** ligand by europium perchlorate. Maximal emission reached at ⅓ of europium per ligand ratio. The lifetime at those maxima is 1.4 ms for all the ligands.

The dpa coordination site is, as expected, not sterically hindered with this series of distant coumarins. The stability of the lanthanide complexes is then assumed to be similar to that of the parent dpa complexes.

3.4   Emission as a function of pH

An important parameter of an aqueous solution is its pH value. The luminescence of a lanthanide complex is often sensitive to the pH of the solution. This may happen either because of a direct contact between the lanthanide ion and the solution, e.g. in complexes with water molecules in their first coordination sphere, because of a modification of the stability of the complex as a function of pH, or because of a protonation of the sensitizer. Here, the trisdipicolinate complexes have no water molecules in their first coordination sphere, as demonstrated in the previous section, and the coumarins have no protonable groups. Thus, any modification of the emission intensity as a function of pH should come from a modification of the amount of tris species because of acid/base induced effects on the stability.

From the literature, dpa complexes are usually investigated in aqueous solution under neutral to slightly basic conditions, the luminescence decreasing outside the 4-10 pH range.[14, 15, 23, 89] As demonstrated in Chapter 2 about the 6-phosphorylated picolinic acid ligands, changing the coordination site of the ligand can alter the optimal pH value and shift it towards more acidic or more basic values. Therefore, the sensitivity of the luminescence to the pH value of the solution seems to be related to the stability of the complex and to the acid/base behavior of the coordinating functional groups. If the coordination site is unchanged, this behavior should not be modified and hence, the optimal pH value of the emission from the lanthanide ion should be the same.

In order to check whether the best conditions for luminescence with the investigated dipicolinate complexes are comparable to those reported in the literature for similar compounds, the emission spectrum of an aqueous solution of **[Eu(dp3C1)$_3$]$^{3-}$** was monitored as a function of pH (Figure 31). Two excitation wavelengths have been chosen. The first one at 280 nm is centered on the absorption of the dpa and coumarin moieties. The second one at 320 nm is at the maximum of absorption of the coumarin chromophore, where dpa does not absorb any light.

The emission of the 4-methylumbelliferone moiety has a maximum at 389 nm. Upon excitation at 280 nm or 320 nm, its intensity increases 1.7 times as the pH value increases from pH 2.5 to pH 10.4. The coumarin is yet more emissive under an excitation at 320 nm than at 280 nm, because dpa also absorbs at 280 nm and thus decreases the amount of excitation light available for the coumarin.

On the other hand, the emission intensity of the europium ion is higher when exciting at 280 nm rather than 320 nm. The difference between the emission intensity from the Eu^{3+} ion for the complex excited at 280 nm and for the complex excited at 320 nm is quite constant and close to a ratio of 1.8. Above pH = 6.3, the ratio of the Eu^{3+} / coumarin emission is quite constant, whereas below pH 6, the emission from the europium ion is more affected than the coumarin one. It thereby reflects that the emission from the coumarin is little affected by a fairly acidic medium, whereas the emission from the europium ion is dependent on the stability of the complex (with competition between complexation and protonation of the carboxylic acid functions at low pH values).
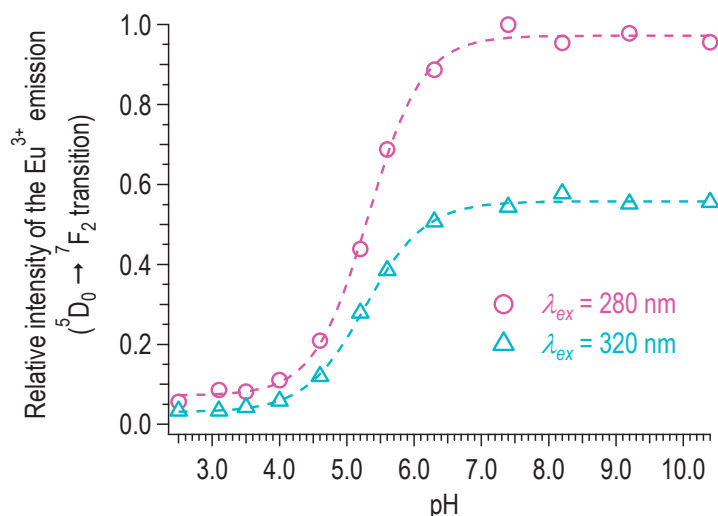
Figure 31. Relative peak intensity of the $^5D_0 \rightarrow {}^7F_2$ transition from $[Eu(dp3C1)_3]^{3-}$ in aqueous solution as a function of the pH value

The detailed investigation of the emission as a function of the pH value with the **$[Eu(dp3C1)_3]^{3-}$** complex sustains the results found in the literature. The distant chromophore should therefore neither alter the stability at a given pH, nor alter the optimal pH, as long as no strong coordinating group is present on the chromophore, and as long as the bulkiness of the chromophore is contained. For comparison purposes with already reported results within this series (by Gassner et al.[15]), the pH value was fixed at 7.4 with a 0.1 M Tris buffer. These conditions are used throughout all the series of investigation that follow.

3.5   Photophysical properties

The photophysical properties of the stable tris complexes will now be studied and the differences induced by the different coumarins will be highlighted.

3.5.1   Absorption spectra

The absorption spectra of the europium complexes are presented in Figure 33 together with the scaled absorption spectra of each coumarin (grafted to the POE side chain but without the dpa moiety for comparison purposes). As intended, the presence of the coumarins extends the absorption range from below 300 nm (absorption of the dpa moiety) up to 360 nm. The shape of the coumarin absorptions

above 300 nm are practically unaffected by the coupling to the dpa coordination site and by the complexation of the ligands to the europium ion. Even though the extinction coefficients of the maxima (attributed to π→π* transitions) are changed upon coordination, when the absorption spectra are scaled at the maximum of the coumarin absorption, only small differences between the peak and shoulder of the absorption of the coumarin moieties above 300 nm are observed. This behaviour was anticipated because the coumarins are not directly involved in the coordination, which is performed by the dpa moiety. On the parent dpa, the coordination indeed induces an increase of the extinction coefficient, a narrowing of the transitions, and a small bathochromic shift (red-shift) as shown in Figure 32, together with the effect of the coordination on the absorption from the dp3C1 ligand. The shifts at the dpa absorption range are however not observed with the dp3Cy ligands because the superposed absorptions of the coumarins mask the structure of the absorbance of the dpa moiety.

  Besides those coordination consequences, an essential result is that an excitation above 300 nm (e.g. 320 nm) only populates the coumarins, since the dpa moiety absorbs only below 300 nm. In a first step, all photophysical measurements were performed under excitation at 320 nm, in order to solely investigate the sensitization through the coumarins. The sensitization pathways in the complexes with the most efficient of the coumarins (in terms of sensitization efficiency) will be studied then in a separate chapter.
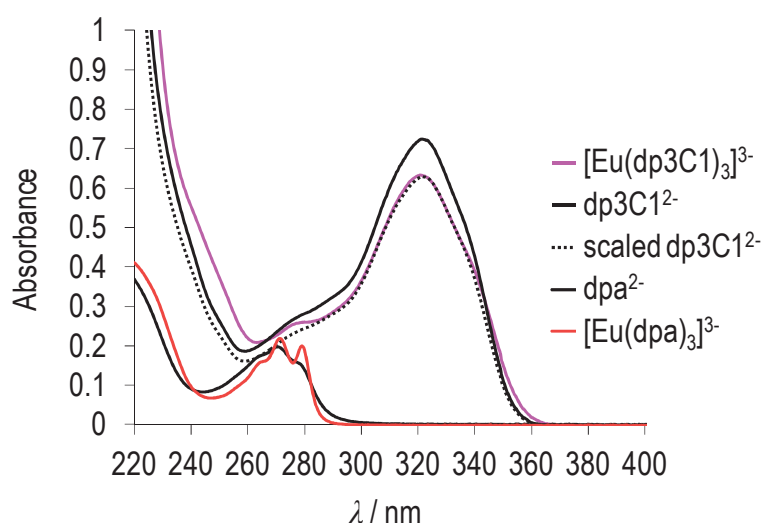
Figure 32. Absorbances of the free ligands dp3C1^{2-} and dpa^{2-} (black solid lines) compared with the absorbances of the complexes [Eu(dp3C1)$_3$]$^{3-}$ and [Eu(dpa)$_3$]$^{3-}$ (magenta and red solid lines) and to the scaled absorbance (at 320 nm) of the free ligand dp3C1^{2-} (dp3C1 scaled, dotted black line).
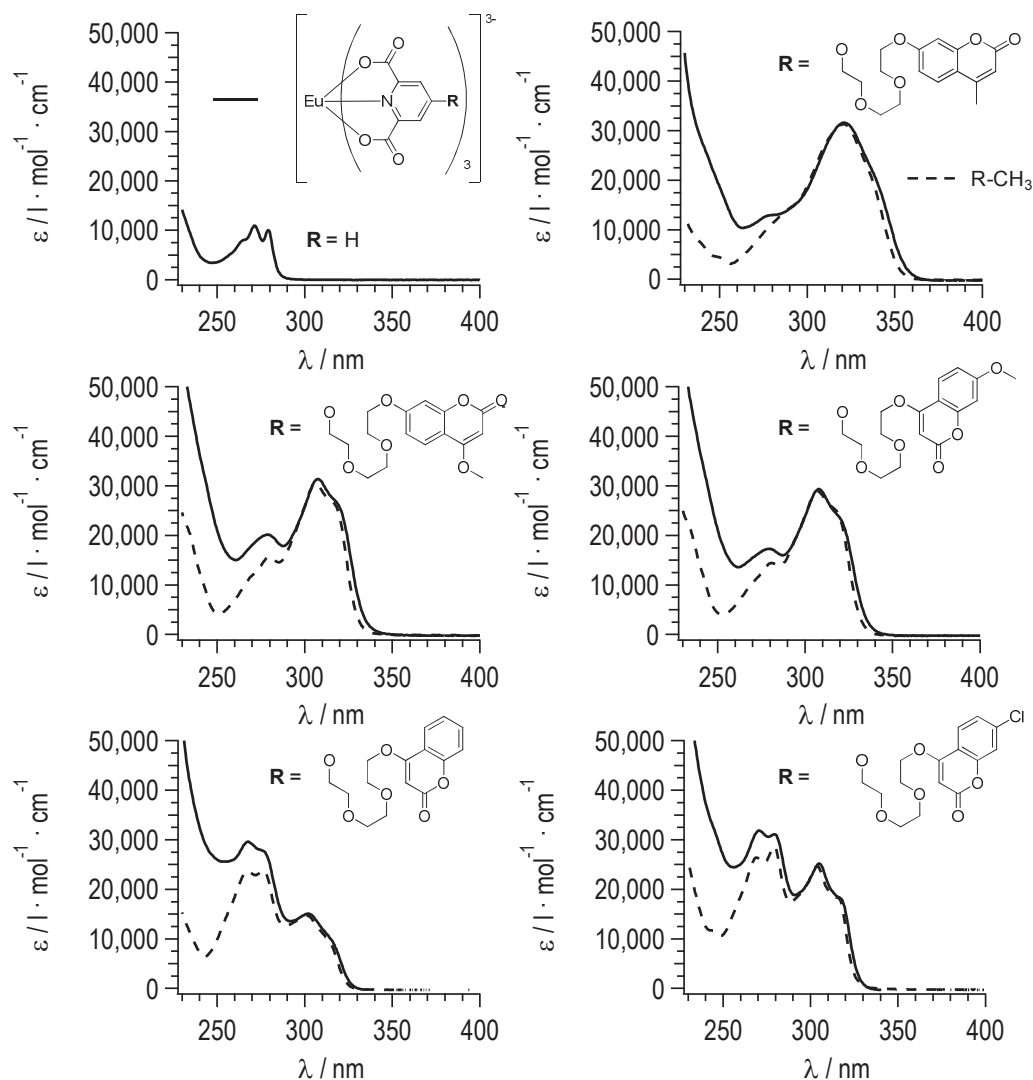
Figure 33. Molar extinction coefficients of the $[Eu(dp3Cy)_3]^{3-}$ complexes (plain) and the corresponding coumarin-trioxyethylene monomethyl ether (dashed) scaled to show their absorption range in the complexes. Aqueous Tris-buffered solution (0.1 mM in complex), pH 7.4.

3.5.2 Ligand-centered emission

The ligand-centred emissions from the gadolinium complexes (non emissive under those conditions) upon variation of the terminal coumarin are shown in Figure 34. The fluorescence from the singlet state (S_1) was measured at room temperature, whereas the phosphorescence from the triplet state (T_1) was recorded at 77 K, 50 µs after a pulsed irradiation.
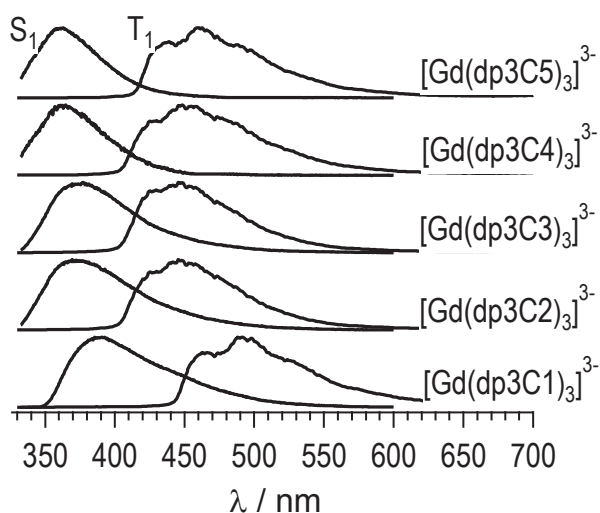
Figure 34. Fluorescence from S_1 and phosphorescence from T_1 of the $[Gd(dp3Cy)_3]^{3-}$ complexes (λ_{ex} = 320 nm). Aqueous Tris-buffered solution (0.1 mM in complex), pH 7.4 (S_1), and frozen solution at 77 K (10 % glycerol added), 50 µs after a pulsed irradiation (T_1).

Table 8. Location of the singlet (S_1) and triplet (T_1) excited state of the dp3Cy ligands in their gadolinium complex in wavenumber ($\pm$ 300 cm^{-1})

$[Gd(dp3Cy)_3]^{3-}$	S_1(max) / cm^{-1}	T_1(0-0) / cm^{-1}
y = 1	26,000	21,500
y = 2	27,000	23,500
y = 3	27,000	23,500
y = 4	28,000	23,500
y = 5	28,000	23,000

According to the data in Table 8, a correlation exists between the structure of the coumarin (presented in Scheme 15, page 86) and the location of its excited states. For instance, dp3C2 and dp3C3 only differ by the coupling position on the coumarin, seventh *vs.* fourth respectively, and are characterised by the same singlet and triplet values (singlet at 27,000 cm^{-1} and triplet at 23,500 cm^{-1}). However, a similar value for the singlet state of two ligands does not imply that the triplet sates are located at the same energy. For example, dp3C4 and dp3C5 have a first excited singlet state at the same position (i.e. 28,000 cm^{-1}), but a first triplet excited state that is slightly shifted by *calc.* 500 cm^{-1}. It probably comes from a slightly better stabilization of the triplet excited state in the dp3C5 structure (7-chloro) compared to the dp3C4 structure (unsubstituted seventh position).

The ligand-centered properties give an important insight over the excited states of the ligand, which might sensitize a lanthanide ion. They will be further investigated in the next chapter, when endeavoring to decipher the sensitization pathways in the ligand with the most efficient coumarin sensitizer.

In the next section, the metal-centered properties will be discussed. It will enable finding which coumarin is more suited than the others, and possibly correlating the ligand-centered properties with the sensitization efficiencies.

3.5.3　　　Metal-centered emission

The metal-centered emissions from the europium complexes upon variation of the terminal coumarin are shown in Figure 35. They all exhibit the characteristic europium $^5D_0 \rightarrow ^7F_J$ f-f transitions (J = 1-4) under excitation at 320 nm, meaning that the europium is sensitized by each coumarin (so-called antenna effect). A residual fluorescence of the coumarin is also observed alongside. These short-lived coumarin emissions are absent on time-resolved spectra when a delay of a few microseconds is applied between the pulsed excitation and the measurement. The efficiencies of the ligand-centered and metal-centered emissions for the europium complexes are presented in Table 9.
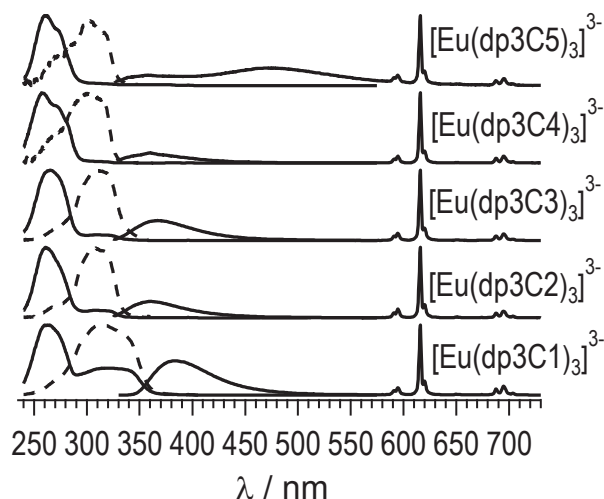
Figure 35. Excitation (left hand side, plain for the Eu-centred emission, dashed for the residual coumarin emission) and emission spectra (right hand side, λ_{ex} = 320 nm) of the $[Eu(dp3Cy)_3]^{3-}$ complexes (0.1 mM) in Tris-buffered aqueous solution, pH 7.4

An important observation from the emission spectra on Figure 35 is that all the europium emission spectra have exactly the same shape. Consequently, the radiative lifetimes τ_r calculated from Equation 7 (page 15) are all identical (4.2 ms) whatever the terminal coumarin. This result is consistent with other results found in the literature (from europium complexes of dpa derivatives as well as of other types of ligands), which seems to indicate that the radiative lifetime depends mostly on the coordination sphere and on the close environment.[15, 49] The observed lifetime τ_{obs} (defined as the inverse of the sum of the radiative rate constant with all other deactivation rate constants), which is fitted from the exponential decay of the emission after a pulsed excitation, is also indistinguishable at 1.4 ms (within experimental error) for all the europium complexes in Table 9. These lifetimes are similar to those of other dpa derivatives. As a consequence, the intrinsic quantum yield, which represents the efficiency of the radiative deactivation of the lanthanide ion relative to all its deactivations, has to be the same for each of the $[Eu(dp3Cy)_3]^{3-}$ complex. This suggests that the deactivation of the europium ion does not involve the distant sensitizer. Therefore, we can fairly assume that the difference in quantum yields Φ_L^{Eu} between the complexes in Table 9 is only due to the difference in sensitization efficiency.

Table 9. Photophysical properties of the $[Ln(dp3Cy)_3]^{3-}$ complexes at room temperature (λ_{ex} = 320 nm). τ_{obs}^{Eu} = 1.4 ms ± 0.1 ms, τ_r^{Eu} = 4.2 ms ± 0.4 ms Φ_{Eu}^{Eu} = 33 % ± 5 %, for all complexes in this table. Estimated error of 10 % on the quantum yields (sensitised quantum yields of the europium emission Φ_L^{Eu}, quantum yields of the ligand-centered emission Φ_L^L).

$[Eu(dp3Cy)_3]^{3-}$	Φ_L^{Eu} / %	Φ_L^L / %	η_{sens} / %
y = 1	1.7	7.7	5.1
y = 2	0.4	0.9	1.2
y = 3	0.7	1.1	2.1
y = 4	n.d.	n.d.	<0.6
y = 5	0.3	n.d.	0.8
$[Tb(dp3Cy)_3]^{3-}$	Φ_L^{Tb} / %	Φ_L^L / %	τ_{obs} / ms
y = 1	0.5	7.6	0.6
y = 2	1.4	1.0	1.6
y = 3	1.7	1.3	1.6
y = 4	n.d.	n.d.	1.8
y = 5	0.3	n.d.	1.7
$[Gd(dp3Cy)_3]^{3-}$	Φ_L^{Gd} / %	Φ_L^L / %	
y = 1	0	9.1	
y = 2	0	1.1	
y = 3	0	1.6	
y = 4	0	n.d.	
y = 5	0	n.d.	

N.d. values were too low to be properly measured with the available setup

This conclusion is however limited to these $[Eu(dp3Cy)_3]^{3-}$ complexes. A comparable study was performed with the terbium complexes, and points to a strong deactivation of the terbium excited state. This was particularly demonstrated with the short observed lifetime for the $[Tb(dp3C1)_3]^{3-}$ complex (0.6 ms ± 0.1 ms). This is expected because the dp3C1 ligand has the lowest excited states (either singlet at 26,000 cm^{-1} or triplet at 21,500 cm^{-1}). The $^5D_4$ spectroscopic level of terbium(III) being located at 20,500 cm^{-1}, a back-transfer seems highly probable. This also explains why both the dp3C2 and dp3C3 ligands, with higher excited states, are better than dp3C1 for the terbium sensitization (Φ_L^{Tb} = 1.4 % and 1.7 % versus 0.5 % respectively).

The $^5D_2$ spectroscopic level of europium(III), located at 21,500 cm^{-1}, is at the same energy as the triplet of dp3C1. Since no particular deactivation relative to the other complexes was observed here, it suggests that the energy transfer occurs on a lower spectroscopic level such as the $^5D_1$ (at 19,000 cm^{-1}) or the emissive $^5D_0$ (*calc.* 17,223 cm^{-1} from the high resolution measurement of the $^5D_0 \leftarrow {}^7F_0$ transition of Cs$_3$[Eu(dp3C1)$_3$] in Section 3.3, Figure 29, page 91).

A comparison of the ligand-centered quantum yields of the non-emissive gadolinium complexes Φ_L^L(Ln=Gd) with those of the emissive europium complexes Φ_L^L(Ln=Eu), reveals that the ligand-centered quantum yields of the gadolinium complexes are always higher than those of the corresponding europium complexes. A certain correlation exists between the ligand-centered quantum yield of the non-emissive complex Φ_L^L(Ln=Gd) with the corresponding europium-centered sensitized quantum yield Φ_L^{Eu}. When the ligand-centered quantum yield was too low to be measured, the europium quantum yield was also at the threshold limit of the setup. The emission from the dp3C1 ligand in the gadolinium complex (9.1 %) results in the highest europium quantum yield of the series (1.7 %). The lower emission from the dp3C2 and dp3C3 ligands (1.1-1.6 %) yields lower quantum yields (0.4-0.7 %), whereas the very few emitting dp3C4 and dp3C5 ligands have a very weak europium emission. An expected quenching of the ligand emission by the emissive lanthanide ion is however observed when measurable.

These first results obtained by variation of the distant sensitizer indicate several important limitations of the sensitization process. First of all, an appropriate energy difference between the acceptor spectroscopic level of the lanthanide ion and the donor excited states of the sensitizer is a very important limitation and has to be optimized to maximize the sensitization efficiency. This was demonstrated by

pointing at the strong deactivation of the terbium excited state in the ligand with the lowest excited states. When this limitation is overcome, the sensitization is then limited by the structure of the sensitizer. Small changes on a same backbone can indeed have drastic impacts on the photophysics of this molecule. For example, it is well known that the incorporation of a heavy atom such as a bromine or an iodine atom on a fluorophore increases the intersystem crossing rate by spin-orbit coupling.[90] In our case, we observed that several complexes with similar excited states but different structures exhibit completely different quantum yields. The limitation is then probably the competing deactivation processes, and particularly the quenching of each sensitizer by its environment.

The sensitization efficiency, which is defined as the ratio of the number of sensitized lanthanide ion per number of excited sensitizer, can be divided into several contributions according to the sensitization pathways (see Section 1.3.4, page 11). For a sensitization through the triplet state of the sensitizer, it is defined as the product of the intersystem crossing efficiency, η_{isc} (number of triplet state populated per number of excited singlet state), by the energy transfer efficiency, η_{et} (number of sensitized lanthanide ion per number of triplet sate sensitizer). To better understand the sensitisation process, the rate constants of each photophysical phenomenon must be considered, because the sensitization is in competition with many different deactivation pathways. To maximize the sensitization efficiency, the energy transfer rate constant has to be as high as possible compared to the other deactivations, ideally much higher, so that the other processes can be neglected, which would yield to a sensitization efficiency of 100 %.

The rate constant of the energy transfer is assumed to depend on the overlap between the donor state of the sensitizer and the acceptor state of the lanthanide ion, as well as on the distance between the donor and the acceptor. The importance of the energy of the excited states have already been illustrated in this first part, but the importance of the competing processes that can easily overcome the energy transfer rate was also pointed at. In an attempt to rationalize the mechanism of the energy transfer in a sensitized luminescent lanthanide complex, two steps will be undertaken. First, the sensitization pathways of the most efficient europium complex will be investigated in details by looking at the photophysical properties under different conditions, for example under different excitation wavelengths. In a second time, a shortening of the POE side chain of the best ligand i.e. dp3C1 will be carried out.

3.6   Concluding remarks

In this chapter, the stability of the dp3Cy complexes was demonstrated to be fairly independent on the terminal coumarin and probably similar to other dipicolinate derivatives. It was also shown that ligands with similar excited states can have different sensitization efficiencies, thus highlighting the importance of the structure dependent non-radiative deactivations of the coumarin chromophores. A similar observation from the 6-phosphorylated picolinate complexes showed that different ligands with a similar excited triplet state location can have different photophysical properties of the lanthanide ion and as well as different sensitization efficiencies. With the dp3Cy complexes, the photophysical properties of the europium ion are however identical. Only the effect of the coumarin chromophore is then investigated.

The dp3C1 ligand with 4-methylumbelliferone as a terminal coumarin displayed the best sensitization efficiency of the distant europium ion. The forthcoming chapters will then study the sensitization pathways in $[Eu(dp3C1)_3]^{3-}$ complexes and $[Eu(dpxC1)_3]^{3-}$ complexes where the polyoxyethylene side chain was shortened.

Chapter 4

Dipicolinate trioxyethylenated 4-methylumbelliferone ligand

Investigating the sensitization pathways

4.1 Introduction

This chapter reports a detailed investigation of the photophysical properties of $[Ln(dp3C1)_3]^{3-}$ complexes. The purpose is to determine the sensitization pathways that yield from a ligand excitation to a lanthanide emission. Figure 36 is a reminder of the structure of a $[Ln(dp3C1)_3]^{3-}$ complex.
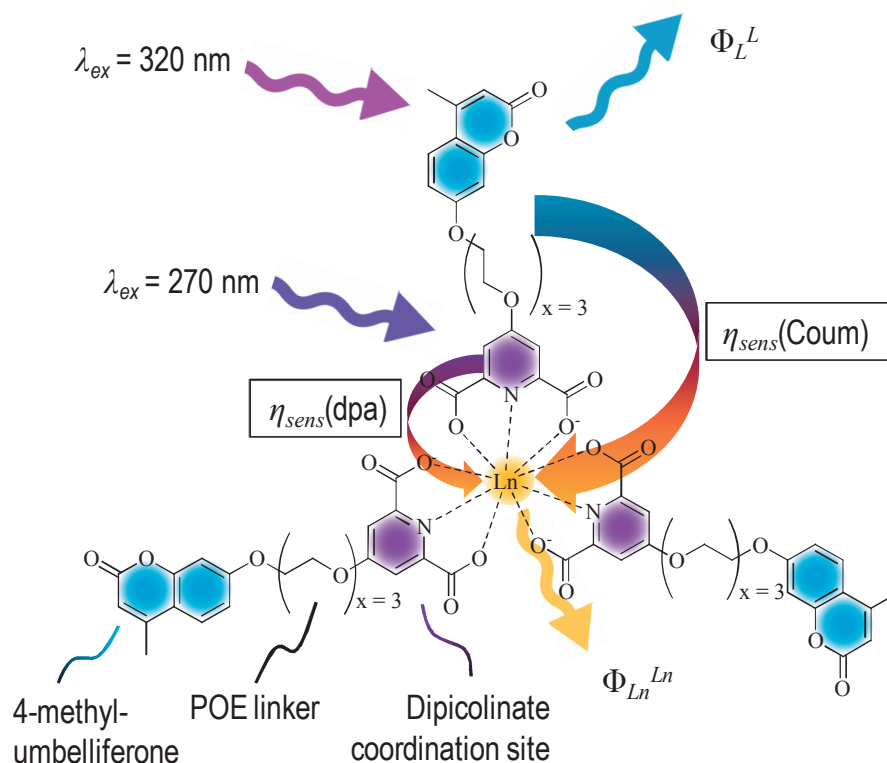
Figure 36. $[Ln(dp3C1)_3]^{3-}$ complexes with a trioxyethylene linker (POE, x = 3). Investigation of the sensitization pathways by excitation of the coumarin alone (320 nm) or by excitation of the coumarin and dpa together (270 nm).

In most molecular photophysical systems, the photophysical properties such as the emission spectrum, the quantum yield and the lifetime are independent of the excitation wavelength (so called Kasha-Vavilov's rule).[91] This statement is true for single component systems, where the absorption of the emissive compound is unscreened by another chromophore. Lanthanide complexes regularly experience

no wavelength dependence of their photophysical properties because the absorption is performed by a single component ligand, such as dpa. If the absorbption occurs via f-f transitions, the quantum yield, which corresponds to the intrinsic quantum yield, is higher than the quantum yield upon sensitization, because of the losses encountered during the sensitization pathway. Nevertheless, the very weak f-f ransitions are often neglected in diluted solution.

In the dipicolinate *para*-polyoxyethylenated coumarin architecture, the Kasha-Vavilov's rule no longer holds because two distinct chromophores (the coumarin one and the dpa one) are present in a single ligand. The additional coumarin chromophore enables an excitation of the ligand above 300 nm, as shown in Figure 33 of the previous chapter (page 96). The excitation range of the coumarin moiety yet spans beyond 300 nm, so that the dpa moiety cannot be excited without a concomitant absorption of the coumarin. Therefore, the dpa chromophore is shielded or screened by the coumarin and vice versa, the coumarin is screened by the dpa when exciting below 300 nm. As a consequence, the quantum yield of the coumarin emission in the free ligand, or in the non-emissive lanthanide complexes (where no sensitization occurs, neither from the dpa, nor from the coumarin) should drop as soon as the excitation also populates the dpa moiety. The absorption is indeed divided between the two chromophores, while the emission only comes from the coumarin. Hence, part of the energy is lost by the dpa. However, if a luminescent lanthanide ion is coordinated to the ligand, the energy that would be lost in the free ligand can now be transferred to the lanthanide ion and therefore sensitize its luminescence. Similarly, the energy that was released as a fluorescent emission from the coumarin may now be transferred to the lanthanide ion, at least partly, and thus contribute to its emission.

In order to understand the photophysical properties of the luminescent lanthanide complexes, knowing the location of the excited states of the ligand is often mandatory. This is usually achieved by measuring the ligand-centered fluorescence and phosphorescence spectra. In the dp3C1 architecture, the sensitization is expected to take place either from the coumarin moiety or from the dpa moiety. Nevertheless, since the dpa chromophore cannot be excited alone, the dpa sensitization must happen together with a coumarin energy transfer. The excited states corresponding to the coumarin and to the dpa chromophore and accessible under 320 nm excitation and under 270 nm excitation have then to be located, with the difficulty that some of these excited states should probably overlap.

With the different excited states at hand, the sensitization mechanisms can then be investigated in details. Since at least two different excited states, i.e., one from the coumarin and one from the dpa, are expected, the sensitization pathways for each chromophore have to be explored. This study will be carried out by time-resolved spectroscopy. The photophysical properties of the lanthanide tris dp3C1 complexes will be presented both under excitation at 320 nm, which only populates the coumarin moiety, and under excitation at 270 nm, which populates the dpa chromophore as well.

Finally, a photobleaching experiment will be presented in order to test the robustness of the emission intensity of the lanthanide luminescence and of the ligand emission upon continuous excitation.

4.2   Photophysical properties as a function of the excitation wavelength

The quantum yields of the lanthanide emission and of the coumarin emission under the two studied excitation wavelengths are shown in Table 10 for the europium, terbium, and gadolinium complexes, as well as for the free ligand. Since the absorption is multicomponent below 300 nm, the quantum yields measured with an excitation below or close to 300 nm depend on the bandwidth of the monochromatic excitation. Therefore, some discrepancies with other measurements made on a different setup may appear here, particularly for the excitation at 270 nm. To minimize this effect, the values presented in Table 10 come from a series of measurements on the same setup. This setup consists in an integrating sphere, a Xenon light source with a monochromator and a Hamamatsu multichannel analyser C8808 detector.

A more efficient excitation at 270 nm is observed for the sensitized emission from both europium and for the terbium ion in the corresponding complexes (Table 10). On the other hand, the emission of the coumarin moiety is more efficient under an excitation at 320 nm, as expected by the screening effect of the dpa chromophore for excitations below 300 nm (Figure 33, page 96). This is true for all the coumarin emission in all the lanthanide complexes, as well as for the free ligand emission.

Table 10. Ligand-centered and metal-centered quantum yield for the emission of the dp3C1 lanthanide complexes and the free ligand under excitation at 270 nm and 320 nm in aqueous solution, Tris buffer 0.1 M, pH 7.4, 0.1 mM in complex or 0.3 mM in free ligand

	λ_{ex} = 270 nm		λ_{ex} = 320 nm	
	Φ_L^{Ln} / %	Φ_L^{L} / %	Φ_L^{Ln} / %	Φ_L^{L} / %
$[Eu(dp3C1)_3]^{3-}$	5.4	7.5	1.7	7.7
$[Tb(dp3C1)_3]^{3-}$	1.7	4.2	0.5	7.6
$[Gd(dp3C1)_3]^{3-}$	0	6.3	0	9.1
$(dp3C1)^{2-}$	/	22.9	/	31.0

In addition to the better sensitization of the lanthanide ion by the mixed dpa-coumarin pathway, the important result is that the coumarin quantum yield is decreased upon complexation, as observed when comparing the values for the free ligand (22.9 % under λ_{ex} = 270 nm or 31.0 % under λ_{ex} = 320 nm) and non-emissive gadolinium complex (6.3 % under λ_{ex} = 270 nm or 9.1 % under λ_{ex} = 320 nm). The quantum yield is around 3.5 times higher in the free ligand as it is in the gadolinium complex. Concerning the apparently lower quantum yield of the coumarin emission in the gadolinium complex than in the europium complex under an excitation at 270 nm, this probably comes from the measurement error since the values overlap within a margin of error of 10 %. The lowering of the quantum yield upon complexation is nonetheless undeniable and will be further explored in a forthcoming section.

Besides the quantum yields, the photophysical properties of the lanthanide ions seem not to change when exciting the complexes at different wavelengths. The lifetimes are for example unchanged at 1.4 ms for the europium ion and 0.6 ms for the terbium ion. The shapes of the lanthanide emissions are also unaltered, and particularly, the hypersensitive transition of europium is identical. Therefore, the radiative lifetime of the europium ion and its intrinsic quantum yields have to be identical (i.e., 4.2 ms and 33 %). This is reasonable because the deactivation of the lanthanide ion ought to be independent on the way it was excited.

As a consequence, in order to account for the quantum yield dependence on the excitation wavelength, the sensitization efficiency has to depend on the excitation wavelength. The first step to understand the sensitization pathways is to gain access to the relative energy diagram of the ligand, in order to determine the possible levels from which a sensitization of the lanthanide ion can happen. The excited states of the coumarin and dpa chromophores are then investigated in details by exciting them at 270 nm and at 320 nm and by measuring the fluorescence and phosphorescence spectra at room temperature and at low temperature.

4.3   Towards an energy diagram of the dp3C1 complex

A relative energy diagram often provides useful information about the possible starting points for the energy migration after an excitation of the complex. In order to understand the sensitization pathways in the $[Eu(dp3C1)_3]^{3-}$ complex, such a diagram was drawn from low temperature time-resolved measurements for the triplet states and from room temperature measurements for the singlet states, both carried out on the uncoordinated ligand, its gadolinium complex and the uncoupled chromophore mp3C1 (the structure of which is presented in Scheme 16) with excitations at 320 and 270 nm.
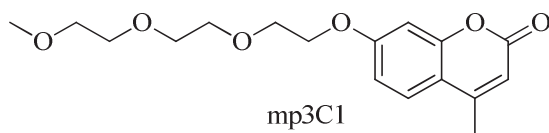
Scheme 16. Structure of the uncoupled methyl-trioxyethylenated 4-methyl-umbelliferone (mp3C1)

The fluorescence and phosphorescence spectra of the coumarin moiety in the galdolinium complex were presented in Figure 34 (on page 96), and the energy of the singlet and triplet excited states in Table 8 (on page 97). The singlet excited state of the coumarin chromophore is higher than 26000 cm^{-1} (which is the wavenumber of the maximum of the singlet emission) and the triplet state is located at 21500 cm^{-1} (which is the 0-0 transition). These values were obtained under an excitation at 320 nm, which only populates the coumarin moiety.
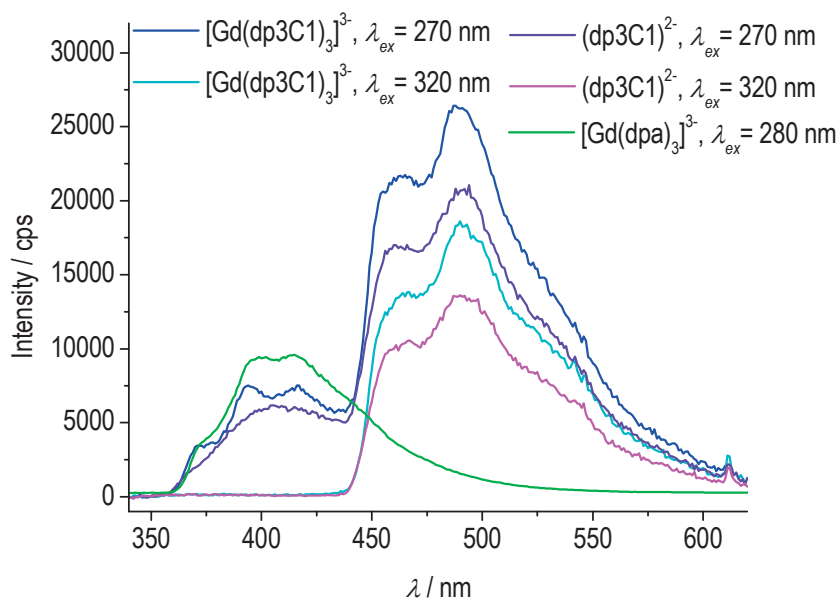
Figure 37. Triplet emission of the dp3C1 ligand and its gadolinium complex 50 μs after pulsed excitation. $[dp3C1^{2-}] = 3 \cdot 10^{-4}$ M, $[Gd^{3+}] = 1 \cdot 10^{-4}$ M in a frozen Tris 0.1 M aqueous solution (10 % glycerol), pH 7.4, T = 77 K. Emission of $[Gd(dpa)_3]^{3-}$ scaled to show location of the triplet emission.

When further investigating the phosphorescent emission at 77 K by exciting the gadolinium complex at 270 nm, a second phosphorescence band centered at 410 nm appears, which is not observed upon excitation at 320 nm. As a comparison, the scaled phosphorescence spectra of the trisdipicolinate gadolinium complex $[Gd(dpa)_3]^{3-}$ is also shown in Figure 37 (green line with no peak between 450 and 550 nm). Its triplet emission is located at the exact position of the higher energy triplet emission. This could indicate that this new band comes from the dpa moiety of the dp3C1 ligand, whereas the other triplet emission that is visible upon both excitations arises from the coumarin moiety. However, the same phenomenon was also observed when measuring the polyoxyethylene coumarin chromophore mp3C1 (Figure 38), meaning that in fact, the high energy triplet emission can come from either the coumarin moiety or the coordinating dpa.
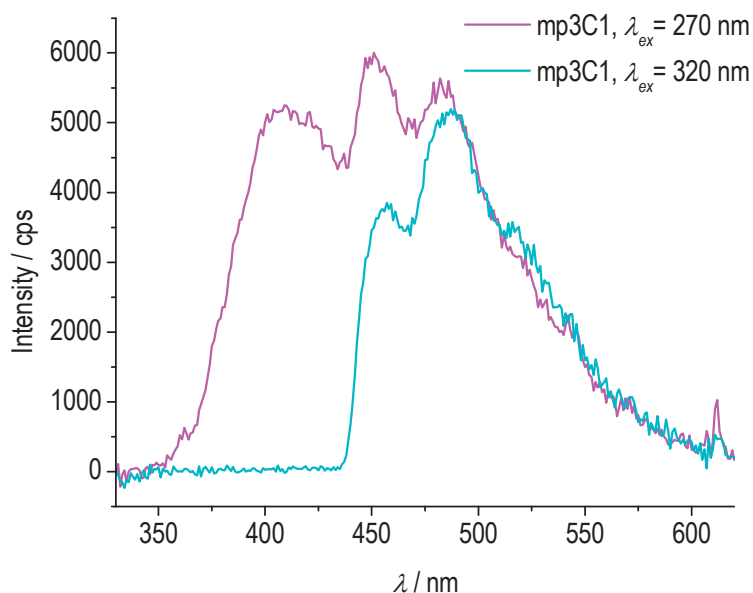
Figure 38. Triplet emission of the polyoxyethylene coumarin chromophore (mp3C1) 50 μs after pulsed excitation. Frozen saturated solution diluted 10 × in Tris 0.1 M aqueous solution (10 % glycerol), pH 7.4, T = 77 K.

A most rational explanation would be that two triplet excited states can be populated on the coumarin chromophore, depending on the excitation wavelength. The higher in energy can be reached by an excitation at 270 nm and is located at the same energy as the dpa triplet state. The second one is reached at 320 nm, where no excitation of the dpa moiety can take place. Its energy is lower compared to the 270 nm excited one, but can also be populated upon excitation at 270 nm. This is perfectly coherent because of the internal conversion from the higher excited state to the lower excited state.

To confirm this hypothesis, calculations of the molecular orbitals using INDO/S parameters after optimizing geometry with ZINDO INDO/1 calculations were performed with the Scigress Explorer software. Two absorption bands at 286.5 nm and at 309.9 nm were predicted and attributed to $\pi\pi*$ transitions. The band located at 309.9 nm is more intense than the one at 286.5 nm. It involves the same π Highest Occupied Molecular Orbital (HOMO) as the band at 286.5 nm, but lower $\pi_\alpha*$ Lowest Unoccupied Molecular Orbital (LUMO), compared to the higher energy $\pi_\beta*$ molecular orbital. Finally, a third weak transition is predicted at 348.6 nm and is attributed to an $n\pi*$ transition from an n HOMO to the $\pi_\alpha*$ LUMO. The calculated molecular orbitals (MO) involved in these transitions are depicted in

Figure 39. The nπ* transition is very weak according to its forbidden character and is barely seen in the experimental absorption spectrum or excitation spectrum as a slight shoulder at 340 nm. The most intense $\pi\pi_\alpha$* transition is experimentally observed as the absorption maximum at 320 nm, whereas the more energetic $\pi\pi_\beta$* transition is observed on the excitation spectrum as an apparent shoulder at 284 nm. Similar calculations performed on the dp3OMe ligand demonstrated that one major $\pi\pi$* transition (predicted at 272.5 nm) is responsible for the absorption around 270 nm. The corresponding calculated MOs are displayed in Figure 40.
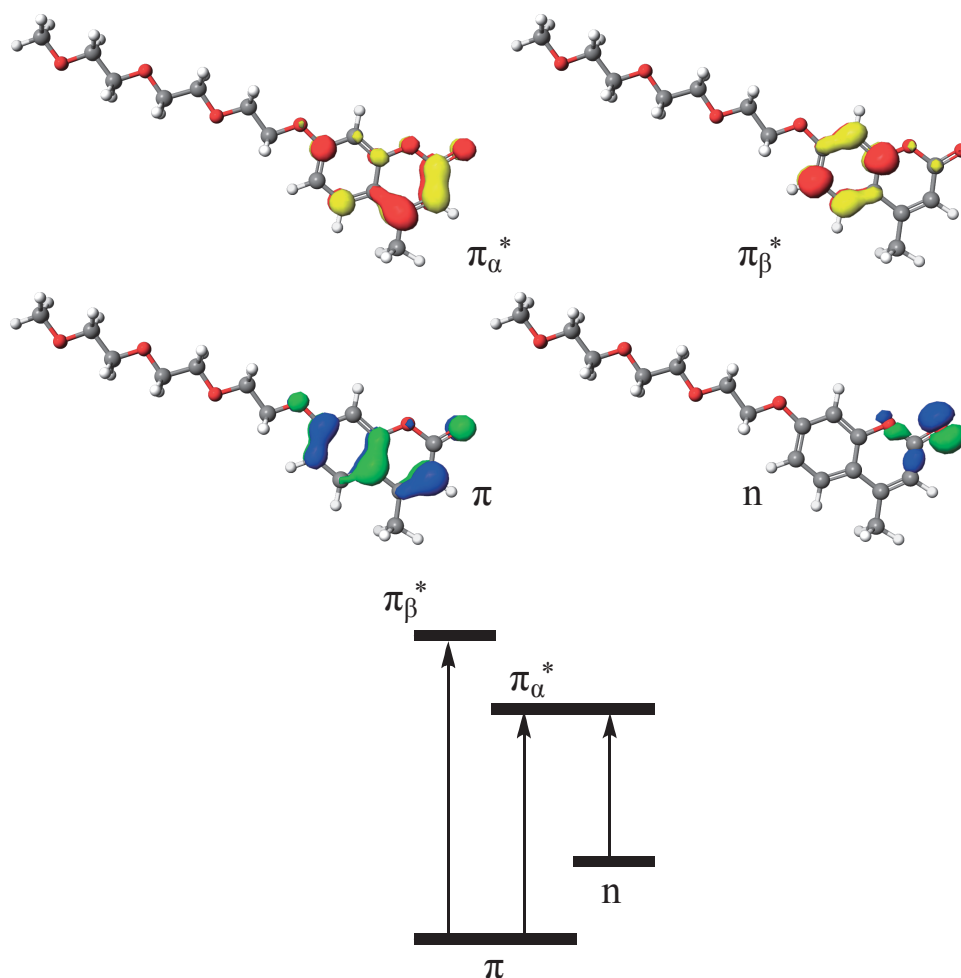
Figure 39. Molecular orbitals (MO) involved in the absorption of 250-380 nm UV light by the mp3C1 chromophore according to ZINDO INDO/1 calculations. Blue and green orbitals represents the two phases of the MO of the ground state, red and yellow orbitals represents the two phases of the MO of the excited state
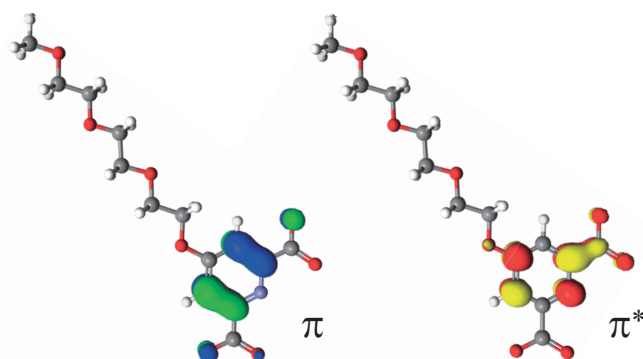
Figure 40. Molecular orbitals involved in the ππ* transition of the coordinating methoxytrioxyethylenated dipicolinate chromophore (dp3OMe) according to ZINDO INDO/1 calculations. Blue and green orbitals represents the two phases of the MO of the ground state, red and yellow orbitals represents the two phases of the MO of the excited state
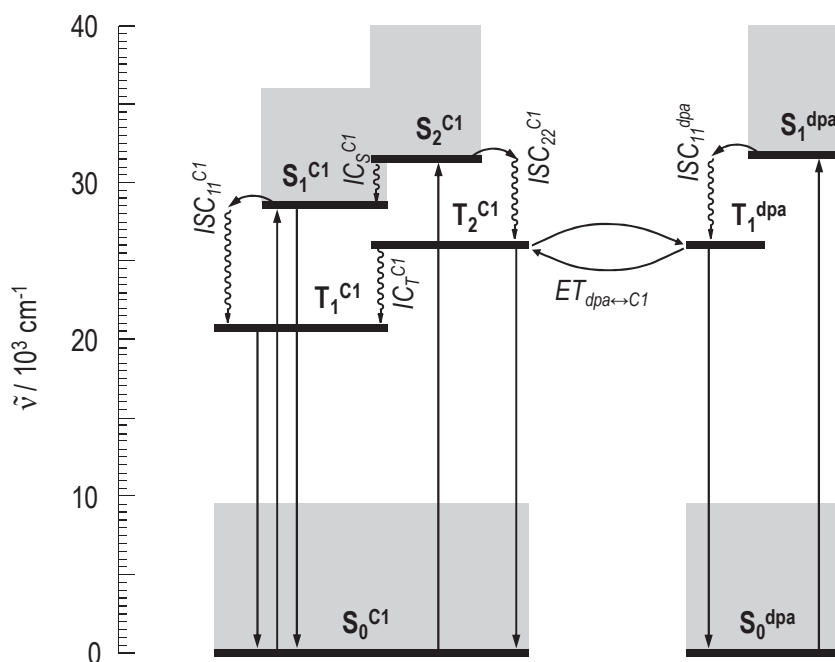
Figure 41: Relative energy diagram of the coumarin (C1) and dipicolinate (dpa) moieties with their possible interactions (ISC_{xy}: InterSystem Crossing from x^{th} to y^{th} excited state, $ET_{dpa\leftrightarrow C1}$: Energy Transfer between the dpa moiety and the coumarin C1 moiety, IC_T: Internal Conversion between triplet states, IC_S: Internal Conversion between singlet states). Wavy arrows are pointing at non-radiative deactivation, whereas straight arrows are pointing at radiative transitions (absorptions: pointing up, emissions: pointing down). Plain black lines are indicating the lower energy states of the energy levels and gray areas are the approximative vibronic extend of the energy levels (not determined for the triplet states) found from the absorption and emission spectra.

The relative energy diagram of the $[Ln(dp3C1)_3]^{3-}$ complexes could then be simplified as in Figure 41. The excitation of the coumarin chromophore under 320 nm UV-light first populates the first excited singlet state S_1^{C1}. The radiative deactivation of this singlet state yields to the fluorescent emission shown in Figure 34. If the excited coumarin undergoes an intersystem crossing (ISC_{11}^{C1}), the first excited triplet state T_1^{C1} can be populated. The radiative relaxation of this triplet state down to the ground state S_0^{C1} is observed as a phosphorescent emission in Figure 34 and Figure 38.

Upon excitation at 270 nm, both the coumarin and the dpa moieties can be populated. From the dpa point of view, the excitation populates a first excited singlet state that cannot be observed in emission, certainly because of a fast deactivation. One of these relaxations forms the first excited triplet state T_1^{dpa}, the phosphorescence of which is observed at low temperature. On the other hand, if the excitation takes place on the coumarin chromophore, a second excited singlet state S_2^{C1} is populated instead of the lower first one reached with an excitation at 320 nm. A fast relaxation down to the S_1^{C1} excited state (by the IC_S^{C1} pathways) probably precludes its observation by fluorescence at room temperature, however, the formation of a second excited triplet state T_2^{C1} can be observed at low temperature as an additional emission peak before the phosphorescent emission from T_1^{C1}. This peak is located at the same position as the phosphorescent emission from dpa. Furthermore, because the emission from T_1^{C1} is also observed by exciting S_2^{C1}, an internal conversion from T_2^{C1} down to T_1^{C1} (IC_T^{C1}) seems reasonable, similarly to the internal conversion in the singlet excited states. On the other hand, since the T_2^{C1} phosphorescence by exciting the S_1^{C1} level at 320 nm is not observed, an intersystem crossing from the first singlet excited state to the second triplet excited state seems not possible.

4.4   Time-resolved luminescence: sensitization pathways

The investigation carried out in the previous section gives a wide overview of the different excited states of the ligand that can transfer energy to, and thus sensitize, the lanthanide ion. In order to determine whether a preferential sensitization

pathway is followed in our case, the sensitization mechanisms were studied on the europium complex by time-resolved spectroscopy both for the solid state samples and for the frozen aqueous solution at 77 K.
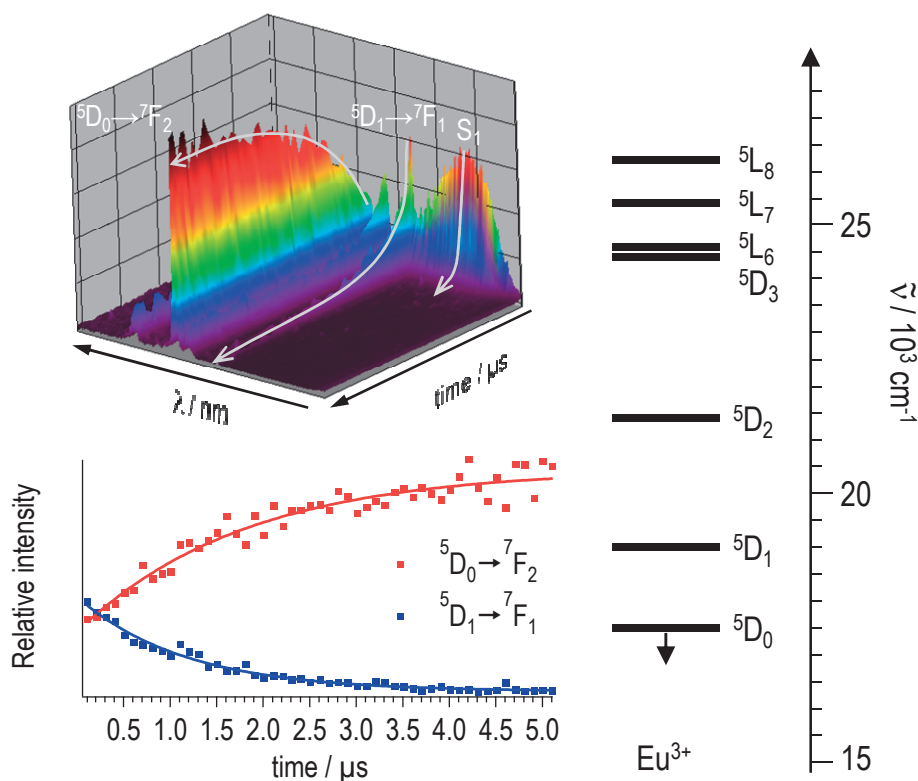
Figure 42. Time-resolved emission spectrum of $Na_3[Eu(dp3C1)_3]$ in solid state ($\lambda_{ex} = 320$ nm) and the extracted decay of the $^5D_1$ and rise of the $^5D_0$ spectroscopic levels (left), excited spectroscopic levels of Eu^{3+} (right)

On the nanosecond time-resolved emission spectra of the solid state and frozen solution samples, the fluorescence from the coumarin is observed together with the transitions from the higher $^5D_1$ spectroscopic level of europium. The transitions from the typical $^5D_0$ state are however absent. It then means that the energy transfer most probably occurs mainly on the $^5D_1$ level, which lies ~1700 cm^{-1} higher than the $^5D_0$. In the microsecond time scale (see Figure 42), the $^5D_1$ emission bands decrease while the $^5D_0$ peaks rise. The decay rate of the $^5D_1$ yields a lifetime at 1.3 μs ± 0.2 μs. This decay is also observed on the parent dipicolinate complex, so that it seems to be defined mostly by the coordination sphere. The rise time of the

transitions from the $^5D_0$ is in the same range than the decay time of the $^5D_1$ level. It is therefore obvious that the energy is first transferred from the sensitizer onto the $^5D_1$ level and from there on the $^5D_0$ level. In aqueous solution and at room temperature, the emission from the $^5D_1$ level is very difficult to observe (very weak intensity). It probably comes from the rapid quenching of this level by water molecules, which relax the europium ion down to the $^5D_0$ spectroscopic level. Water has indeed a vibrational bending transition at 1645 cm^{-1}, which would be a good acceptor for the energy gap between the $^5D_1$ (19,000 cm^{-1}) and the $^5D_0$ states (17,223 cm^{-1}).

By increasing the time scale up to the milliseconds, the decay of the $^5D_0$ spectroscopic level of the europium ion down to the ^7F_J spectroscopic levels is clearly seen by the luminescence decays of the characteristic transitions. On the other hand, the triplet state was not observed on any time scale. At 77 K, it was found to be in the second time scale, resulting in an emission that is clearly visible up to 5 seconds after a laser excitation. Because the europium emission is not present during this long-lived triplet emission, the sensitization through the triplet state of the coumarin (T_1^{C1}) does certainly not happen in frozen solution at 77 K. Furthermore, the decay of the singlet state is clearly in the nanosecond time scale (<100 ns). Those data are in agreement with a sensitization through the singlet state of the coumarin (S_1^{C1}) since the energy transfer seems to occur in the same time scale as the deactivation of the singlet state.

Under excitation at 270 nm, both the dpa and coumarin moieties are excited. The sensitization from the dipicolinate chromophore is known to occur through the triplet excited state. The triplet state is indeed quenched in the trisdipicolinate europium complex at low temperature. On the other hand, the population of T_2^{C1} seems highly unlikely because of the fast internal conversion of S_2^{C1} down to S_1^{C1}. Therefore, an excitation below 300 nm of the complex should sensitize the europium ion on its $^5D_1$ spectroscopic level from a mixed triplet singlet pathway that comes from the excited dpa and coumarin chromophores respectively. An energy diagram summing up the energy migrations in the [Eu(dp3C1)$_3$]$^{3-}$ complex and highlighting the energy transfers from the different sensitizing moieties to the europium ion is presented in Figure 43.
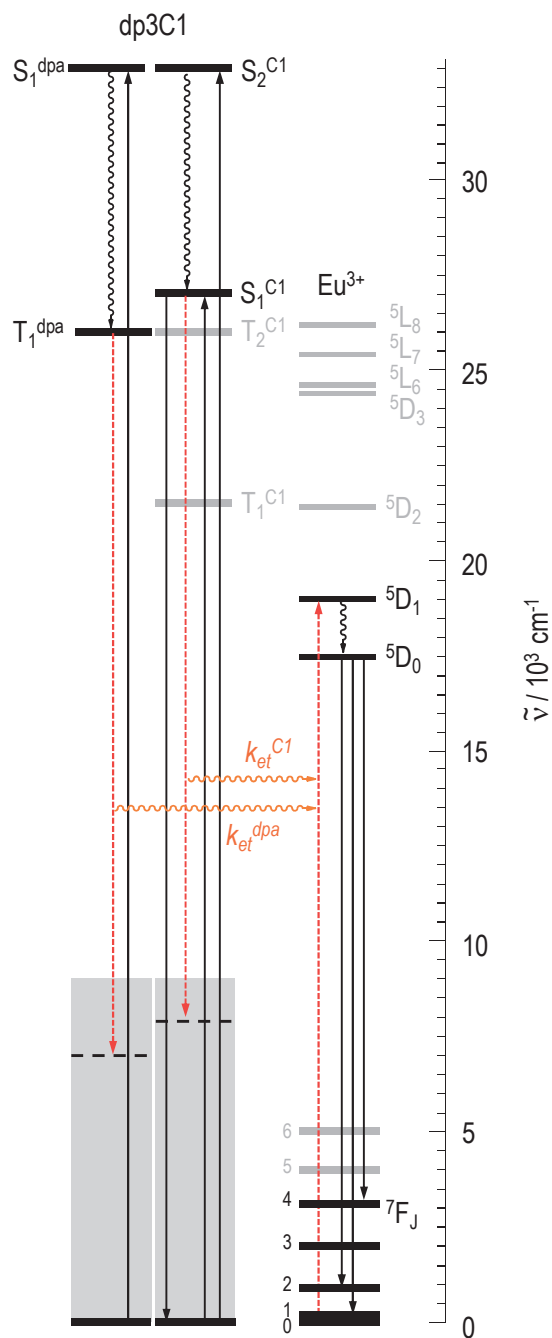
Figure 43. Observed energy migrations in the [Eu(dp3C1)$_3$]$^{3-}$ complex showing energy transfer from the singlet pathway of the coumarin k_{et}^{C1} chromophore and from the triplet pathway of the dpa k_{et}^{dpa} moiety to the $^5D_1$ spectroscopic level of the europium ion.

4.5   Europium complex with mixed ligands: investigating self-quenching phenomena

As introduced in the first section of this chapter, the emission quantum yield of the coumarin chromophore in the uncoordinated ligand is much higher than any of its lanthanide complexes, with 31.0 % of the absorbed photon being reemitted in aqueous solution under an excitation at 320 nm versus 9.1 % in the gadolinium complex. Such decreases of the quantum yield upon lanthanide coordination can be accounted to structural changes of the ligand upon complexation affecting its photophysical properties, to the influence of the coordinating ion on the photophysical properties of the ligand, or to self-quenching phenomena that non-radiatively deactivate the excited coumarin. This last possibility seems more probable than the other though. Despite the fact that the photophysical interactions of the three ligands forming a tris complex are often neglected, the close proximity of the chromophores should tend to favor quenching phenomena. In order to highlight such self-quenching behaviors, the dp3C1 ligand was diluted with several ratios of dpa and the resulting photophysical properties were determined.

The advantage of mixing dpa and dp3C1 ligands is that dp3C1 can be diluted without diluting the Eu^{3+}, thus really changing the ratio of dp3C1 / Eu^{3+}. Furthermore, since the dpa ligand does not absorb at 320 nm, no photophysical interaction should occur. The constant Eu:Ligand^{tot} ratio being set at 1:3, a constant concentration in complex is kept, so that only the effect of the dilution of the coumarin sensitizing group should be studied in that way.

According to the previous chapter, the coordination ability of the dipicolinate moiety in dp3R ligands is only slightly affected by the nature of the R group. Hence, mixed Eu:dpa:dp3C1 complexes might be obtain by mixing both ligands in different ratios ranging from 0.33:x:(3-x) with x = 0-3. In the following discussion, the $[Eu(dpa)_x(dp3C1)_{3-x}]$ complexes will be labeled as [x:(3-x)] for clarity purposes.

Quantum yields upon excitation at 320 nm were then measured for the europium and coumarin emissions. As shown on Figure 44, both europium and coumarin quantum yields are increasing when changing the stoichiometry from the pure $[Eu(dp3C1)_3]^{3-}$ to increasing amounts of dpa ligand. Nevertheless, the absorption at 320 nm is of course reduced when keeping the concentration of the complex

constant until no more photons are absorbed at 320 nm by the pure $[Eu(dpa)_3]^{3-}$ complex. By plotting the inverse of these quantum yields as a function of the concentration of the dp3C1 ligand, a good linearity of the values is highlighted (see Figure 45). The quenching thus happens according to a Stern-Volmer deactivation kinetics, presented in Equation 19, with k_q the quenching rate constant, $[Q]$ the concentration of the quencher, Φ_{em}^0 the quantum yield without any quencher, k_{obs}^0 the observed deactivation rate constant without any quencher, τ_{obs}^0 the observed lifetime without any quencher, Φ_{em} the quantum yield in the presence of the quencher, k_r the radiative rate constant and τ_r the radiative lifetime.
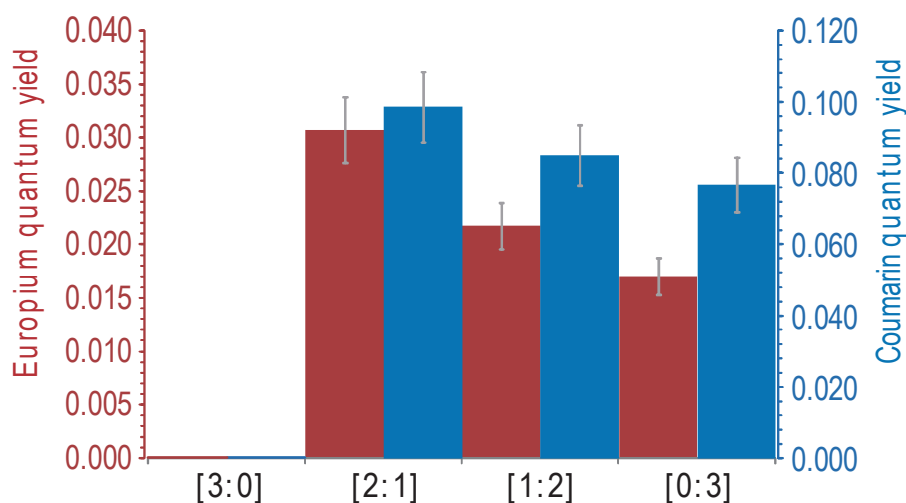
Figure 44. Quantum yield for the europium (red) and coumarin (blue) emission of the mixed ligand complexes upon excitation at 320 nm.

$$\frac{\Phi_{em}^0}{\Phi_{em}} = 1 + k_q \cdot \tau_{obs}^0 \cdot [Q]$$

$$\Rightarrow \frac{1}{\Phi_{em}} = \frac{1}{\Phi_{em}^0} + k_q \cdot \frac{\tau_{obs}^0}{\Phi_{em}^0} \cdot [Q]$$

$$\Phi_{em}^0 = \frac{k_r}{k_{obs}^0} = \frac{\tau_{obs}^0}{\tau_r}$$ (19)

$$\Rightarrow \frac{1}{\Phi_{em}} = \frac{1}{\Phi_{em}^0} + k_q \cdot \tau_r \cdot [Q]$$

$1/\Phi_{em} = 13962 \cdot [dp3C1] + 8.8356$
$R^2 = 0.9963$

$[dp3C1] + [dpa] = 3 \cdot 10^{-4}$ M
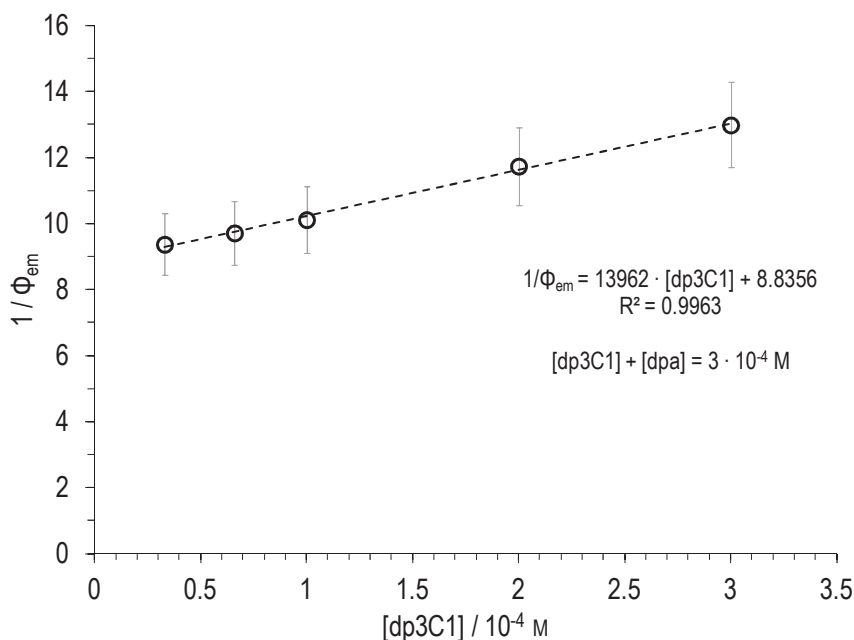
Figure 45. Stern-Volmer plot from the emission of the coumarin

The Stern-Volmer plot for the emission of the coumarin as a function of $[dp3C1]$ points to a self-quenching of the coumarin excited states by the coumarin moiety itself. From the linear fit, the emission quantum yields without quenching can be extracted as the inverse of the y-intercept. For the emission of the europium ion, $\Phi_{em}^0(Eu^{3+}) = 5.1$ %, whereas for the coumarin, $\Phi_{em}^0(Coum) = 11.3$ %. These values indicate that a virtual complex with an unquenched coumarin moiety would have a sensitized europium quantum yield of 5.1 % instead of 1.7 % and a coumarin quantum yield of 11.3 % instead of 7.7 %. The unquenched coumarin quantum yield is yet not as high as the free ligand quantum yield because part of the energy is transferred on the europium ion. Assuming the intrinsic quantum yield of the europium ion in this virtual complex is similar to the intrinsic quantum yield of the quenched tris complex (i.e., 33 %), the sensitization efficiency would be increased due to the unquenched ligand up to 15.5 %. Therefore, combined with the 11.3 % which yields a fluorescent emission, 26.8 % of the number of excited coumarin may yield either an emission or a sensitization of the europium ion. This value is not so far away from the 31 % of the coumarin quantum yield in the free ligand. It seems then reasonable to incriminate a self-quenching of the coumarin moiety as a cause of the reduction of the coumarin quantum yield in a lanthanide tris complex relative to the free ligand.

4.6 Photobleaching

The stability of the complex towards excitation by UV light has been carried out by measuring the emission intensity at the maxima of the coumarin and europium emission spectrum as a function of time. Both a $1 \cdot 10^{-4}$ M aqueous solution in Tris 0.1 M pH 7.4 and solid state samples have been submitted to a 320 nm or 280 nm continuous excitation light source, and the intensity of the emission monitored each second over a period of 5 minutes. The resulting intensities have been corrected to take into account the variation of the intensity of the excitation light source and further normalized relative to the initial intensity.

A decrease of the intensity of both coumarin and europium peaks was observed in aqueous solution upon excitation at 320 nm (Figure 46). A loss of nearly 25 % of the initial intensity was measured. On the other hand, under excitation at 280 nm, very little variations (5 %) were encountered. The emission of the coumarin decreases, whereas the emission of the europium slightly increases. This behavior can be explained by the photobleaching of the coumarin moiety that, when excited at 320 nm, is correlated to the loss in intensity of the coumarin sensitized europium emission. In contrast, when the complex is excited at 280 nm, where the dpa moiety also absorbs significantly, the slight photobleaching of the coumarin is beneficial to the emission of the europium because more excitation energy is available for the dpa once the coumarin is destroyed (screening effect of the coumarin chromophore), and because the quenching of the europium by the intact coumarin, as highlighted in the previous section, is lowered.

Concerning the solid state samples, no photobleaching was observed (Figure 47). The signal is more noisy (5 % variation of the total intensities), but remains fairly constant within more or less 10 % of the initial intensities. This result is consistent with the pigment nature of solid state powder or crystalline samples, which shows better lightfastness than solutions due to their bulk nature.
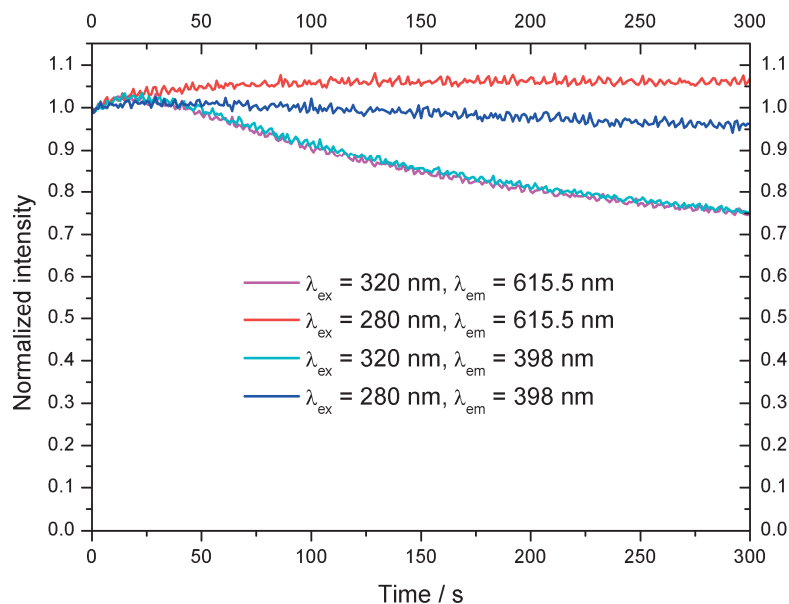
Figure 46. Photobleaching of $[Eu(dp3C1)_3]^{3-}$ in aqueous solution, Tris 0.1 M, pH 7.4, time increments of 1 s
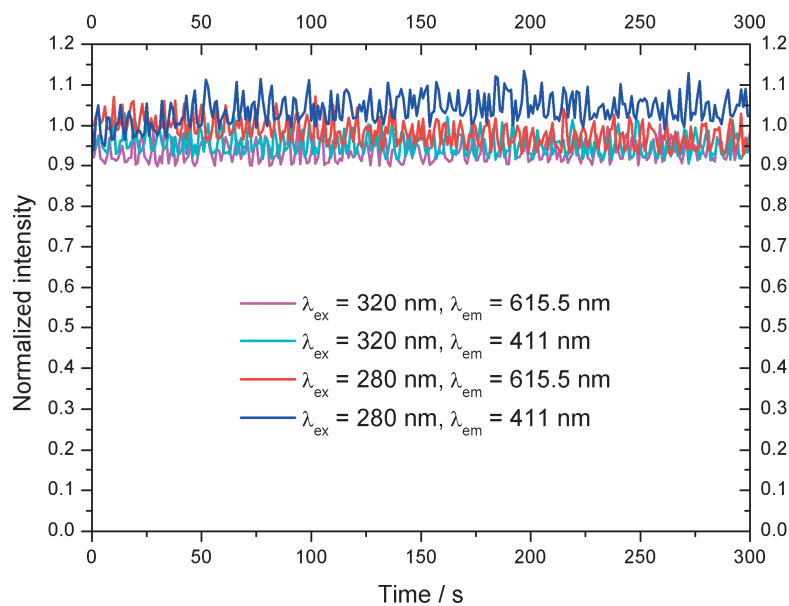
Figure 47. Photobleaching of $Na_3[Eu(dp3C1)_3]$ solid state powder, time increments 1 s.

4.7   Concluding remarks

The dp3C1 complex is composed of three photophysically active moieties: the lanthanide ion, here europium(III), the dpa moiety, and the coumarin chromophore. The europium ion is coordinated to the dpa moiety and emits light when sensitized either by the dpa or by the coumarin chromophores. Whatever the sensitization pathway, the emission from the europium ion always has the same properties such as intrinsic quantum yield and observed lifetime, because such properties are only defined by the coordination environment as demonstrated in the previous chapter. However, the sensitization efficiency from the dpa or from the coumarin moieties is not the same. The sensitization efficiency depends on the energy migration path and therefore, on the sensitizing chromophore. The sensitization from the coumarin is achieved by exciting the complex with an excitation wavelength above 300 nm. Below this value, the dpa moiety is also excited. It was shown that the concomitant excitation of the dpa chromophore and hence the parallel activation of the dpa pathway increases the overall sensitization efficiency. The dpa pathway is therefore more efficient than the coumarin pathway as expected by the closer distance of the dpa moiety relative to the europium ion.

The ligand-centered fluorescence and phosphorescence spectra with the gadolinium complex provided a relative energy diagram of the liand excited states. From time-resolved spectra, the sensitization pathway from the coumarin was proved to occur through its first singlet excited state in frozen solution at 77 K. The energy is most probably transferred onto the $^5D_1$ spectroscopic level of Eu^{3+}, which relaxes down to the $^5D_0$ spectroscopic level from which the characteristic long lived emission of the europium ion takes place.

By diluting the dp3C1 ligand with dpa and keeping a constant europium concentration and metal to ligands ratio, quenching phenomena were highlighted and might provide important radiationless relaxation processes for both the coumarin chromophore and the europium ion.

Finally, photobleaching experiments showed that the photobleaching of the coumarin emission under an excitation at 280 nm (activation of the dpa and coumarin pathways) improved the emission intensity from the europium ion, as expected by the screening and quenching effects of the less efficiently sensitizing coumarin moiety.

Chapter 5

Dipicolinate polyoxyethylenated coumarin ligands with shorter POE linkers

Testing energy transfer theories

5.1 Introduction

The last two previous chapters introduced the dipicolinate *para*-trioxyethylenated coumarin architecture, presented different variations of the coumarin chromophore and the resulting effect on the sensitization efficiency of the coordinated lanthanide ion, and investigated the sensitization pathways with the most efficient terminal coumarin encountered here. In this chapter, the polyoxyethylene linker will be shortened as an endeavor to control the distance between the coordinated lanthanide ion and the distant coumarin. From the energy transfer theories, an improvement of the energy transfer rate is indeed expected when the donor is closer to the acceptor. The same coumarin (4-methylumbelliferone) as in the previous chapter is used thereof. The photophysical properties of the europium complexes will be considered both in aqueous solution under the same condition than the previous studies (i.e., Tris-buffered solution, pH 7.4, 0.1 mM in complex) and in solid state in a Tris matrix (obtained by drying the corresponding aqueous solution).
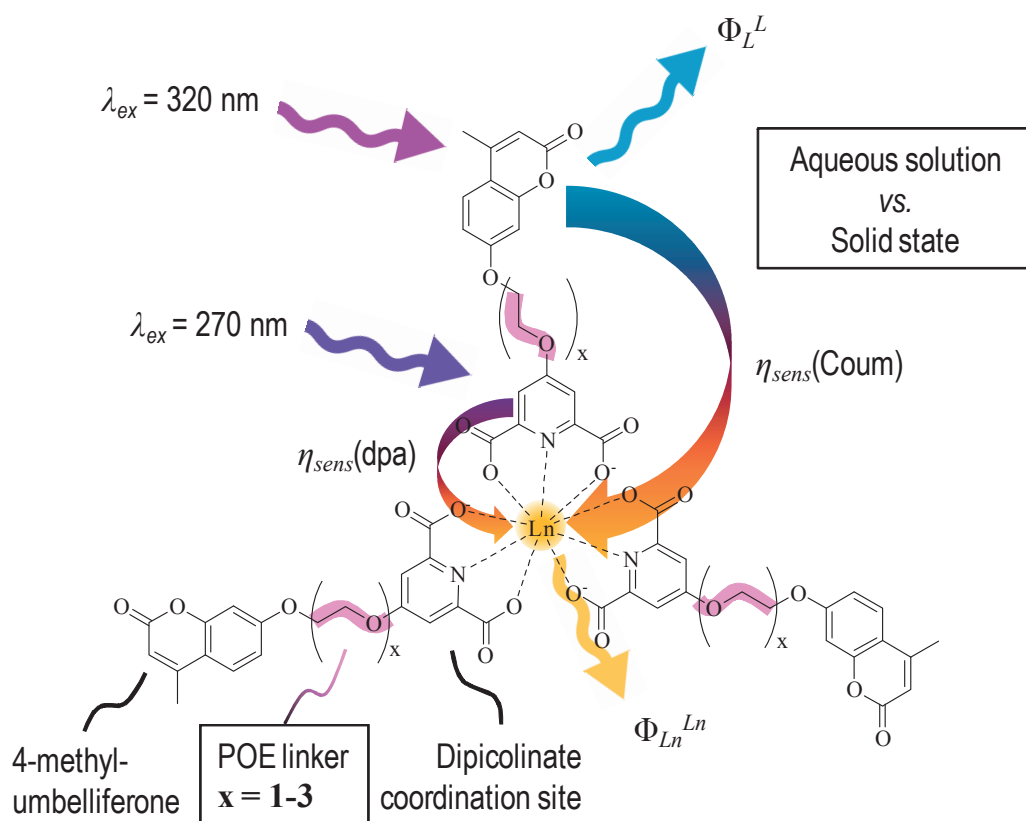
Figure 48. $[Ln(dp\mathbf{x}C1)_3]^{3-}$ complexes with variable lengths of the polyoxyethylene linker (POE, x = 1-3) investigated in aqueous solution (aq) and in solid state (s)

The ligands were synthesized from 4-methylumbelliferone according to the synthetic pathway developed in Section 3.2, except for the tosylated methoxytrioxyethylene linker, which was replaced by the desired polyoxyethylene length, i.e., tosylated methoxydioxyethylene linker and tosylated methoxymonooxyethylene linker. The ligands are called hereafter dp3C1, dp2C1 and dp1C1 for the dipicolinate trioxy-, dioxy-, and monooxy-ethylenated 4-methyl-umbelliferone respectively.

To begin with, a brief overview of the differences between the photophysical properties in aqueous solution and in solid state will be undertaken. Indeed, the chemical environment of the complexes changes quite a lot once in solid state (compared to the situation in aqueous solution). The refractive index is higher in solid state (1.517 from Aebischer et al.[23] versus 1.333 in water), there is a high density of complexes probably in close contact, and a more rigid environment than in solution. Therefore, the ligand-centered and metal-centered photophysical properties of the solid state samples should be measured from the solid state samples and not extrapolated from the aqueous solution.

Afterwards, the effect of the shortening of the polyoxyethylene linker will be carefully investigated in aqueous solution and in solid state. Since a relationship between the length of the linker and the sensitization from the coumarin is experimented, the excitation wavelength is set at 320 nm. However, in order to compare with the efficiency of the sensitization by the dpa moiety, the excitation at 270 nm will also be tested. If an improvement of the quantum yield is observed for the sole coumarin sensitization (i.e., under an excitation at 320 nm), the contribution of the coumarin under an excitation at 270 nm also has to be improved, whereas the dpa contribution should be fixed since it is always at the same location relative to the lanthanide ion.

5.2   Differences between dp3C1 sensitized europium luminescence in aqueous solution and in solid state

The excitation and emission spectra of $[Eu(dp3C1)_3]^{3-}$ $1 \cdot 10^{-4}$ M in Tris 0.1 M pH 7.4 and the solid $Na_3[Eu(dp3C1)_3]$ powder were measured at room temperature. Considerable differences in the excitation spectra are observed (Figure 49). The major difference is the observation of the absorption bands of the direct f-f

transitions in solid state. The most intense one is the $^5L_6 \leftarrow {}^7F_0$ (at 395 nm); the $^5D_2 \leftarrow {}^7F_0$ at 464.5 nm is also rather strong, whereas the $^5D_3 \leftarrow {}^7F_0$ and $^5D_1 \leftarrow {}^7F_0$ are less intense. The absorption band of the coumarin chromophore is also different in solid state compared to the situation in aqueous solution. The absorption range is extended until the visible range up to the peak of the $^5L_6 \leftarrow {}^7F_0$ and $^5D_3 \leftarrow {}^7F_0$ transitions.
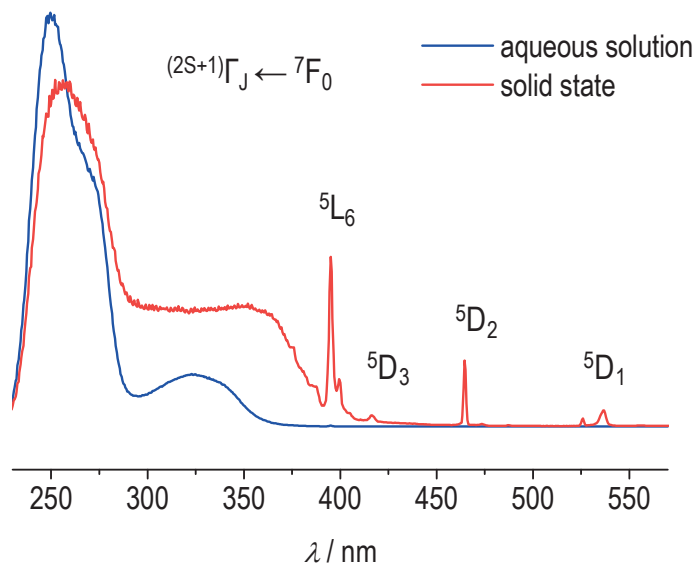
Figure 49. Excitation spectra of $[Eu(dp3C1)_3]^{3-}$ aqueous solution ($1 \cdot 10^{-4}$ M in Tris 0.1 M, pH 7.4, blue curve) and $Na_3[Eu(dp3C1)_3]$ solid state sample (red curve), both at room temperature with $\lambda_{em} = 615$ nm.

The same shift of the coumarin absorption band is observed with the coumarin chromophore alone in mp3C1 (structure shown in Scheme 16, page 111), when measuring the excitation of a solid state sample. This result suggests that the shift of the excitation is only due to the solid state nature of the samples rather than to a ligand to metal charge transfer (LMCT) band. Occurences of LMCT bands in solid state europium complexes have been investigated by Puntus and coworkers.[92, 93] Because the coumarin is far from the europium ion, a charge transfer transition involving an electron transfer from the distant coumarin onto the europium ion seems however more difficult than for chromophores in direct contact with the lanthanide ion, as is the case with the dpa chromophore.

Concerning the f-f transitions, they are also present in the excitation spectrum of microcrystalline europium trisdipicolinate.[23] Transitions with energies higher than the $^5L_6 \leftarrow {}^7F_0$ transition ($^5L_7, {}^5G_J \leftarrow {}^7F_{0,1}$, $^5D_4 \leftarrow {}^7F_1$, and $^5D_4 \leftarrow {}^7F_0$ transitions) are even

better defined for the dpa complex because the ligand transitions do not overlap with them between 350 and 400 nm.

Regarding the emission spectrum upon 320 nm excitation (Figure 50), the emission of the coumarin provides the major difference between solution and solid state. A significant bathochromic shift of the emission band of the coumarin is observed upon the whole excitation range. The maximum is located at 389 nm in aqueous solution and 411 nm in solid state. In addition, the $^5L_6 \leftarrow {}^7F_0$ transition is also slightly visible in the emission spectrum in solid state. This is due to a reabsorption of the coumarin emission by the europium ion (via a direct f-f transition, no energy transfer involved), thus reinforcing the emission of the europium. The bathochromic shift of the coumarin emission in solid state is also due to reabsorption linked phenomena. Indeed, the excitation spectrum of the solid state sample have shown that the absorption can go up to 400 nm, with a strong absorption still occurring at 380 nm. Consequently, part of the emission of the coumarin that would take place below 380 nm can be significantly reabsorbed by the ligand. The maximum of the emission being located near this region, reabsorption shifts it towards higher wavelengths.
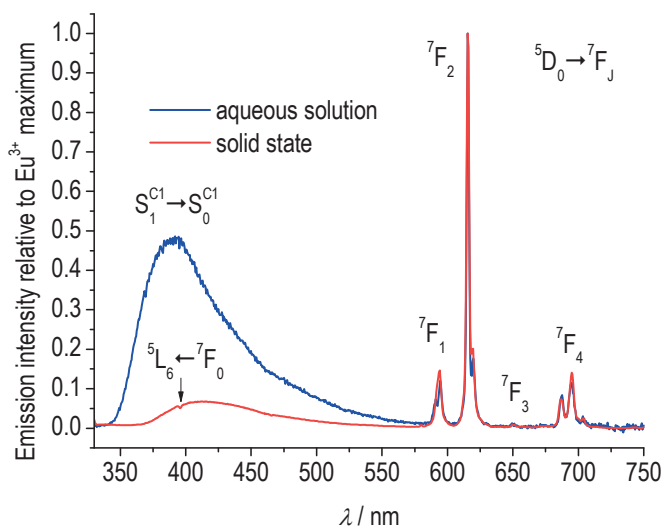
Figure 50. Emission spectra (λ_{ex} = 320 nm, room temperature) of [Eu(dp3C1)$_3$]$^{3-}$ aqueous solution ($1 \cdot 10^{-4}$ M in Tris 0.1 M, pH 7.4, blue curve) and Cs$_3$[Eu(dp3C1)$_3$] solid state sample (red curve) normalized by the maximum emission intensity from the Eu^{3+} ion ($^5D_0 \rightarrow {}^7F_2$ transition)

As seen in Figure 50, the emission of the coumarin is also significantly decreased in solid state, relative to the emission of the europium ion. The maximum emission

of the coumarin in aqueous solution is up to 50 % of the $^5D_0 \rightarrow {^7F_2}$ europium transition, while it is less than 10 % in solid state. The europium emission represents 48 % of the total emission in solid state, which means that coumarin and europium emit a similar amount of photons (the ratio of coumarin emission over europium emission is 1.1). In aqueous solution, the europium emission represents only 12 % of the total emission. The coumarin emits then 7.4 times more photons than the europium ion. With respect to the europium emission, the only structural difference between solid sate and solution is due to the $^5D_0 \rightarrow {^7F_1}$ transition, which is split in two in aqueous solution, consistently with the emission from the parent europium trisdipicolinate. This difference in relative intensity between europium and coumarin induces a significant shift in color. Under an excitation with a long-wave UV lamp (366 nm) the solid state sample looks magenta, whereas in solution, the color has a stronger blue component and looks more like lavender. On the other hand, upon an excitation at 254 nm (short-wave UV lamp), the color becomes nearly as red as $Na_3[Eu(dpa)_3]$, most of the blue component from the coumarin being lost.

The excitation spectra with $\lambda_{em} = 615.5$ nm, either in solid state or in aqueous solution, are then different from the ones for the emission at 411 nm (solid) or 389 nm (aqueous solution). A fairly constant ratio between the europium maximum emission peak ($^5D_0 \rightarrow {^7F_2}$ transition, 615.5 nm) and the coumarin maximum emission peak (411 nm) is observed from 310 to 340 nm, where the absorption range of the coumarin chromophore is mainly located. Below 310 nm, the absorption of the dpa moiety becomes significant in solid samples, whereas at higher wavelengths, the additional absorptions, are responsible for the europium emission. This also rationalizes the red color under 254 nm UV lamp, where the ratio of the coumarin over europium emission falls down to 0.1 under an excitation at 250 nm.

To summarize, there are quite important differences in photophysical properties between powder solid state samples and solution. Many of these differences certainly arise from the difference in molecular surrounding and induce modulations of both the excitation and the emission characteristics.

The sensitized quantum yields, intrinsic quantum yields, observed lifetimes, radiative lifetimes, and sensitization efficiencies of the europium complexes in aqueous solution and solid state for the dp3C1 complex and the complexes with the shorter linkers dp2C1 and dp1C1, will now be investigated.

5.3 Photophysical properties upon variations of the length of the polyoxyethylene linker

In aqueous solution, all the $[Eu(dpxC1)_3]^{3-}$ (x= 1-3) complexes exhibit the same characteristic red emission from the europium center as well as the residual coumarin emission. The ligand-centered fluorescence and phosphorescence spectra are unchanged upon variation of the length of the side chain (same as Figure 34, with $[Gd(dp3C1)_3]^{3-}$ at 26,000 and 21,500 cm^{-1}, see Figure 51), meaning that any difference in metal-centered photophysical properties ought to be due to the shorter side chain and not to a different location of the donor excited state. The quantum yields together with other photophysical properties of the corresponding $[Ln(dpxC1)_3]^{3-}$ (x= 1-3) complexes are presented in Table 11.
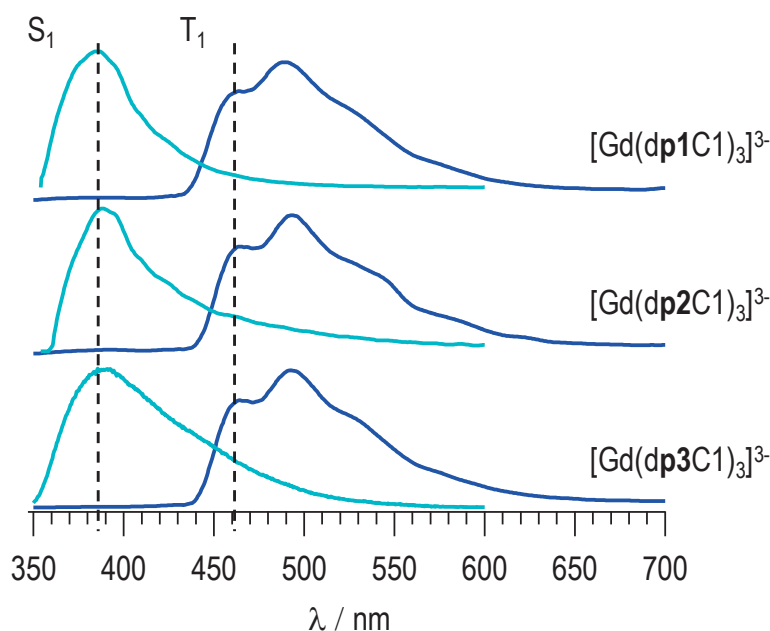
Figure 51. Fluorescence and phosphorescence spectra of the $[Gd(dpxC1)_3]^{3-}$ complexes at room temperature and at 77 K (50 μs after pulsed excitation) respectively. λ_{ex}=320 nm, 0.1 mM in Tris-buffered aqueous solution, pH 7.4. 10 % glycerol for the measurements at 77 K.

Unexpectedly, the shortening of the side chain has practically no influence on the quantum yield Φ_L^{Eu} in aqueous solution, which remains between 1.2 and 1.8 % (see Table 11). The ligand with the intermediate length (dp2C1) seems even slightly less

efficient than the other two ligands with a quantum yield $\Phi_L^{Eu} = 1.2$ %. It suggests that any increase of the energy transfer rate that would be due to the shorter side chain (if any), would be compensated by a decrease of another component of the sensitization efficiency, or of the europium intrinsic quantum yield. In terms of rate constants, it then corresponds to a competitive process that deactivates the sensitizer or the europium ion.

In order to identify why the shortening of the side chain has no real impact on the quantum yield in aqueous solution, quenching phenomena have to be reduced as much as possible. The solid state samples and frozen aqueous solutions at 77 K, are therefore valuable assets. They indeed suppress most of the quenching due to the presence of water molecules, and lower the rate constants of diffusion limited quenching phenomena, respectively. As seen in Table 11, nearly all photophysical properties are altered relative to those in aqueous solution.

Table 11. Photophysical properties of the $[Eu(dpxC1)_3]^{3-}$ and $[Gd(dpxC1)_3]^{3-}$ complexes at room temperature in aqueous solution (aq) and in solid state (s). $\lambda_{ex} = 320$ nm. $\tau_{obs}^{Eu} = 1.4$ ms ± 0.1 ms, $\tau_r^{Eu} = 4.2$ ms ± 0.4 ms (aq) and 2.8 ms ± 0.4 ms (s), $\Phi_{Eu}^{Eu} = 33$ % ± 5 % (aq) and 50 % ± 5 % (s), for all complexes in this table. Estimated error of 10 % on the quantum yields (sensitized quantum yields of the europium emission Φ_L^{Eu}, quantum yields of the ligand-centered emission Φ_L^{L}).

$[Ln(dpxC1)_3]^{3-}$	Φ_L^{Eu} / %		Φ_L^{L} / %		η_{sens} / %		Φ_L^{L} / %	
			Ln = Eu				Ln = Gd	
	aq	s	aq	s	aq	s	aq	s
x = 3	1.7	4.5	7.7	5.6	5.1	9.0	9.1	6.1
x = 2	1.2	6.8	6.3	5.7	3.6	13.6	7.1	6.3
x = 1	1.8	25.2	14.7	7.8	5.4	50.4	15.5	10.7

The trend in solid state demonstrates the expected behavior when the side chain is shortened, i.e. an increase of the quantum yield. The quantum yield Φ_L^{Eu} increases up to 25 % when the sensitizer is only separated from the coordination site by one -CH₂CH₂O- unit. The shape of each characteristic europium emission in solid state is very similar throughout the series though, so that the radiative lifetime can be estimated to be fairly identical for the three complexes. Since the observed lifetime is also not altered, the intrinsic quantum yield stays at 50 %. The difference in sensitized quantum yield then ought to come from an increased sensitization

efficiency, and certainly from a higher energy transfer rate, since the sensitization occurs though a singlet pathway (no intersystem crossing contribution).

Noteworthy, the emission from the coumarin seems also affected by the length of the side chain. This is even true in aqueous solution where the quantum yield of the coumarin emission is twice that of the ligands with the longer linkers. This last point stresses one of the major problems of any system that endeavors to investigate the relationship between the distance of a donor-acceptor and the rate of the energy transfer: at close distances, the environment of the donor and of the acceptor is altered by the presence of its partner. In this case, the presence of the coordination site seems somehow to increase the efficiency of the coumarin emission, which means either that the radiative lifetime of the coumarin is increased, or that the quenching and/or non-radiative relaxations are decreased. By measuring the lifetimes of the europium $^5D_0$ spectroscopic level at 77 K, we also noticed that it jumped from 2.2 ms with the longer linkers up to 4.7 ms for the shortest side chain, while the room temperature lifetimes in aqueous solution are similar within experimental error (at 1.4 ms ± 0.1 ms). This result strongly suggests that the efficiency in aqueous solution is limited by the quenching from diffusing molecules, either from the solvent and/or from the ligand itself. In addition, when the coumarin is close to the coordination site and frozen it may also participate in the second coordination sphere and help prevent the non-radiative deactivations of the europium ion. The lifetime of 4.7 ms is indeed what may be expected from a purely radiative relaxation, since the radiative lifetime was calculated in aqueous solution at 4.2 ms (the radiative lifetime is identical with the three ligands).

On the other hand, the fact that the quantum yield Φ_L^{Eu} is unchanged upon shortening of the linker may also be understood as a proof that the sensitizer is standing at a similar average distance from the lanthanide ion in aqueous solution and at room temperature, which should be at the upper limit the length of the shortest side chain (~5 Å). It would mean that the polyoxyethylene side chain may be fairly folded rather than extended. However, it may also come from a diffusion limited energy transfer. The excited sensitizer at the end of the side chain moves around the complex until the energy transfer rate is sufficiently high, and therefore until the sensitizer is close enough to the lanthanide ion, to allow an excitation transfer onto the lanthanide ion. Those phenomena would be removed in solid state since the structure is in that case more rigid and hence better defined. The increased quantum yield of the coumarin emission Φ_L^L for the complex with the shortest side chain (i.e. with the dp1C1 ligand) in aqueous solution could then be understood as a decreased self-quenching of the coumarin by the other coumarins on the two

remaining ligands of the complex. Self-quenching was indeed observed in the previous chapter to be a significant deactivation process in the $[Eu(dp3C1)_3]^{3-}$ complex. This decreased self-quenching in the dp1C1 complex could be due to a limited diffusion range when the linker is smaller, thus restricting the contact of the coumarin moieties within the complex.

The same conclusions can be extracted from the photophysical properties under an excitation at 270 nm, which activates the dpa triplet pathway in addition to the coumarin singlet pathway. The sensitized quantum yields for the dpxC1 europium complexes in aqueous solution and in solid state under an excitation at 270 nm are shown in Table 12 together with the same quantum yields under an excitation at 320 nm.

Table 12. Sensitized quantum yields of the europium luminescence in aqueous solution, Tris-buffered, pH 7.4, 0.1 mM in complex and in solid state

λ_{ex} / nm	Φ_L^{Eu} / % in **aqueous solution**		
	$[Eu(dp3C1)_3]^{3-}$	$[Eu(dp2C1)_3]^{3-}$	$[Eu(dp1C1)_3]^{3-}$
320	1.7	1.2	1.8
270	3.3	2.9	2.5
λ_{ex} / nm	Φ_L^{Eu} / % in **solid state**		
	$[Eu(dp3C1)_3]^{3-}$	$[Eu(dp2C1)_3]^{3-}$	$[Eu(dp1C1)_3]^{3-}$
320	4.5	6.8	25.2
270	5.7	8.0	14.6

Interestingly, in the europium complex with the ligand that has the shortest linker, the quantum yield resulting from the mixed sensitization pathway (under an excitation at 270 nm) yields a lower efficiency of 14.6 % than the sole coumarin sensitization (under an excitation at 320 nm), which has a high quantum yield of 25.2 %. It then means that under the correct conditions, the coumarin chromophore is a better sensitizer than the *para*-polyoxyethylenated dpa chromophore, since the addition of the dpa pathway reduces the sensitization efficiency.

5.4 Concluding remarks

This chapter investigated the effect of the shortening of the polyoxyethylene linker in the dpxC1 architecture. It was shown that, as expected, the shorteneing has no impact on the excited states of the coumarin chromophore. On the other hand, the anticipated improvement of the sensitization efficiency for shorter linkers was not observed in aqueous solution. Several tentative explanations were given. From the results obtained in the previous chapter for the dp3C1 complex, it seems that quenching phenomena and a plausible diffusion limited energy transfer may account for such behaviors. The flexible structure of the polyoxyethylene side chain in solution may indeed either be folded in a "mushroom structure" with the coumarin in a similar distance from the lanthanide ion whatever the length of the pendent arm, or diffuse and bend freely from the extended "brush like structure" to more compact configurations, in which case, the energy transfer may occur from the most efficient of these dynamic configurations and would be diffusion limited.

These assumptions are reinforced by the observation of the expected improvement of the sensitization efficiency in solid state samples, where quenching solvent molecules are removed, and where the structure should be more rigid. The polyoxyethylene linker may then adopt its extended trans-gauche-trans helical arrangement, and therefore provide shorter distances between the coumarin chromophore and the lanthanide ion.

When exciting the solid state dp1C1 complex with the shortest side chain in the series, the sensitization efficiency from the coumarin pathway seems even more efficient than the dpa pathway. It was indeed observed that the excitation below 300 nm, where dpa also absorbs, decreases the quantum yield relative to the pure coumarin excitation above 300 nm.

With this chapter, the pure chemistry part of this thesis is over. One of the purposes of the dpa-polyoxyethylene-coumarin architecture was to increase the absorption wavelengths of the luminescent complexes towards the near visible region, in particular due to a more convenient utilization as luminescent dyes for color reproduction. This increase of the absorption range was achieved, yet at the expense of the color purity due to the incomplete energy transfer from the fluorescent coumarin. The forthcoming chapters will deal mainly with color reproduction. As a transient part, the next chapter will show both applied chemistry and color reproduction sections.

Chapter 6

Printing lanthanide trisdipicolinate complexes for color reproduction

Additive color synthesis with invisible luminescent inks

6.1 Introduction

This chapter marks the beginning of the color science part of this thesis. It explores the potential of lanthanide complexes, and more particularly, of europium and terbium complexes for color reproduction and document security with luminescent inks. Most of the notions presented in the introduction and regarding color science (Section 1.5-1.7 from page 34) will be applied for the reproduction of luminescent full color images that are invisible under white light. These notions include halftoning, colorimetric characterizations of emission spectra, spectral prediction models, the determination of gamuts and the utilization of gamut mapping.

The chapter is yet a bridge between the pure chemistry side and the color reproduction side of this work. It will show how to create luminescent inks from water soluble lanthanide complexes, how to print the inks, how to model the emission spectra and hence the color resulting from the luminescent emission under UV light, how to rationalize the results of the model with the photophysical properties of the printed luminescent lanthanide complexes, and finally, how to generate luminescent full color images.

6.1.1   Motivations

In this chapter, the utilization of water soluble lanthanide complexes as luminescent inks is demonstrated. The *red* emitting europium trisdipicolinate complex and *green* emitting terbium trisdipicolinate complex presented in the introduction (Section 1.4, pages 16-22) are formulated as luminescent inks suitable for ink-jet printing and printed on natural papers (without optical brightening agents, OBA). In order to complete the set of primary colors, a commercial *blue* emitting luminescent ink is also used.

The primary purpose for printing these three luminescent inks is to be able to reproduce full color images that are invisible under normal light and can be revealed under UV light. Because of the photophysical properties of the lanthanide trisdipicolinate complexes, short wave UV light is required to excite the red and green emission. An uncoated UV mercury lamp with a UV bandpass filter was used thereof, which yield a narrow 254 nm excitation peak.

Luminescent lanthanide complexes are often claimed in the patent literature to be good luminescent dyes in luminescent inks (see Section 1.7, page 49). Lanthanide trisdipicolinate complexes are even found in some of them. However, apart from the print quality of these inks, their capability to reproduce colors is never really addressed. It seems therefore important to be able to investigate the color range that can be additively synthesized with a characteristic europium and terbium emission, and hence, to study their capability to be superposed and halftoned.

Because of the difficulty to measure the emission spectra of a sufficient number of halftoned variations of the three inks, the applicability of a simple spectral prediction model for spectral radiant emittances is also tested. Such models were already successfully applied with luminescent inks in offset printing, but the luminescent inks were printed in juxtaposed halftones to guarantee a good additivity of the emissions.[77] In the present contribution, the color reproduction framework normally used for subtractive color synthesis (in reflectance) is shown to be adaptable to additive color synthesis (in spectral radiant emittrance) with invisible luminescent inks.

Finally, a justification for the accuracy of the spectral prediction model might be found by measuring the photophysical properties of the lanthanide complexes in different superposition conditions. The measurement of the photophysical properties of the printed lanthanide complexes might then be an easy way to check their aptitude as luminescent dyes for color reproduction.

6.1.2   Challenges

The main challenge here is to be able to start from chemicals and finally create luminescent full color images. The chemicals need therefore to be formulated as inks, and these inks are then to be printed. The photophysical properties of the printed inks might also be determined, noteworthy, the effect of the amount of ink printed on paper and the effect of the superposition with the other inks. In order to have multilevels colors, the inks have to be printed as halftones. With the purpose of relating the colors emitted from these halftones to surface coverages of the luminescent inks, emitted colors need to be predicted by relying on a spectral prediction model. It is yet necessary to map the input image colors into the gamut of the ink halftones so that differences between the input sRGB gamut and the destination gamut are compensated. The amount of each ink required to obtain the desired mapped colors can be found by the spectral prediction model.

6.2 Lanthanide trisdipicolinate complexes as luminescent dyes: ink formula for ink-jet printing

6.2.1 Ink-jet printing and corresponding ink formula

Non-industrial ink-jet printers are usually drop-on-demand printers, which print water based inks. In this configuration, the ink is loaded in the print head and ejected at the desired location "on-demand" on the substrate to be printed. Two different mechanisms exist thereof: thermal ejection and mechanical ejection. In the first mechanism, the ink is heated until a bubble forms and pushes the ink out of the nozzle. In the second mechanism, the ink is pushed out of the nozzle by a moving part. In this chapter, two printers were used, a Canon Pixma iP4000, which is a thermal type ink-jet printer (bubblejet technology), and an Epson Stylus Photo P50, which has a mechanical type print head (micropiezo technology).

A very simple ink-jet formula for dyes includes a water base, usually with more than 60 %w of water, some co-solvents, usually alcohols, to adjust the physical properties of the inks, humectants to avoid the fast drying of the ink on the print head, which would clog the nozzles, typically polyalcohols, defoamers to limit the formation of foams that would introduce some air in the print head, and dyes to give the ink its tint. Biocides agents and surfactants are sometime added to avoid the proliferation of microorganisms in the inks and to adjust its surface tension. Polymers are also found in some cases, to improve the film forming properties of the inks. The formulation of pigmented inks is more complex and will not be described here.

The formula for producing the europium and terbium trisdipicolinate based inks was not optimized. The purpose is to be able to print the inks with a sufficient print quality, so that the printing process is reliable and operates without clogging the print head. The time-consuming improvement of the ink formula shown in Table 13 was therefore not necessary. Evaluating the print quality in details is outside the scope of this thesis.

The luminescent inks are solutions of the luminescent dyes in an ink base. The formula of the ink base is presented in Table 13.

Table 13. Formula of the ink base (without the dye), d = 1.03

Components	Relative amount (weight)
Water	80 %
Glycerol	7 %
Ethylene glycol	5 %
Diethylene glycol	5 %
Isopropanol	3 %

In this formula, water is the solvent, whereas ethylene glycol, diethylene glycol and isopropanol are co-solvents. Together with glycerol, ethylene glycol and diethylene glycol are also humectants, whereas isopropanol also acts as a defoamer.

The luminescent dyes were formed by recrystallizing europium and terbium trisdipicolinate in water from highly concentrated hot solutions. The filtered crystals were then dried at 65°C overnight and used without further purifications. The ink base was loaded with 4.5 % weight (%w) of the europium trisdipicolinate sodium salt for the red emitting luminescent ink, and with 5 %w of terbium trisdipicolinate sodium salt for the green emitting luminescent ink. The inks were finally filtered through 0.45 μm filters to ensure that no solid residue (dust, fibers or undissolved compound) remained in the ink, which could clog the print head.

6.3 Effect of the amount of ink on the photophysical properties of the lanthanide ions

In order to determine if the concentrations in luminescent lanthanide complexes are appropriate and if the amount of printed lanthanide complexes has an impact on their photophysical properties, several layers of solid patches of the ink (100 % of the ink) were printed on a natural paper (Entrada fine art natural paper) with the Canon iP4000 printer. The emission intensity from the lanthanide ions were measured from 0 layer (no lanthanide ion, emission from the paper) up to 10

superimposed layers. As seen in Figure 52, the increase of the emission intensity as a function of the number of layer, and hence of the concentration in lanthanide complex, is non-linear. The emission intensity quickly saturates above three layers of solid ink, so that little gain is obtained by printing more ink. This behavior is observed for the europium trisdipicolinate ink as well as for the terbium trisdipicolinate ink.
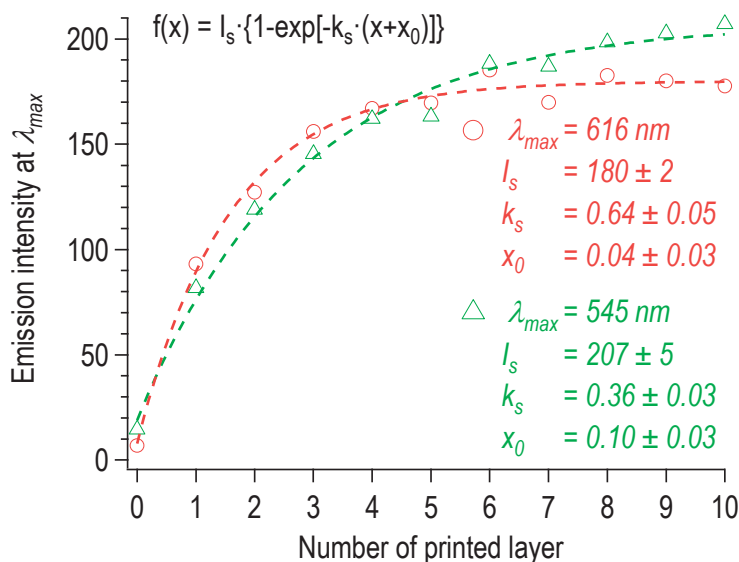
Figure 52. Saturation of the emission intensity of the lanthanide ions by increasing the concentration of the printed complexes. Red circles: emission of the $^5D_0 \rightarrow {}^7F_2$ transition of $[Eu(dpa)_3]^{3-}$. Green triangles: $^5D_4 \rightarrow {}^7F_5$ transition of $[Tb(dpa)_3]^{3-}$.

There are two phenomena that can explain such a saturation. Either the saturation is due to a saturation of the absorption, by a so-called inner filter effect, or is due to a modification of the photophysical properties of the lanthanide ion by self-quenching. In order to identify the mechanism, the measurement of the observed lifetime of the lanthanide emission was undertaken.

A self-quenching of a compound is a non-radiative deactivation of the excited compound D^* by interaction with another molecule of the same compound D. This radiationless relaxation decreases the observed lifetime τ_{obs} when the concentration of the compound $[D]$ is increased, as shown in Equation 20 (k_{abs} absorption rate constant, k_r radiative deactivation rate constant, k_{nr} non-radiative deactivation rate constant, k_{sq} self-quenching deactivation rate constant, k_{obs} observed deactivation rate constant).

$$D + photon \xrightarrow{k_{abs}} D*$$

$$D* \xrightarrow{k_r} D + photon'$$

$$D* \xrightarrow{k_{nr}} D \tag{20}$$

$$D* + D \xrightarrow{k_{sq}} 2D$$

$$k_{obs} = k_r + k_{nr} + k_{sq} \cdot [D] \qquad \Rightarrow \qquad \tau_{obs} = \frac{1}{k_r + k_{nr} + k_{sq} \cdot [D]}$$
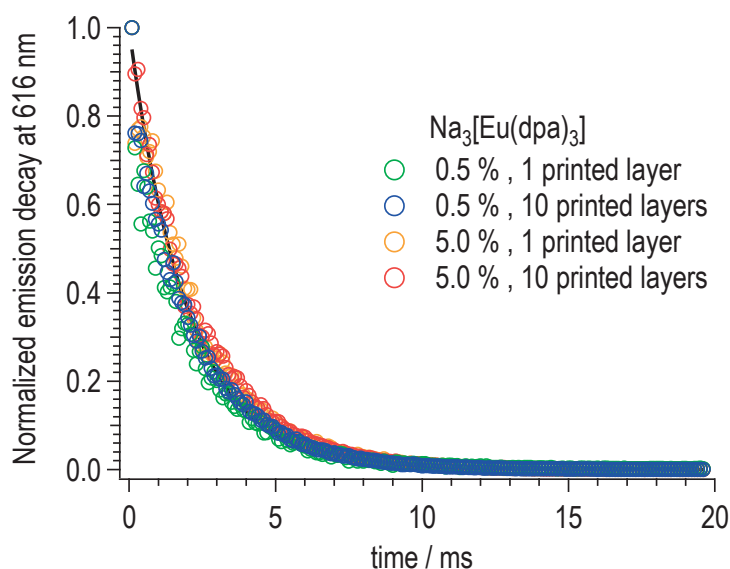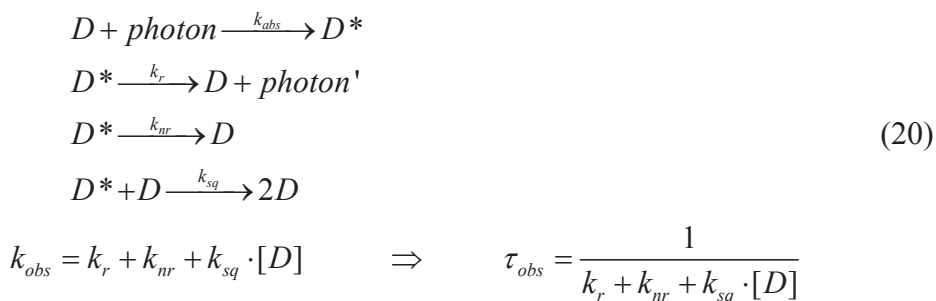
Figure 53. Normalized emission decay of the $^5D_0 \rightarrow ^7F_2$ transition of $[Eu(dpa)_3]^{3-}$ printed with one ink layer or with ten ink layers on paper and at different concentrations. The black line is the average fit of the decay.

Figure 53 shows the observed lifetime of the europium ion at two different concentrations for the extreme number of layers (i.e., 1 layer and 10 layers). No net change of the observed lifetime is observed when increasing the number of printed layer, and when changing the concentration of the ink (original concentration and 10 times diluted ink).

The same observation was true for the terbium trisdipicolinate ink. Therefore, the concentration of the ink has no impact on the photophysical properties of the lanthanide ions in the trisdipicolinate complexes. The saturation of the emission intensity is thus only due to the inner filter effect of the absorbing complexes.

This result suggests that the lanthanide complexes are well preserved once printed on paper, and that the complexes are not affected by the density of complexes on paper. A higher concentration of complexes in the inks could be used to improve the emission intensity, but precipitation becomes an issue at loadings higher than the 4.5-5 %w of lanthanide complexes used in this work. When the concentration is increased, the gain in emission intensity would anyway be less and less attractive because of the inner filter effect. If several layers would be used to increase the density of the inks, the emission intensity would be limited to a maximal intensity, which depends on the photophysical properties of the luminescent dyes and on the absorbance (optical density) of the ink layer. A more powerful UV light source would therefore be necessary to increase the emission intensity further.

The next step in the characterization of these luminescent inks is to check whether the superposition with the other inks has an effect on the photophysical properties of the lanthanide ions.

6.4   Effect of the superposition of the inks on the photophysical properties of the lanthanide ions

In order to test if the luminescent dyes can be printed on top of each other and yet retain their photophysical properties, the observed lifetime of the lanthanide ions were measured in different superposition conditions. A solid patch of europium trisdipicolinate ink, a solid patch of the blue luminescent ink and a solid patch of europium and blue luminescent ink were printed on top of a solid patch of terbium trisdipicolinate, and the observed lifetime of the terbium ion measured under the same conditions as in the self-quenching experiments.

As demonstrated in Figure 54, the lifetime of the terbium emission is unchanged upon superposition with the other inks. Therefore, the terbium ion is unquenched whatever the superposition condition. The same behavior was observed for the europium emission when printing the other inks and superpositions of the inks on top of it.
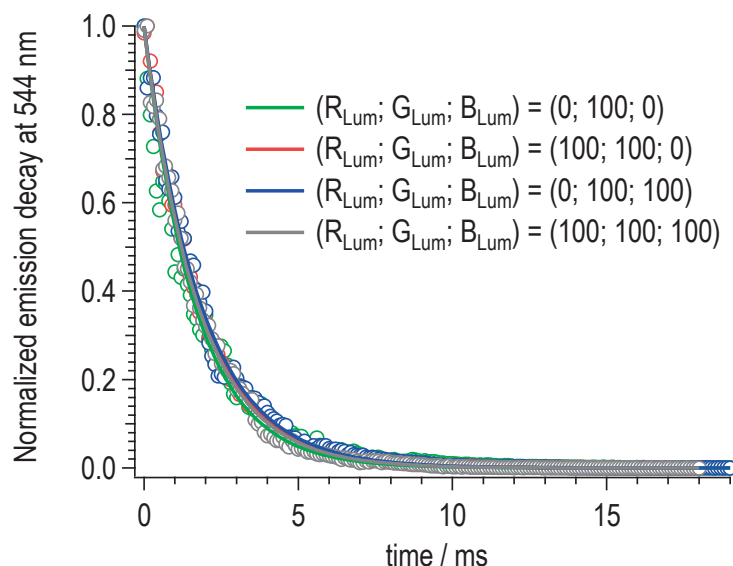
Figure 54. Normalized emission decay of the $^5D_4 \rightarrow {}^7F_5$ transition of $[\text{Tb(dpa)}_3]^{3-}$ in the green, yellow, cyan and white luminescent colorant

The lanthanide trisdipicolinate complexes are then stable when printed with the other inks and keep their good photophysical properties. They seem therefore particularly promising as luminescent dyes for ink-jet printing and color reproduction.

6.5   Spectral radiant emittance prediction model

The previous section proved that the europium and terbium trisdipicolinate complexes are good candidates as luminescent dyes for color reproduction. To confirm that they yield good luminescent colors for a trichromic additive color synthesis, the luminescent inks need to be printed as luminescent halftones and the resulting emissions under short wave UV light need to be determined somehow. The halftone principle was introduced in Section 1.6.1, Figure 5, page 41.

The luminescent colors achievable by printing the luminescent inks with a defined ink-jet printer on a definite substrate form the gamut of the luminescent inks. The gamut was defined in Section 1.6, page 39. It is the volume of the color space comprising colors that can be reproduced with a specific color reproduction system. In the present case, the system is formed by the three luminescent inks printed as definite halftones on a specific paper with a particular ink-jet printer.

There are two ways to find the gamut of the luminescent inks on a given substrate. One may print and measure a sufficient amount of colors to create samples representative of the reproducible colors, or alternatively, one may use a spectral prediction model to calculate, from a set of parameters obtained with a minimal amount of calibration samples, the emission spectrum of any luminescent halftone. The second approach was chosen here.

Because colorimetry is defined from radiometric units, the spectral prediction model, which is used to calculate colors, has to output radiometric emission spectra, or at least, relative emission spectra that have intensities proportional to the energy measured at each wavelength instead of intensities proportional to the photon count. The emission spectra have then to be relative irradiances or relative spectral radiant emittances. In this thesis, the term "emittances" is often encountered instead of spectral radiant emittances. It accounts for emission spectra corrected to take into account the non-linear sensitivity of the detector as a function of the wavelength, and converted from relative photon counts units usually measured with spectrophotometers, to relative radiometric units. The fact that the intensities are normalized, and hence relative, is not important in colorimetry, since the human visual system adapts its sensitivity to the intensity of the stimulus for a large range of intensities. In color images seen either by reflection or transmission of white light, the maximal intensity is typically deteremined by the intensity of the white color. The adaptation relative to the luminance of the white stimulus seems therefore also appropriate for emittances.
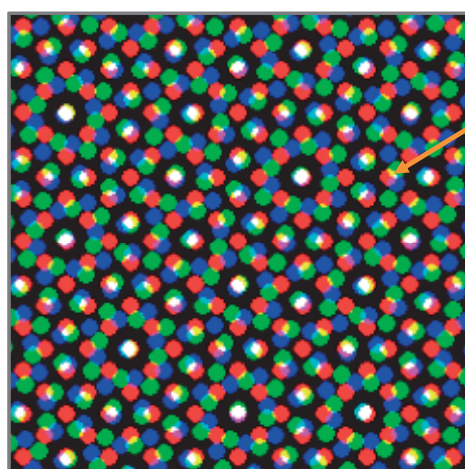
600 dpi, 100 lpi,
75°, 25 % B / 45°, 25 % R / 15°, 25 % G

The superpositions yields additive colors

K	blac**K**	R+G	**Y**ellow
R+K	**R**ed	R+B	**M**agenta
G+K	**G**reen	G+B	**C**yan
B+K	**B**lue	R+G+B	**W**hite

3 inks => 2^3 = **8 colorants**

Figure 55. Superposition of ink halftone dots forming new colors by additive color synthesis

The simplest approach for predicting emittances of luminescent halftones is to combine the spectral radiant emittances of each luminescent ink halftone dot in an additive way. However, because of the inner filter effect that happens when the luminescent inks are superposed (i.e., the decrease of the emission intensity due to the absorption of part of the UV excitation light source by superposed inks), the superposition conditions have to be taken into account when summing the emittances. This is done by defining the superpositions of inks as distinct luminescent colorants (see Figure 55).

For the three luminescent inks, since there are eight combinations of inks, eight luminescent colorants are possible. The red alone (on the paper black), the green alone, the blue alone, the superposition of red with green, which gives a yellow emitting colorant, the superposition of red with blue, which gives a magenta emitting colorant, the superposition of green with blue, which gives a cyan emitting colorant, the superposition of the red, green and blue luminescent ink, which gives a white emitting colorant, and the absence of any luminescent ink, which gives a black colorant. The surface coverages of these luminescent colorants in a halftone screen element, and hence on the measured sample, define the intensity of the resulting emittance relative to the emittance of the fulltone luminescent colorant. The sum of the respective emittances of the eight colorants weighted by their surface coverages yields the total emittance of the luminescent halftone, see Equation (21. In that equation, $E(\lambda)$ is the relative spectral radiant emittance of the halftone, a_f is the effective surface coverage of colorant f and $E_f(\lambda)$ is the relative spectral radiant emittance of the fulltone colorant f.

$$E(\lambda) = \sum_f a_f \cdot E_f(\lambda) \tag{21}$$

In order to take into account the physical dot gain of the luminescent inks due to ink spreading, and the optical dot gain due to lateral propagation of the luminescent emission in the paper substrate, effective surface coverages are required. The dot gain phenomena are illustrated in Figure 56.
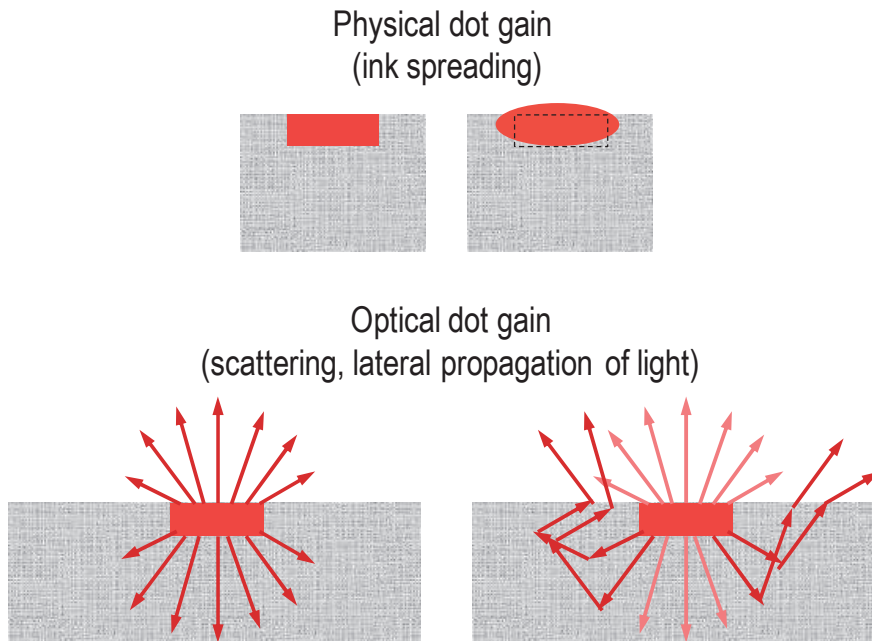
Figure 56. Illustration of the dot gain phenomena

The ink spreading curves represent the reproduction curves, which establish the correspondences between the input nominal surface coverage and the output effective surface coverage of each ink. Furthermore, because the dot gains depend on the superposition conditions of the inks, the ink spreading curves need to be calibrated for each superposition condition. For three inks, the following cases are considered: each ink alone, each ink on a second ink, and each ink on the two other inks. There are therefore twelve superposition conditions, which yield twelve ink spreading curves. By subtracting the nominal surface coverages from the effective surface coverages obtained by calibration, dot gain curves are obtained.
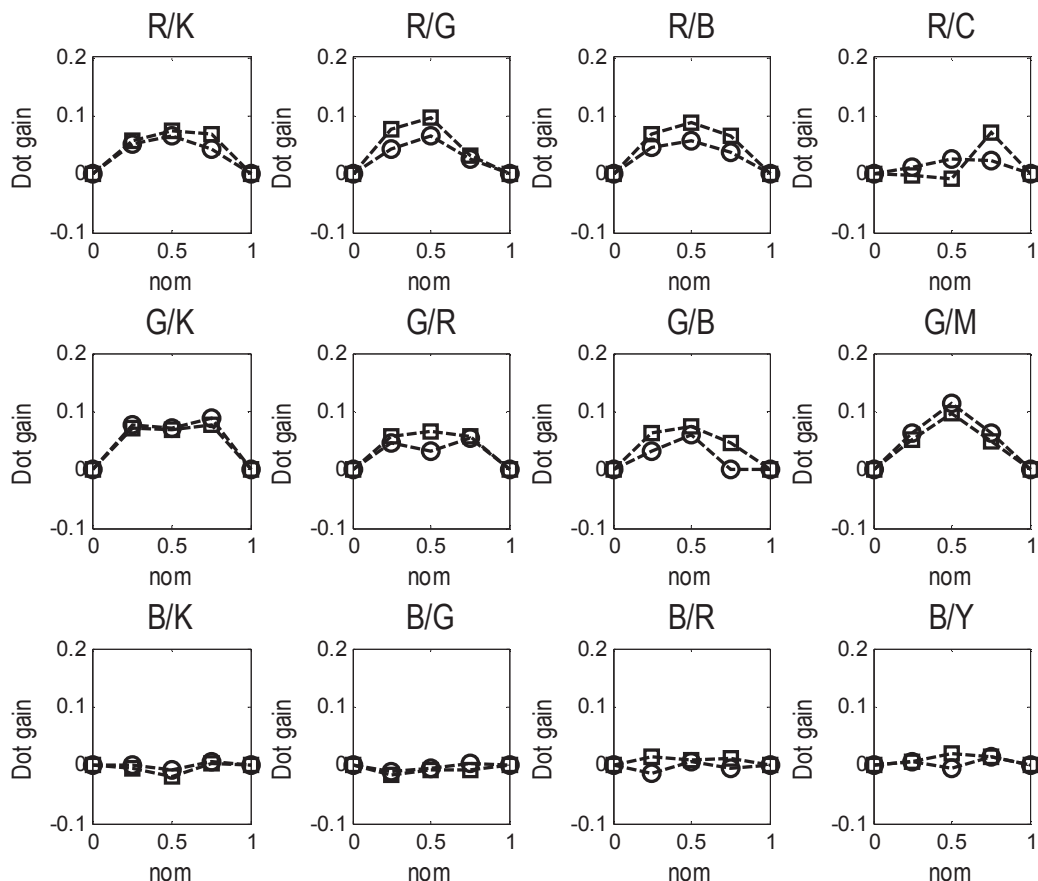
Figure 57. Dot gain curves of the twelve superposition conditions of the red emitting, green emitting and blue emitting luminescent ink on a Canson Rag Photographique paper (circles) and on a Hahnemühle Photo Rag Baryta paper (squares)

The effective surface coverages were determined as follow. First, a set of calibration samples was measured. It encloses the eight colorants and the 25 %, 50 % and 75 % nominal surface coverages of each for each superposition condition (i.e., alone, on each individual ink fulltone, and on the fulltone formed by the superposition of the two other inks). The effective surface coverages of each ink under each superposition condition were then fitted according to Equation (21 by minimizing the root mean square difference between the predicted emittances and the measured ones. The dot gains resulting from the obtained ink spreading curves are shown in Figure 57. Two paper substrates were tested: a Canson Infinity Rag Photographique paper (210 gsm) and a Hahnemühle Photo Rag Baryta paper (315 gsm). The halftone screen for the print of the luminescent inks was a classical

rotated screen with a round shape. It was printed at 720 dpi at a frequency of 100 lpi and halftone screen angles of 75° for the blue luminescent ink, 45° for the red luminescent ink and 15° for the green luminescent ink. The printer was the Epson Stylus Photo P50 ink-jet printer. The spectral prediction model needs to be calibrated for each type of paper. The luminescent colorants, dot gains and gamuts may indeed be different depending on the paper.

Once calibrated, the model was tested by measuring the 125 combinations of 0 %, 25 %, 50 %, 75 % and 100 % nominal surface coverages of the three inks, and by comparing the ΔE_{94} color difference between the measurements and the predictions (calculated according to Equation 14, page 40).

The predicted CIELAB colors were obtained by running the spectral prediction model and converting the emittances into CIE-XYZ and then into CIELAB colors. First, the effective surface coverages (r', g', b') of the three luminescent inks corresponding to the input nominal surface coverage were found according to the ink spreading equations (Equation 22), by solving them iteratively from the nominal surface coverages (r, g, b).

$$r' = f_{r/k}(r) \cdot (1\text{-}g') \cdot (1\text{-}b') + f_{r/g}(r) \cdot g' \cdot (1\text{-}b') + f_{r/b}(r) \cdot (1\text{-}g') \cdot b' + f_{r/c}(r) \cdot g' \cdot b'$$

$$g' = f_{g/k}(g) \cdot (1\text{-}r') \cdot (1\text{-}b') + f_{g/r}(g) \cdot r' \cdot (1\text{-}b') + f_{g/b}(g) \cdot (1\text{-}r') \cdot b' + f_{g/m}(g) \cdot r' \cdot b' \quad (22)$$

$$b' = f_{b/k}(b) \cdot (1\text{-}r') \cdot (1\text{-}g') + f_{b/g}(b) \cdot g' \cdot (1\text{-}r') + f_{b/r}(b) \cdot (1\text{-}g') \cdot r' + f_{b/y}(b) \cdot r' \cdot g'$$

The surface coverages of the colorants were obtained next from the effective surface coverages of the inks according to the Demichel equations (Equation 23).

$$
\begin{aligned}
a_k &= (1-r') \cdot (1-g') \cdot (1-b') & a_y &= r' \cdot g' \cdot (1-b') \\
a_r &= r' \cdot (1-g') \cdot (1-b') & a_m &= r' \cdot b' \cdot (1-g') \\
a_g &= g' \cdot (1-r') \cdot (1-b') & a_c &= g' \cdot b' \cdot (1-r') \\
a_b &= b' \cdot (1-r') \cdot (1-g') & a_w &= r' \cdot g' \cdot b'
\end{aligned}
\qquad (23)
$$

The measured relative spectral radiant emittances of the eight colorants are shown in Figure 58. The emission intensity from the luminescent colorants composed of ink superpositions, is slightly inferior to the same emission peak of the ink alone, due to the inner filter effect.
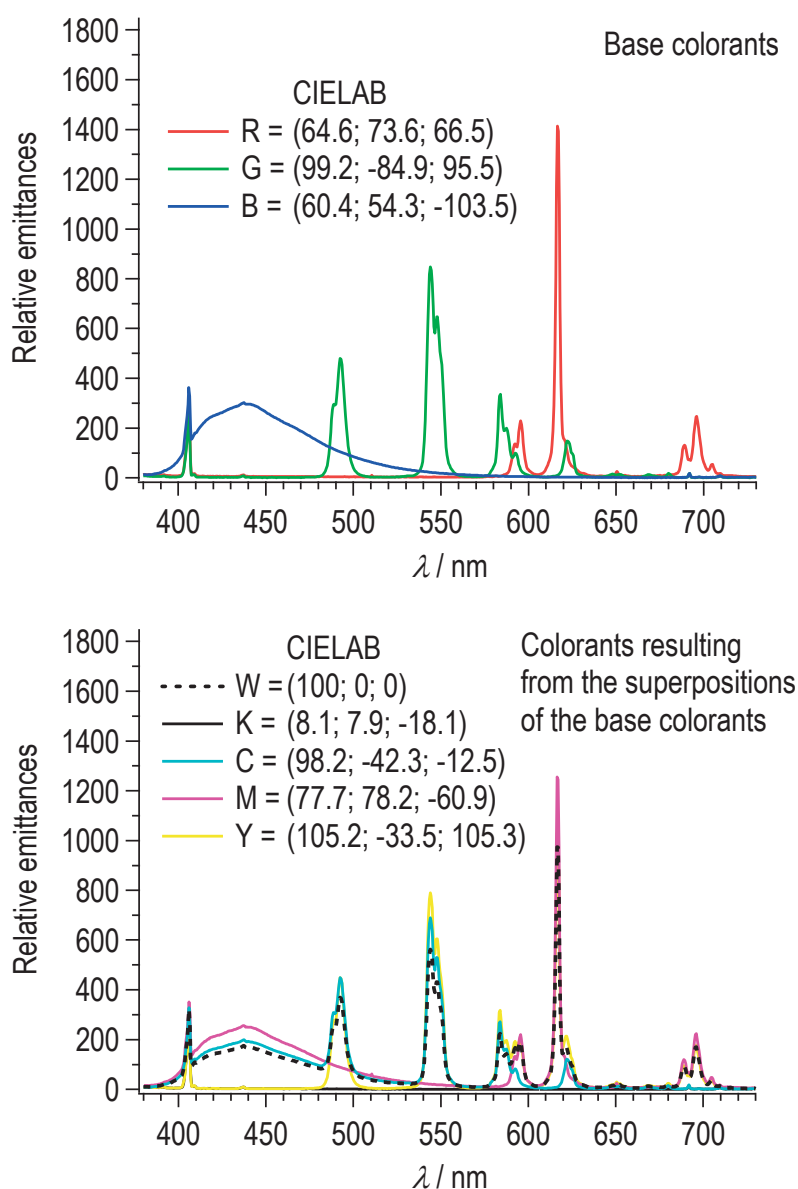
Figure 58. Relative spectral radiant emittances of the eight luminescent colorants printed on the Canson Rag Photographique paper, displayed in their respective colors, except for the white, which appears as a dashed black line

The prediction accuracy of the model is very good as demonstrated in Figure 59, considering that the model is very simple and that the colors are due to luminescent emissions. The average color difference is below 1.0 on the two tested papers (0.9 on the Canson paper and on the Hahnemühle paper). The maximal error is also relatively low with a maximal ΔE_{94} value of 3.1 on the Canson paper and of 2.5 on the Hahnemühle paper. The 95 % quantile is around 2.0 for both papers.

ΔE_{94}: Avg = 0.9, Max = 3.1, 95%-quantile = 2.1 ΔE_{94}: Avg = 0.9, Max = 2.5, 95%-quantile = 1.9
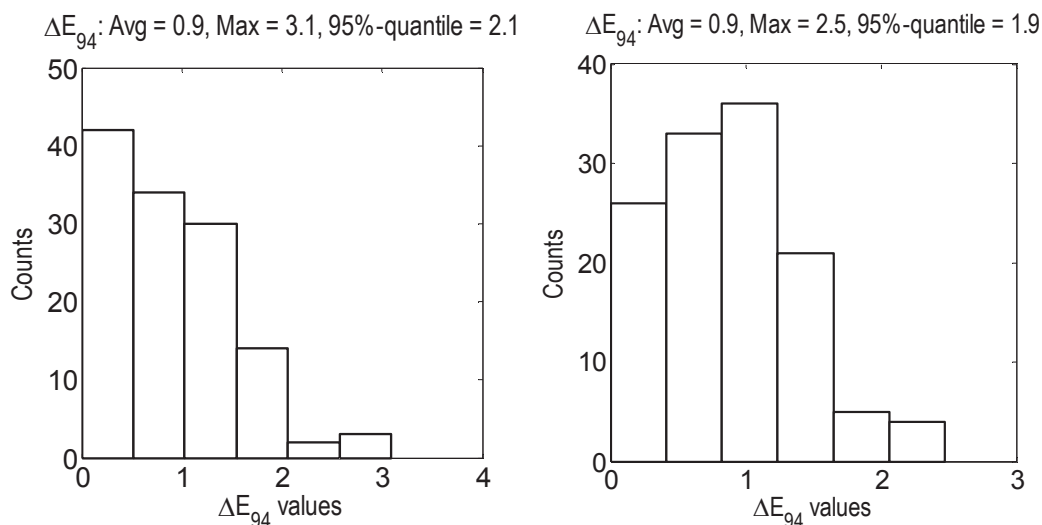
Figure 59. Distribution diagram of the color difference between the measured CIELAB colors and the corresponding predicted CIELAB colors for the print on the Canson Rag Photographique paper (left) and for the print on the Hahnemühle Photo Rag Baryta paper (right)

Such a good accuracy can be rationalized by the inertness of the lanthanide trispicolinate complexes when printed on top of each other or on the blue luminescent ink. The inner filter effect, which results in a lower emission intensity when superposing the inks, is not problematic since it is taken into account in the emittances of the luminescent colorants (Neugebauer primaries, see Figure 58). The dot gain curves (Figure 57) show that the commercial blue luminescent ink has nearly no dot gain, whereas the trisdipicolinate inks show dot gains up to 10 %. This may come from the poorer quality of the unoptimized ink formula presented in Table 13, page 144, compared with a commercial ink.

Since the model is accurate, the emission spectrum and hence the luminescent color of any luminescent halftone can be predicted precisely. The gamut of the color reproduction systems can now be determined from the spectral prediction model. Furthermore, the spectral prediction model can be used to find the surface coverages of the three luminescent inks that create a desired luminescent color under the UV bandpass filtered uncoated mercury light.

6.6   Color gamut of the luminescent inks

Since the spectral radiant emittance prediction model is accurate, it can be used to predict the large number of spectra, and thus colors, needed to determine the gamut of the luminescent inks. The emittance of each combination of the surface coverages of the inks by step of 2.5 % of nominal surface coverage was first predicted, converted to CIE-XYZ tristimulus values providing the reference white produced by the white emitting fulltone (100 % of each ink), and then to CIELAB colors. From the resulting 68,921 CIELAB colors, the gamut boundary was computed by applying a Delaunay triangulation and then the ball-pivoting algorithm developed by Bernardini et al.[78]
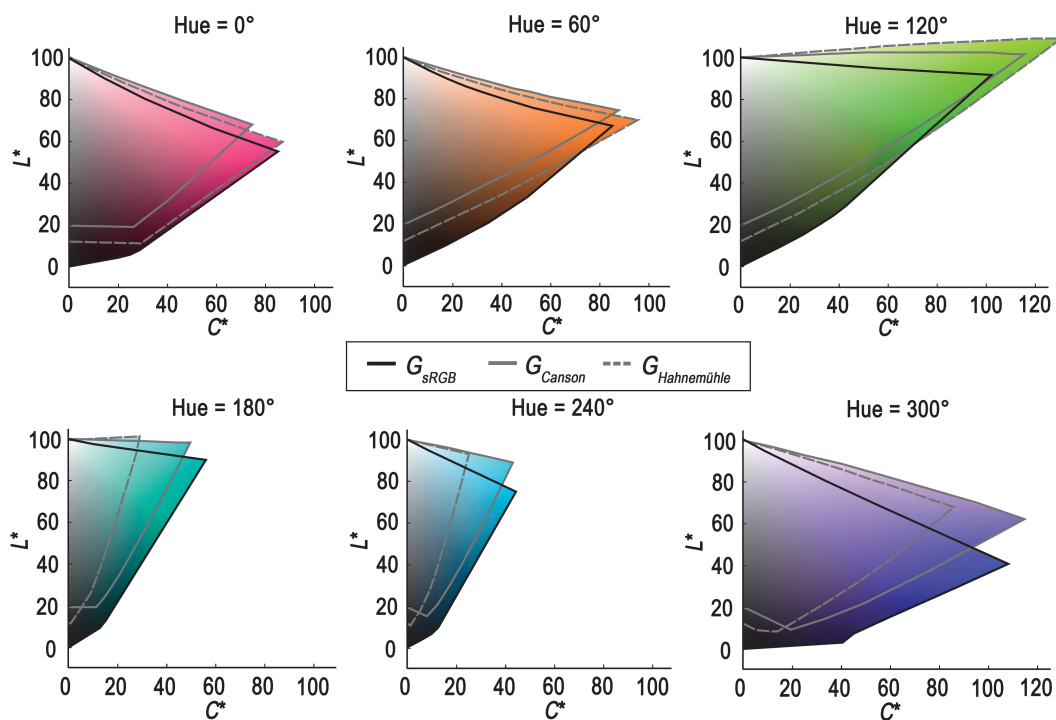
Figure 60. Gamut of the luminescent inks printed on the Canson paper and on the Hahnemühle paper compared with the sRGB gamut

This procedure was performed for the two paper substrates. As shown in Figure 60, the gamut of the luminescent ink depends on the substrate on which they are printed. Actually, the emittances of each colorant are slightly different. The

white emittance is for example not the same, although it is composed in both cases of 100 % surface coverages of each luminescent ink. On the Canson paper, the white luminescent color looks, compared to the same sample printed on the Hahnemühle paper, more reddish (or the other way round, more bluish on the Hahnemühle paper than on the Canson paper). This probably comes from different layouts of the ink dots penetrating and diffusing more or less in the paper and yielding different inner filter effects, which results in a different excitation of the inks. Paper properties such as the coating, the glossiness, the scattering of the excitation UV light inside the paper, etc. may thus have an impact on the absorption of UV light by the individual inks.

Compared to the gamut of a standard sRGB display, the gamut of the luminescent inks is close to the sRGB gamut in most hues, except in the blue colors where it is significantly smaller. However, because of the inner filter effect that decreases the emission intensity of the colorants formed by superposed inks, the emission intensity of the white (superposition of the three inks) is the lowest of the colorants. As a result, some colorants with a green component have luminances higher than $Y = 100$, and hence, lightness higher than $L^* = 100$. For the Canson paper, only the yellow colorant has a lightness $L^* = 105.2$ higher than $L^* = 100$. However, for the Hahnemühle paper, the green $L^* = 109.7$, yellow $L^* = 108.9$ and cyan colorants $L^* = 101.3$ have lightnesses higher than the lightness of the white. Therefore, the gamut in the green colors (with hue angles around $h_{ab} = 135°$) is larger than the sRGB gamut in the high lightnesses. This is also true, yet to a smaller extent, for the other hues. Finally, the gamut of the luminescent inks does not include as many dark colors as the sRGB gamut. The lowest lightness on the grayscale axis is between 10 and 20, which is better than most lower lightnesses in subtractive color synthesis by classical cyan, magenta and yellow inks. This probably comes from the reflection of the UV light source on the unprinted paper, which also emits in the visible, despite the presence of a UV bandpass filter. The unprinted paper does not look black, but bluish due to the presence of a strong peak from the mercury lamp at 406 nm. To compensate for this blueish tone, slight amounts of luminescent inks need to be printed in order to obtain a neutral black that is inexorably higher in lightness, compared with the unprinted sheet.

As a result of the large gamut of the luminescent inks, nicely vivid images are expected, with little color differences between the input images viewed on an sRGB display and those observed under UV excitation.

6.7   Color reproduction with the luminescent inks

The procedure for producing luminescent full color images visible under UV is similar to the standard procedure described in the first chapter. The main steps are the following: First, the compression (here linear) of the lightness range of the input sRGB color image to the corresponding lightness range of the luminescent inks output gamut. The second step consists in mapping the lightness compressed sRGB CIELAB colors into the gamut of the luminescent inks according to a multiple foci gamut mapping algorithm ($L^*_{low} = 40$, $L^*_{high} = 80$). Finally, the spectral prediction model is used to recover the surface coverages of the luminescent inks that reproduce the desired mapped CIELAB colors.

To quickly establish the correspondences between the mapped CIELAB colors and the correct surface coverages of the luminescent inks, a 3D lookup table is used. The 3D lookup table consists in a 3D grid in CIELAB with the precomputed corresponding surface coverages of the red emitting, green emitting and blue emitting luminescent ink at each point of the grid (i.e., for each CIELAB color in the grid). At image generation time, the desired mapped CIELAB colors present in the image are located in the 3D grid, and the corresponding surface coverages of the luminescent inks are interpolated from neighbor vertices. This solution is much quicker than asking the spectral prediction model to fit the surface coverages that minimize the color difference between the desired color and the predicted color. With a 3D lookup table, the computation needs to be performed once for the whole lookup table, and not for each input image pixel. The accuracy of the method is not as accurate as a direct minimization of the input image colors, but for a 3D grid with small enough steps in L^*, a^* and b^*, the results are as good as the time-consuming surface coverage fitting method.

After obtaining the surface coverages of the luminescent inks, the three red, green and blue luminescent ink separation layers each containing the surface coverages of the corresponding luminescent ink are saved. The layers are then halftoned according to the same method than the one used in the calibration of the spectral prediction model (i.e. with a classical rotated screen, round shape, 720 dpi, 100 lpi, 75° B_{lum}, 45° R_{lum}, 15° G_{lum}). The halftoned luminescent ink layers can then be printed on the same printer and on the same substrate as those used in the calibration of the spectral prediction model. Since two paper substrates were tested here, two 3D lookup tables were created (one per paper). At image generation time,

the substrate is chosen and the proper lookup table used to interpolate the correct surface coverages of the luminescent inks.
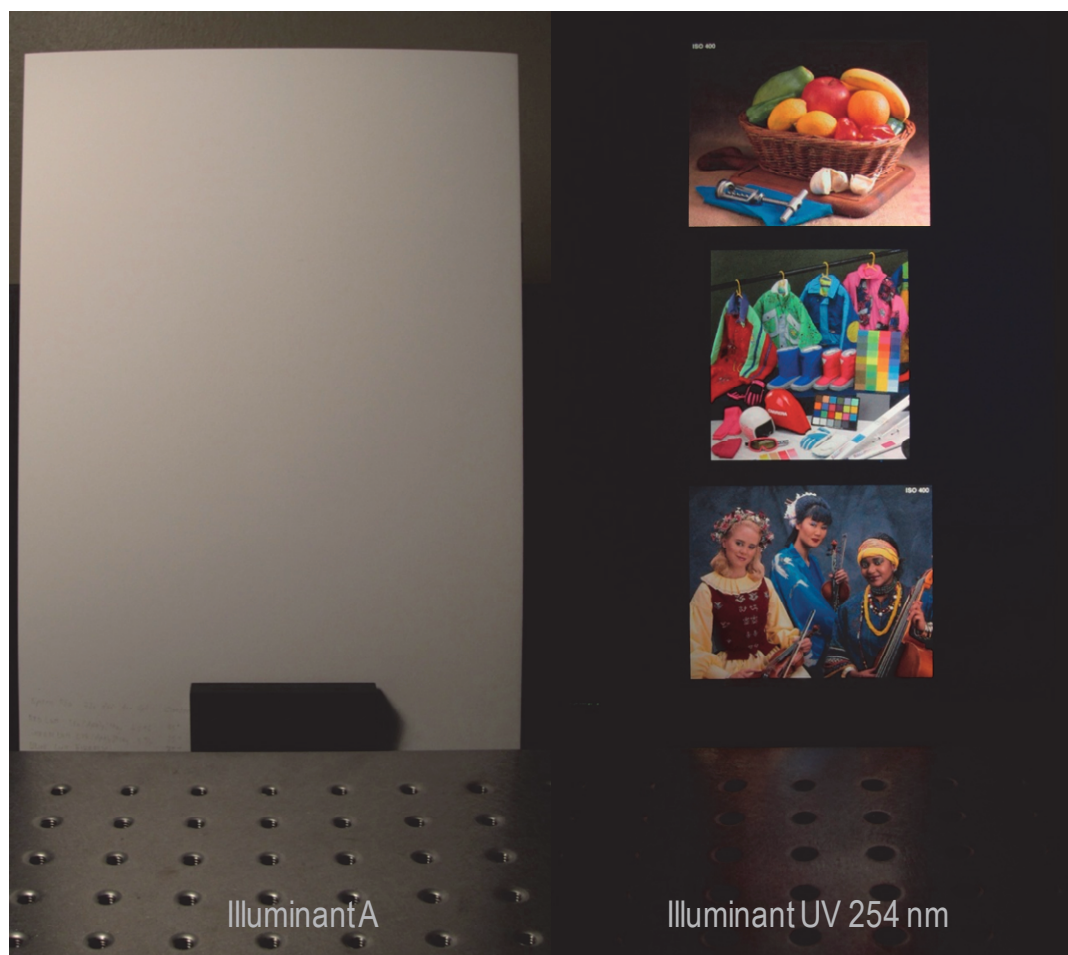
Figure 61. Photographs of a set of standard images reproduced with the luminescent inks on the Canson paper. On the left, a printed paper sheet under an A illuminant: the luminescent image is invisible. On the right, the same printed paper sheet under UV excitation at 254 nm: the luminescent images are visible and accurately reproduced.

Figure 61 displays a picture taken by a camera of three standard images printed with the luminescent inks on the Canson paper. These three images were chosen because they enable a representation of a wide range of natural colors in the fruits, of saturated colors in the ski picture, and of people with skin tones in the orchestra image. Therefore, they provide a good indication of the quality of the color reproduction. Other images have also been reproduced. Photographs of the resulting luminescent images are presented in the appendices (page 237-242).

Compared to previous state of the art luminescent images, produced by the comparable approach of Hersch et al.,[77] the present luminescent image made of lanthanide trisdipicolinate inks looks better, as shown in Figure 62. The visual quality is superior because there is no need for the low frequency screens required by juxtaposed halftoning. As a result of the large gamut of the luminescent inks, the colors are more vivid and match more closely the sRGB colors of the display device. And finally, printing with the luminescent inks is performed on a cheap desktop ink-jet printer instead of an expensive professional offset printer.

Figure 62. Top: photographs of the ski picture reproduced with offset inks on BioTop paper by the method of Hersch et al.[77] (left) and reproduced with the present ink-jet inks on Canson paper by the method developed in this thesis (right). Bottom: corresponding zoomed area of the photographs representing a 24 color samples Macbeth ColorChecker.

6.8 Conclusions

Full color images invisible under normal light but appearing under UV excitation at 254 nm were printed with luminescent inks. The red emitting and green emitting luminescent inks were synthesized by diluting europium and terbium trisdipicolinate in a simple aqueous ink-jet ink base formula. A commercial blue emitting luminescent ink was used to complete a set of luminescent inks that would be suitable for trichromic additive color synthesis.

A simple spectral radiant emittance prediction model for the emission of the luminescent halftones printed on natural papers turned out to be very accurate. The good accuracy can be rationalized by the inertness of the photophysical properties of the lanthanide trisdipicolinate complexes, whose emission intensity is reduced when superposing the luminescent inks by an inner filter effect.

The color gamut of the luminescent inks is wide and saturated. In the high lightnesses, it is even larger than the sRGB gamut of a standard display device. The luminescent printed images obtained with the luminescent inks are therefore pleasant and looks similar to the same image viewed on an sRGB display device, except in the dark tones, which are not as dark. Compared to the images obtained from the patented method using juxtaposed halftones to produce luminescent images with commercial luminescent inks, the images obtained here have a better quality. The halftone screen frequency is higher and the colors seem more accurately reproduced.

The europium and terbium trisdipicolinate inks yet require an excitation light source in the UV-C (i.e. below 300 nm). The light source used here was an uncoated mercury lamp with a UV-bandpass filter resulting in a sharp main emission centered at 254 nm. On the other hand, the commercial blue luminescent inks as well as the offset inks can be excited under a coated UV mercury lamp with a UV-bandpass filter resulting in a broad band centered at 365 nm.

This application represents an important step towards easily implemented attractive document security features that is not achievable without the proper luminescent inks, substate printer and color management software. The luminescent inks could even be used to secure documents by other means than luminescent color images, for example, by using the lifetimes of the lanthanide complexes, and by modulating them through quenching, for example by introducing metal ions (such as copper) that can bind to the ligands and disrupt the coordination sphere of the

lanthanide complexes. This work is a unique example of an application of lanthanide complexes for color reproduction that is mastered from the creation of the luminescent dyes and inks up to the color management. Nevertheless, a few points could still be improved or explored: for example, the synthesis of a blue luminescent ink instead of the utilization of a commercial product.

Coumarins could be interesting to produce a blue luminescent ink. The dp3C1 ligand formed by a coordinating dpa moiety separated from a coumarin fluorophore by a trioxyethylene linker and investigated in the previous chapters was tested as a blue luminescent ink. Unfortunately, the high concentration required to obtain a nice blue luminescent ink with an emission intensity once printed that is comparable to that of the other inks induced precipitation or flocculation issues. Therefore, the dpa-polyoxyethylene-coumarin complexes could not be used direcly as luminescent dyes under the same conditions. In Chapters 3-5, the investigation of the photophysical properties of the complexes were performed at concentrations 500 times lower than the concentration in the ink formula of this chapter. Should a high concentration of complex be incorporated in the ink, a better ink formula would be required for this particular class of compound. As an alternative to a new formulation, the water soluble dp3C1 ligand was printed separately from the metal ion in order to allow such high concentrations. The ligand is indeed water soluble at high concentrations, whereas the complex precipitates or flocculates. This separation procedure resulted in lower print quality. It could yet be an attractive way to form pre-printed substrate with a blue emission, but which forms a red-magenta emitting complex when europium ion is printed on top of it, or green-cyan emitting complex when terbium is printed on top of it. A blue emitting compound could be achieved by printing a non-emissive lanthanide ion such as gadolinium on top of it, or when left as a free ligand.

Alternatively, Dy^{3+} could produce a white emitting complex when printed on top of the dp3C1 pre-printed substrate. This technique could be valuable as a single component white luminescent compound instead of a trichromic white formed by the superposition of red, green and blue luminescent inks. A ligand with a cyan emission and a sensitization of europium emitting in the red could also provide a single component white emitter. As it will be shown in Chapter 8, the luminescence from a white emitting substrate can also be used to reproduce luminescent color images by attenuating the white emission through colored halftones.

Chapter 7

The Ink Spreading enhanced Spectral Absorption Model

A simplified spectral prediction model for the transmittances of color halftones and its application to reflectances

7.1   Introduction

In this chapter, a new spectral prediction model for predicting transmittances of color halftones is developed and tested. Its application to the prediction of reflectances is also investigated. It is an alternative to the spectral prediction models presented in Section 1.6.2, page 43 and an extension of the spectral prediction model for predicting spectral radiant emittances of the previous chapter in view of a combination of luminescence with color halftones as studied in the next chapter.

To begin with, the model is contextualized relative to the simple Neugebauer approach (summation of the surface coverage weighted spectra of the primaries) also used with emittances in the previous chapter, and relative to the Yule-Nielsen modification of the spectral Neugebauer model, which is usually preferred to the spectral Neugebauer prediction model. The physical justification of the proposed model is then assessed. Finally, the model is tested both with transmittances and with reflectances. The accuracy of the new model compared with the IS-YNSN model and its limitations are also highlighted.

7.2   Transmittance in simple spectral prediction models

The transmittance is the ratio of the intensity of light that comes out of a substrate after passing through it relative to the intensity of light that enters inside it. The transmittances of inks are useful in color reproduction because they enable to model complex phenomena such as multiple reflections in a printed substrate, for example in the Clapper-Yule spectral prediction model.[94] Transmittances are also very important to characterize the color of transmissive surfaces (transparent or translucent). Transmissive colors are found for example in transparent plastic sheets[95] and in backlit prints, as it will be shown in the next chapter.

Several spectral prediction models exist to calculate the transmittance of a color halftoned sample printed on a transmissive substrate from a minimal amount of calibration samples. One of the most convenient and simple spectral prediction

models that can predict transmittances is based on the ink spreading enhanced Yule-Nielsen modified spectral Neugebauer model.[76] This model is inspired by the spectral Neugebauer approach[71] applied to transmittances which states that the transmittance of a halftone can be predicted by the sum of the transmittances of the colorants weighted by the surface coverage of each colorant in the considered halftone. The surface coverage of the halftone can also be improved by fitting an effective surface coverage that depends on the superposition condition of the ink (depends on the solid colorant background).[73] The effective surface coverage takes into account the physical dot gain due to ink spreading, and to some extent, the optical dot gain due to lateral propagation of light in the halftone. By fitting effective surface coverages ink spreading enhanced models are obtained.

$$T(\lambda) = \sum_j a_j \cdot T_j(\lambda) \tag{24}$$

Equation 24 predicts the transmittance of a color halftone $T(\lambda)$ according to the Neugebauer approach as a sum of the transmittances $T_j(\lambda)$ of each colorant j in the color halftone weighted by their effective surface coverages a_j. The Neugebauer approach, even with fitted effective surface coverages, is however not accurate in most cases. An additional correction proposed by Yule and Nielsen, consists in introducing an exponent factor which raises the transmittances of the colorants by an exponent $1/n$ and then applies a power n on the weighted sum of the modified transmittances, as shown in Equation 25, where a_j is the effective surface coverage of the colorant j, $T_j(\lambda)$ the transmittance of the colorant j, and n the Yule-Nielsen factor.[72]

$$T(\lambda) = \left[\sum_j a_j \cdot T_j(\lambda)^{1/n} \right]^n \tag{25}$$

In the ink spreading enhanced Yule-Nielsen modified spectral Neugebauer model (IS-YNSN), the n-factor needs to be optimized, because it depends on the printer technology, on the halftoning method and particularly on the halftone screen frequency, on the inks and on the substrate on which they are printed. This optimization is typically performed by calibrating the model for a set of n-factors, testing the model for each n-factor, and then choosing the n-factor which yields the most accurate prediction. This n-factor introduces a certain flexibility into the model which enables its application to reflectances, transmittances and even emission spectra, but its physical significance is not straightforward.

The n-factor is needed to correct the transmittances in order to take into account the lateral propagation of light in the halftone. This lateral propagation of light is due to scattering of light and to multiple reflections between the print-air interface. The result is that a light beam that enters through a defined ink halftone dot (of one of the colorant that composes the halftone) propagates to other colorants in the halftone. As a result, the photons that are collected and measured out of the sample have traveled through several colorants successively before leaving the color halftone.

7.3   From lateral propagation of light towards a new model

Compared to the Neugebauer approach, the lateral scattering of light increases the optical pathlength in the illuminated colorant, and introduces a component that depends on the surrounding colorants. If lateral propagation is important relative to the size of a color ink halftone dot, scattered light might travel through each colorant. Furthermore, if the scattering is randomly distributed across the whole halftone, the average optical pathlength inside each colorant can be assumed to be proportional to its surface coverage, since the probability for photons to travel across a given colorant is equal to the surface coverage of that colorant. In the extreme case, the transmittance of a color halftone would thus be defined independently of the entering point of light inside the color halftone area as the multiplication of the transmittances $T_j(\lambda)$ of each colorant in the halftone, with an average optical pathlength within each colorant that depends on its surface coverage a_j.

$$T(\lambda) = \prod_j T_j(\lambda)^{a_j} \tag{26}$$

The justification of Equation 26 can be related to the Beer-Lambert law of absorption. The absorbance is defined as $A = -\log(T)$, and is proportional to the concentration c of the absorbing compound, the extinction coefficient ε of this absorbing compound, and the optical pathlength ℓ through which the light is absorbed.

$$A(\lambda) = c \cdot \varepsilon(\lambda) \cdot \ell \tag{27}$$

The Beer-Lambert law is valid in non-scattering media. A color halftone printed on paper is however a scattering material. At a microscopic level, it consists in a complex network of paper fibers with colorants absorbed by the fibers, or even possibly filling cavities created by the porosity of the paper bulk. As an approximation, a color halftone can nevertheless be modeled as non-scattering absorbing colorants in a scattering matrix. Therefore, the Beer-Lambert law is valid for the absorption by the colorants, except that the diffusion of light by the matrix changes the optical pathlength. The modified Beer-Lambert law (Equation 28) thus takes into account the total optical pathlength and adds an attenuation factor G that depends on the geometry of the measurement conditions and that accounts for the losses due to the scattereing properties of the medium.[96]

$$A(\lambda) = \mu_a(\lambda) \cdot \ell \cdot \delta + G \tag{28}$$
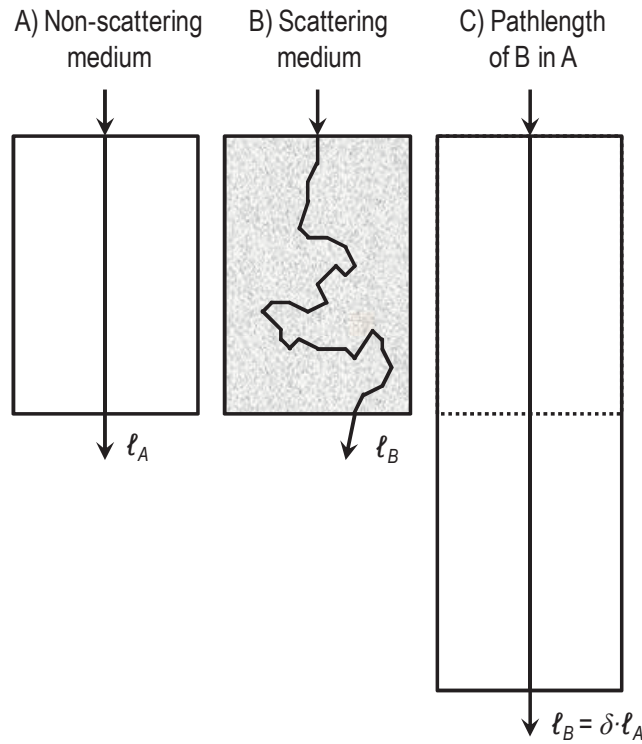
Figure 63. Illustration of the effect of scattering on the pathlength of light in an absorbing medium

If both the illumination light source and transmitted light source are homogeneously diffused, if the measurement conditions are kept constant, and if a reference spectrum that encloses the losses due to the scattering of the medium in

the absence of any colorant is subtracted from the measurements, one may neglect the geometry factor *G*. The absorbance might therefore be defined only as a modified optical pathlength version of the Beer-Lambert law (as illustrated in Figure 63). For prints, the modified Beer-Lambert law then applies to the absorbance of the halftones only ($A_{HT} = A_{tot} - A_{paper}$), where the contribution from the paper (A_{paper}) was subtracted from the total absorbance (A_{tot}). This is expressed in transmittance mode by dividing the total transmittance (of the paper and halftone) by the transmittance of the paper ($T_{HT} = T_{tot} / T_{paper}$).

In Equation 28, the concentration of the absorbing compound in a colorant is assumed to be constant, the product of the concentration with the extinction coefficient can be defined by an absorption coefficient $\mu_a(\lambda) = \varepsilon(\lambda) \cdot c$.

The modification factor δ of the optical pathlength should depend on the scattering properties of the medium, strongly scattering media inducing a much larger pathlength, i.e., a large δ. For a defined medium, δ should however be constant. In a color halftone, under the assumption that the colorants are not participating in the scattering properties of the medium, the total optical pathlength ($\ell_{tot} = \ell \cdot \delta$) should therefore be the same for all the color halftones.

In a color halftone, the total optical pathlength can be split as a sum of optical pathlengths in each colorant. If this pathlength is long enough so that it propagates over all the colorants in a halftone screen element, and if the volume sampled by the optical pathlength is larger or equal to the volume of a halftone screen element, which is reasonable in a highly scattering medium with small halftone screen elements, the probability that the pathlength is located in a defined colorant is proportional to the volume of the colorant in the halftone screen element divided by the volume of a halftone screen element. Since this ratio is equal to the surface coverage of the colorant, the probability that the optical pathlength crosses a colorant is given by its surface coverage. Therefore, the average optical pathlength inside a colorant is the total optical pathlength multiplied by the probability to be in this colorant, i.e., the total optical pathlength multiplied by the surface coverage.

$$A(\lambda) = \sum_j \mu_{a,j}(\lambda) \cdot \ell_j = \sum_j \mu_{a,j}(\lambda) \cdot \ell_{tot} \cdot a_j \qquad (29)$$

The absorbance of a colorant $A_j(\lambda)$ is defined as $\mu_{a,j}(\lambda) \cdot \ell_{tot}$, and therefore, Equation 29 yields Equation 30, which is the expression of Equation 26 in the absorbance space.

$$A(\lambda) = \sum_j a_j \cdot A_j(\lambda) \qquad (30)$$

The spectral prediction model that uses either Equation 26 or 30 for predicting the transmittance of color halftone samples is called hereafter ink spreading enhanced spectral absorption model (ISA model). The surface coverages a_j of the colorants are found from the effective surface coverages of the inks similar to an IS-YNSN model by relying on the ink spreading equations and on the Demichel equations for independently laid out halftones.

7.4   From transmittances to reflectances

The reflectance is defined as the ratio of the light intensity coming out of a surface divided by the light intensity that falls on that same surface. In prints, the reflectance is due to the specular reflection of light on the surface, to multiple internal reflections between the paper bulk and the print-air interface, and by the absorption of light by the inks located close to the surface. In a simple approach, the reflectance can be modeled as a back and forth traveling of light in a material. For a color halftone printed on a reflective substrate such as paper, the reflectance can then be assumed to be due to a transmittance of light through the color halftone $T(\lambda)$, its backward reflection by the paper bulk $R_{sub}(\lambda)$, and the same transmittance $T(\lambda)$ again through the color halftone back to the surface (Equation 31).

$$R(\lambda) = T(\lambda)^2 \cdot R_{sub}(\lambda) \qquad (31)$$

An ink spreading enhanced spectral absorption model in reflectance (ISA-R) can therefore be developed by predicting the transmittances with the ISA model and by using the reflectance of the bare paper as $R_{sub}(\lambda)$ (Equation 32).

$$R(\lambda) = \prod_j T_j(\lambda)^{2 \cdot a_j} \cdot R_{sub}(\lambda) \qquad (32)$$

The transmittances of the colorants are calculated from the reflectances of the fulltones by dividing them with the reflectance of the bare paper $R_{sub}(\lambda)$, and by taking the square root, as shown in Equation 33.

$$T_j(\lambda) = \sqrt{\frac{R_j(\lambda)}{R_{sub}(\lambda)}} \qquad (33)$$

7.5   Calibration and test of the ISA model in transmittance mode

The ink spreading spectral absorption model (ISA model) for transmittances was tested by using three different substrates. A natural low density (80 g/m^2) paper Bio Top 3, a translucent tracing paper, and a transparent plastic sheet. Their transmittances are shown in Figure 64.
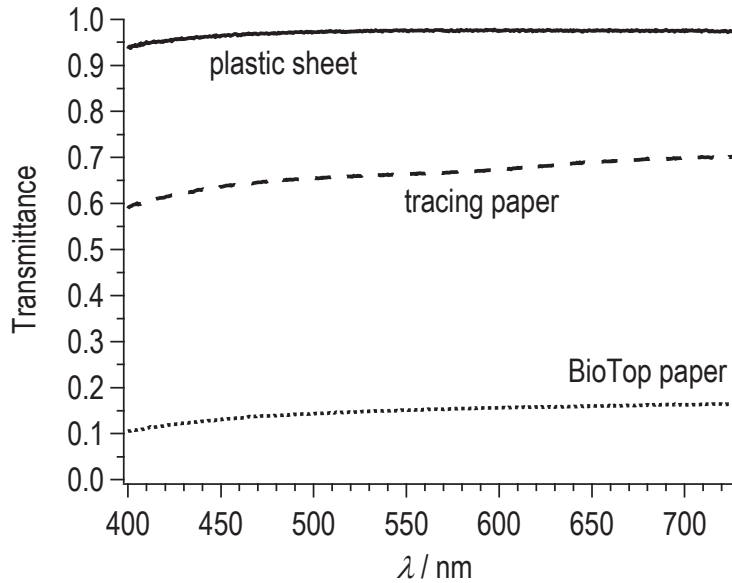
Figure 64. Transmittance of the substrates for the transparent plastic sheet, tracing paper and Bio Top paper

The transmittances are measured on an optical table with a Maya2000 Pro back-thinned CCD spectrophotometer from Ocean Optics. The light source was a 75W Xenon light source filtered through a longpass filter with a cutoff wavelength at 400 nm and a shortpass filter with a cutoff wavelength at 800 nm. This light source was diffused on an opal glass placed in front of a 1 cm diameter illumination window. A 600 μm optical fiber was used to collect the transmitted light. The viewing cone of the fiber was checked to be centered on the sample illumination window when the sample is placed in between the light source and the optical fiber (back

illumination). The dark response of the detector was subtracted from each spectrum and was recorded each five measurements in order to take into account the heating of the CCD once illuminated. The reference spectrum for measuring the transmittance spectra was the filtered Xe light source diffused through the opal glass. It was also recorded each five measurements in order to take into account the variations of the intensity of the light source that might occur.

The 125 color samples, representing the 0 %, 25 %, 50 %, 75 % and 100 % surface coverages variations of three inks (cyan, magenta and yellow), were printed with a Canon Pro9500 ink-jet printer on the Bio Top paper and on a tracing paper, and with a Xerox Phaser 6360DN PS electrophotographic printer on the transparent plastic sheet. The halftone was round shaped with a frequency of 100 lpi and screen angles of 75°, 45° and 15° for the cyan, magenta and yellow inks respectively. The same halftone was used on both printers with the same resolution of 600 dpi.
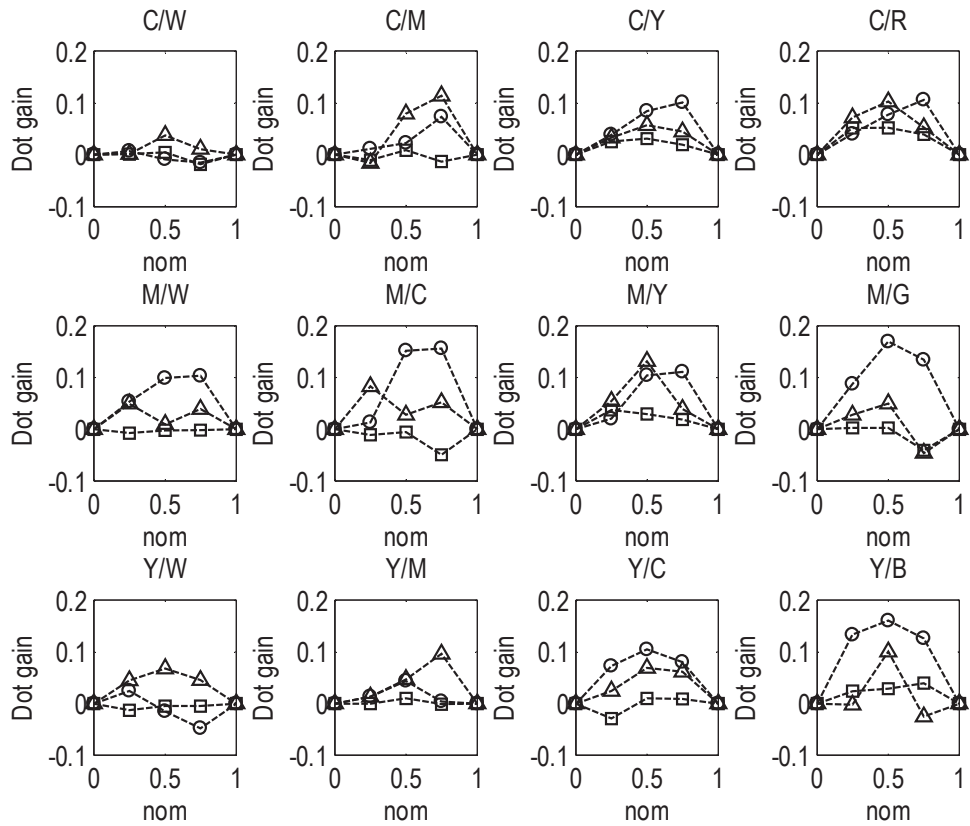
Figure 65. Dot gain curves for the twelve superposition conditions of C, M, and Y inks printed on the transparent plastic sheets with the electrophotographic printer (circles), on the tracing paper (squares) and on the Bio Top paper (triangles) with the ink-jet printer

The model was calibrated by finding the effective surface coverages of the 25 %, 50 % and 75 % nominal surface coverage of cyan, magenta and yellow on all possible solid colorants, which minimize the root mean square differences between the measured and corresponding predicted spectra. The twelve superposition conditions of three inks yield twelve ink spreading curves. The resultant dot gain curves obtained by subtracting the nominal surface coverages from the effective surface coverages are shown in Figure 65.

The model was then tested on the 125 color samples and its accuracy estimated by the ΔE_{94} color difference between the predicted CIELAB colors and the corresponding measured CIELAB colors. The results are presented in Table 14, together with the accuracy of the ink spreading enhanced Yule-Nielsen modified spectral Neugebauer (IS-YNSN) model and ink spreading enhanced spectral Neugebauer (IS-SN) model (n-factor = 1) on the same set of color patches.

Table 14. Accuracy of the model in transmission mode compared to the IS-YNSN model tested on the 125 patches ($\Delta E_{94} \pm 0.1$)

		New model			IS-YNSN model			
		ΔE_{94}			ΔE_{94}			n-fac
		avg	max	$Q_{95\%}$	avg	max	$Q_{95\%}$	
Ink-jet	BioTop paper	1.0	2.4	1.9	0.9	2.4	2.0	-3.8
					1.4	3.3	2.9	1.0
	Tracing paper	0.6	1.3	1.1	0.6	1.2	1.1	-13.0
					0.8	2.4	1.9	1.0
Laser	Plastic sheet	1.5	3.9	3.1	1.4	4.0	3.0	2.8
					1.7	4.5	3.4	1.0

The accuracy of the ink spreading enhanced absorption model (ISA model, or new model in Table 14) is very similar to the accuracy of the IS-YNSN model. The results are identical within experimental error (rounding at ± 0.1). However, the new model has the major advantage to rely only on the ink-spreading calibration,

and not on an additional optimization to find the best n-factor. It is then more efficient, because less demanding. The results are also better than the IS-SN (IS-YNSN, n-fac = 1.0), which is not too bad though.

As usually observed, the ISA model is less efficient with electrophotographic printings (laser). This may come from the difficulty to get precise halftone elements in electrophotography. The results are yet quite good, with an average ΔE_{94} of 1.5. By comparison, the accuracy on the Bio Top paper is 1.0 and on the tracing paper 0.6, which is the most accurate result in our test.

7.6   Calibration and test of the ISA model in reflectance mode

The model was tested for reflectances by using three different substrates. The natural low density (80 g/m^2) paper Bio Top 3 (bp) and the translucent tracing paper (tp), both already used for the test with transmittances, and a Matte Photo paper from Canon (MP-101). Their reflectances are shown in Figure 66.
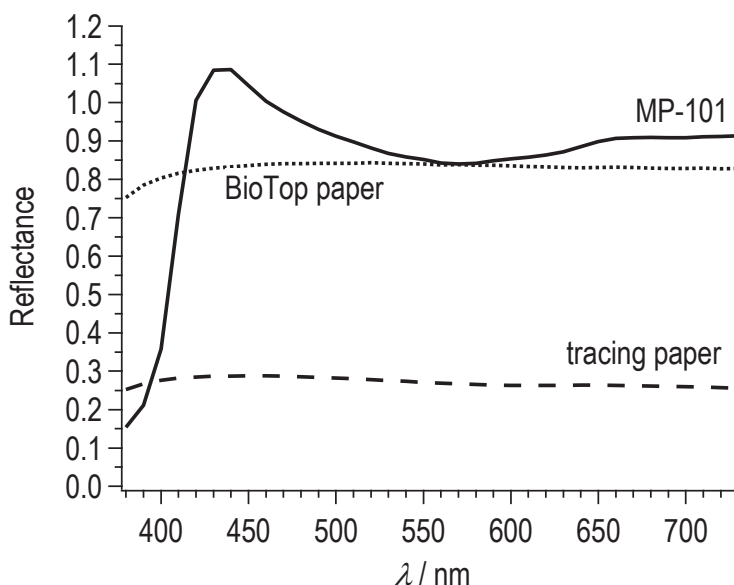
Figure 66. Reflectance of the substrates for the Matte Photo paper from Canon (MP-101), Bio Top paper and tracing paper

The reflectances were measured with an Eye-one spectrophotometer from GretagMacbeth. All reflectances were measured with a black background sheet below the sample. The 125 color patches, representing the 0 %, 25 %, 50 %, 75 % and 100 % surface coverages variations of three inks (cyan, magenta and yellow), were printed with a Canon Pro9500 ink-jet printer on the Matte Photo paper from Canon (MP-101), on the Bio Top paper and on the tracing paper, and also with a Xerox Phaser 6360DN PS electrophotographic printer on the MP-101 paper. The MP-101 paper contains fluorescent optical brightening agents, which increase its reflectance in the blue region above 1.0 due to fluorescence. Tested halftones are those used for the transmittance tests. In addition to the 100 lpi halftone screen frequency, halftones at screen frequency of 50 lpi and 120 lpi were also tested on the MP-101 paper.
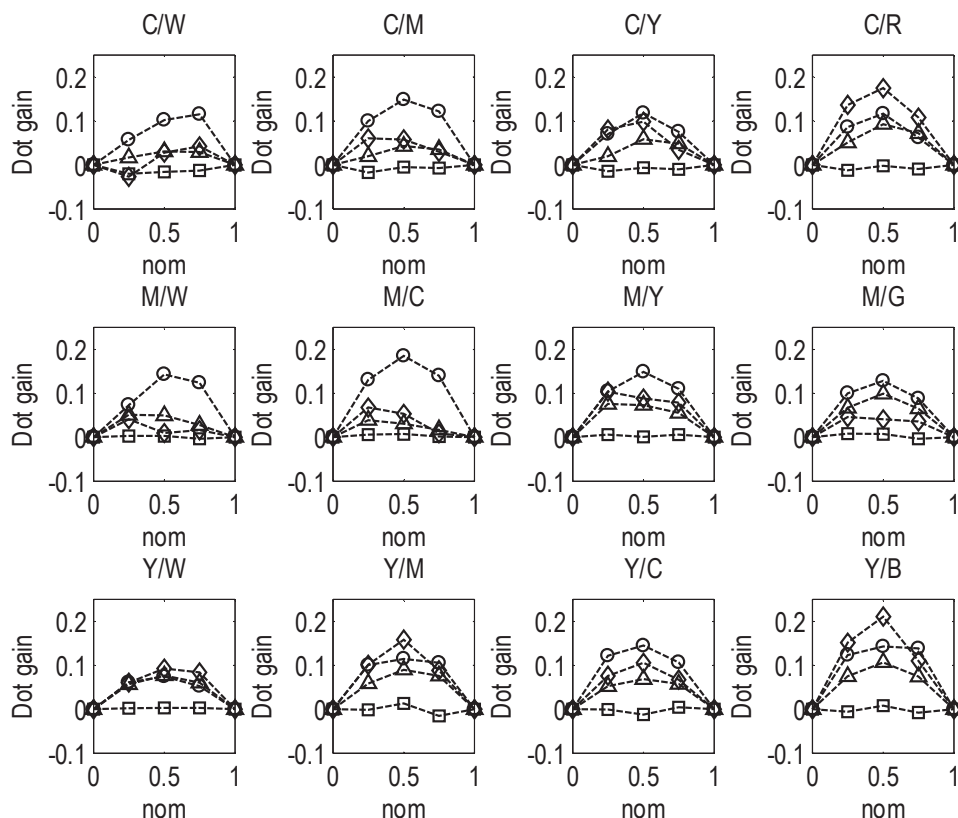
Figure 67. Dot gain curves for the twelve superposition conditions of C, M, and Y inks printed on the Canon MP-101 Matte photo paper printed with the electrophotographic printer (circles), on the Canon MP-101 Matte photo paper printed with the ink-jet printer (squares), on the Bio Top paper (triangles) and on the tracing paper printed with the ink-jet printer (diamonds)

175

The model was calibrated by calculating the transmittances of the fulltones $T_j(\lambda)$ from their measured reflectances $R_j(\lambda)$ and the reflectance of the substrate $R_{sub}(\lambda)$ according to Equation 33, and by fitting the effective surface coverage (a_j in Equation 32) as exponents of the transmittances $T_j(\lambda)$. The dot gain curves obtained by subtracting the nominal surface coverages from the effective surface coverages are shown in Figure 67. The IS-SN is here not equal to the IS-YNSN model with n-fac = 1. The IS-YNSN model uses here directly reflectances, without the calculation of transmittances according to Equation 33, whereas the IS-SN model was adapted to express the reflectances of the colorants according to the back and forth model of Equation 31.
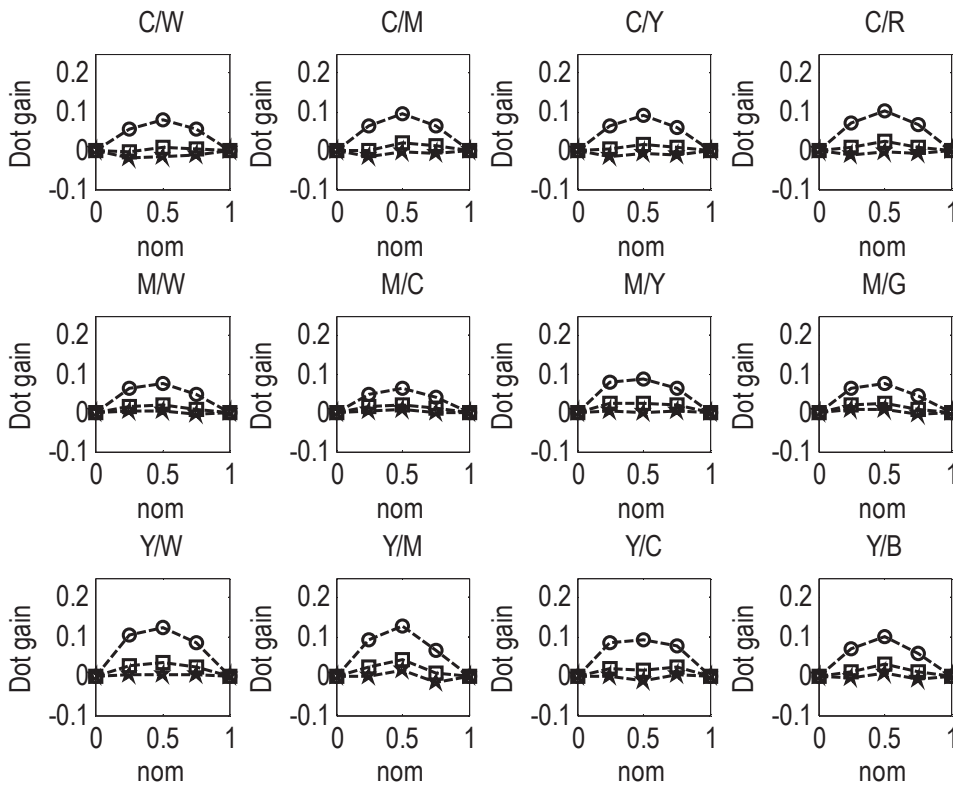
Figure 68. Dot gain curves for the twelve superposition conditions of C, M, and Y inks printed on the Canon MP-101 Matte photo paper printed with the ink-jet printer obtained from the back and forth IS-SN model (circle), IS-YNSN model (square) and ISA-R model (star)

As with transmittances, the dot gain is more pronounced with the electrophotographic printer. The MP-101 on the other hand exhibits nearly no dot gain, whereas the Bio Top paper and the tracing paper have moderate to high dot gains. This probably comes from the poorer quality of these papers compared to the

MP-101 paper. Concerning the different dot gains depending on the prediction model, the back and forth IS-SN approach yields the highest dot gains. The IS-YNSN model has usually less dot gain and the ISA-R model slightly less dot gain than the IS-YNSN model, as shown in Figure 68.

Table 15. Accuracy of the model for reflectances compared to the IS-YNSN model and to the transmittance based IS-SN model for reflectances tested on the 125 patches ($\Delta E_{94} \pm 0.1$). BP: BioTop paper, TP: tracing paper, MP: Canon MP-101 paper

		New model ΔE_{94}			IS-YNSN model ΔE_{94}			n-fac	IS-SN approach ΔE_{94}		
		avg	max	Q$_{95\%}$	avg	max	Q$_{95\%}$		avg	max	Q$_{95\%}$
Ink-jet	BP 100 lpi	0.4	1.4	1.0	0.4	1.0	0.8	-4.2	0.9	2.8	1.8
	TP 100 lpi	1.0	2.6	2.1	0.9	2.5	2.0	-2.0	1.2	2.9	2.3
	MP 100 lpi	0.4	1.1	0.8	0.4	1.2	0.7	8.2	0.6	1.9	1.4
	MP 50 lpi	0.7	1.9	1.4	0.3	1.0	0.5	2.2	0.3	1.2	0.8
	MP 120 lpi	0.2	0.9	0.5	0.3	1.0	0.5	14.0	0.7	1.9	1.5
Laser	MP 100 lpi	1.3	3.8	2.9	1.2	3.8	2.9	4.6	1.4	4.0	3.3

The results (prediction accuracy) found in Table 15 are here consistent with the ones in transmission mode. The ISA-R model is most of the time as accurate as the IS-YNSN model and performs better on ink-jet printed color halftones. Noteworthy, the reflectances are better predicted on the Bio Top paper compared to the tracing paper, whereas for transmittances, it is the opposite. This may be explained by the diffusing nature of the Bio Top paper which is better suited in reflection mode, while the translucent tracing paper is more suitable in transmission mode. The only

case where the ISA-R model is not as good as the IS-YNSN model is, as expected, in the case of a low halftone frequency (here 50 lpi). In this case, the prediction of the transmittance of the halftones using a back and forth transmittance IS-SN model yielded better results, similar to the IS-YNSN model. The exact opposite happens when the frequency is increased up to 120 lpi. At this high frequency, the back and forth IS-SN approach to calculate the transmittance of the halftones is poorer than the new model. This behavior is expected because, at low frequency, the assumption that light travels through the whole halftone, and therefore, that the optical pathlength in each colorant is proportional to their surface coverage is less and less correct. Indeed, the halftone elements become larger and each colorant well separated from its neighbors, as illustrated in Figure 69.
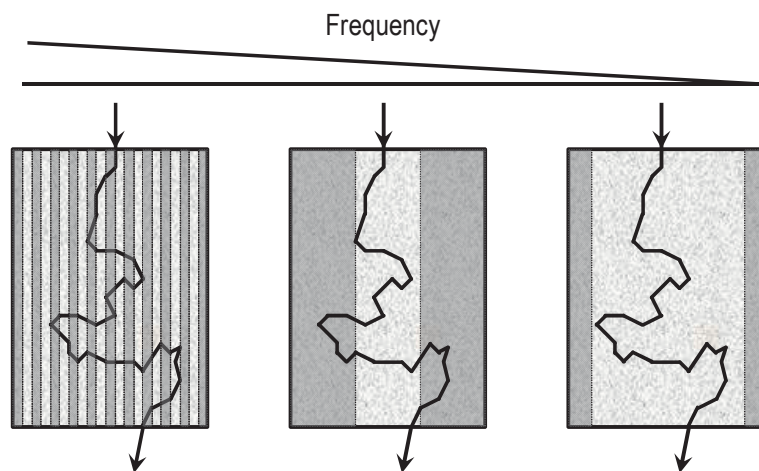
Figure 69. Illustration of the effect of the lowering of the halftone screen frequency on the distribution of the optical pathlength of light in each colorant

7.7   Conclusions

A new spectral prediction model was investigated. This model is based on the assumption that lateral propagation of light in a halftone results in an increased optical pathlength that goes through every colorant in the halftone. The optical pathlength in each of the colorants is assumed to be proportional to the effective surface coverage of this colorant in the halftone. The surface coverages of a halftone are then associated to the transmittances of the fulltones by introducing

them as a power of the transmittance. In absorbance, it corresponds to the sum of the absorbances of the colorants wighted by their surface coverages. This yields a model similar to the ink-spreading enhanced spectral Neugebauer, but with absorptions. The model is therefore called ink-spreading enhanced spectral absorption model (ISA model).

This concept was then further extended to the prediction of reflectances by separating the absorbing halftone layer from the reflective substrate layer. Hence, the reflectance of a halftone is defined as the square of the transmittance of the halftone layer, corresponding to the back and forth crossing of the halftone layer multiplied by the reflectance of the substrate.

A comparison with the ink spreading enhanced Yule-Nielsen modified spectral Neugebauer model (IS-YNSN model) showed that the ISA model is consistently as good as the IS-YNSN model at moderate to high halftone frequencies. The model is however simpler than the IS-YNSN model because there is no n-factor to optimize. The calibration is actually similar to the IS-YNSN model, except that no optimization of the n-factor is required.

The model performs well for transmittances on a variety of substrates such as transparent plastic sheets, translucent tracing paper and low density paper and equally well for reflectances on substrates such as matte photo paper with fluorescent optical brightening agents (OBA), low density paper and tracing paper with no fluorescent OBA. The model is also as good as the IS-YNSN model with electrophotographic printers, while the accuracy is better in both models with an ink-jet printer. It is however limited to moderate and high frequency halftone screens. It was demonstrated that at low frequency (50 lpi), an ink spreading enhanced spectral Neugebauer approach combined with the back and forth method to calculate the transmittance of the halftone is more accurate, and therefore better suited.

This approach may also be undertaken with a cellular spectral prediction model such as the ink spreading cellular Yule-Nielsen modified spectral Neugebauer model (IS-CYNSN). The accuracy is expected to be better with a cellular model because most of the high ΔE_{94} values between the measured and the predicted color are for color halftones close to the 50 % grey (surface coverage of 50 % for each ink). Furthermore, the model could be extended to colorants formed by more than three inks, and particularly, to the classical CMYK set of inks.

In the next chapter, transmittances of color halftones are needed. The ink spreading enhanced spectral absorption model will therefore be used instead of the ink spreading enhanced Yule-Nielsen modified spectral Neugebauer model.

Chapter 8

Color reproduction with luminescent backlit colors

An anti-counterfeiting technique for document security

8.1   Introduction

8.1.1   Motivations

In this chapter, new security features combining halftoned luminescent colors with halftoned non-luminescent ones are presented. The primary motivation for this combination is to be able to have a color image, which has one appearance under visible normal light (e.g. daylight), and the same appearance or a different predictable appearance in the dark under UV excitation. Two types of inks are therefore involved: one set of classical inks forming color halftoned images visible under normal light, and a set of invisible inks enabling the visualization under UV light. The superposition of classical and luminescent inks is not promising because the UV excitation would be partially filtered and because quenching may occur due to the superposed classical inks. Therefore, a separation between the luminescent and non-luminescent inks is required. Instead of a juxtaposed approach, where classical and luminescent inks are laid out side by side, a recto-verso separation is considered.

Under UV excitation, the luminescent image is transmission through the substrate and through the non-luminescent color halftone image. The resulting color image is formed by backlighting of the non-luminescent color halftone image by the luminescent image. It will be called "luminescent backlit color image".

Recto-verso imaging is interesting for document security because it involves front-back registration issues. See-through devices, which are composed by front and back images forming a new image when viewed by transmission of a normal light source through the device are present on some security documents, for example the Swiss passports and banknotes. In the present contribution, a recto-verso imaging technique is developed by relying on luminescent emissions through non-luminescent colors.

8.1.2   Challenges

In order to control the appearance of the color image under both illuminations (normal light and UV light), a correspondence between the surface coverage of the luminescent and non-luminescent inks and the resulting color under each illumination mode is required. Spectral color prediction models exist for predicting

transmittances, reflectances or even emittances as already seen in the previous chapters, but the combination of emittances printed on one side of a transmissive substrate with transmittances of color halftones printed on the other side of the same substrate was never addressed.

The reproduction of luminescent backlit color images requires, in addition to a spectral prediction model, to adapt a color reproduction framework to the special case of the luminescent backlighting. The adaptation starts with the correction of the emission spectra to account for the sensitivity of the spectrophotometer and to convert to relative radiometric units. The combination of the corrected relative spectral emittances with transmittances can then be undertaken. When calculating luminescent backlit colors, the correct white reference has to be defined. The resulting luminescent backlit colors can finally be used to compute gamuts, complete gamut mapping and build lookup tables according to the luminescent backlighting model.

This color reproduction technique relies mostly on the accuracy of the luminescent backlighting prediction model. The model was first tested by using as a luminescent backlight a single white luminescent layer printed on the verso side with red emitting, yellow-green emitting and blue emitting luminescent inks. This backlight is attenuated by color halftones generated from cyan, magenta and yellow inks printed on the recto side of a transmissive substrate. The emission of the luminescent layer transmitted through the substrate and color halftones is modeled in a first approach as a simple multiplicative filtering process. For a known luminescent layer emission, the luminescent backlit colors are then simply predicted by predicting the transmittance of the color halftones.

8.2   Backlighting prediction model

8.2.1   Definition of the model

A simple approach to model backlit images is to multiply the backlight emittance with the transmittance of the backlit layer. Here, the backlight source is a luminescent layer printed on the verso side of a transmissive substrate. The backlit layer is therefore the transmissive substrate printed with colored halftones. The global transmittance of the backlit layer is hence the multiplication of the

transmittance of the substrate $T_{sub}(\lambda)$ with the intrinsic transmittance of the color halftone $T_{HTcolor}(\lambda)$. The emittance $E(\lambda)$ resulting from the luminescent backlit color halftone is then the multiplication of the backlight emittance $E_{bl}(\lambda)$ with this global transmittance, as formulated in Equation 34 and illustrated in Figure 70.

$$E(\lambda) = E_{bl}(\lambda) \cdot T_{sub}(\lambda) \cdot T_{HTcolor}(\lambda) \tag{34}$$
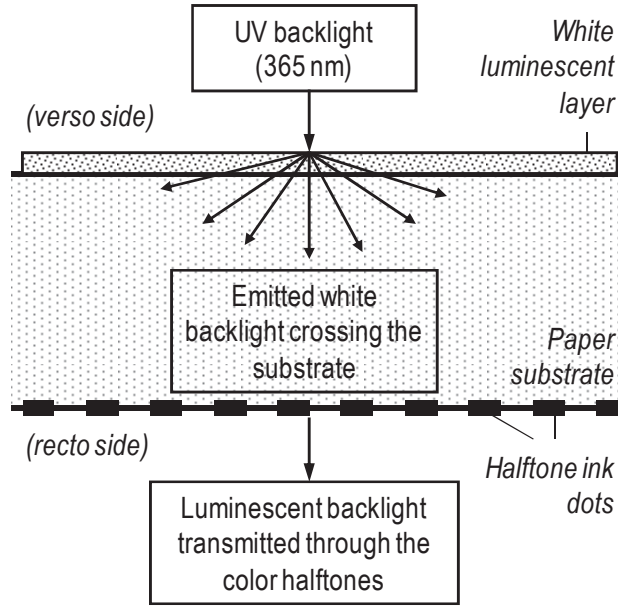
Figure 70. Luminescent backlit colors produced by UV excitation of a white luminescent layer, the attenuation of the white luminescent backlight through the transmissive substrate and its transmission through a colored halftone.

With a known substrate and luminescent backlight, only the transmittances of the color halftones are required to determine the luminescent backlit emittance. In this configuration, the only variable is the color halftone, which is formed by the cyan, magenta and yellow inks. By predicting the transmittances of the color halftones with a spectral prediction model, any luminescent backlit image should then be predictable.

The spectral prediction model developed during this thesis was used. The ink spreading enhanced spectral absorption model (ISA model) enables predicting transmittances of color halftones by summing the absorbances ($A_j = -\log T_j$) of the eight colorants each weighted by their respective surface coverages. This model expressed in terms of transmittances becomes multiplicative and the surface coverages weight the transmittances of the colorants as exponents (Equation 35).

$$T_{HTcolor}(\lambda) = \prod_j T_j(\lambda)^{a_j} \qquad (35)$$

Therefore, the prediction of the luminescent backlit emittances can becomes Equation 36.

$$E(\lambda) = E_{bl}(\lambda) \cdot T_{sub}(\lambda) \cdot \prod_j T_j(\lambda)^{a_j} \qquad (36)$$

8.2.1   Luminescent backlight source

The backlight source is formed by a white luminescent layer printed on the verso side of the transmissive substrate. The white luminescent layer was printed in offset by superimposition of solid red, green-yellow, and blue emissive luminescent invisible inks (SICPA 360030F invisible red fluorescent ink, 360011F invisible yellow fluorescent ink, 360004F invisible blue fluorescent ink). The luminescent inks are excited under UV light at 365 nm. One may select different combinations of ink amounts in order to create the emissive white. A single uniform white emissive layer with a maximal emission intensity and a good white appearance was selected here.

The emittance of the luminescent layer was measured using the same apparatus as the transmittances of the previous chapter (in Section 7.5, page 171). The light source was replaced with a 9W mercury lamp (with a broad peak at 365 nm), and with a 365 nm bandpass filter (Schott UV11 filter). Because the luminescent layer emits diffusely, there is no need for an opal glass diffuser in front of the illuminated sample. The excitation light source was facing the luminescent layer located on the verso side of the unprinted substrate and the resulting emission was recorded with the Maya 2000 Pro spectrophotometer on the recto side of the unprinted substrate. The captured emission spectra were corrected to account for the wavelength non-linearity of the detector and to yield relative radiometric units. The correction was performed using a calibrated DHL-2000-BAL lamp from Ocean Optics.

The emittances shown in Figure 71 represent the luminescent backlight attenuated by the unprinted transmissive substrate. They correspond to the product $E_{bl}(\lambda) \cdot T_{sub}(\lambda)$ of Equation 34 or 36 and are the white luminescent backlit colorants of the substrates.
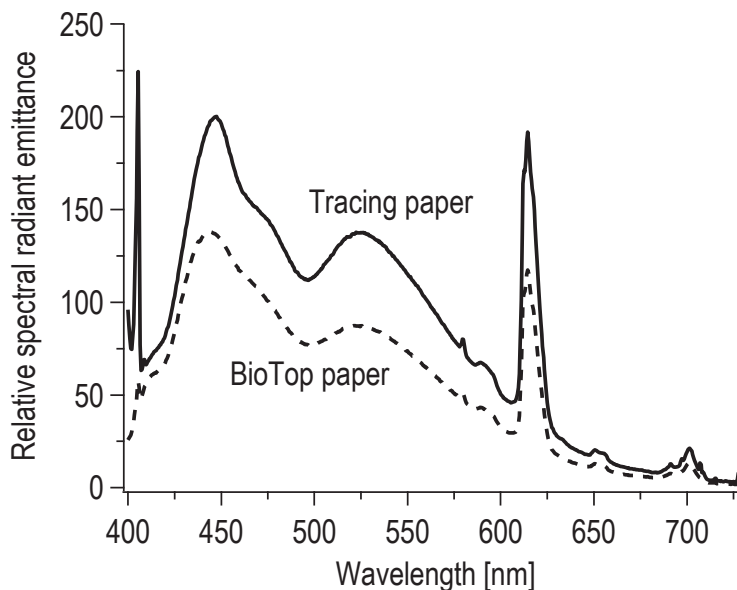
Figure 71. Relative spectral radiant emittances of the luminescent layers measured through the Bio Top paper and through the tracing paper. The intensity ratio between the two emittances is conserved.

The emission of the luminescent backlight measured through the tracing paper yields a CIE-xyY of (0.26; 0.29; 100) and through the biotop paper a CIE-xyY value of (0.25; 0.28; 66). The chromaticities of the luminescent backlight through both substrates are therefore similar. They indicate a bluish white. However, the luminance through the biotop paper is ⅔ of the luminance through the tracing paper.

8.2.2 Test of the model with transmittances measured from an external light source without any luminescent ink printed on the verso side

In a first step, the transmittances predicted by the ink spreading enhanced spectral absorption model (ISA model, Section 7.5, page 171) when no luminescent layer is printed on the verso side of the transmissive substrate were used to test the backlighting model. The purpose was to calibrate the transmittances for a given substrate and then use them for any luminescent backlight. A low density natural paper (Bio Top) and a translucent tracing paper, both without optical brightening agents, were used as transmissive substrates. The dot gains and the prediction accuracies of the ISA model for transmittances printed on these two substrates are presented in the previous chapter.

The backlighting model was tested by measuring the emittance of the eight luminescent backlit colorants together with the 27 variations of 25 %, 50 % and 75 % surface coverages of cyan, magenta and yellow classical inks, and comparing the measurements with the corresponding predicted spectra. The predicted luminescent backlit emittances are obtained by predicting the transmittances corresponding to these 35 color samples, measuring the luminescent backlight emittance (luminescent backlight source presented in 8.2.1) and applying the backlighting model.

The accuracy of the prediction was obtained by expressing the differences between the measured and the predicted emittances as ΔE_{94} color differences. As seen in Table 16, the accuracy is insufficient, with average of 3.9 and 8.1 for the Bio Top paper and tracing paper as transmissive substrates respectively.

Table 16. Accuracy of the luminescent backlit model on 27 test patches, with separately measured ink transmittances

	$\overline{\Delta E_{94}}$	$\max(\Delta E_{94})$	$Q_{95\%}(\Delta E_{94})$
Bio Top paper	3.9	6.4	5.4
Tracing paper	8.1	12.3	10.9

The model given by Equation 36 is not accurate enough when using the transmittance model (Equation 35) that relies on separately measured colorant intrinsic transmittances. Actually, all the predicted luminescent backlit spectra are too high compared with the measurements. The prediction inaccuracy therefore seems to be related to the characterization of the intrinsic transmittances of the color halftones.

There are two important factors that may influence the characterization of the transmittances of the color halftones. The first one comes from the measurement conditions that are not exactly the same when the transmittance is measured with an external diffused light source or when the light source is partly at the surface and partly inside the substrate as is the case when the backlight is the luminescent layer printed on the verso side of the substrate. The other factor comes from the fact that printing a color halftone on a porous substrate such as a paper might be altered by the presence of the luminescent offset printed layer on the verso side. The inks

might for example not spread in the same way inside the substrate if an offset layer is printed on the verso side of the paper. This assumption is verified by the fact that the transmittances (measured with an external visible light source) of recto printed solid inks are different if printed on bare paper or on paper bearing on its verso side an invisible white luminescent layer printed in offset.

8.2.3   Recalibration of the transmittance prediction model by relying on the luminescent backlit emittances

To account for these discrepancies, the transmittances of the colorants were recalibrated by dividing their luminescent backlit emittances with the emittance of the luminescent backlit substrate. The new transmittances of the colorants were then used in the ISA model with the same ink spreading curves as those obtained prior to the recalibration of the transmittances of the colorants. Figure 72 gives an example of the differences between the original color halftone transmittances obtained by relying on an external visible light source with a paper without the printed luminescent layer on the verso side, and the new transmittances obtained by relying on the luminescent backlight from the luminescent layer on the verso side of the substrate.
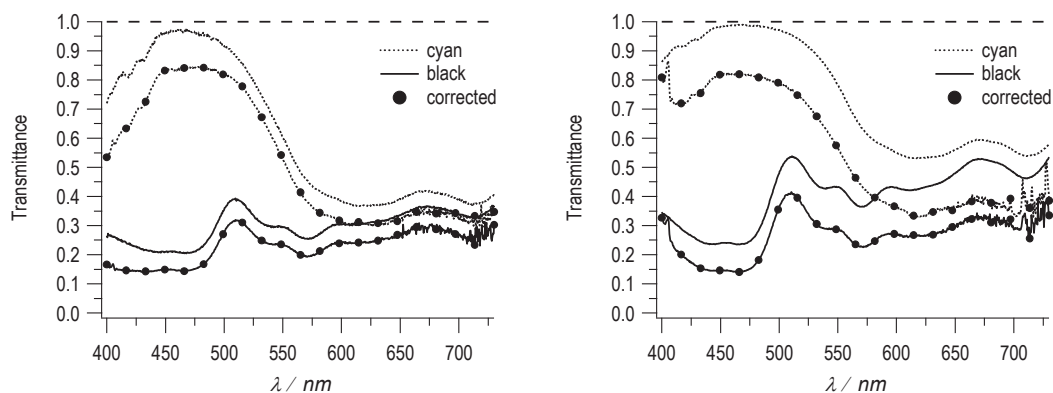
Figure 72. Example of the originally measured and recalibrated transmittances of the colorants for the Bio Top paper (left) and for the tracing paper (right)

Table 17. Accuracy of the luminescent backlit model on 27 test patches using the recalibrated transmittance model

	$\overline{\Delta E_{94}}$	$\max(\Delta E_{94})$	$Q_{95\%}(\Delta E_{94})$
Bio Top paper	1.8	4.9	4.2
Tracing paper	1.4	2.6	2.5

With the recalibrated transmittances, the model is now accurate on both papers (see Table 17). The recalibration of the ink spreading curves is therefore unnecessary. The prediction accuracy on the tracing paper was especially strongly improved thanks to the recalibrated transmittances of the colorants.

The luminescent backlit model enables an accurate prediction of the luminescent backlit emission spectra, and hence of the luminescent backlit colors. It is therefore suitable for color reproduction. First, the gamut of the luminescent backlit colors is computed and compared with the input gamut of an sRGB display.

8.3   Luminescent backlit color gamut

The luminescent backlit model was used to calculate all the possible luminescent backlit colors that can be generated by variations of the cyan, magenta and yellow ink surface coverages. The boundary of the gamut volume was obtained from the set of CIELAB points by applying a Delaunay triangulation and then the ball-pivoting algorithm, as described in the first chapter. The two gamuts generated for the two luminescent backlit color halftoned substrates, G_{bp} for the Bio Top paper and G_{tp} for the tracing paper, are then compared to the $sRGB$ gamut, G_{sRGB} (see Figure 73). This enables determining the colors available for the luminescent backlit color images relative to the colors displayed on a standard $sRGB$ display device.
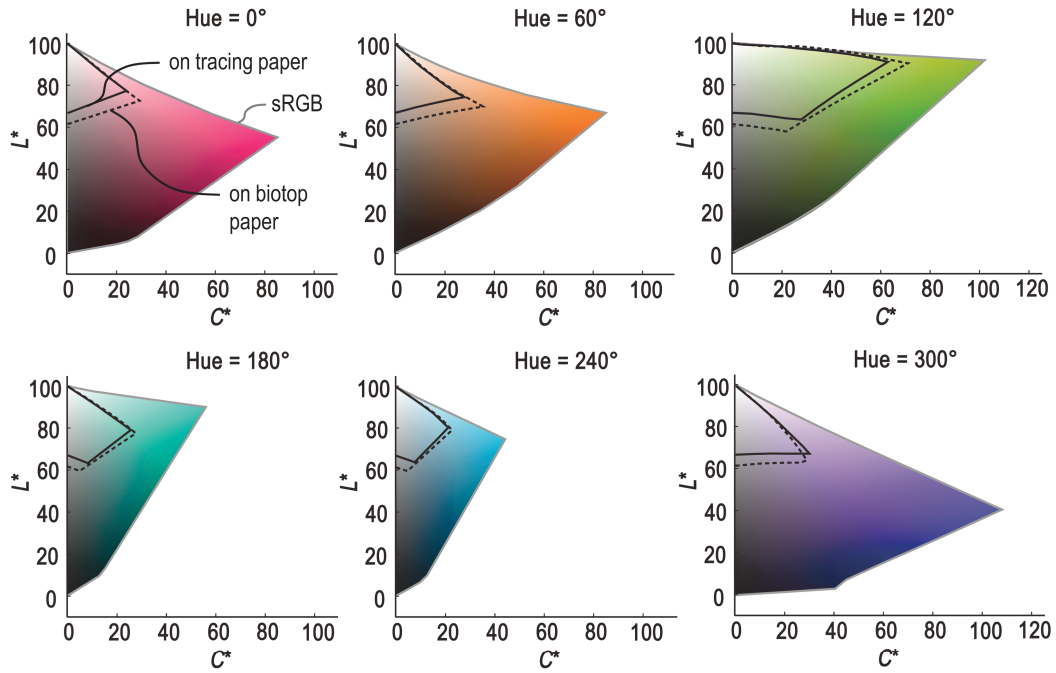
Figure 73. Comparison of the luminescent backlit color gamuts (G_{bp}: Bio Top paper - dashed line, G_{tp}: Tracing paper - solid line) relative to the sRGB gamut (G_{sRGB}: gray solid line).

The computation of the volume of the gamuts was performed by finding a point located inside the considered gamut in the middle of its lightness range, and summing the volumes of all the tetrahedrons generated between this point and the triangles of the boundary.[97] The volume of the gamut of the luminescent backlit colors on the Bio Top paper is larger than the one on the tracing paper. When comparing the two gamuts together, G_{tp} represents 77 % of G_{bp}. Therefore, there are fewer colors reproducible by luminescent backlighting of color halftones printed on the tracing paper than there are on the Bio Top paper. Furthermore, the number of available colors is quite small compared to what can be displayed on a standard display device. The minimum lightness on the grayscale is also very high ($L^*_{min}(G_{bp}) = 62.4$; $L^*_{min}(G_{tp}) = 66.6$). As a consequence, dark colors cannot be reproduced. Such high minimum lightnesses are due to the chromatic black colorant, which transmits up to 30-40 % of the luminescent backlight at 500 nm (see Figure 72). Additionally, the range of chroma is rather limited, except in the green colors. The luminescent backlit colors are therefore not very saturated.

8.4   Increasing the size of the luminescent backlit gamuts

8.4.1   Strategies

In order to increase the volume of the luminescent backlit gamuts, two different strategies can be adopted. First, the transmittance of the halftones may be lowered in order to decrease the amount of transmitted light. The density of the inks can be increased by having more ink printed on the substrate (higher drop size) or by replacing the inks by more absorbing ones. However, printing more inks on transmissive substrates is difficult to achieve because the substrate cannot absorb too much ink. The second strategy is the modification of the luminescent backlight and particularly, the modulation of its intensity. It might be performed by introducing the possibility to print several surface coverages of white inks, but this solution depends on the desired luminescent backlit images, and was not possible to undertake with the available uniform solid tone offset printed luminescent white emissive layer. As an alternative, the modulation of the intensity of the luminescent white emissive layer was performed by printing on the luminescent white emissive layer a UV-absorbing layer that absorbs part of the excitation light source and hence lowers the resulting emission. This solution involves no additional printing with luminescent inks. Actually, any colored ink may be used, because they all absorb in the UV. That is one of the reasons why classical inks cannot be superposed to luminescent inks in reflectance mode without disabling most of their luminescence.

8.4.2   Reduction of the UV excitation with a black UV-absorbing layer on top of the luminescent layer

In order to investigate how the emission of the luminescent layer is decreased by UV-absorbing halftones, black halftones were printed on top of the luminescent layer at surface coverages of 25 %, 50 %, 75 % and 100 %, and the luminescent backlit emission through the substrate was measured. For a good adhesion of the UV-absorbing layer on top of the offset luminescent inks, electrophotographic printing was chosen. The halftoned black layer was printed with a Xerox Phaser 6360DN PostScript electrophotographic printer with the black toner on top of the

luminescent layer at a resolution of 600 dpi, 100 lpi round shaped halftone screen with a screen angle of 0°.

The attenuation of the white luminescent backlight is not a simple scaling of the emittance. As shown in Figure 74, a spectral attenuation factor is needed to obtain the attenuated white luminescent backlight. This could be explained by two plausible reasons. The toner may partly penetrate inside the luminescent layer, and multiple reflections between the luminescent layer and the UV-absorbing black layer may happen. In both cases, part of the luminescent backlight is also absorbed by the UV-absorbing black halftone. To account for the interaction of the luminescent backlight with the UV-absorbing black halftone layer, a spectral attenuation factor $\kappa(\lambda)$ was calculated by dividing the measured attenuated luminescent backlight emission $E_{KWlum}(\lambda)$ by the unattenuated luminescent backlight emission $E_{Wlum}(\lambda)$ according to Equation 37.

$$\kappa(\lambda) = \frac{E_{KWlum}(\lambda)}{E_{Wlum}(\lambda)} \qquad (37)$$

The spectral attenuation factors $\kappa(\lambda)$ were smoothed by a locally weighted polynomial regression because of the noise induced by the narrow peak of the red part of the white emission spectrum.

In order to predict the attenuation resulting from any UV-absorbing black halftone, the emittance of the attenuated luminescent backlight is modeled as the product of the emittance of the unattenuated luminescent backlight with a halftone modulated spectral attenuation factor (Equation 38). This halftone modulated spectral attenuation factor is calculated from the spectral attenuation factor $\kappa(\lambda)$ by raising it to the exponent of the effective surface coverage of the UV-absorbing black a_{KWlum}, as shown in the first term of Equation 38. The modulation of the spectral attenuation factor by having the surface coverage as exponent assumes that the attenuation of the scattered white emission by the UV-absorbing black halftone behaves according to the Beer-Lambert law, i.e. the attenuation is to the power of the optical pathlengths of light. In a similar manner as the ink spreading enhanced spectral absorption model, the optical pathlength is assumed to be proportional to the UV-absorbing black ink surface coverage.

$$E_{bl}(\lambda) = \kappa(\lambda)^{a_{KWlum}} \cdot E_{Wlum}(\lambda) \qquad (38)$$
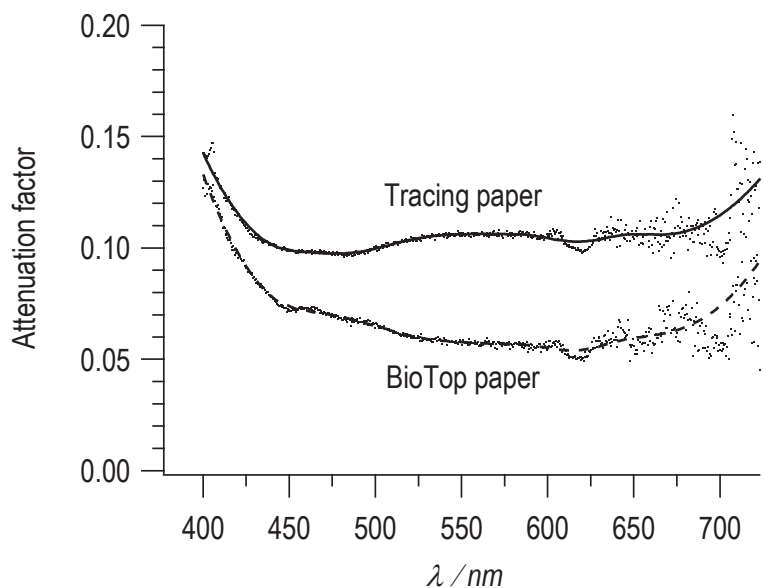
Figure 74. Spectral attenuation factor $\kappa(\lambda)$ of the black UV-absorbing solid patch printed on top of the luminescent layer
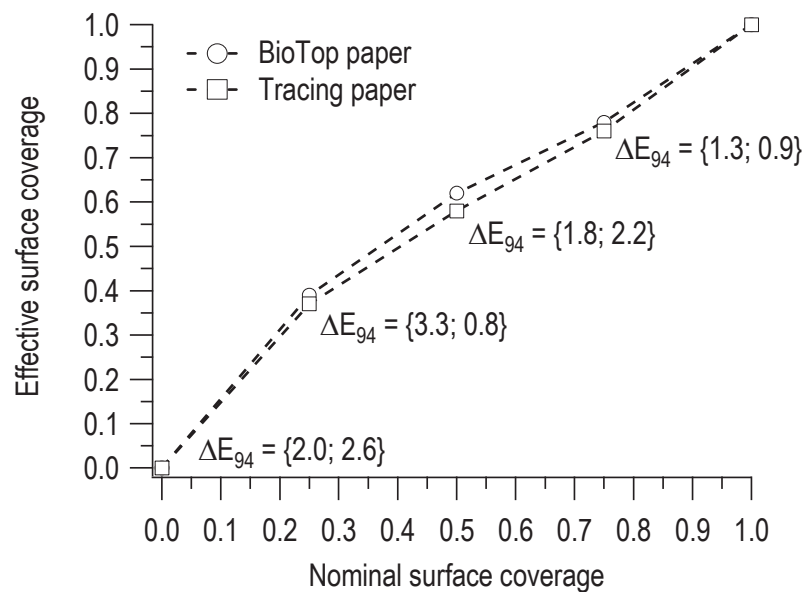
Figure 75. Ink spreading curve of the black UV-absorbing halftones printed on top of the luminescent layer for Bio Top paper and tracing paper. The prediction accuracies are given as ΔE_{94} values for the Bio Top paper and tracing paper respectively.

The calibration of the effective surface coverages resulting from the 25 %, 50 % and 75 % nominal surface coverages of UV-absorbing black was performed by fitting them according to Equation 38 and by minimizing the square difference between the predicted attenuated emittance and the measured one.

The accuracy of the fit is not very good, as shown by the ΔE_{94} values on Figure 75. According to the variability of the unattenuated luminescent backlight shown by the ΔE_{94} values of {2.0; 2.6} at 0 surface coverage, the limitation seems to be due to the slight inhomogeneities of the luminescent white emission across the page. Therefore, the accuracy is probably as good as it can be with a variable unattenuated luminescent backlight.

From this calibration of the attenuation of the luminescent white emission backlight according to the surface coverage of UV-absorbing black printed on top of the luminescent layer on the verso side, the accuracy of the prediction of the luminescent backlit colors was tested again.

Test sets of the 25 %, 50 % and 75 % surface coverages variations of cyan, magenta and yellow inks were printed on the recto side of the Bio Top paper, and two different surface coverages of UV-absorbing black were printed on the verso side on top of the luminescent layer. Nominal surface coverages of 38 % and 63 % of UV-absorbing black (not part of the calibration set used to obtain the ink spreading curves of Figure 75) were chosen.

The two test sets were measured in the same condition as the test set without any UV-absorbing black ink on the verso side. The attenuation factor $\kappa(\lambda)$ was used to predict the attenuated luminescent backlight emittance $E_{bl}(\lambda)$ with effective surface coverages a_{KWlum} linearly interpolated from the UV-absorbing black ink spreading curves (Figure 75).

The resulting attenuated luminescent backlight emittances were then used as a backlight source for the 27 transmissive color halftones of the test set. The same transmittances of the 27 halftoned color patches were used as those predicted after the recalibration of the transmittance prediction model by relying on the luminescent backlit emission. The accuracy of the 38 % and 63 % UV-absorbing black attenuated luminescent backlit colors are given in Table 18.

The prediction accuracy is now good with average ΔE_{94} values below 2. The introduction of the black layer even improves the accuracy of the model compared to the model without the black layer.

Table 18. Accuracy of the UV-absorbing black attenuated luminescent backlit model on the Bio Top paper for 27 test patches using the recalibrated transmittance model for the transmittances of the color halftones and the UV-absorbing black attenuation model for the emittances of the luminescent backlight

a_{nom} (K_{UV}/W_{Lum})	$\overline{\Delta E_{94}}$	$\max(\Delta E_{94})$	$Q_{95\%}(\Delta E_{94})$
38 %	1.3	2.5	2.1
63 %	1.9	3.8	2.9
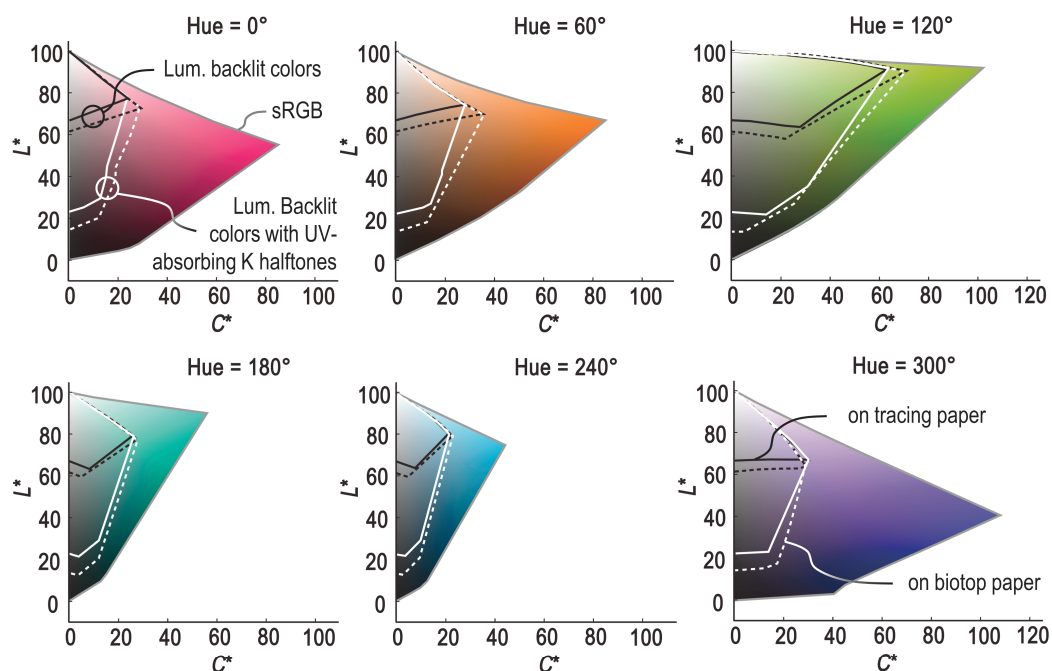
Figure 76. Increase of the gamuts (white lines) by addition of the black UV-absorbing layer on top of the luminescent layer

The new gamuts for the UV-absorbing black attenuated luminescent backlit colors were determined by considering the CIELAB colors obtained when 0 %, 25 %, 50 %, 75 % and 100 % of UV-absorbing black are printed on top of the luminescent layer, and by computing the gamut boundary as previously done. The extended gamuts are outlined in white on Figure 76.

The increase of the luminescent backlit gamut obtained by introducing a UV absorbing black layer on top of the luminescent layer is impressive. The lightness range is now much more important. The volume of the black extended gamut $G^K_{bp} = 2.3 \cdot G_{bp}$ on the Bio Top paper and $G^K_{tp} = 2.5 \cdot G_{tp}$ on the tracing paper. The minimum lightesses is now as low as $L^*_{min}(G^K_{bp}) = 13.2$, and $L^*_{min}(G^K_{tp}) = 22.6$. Nevertheless, no gain in chroma is obtained. Printing a UV-absorbing black halftoned layer on top of the luminescent layer therefore enables more contrasted luminescent backlit images, without however improving their chroma.

8.5　Reproduction of luminescent backlit color images

In order to create color prints viewable under luminescent backlighting, a correspondence between the input device sRGB lightness range and the lightness range of the luminescent backlit color gamut is first established. A linear lightness compression was chosen.

Once lightness compressed, the sRGB' gamut (G_{sRGB}') is mapped into the destination gamut according to the multiple foci gamut mapping algorithm described in the first chapter. In the presently produced images, the α factor was set at 0, the L_{low}^* point was set at 70 and the L_{high}^* point at 87.

The surface coverages of the inks need then to be deduced from the mapped colors. If the gamut mapping is performed correctly, all the mapped colors can be reproduced by the appropriate amounts of cyan, magenta, and yellow, possibly also of UV-absorbing black if the option to add a UV-absorbing black halftone on top of the luminescent layer is chosen. In order to be able to quickly establish the relationship between the desired CIELAB color and the corresponding surface coverages of the inks, a 3D lookup table setting up the correspondences was build, as described in the first chapter. The 3D lookup table is formed by a regular grid in CIELAB. At each point of the grid, the surface coverages of cyan, magenta and yellow for the images produced without the addition of the UV-absorbing black layer, and of cyan, magenta, yellow and UV-absorbing black for the images produced with the addition of a UV-absorbing black halftoned layer are deduced

from the spectral prediction model by minimizing the color difference between the desired color and the predicted color. For the images without the addition of a UV-absorbing black layer, the gamut mapping is performed into the luminescent backlit gamut without UV-absorbing black (shown in Figure 73). The minimization is then performed under the constraint that the surface coverage of the UV-absorbing black is zero. On the other hand, for the images that are printed with the addition of a UV-absorbing halftoned black layer, the gamut mapping is performed into the luminescent backlit gamut with UV-absorbing black halftones (shown in Figure 76). In this case, the minimization also involves fitting the UV-absorbing black surface coverage. There is therefore one 3D LUT for reproducing with and one for reproducing without UV-absorbing black. At image generation time, any desired gamut mapped CIELAB color can then be located in the mesh grid and the surface coverage of the inks interpolated from the neighbor vertices.

The cyan, magenta, yellow and UV-absorbing black layers are then halftoned according to the selected halftoning method, in our case a classical halftone screen printed at 600 dpi, with a screen frequency of 100 lpi, and with 75°, 45°, 15° and 0° screen angles for the cyan, magenta yellow and UV-absorbing black layers respectively. The cyan, magenta and yellow halftoned layers are finally printed on the recto side of the transmissive substrate, whereas the UV-absorbing black halftoned layer is printed on the verso side on top of the previously offset printed luminescent layer

The luminescent backlight images appear when illuminating the verso side under UV backlight. The resulting luminescent backlit images are very similar on the Bio Top paper and on the tracing paper. For both substrates, the improved quality gained from the printing of a black UV-absorbing layer on top of the luminescent layer is impressive (Figure 77). As a result of the black UV-absorbing layer modulating the luminescent backlight, the luminescent backlit images are much more contrasted.

Figure 77. Photographs of three luminescent backlit images printed on the Bio Top paper: on the left side without any back layer on top of the luminescent layer, and on the right side with a black UV-absorbing halftoned image on top of the luminescent layer.

The appearance of the images is however substantially different when observed in reflectance under normal light. Because there is less reflected light on the tracing paper, the saturation on the tracing paper is lower than on the Bio Top paper. The appearance of the black modulated images in reflectance is also very different from the image without any black modulation (see Figure 78). The reflected image looks like a chroma version of the image without the lightness scale when the black layer is printed on the luminescent layer, whereas the same image without the black layer looks similar to the original image.

Figure 78. Photographs of the Ski picture printed on the Bio Top paper and observed in reflectance under normal light. Top is without the black UV-cutting layer, bottom left is with the black UV-absorbing layer shown on the right side of the figure

8.6 Hiding or revealing patterns under luminescent backlighting

Color reproduction by luminescent backlight of transmissive colors is interesting because it combines luminescence, transmittance and recto-verso printing, thereby enabling the creation of strong security features. In this section, two security features are tested. The first one takes advantage of the invisibility of the luminescent layer under daylight to incorporate patterns or watermarks that are displayed only under luminescent backlighting. The second feature conceals patterns under luminescent backlighting and makes them visible under normal light.

8.6.1   Revealing under luminescent backlighting invisible patterns or watermarks embedded in the luminescent layer

Up to now, the luminescent layer was a single white emissive fulltone composed of the superposition of red emissive, yellow-green emissive and blue emissive invisible luminescent inks. Nevertheless, if a message is incorporated onto the luminescent layer on the verso side by printing it with a different combination of the luminescent inks, the message, which is invisible under normal white light, will appear under luminescent backlighting on the luminescent backlit color image.

Under UV excitation light, the luminescent layer illuminates the non-luminescent transmissive color image. If the luminescent layer has two different luminescent tones for the hidden message foreground and for the the background, the luminescent backlit image will display the message incorporated within the luminescent layer.

Furthermore, different messages formed by different luminescent tones can be revealed. In addition, the luminescent backlit message can be a variable intensity or variable color mark that is visible only under the excitation light source.

In the example given in Figure 79, the color halftone image is reproduced to appear accurately under luminescent backlighting with the luminescent tone of the background. This is achieved by mapping the colors of the input image into the luminescent backlit color gamut, and using the corresponding 3D lookup table (3D LUT) in order to retrieve the surface coverages of the three classical inks from the mapped CIELAB colors of the input image. The authenticity of the document is verified by observing if its luminescent backlit image incorporates the expected VALID message.

The message is embedded in the luminescent layer as a darker white emission, which forms the hidden message foreground. The luminescent layer was printed in offset. The luminescent background is produced by printing a 100 % surface coverage of each luminescent ink, whereas the hidden message foreground is produced by a 25 % surface coverage of each luminescent ink.

Alternatively, the input image can be mapped to be accurately reproduced under normal light. Under luminescent backlighting, the colors of the luminescent backlit

image would thus not be precise. The only purpose of the luminescent backlighting would thus be to check the authenticity of the document with the presence of the luminescent message.

Figure 79. Color halftoned image for luminescent backlighting viewed under normal light (illuminant A), luminescent backlit substrate with embedded VALID patterns under UV backlight, luminescent backlit color halftoned image with the embedded patterns under UV backlight

8.6.2   Hiding under luminescent backlighting visible patterns embedded in the color halftoned image by relying on the UV-absorbing halftoned black image printed on the luminescent layer

The possibility to have different luminescent backlight source or different luminescent tones, for example by printing UV-absorbing black halftones on top of the luminescent backlighting layer (resulting in attenuated luminescent tones), or by directly printing multilevel luminescent halftones as luminescent tones forming the

luminescent layer (not tested in this work), enables reproducing luminescent backlit colors by different combinations of color halftones and luminescent tones.

Since different luminescent tones can yield the same luminescent backlit color once filtered through the non-luminescent transmissive halftones, a message can be hidden on the recto side upon luminescent backlighting from the excited verso side, but be visible on the verso side as a direct luminescent message. The authentication is then performed by verifying that the message appearing on the verso side is completely hidden on the recto side, when illuminated with an excitation light source (UV light).

In order to take advantage of the UV-absorbing black halftoned layer to create such a security feature, two different 3D lookup tables were created by constraining differently the surface coverage of UV-absorbing black. The first one was unconstrained so that the model fits the surface coverages of the three classical inks and of the UV-absorbing black ink so as to minimize the color difference between the desired and predicted luminescent backlit colors. On the other hand, the second 3D LUT was generated by constraining a minimal amount of UV-absorbing black. This was performed by weighting the color difference to be minimized with the fitted surface coverage of UV-absorbing black according to Equation 39, where a_K is the surface coverage of UV-absorbing black, $CIELAB_{pred,aK}$ is the predicted CIELAB color using a_K UV-absorbing black, and $CIELAB$ is the desired gamut mapped CIELAB color.

$$a_K = \arg_{a_K} \min \left[\Delta E_{94} \left(CIELAB_{pred,a_K}, CIELAB \right) + 10 \cdot a_K \right] \qquad (39)$$

An image created from the unconstrained 3D LUT and the same input image created from the minimal UV-absorbing black 3D LUT have different combinations of classical inks and UV-absorbing black to obtain the same desired gamut mapped CIELAB color. The gamut of the luminescent backlit colors being identical, the gamut mapping is exactly the same. Only the combinations of inks are different.

As an example, by reproducing an input image with the unconstrained 3D LUT outside a mask and with the minimal UV-absorbing black 3D LUT inside a mask representing a message "OK", the message "OK" appears under normal light because the different surface coverages of the classical inks inside and outside the "OK" mask create a visible color difference between the two surface coverages. This message also appears on the verso side, yet mirror like, because the UV-absorbing black surface coverage is different inside and outside the mask, which

also generates a color difference under normal light. However, under the excitation light, the color shifts disappear in the luminescent backlit color image on the recto side because the luminescent backlit colors inside and outside the mask are similar. This example is shown in Figure 80 where the message "OK" is visible under normal light on both the recto color image and verso black image, but is concealed under luminescent backlighting. In this example, the image was reproduced with the unconstrained 3D LUT inside the "OK" mask and with the minimal UV-absorbing black 3D LUT outside the "OK" mask, as deduced from the darker mirror "OK" message on UV-absorbing black halftoned image printed on the verso side.

Figure 80. Color halftoned image for luminescent backlighting with a UV-absorbing halftoned black image on the luminescent layer under normal light (illuminant A) and showing the text OK at the top left corner, UV-absorbing halftoned black image under normal light (illuminant A) and luminescent backlit color halftoned image with the OK text hidden under UV backlight.

This method enables the creation of simple yet highly difficult to counterfeit security features, since it would require printing the correct luminescent layer, the color halftoned image with the proper surface coverages of the classical inks and

the UV-absorbing black layer with the appropriate surface coverage and with an adequate registration relative to the recto image.

The same approach could be undertaken if different amounts of luminescent inks could be printed in the luminescent layer or if a luminescent full color image could be generated as a luminescent layer. This might be achievable since full color luminescent images can be obtained provided that the correct spectral prediction model is available (see Chapter 6). However, a calibration of the luminescent backlighting model for each surface coverages of the luminescent inks would be required. The correction of the transmittances of the color halftones is indeed dependent on the surface coverages of the luminescent inks.

An advantage of the fixed uniform white luminescent layer though is that sheets of paper could be pre-printed, or pre-coated on their verso-side with the desired luminescent inks or compounds to obtain an important quantity of transmissive substrates ready for the incorporation of the security features on a system with only classical cyan, magenta, yellow and black inks. No additional luminescent ink is needed afterwards. The production costs are thus lower and the color images can be easily printed by classical means on the recto side.

8.7   Conclusions

A new approach for creating color halftone images to be viewed under UV excitation light was presented in this chapter. It consists in a luminescent layer printed on the verso side of a transmissive substrate, and used as a luminescent backlight for a color image printed on the recto side of the same substrate.

The colors of the luminescent backlit halftones were predicted by assuming that the emittance of the luminescent layer is filtered by the transmittances of the substrate and of the color ink halftones. The prediction of the luminescent backlit colors required a calibration of the intrinsic transmittances of the colorants under luminescent backlighting. The good prediction accuracy (with average $\Delta E_{94} < 2.0$) achieved with the proposed multilayer filtering approach enables reproducing luminescent backlit full color images under luminescent backlighting.

The lightness and chroma range of the luminescent backlit gamut are very limited though. As a result, the luminescent backlit images are dull and have low contrast. In order to create more contrasted luminescent backlit images, a UV-absorbing

black layer was printed on top of the luminescent layer. This UV-absorbing black halftoned layer blocks part of the UV excitation light source and thus locally reduces the emittance of the luminescent backlight. A spectral attenuation factor was introduced in order to indicate how much the emittance of the luminescent backlight is reduced as a function of the UV-absorbing black halftone surface coverage. The new gamut resulting from the image dependent attenuation of the luminescent backlight is more than two times larger than the original gamut. The luminescent backlit color images appearing on the recto side with a UV-absorbing black halftoned layer printed on the verso side on top of the luminescent layer look much better and have a higher contrast. However, their chroma cannot be increased.

Color reproduction by luminescent backlight of transmissive colors is interesting because it combines luminescence, transmittance and recto-verso printing, thereby enabling the creation of strong security features. Two examples were shown. In the first one, luminescent patterns or watermarks were embedded within the invisible luminescent layer. Under UV illumination, they appear on the luminescent backlit color image. The second example takes advantage of two different UV-absorbing black halftoned layers reproducing the same luminescent backlit colors to hide under luminescent backlighting visible patterns appearing on the color halftoned image printed on the verso side.

Chapter 9

General conclusions and perspectives

From beginning to end

This chapter concludes the thesis by reviewing the work and results reported here. It also provides perspectives for future developments in this field and endeavors to contextualize the obtained achievements in respect to the current state of the art.

The work can be divided into two parts: a chemistry part and a color science part. The chemistry part covers Chapters 2-5 and part of Chapter 6, whereas the color science part starts with Chapter 6 and extends to Chapters 7 and 8.

In the chemistry section, new ligands for luminescent lanthanide ions were synthesized. These ligands are derivatives of dipicolinic acid (dpa). They represent two possible strategies of derivatization. The first strategy involves the coordination site. One of the carboxylic acid of dpa was replaced by a series of phosphorylated functional groups. Three phosphorylated groups were considered: a diethoxyphosphoryl, a monoethoxyphosphoryl and a dihydroxyphosphoryl or phosphonic acid. The second strategy consists in grafting at the *para* position on the pyridine ring of dpa a series of polyoxyethylenated coumarins. The nature of the coumarin chromophore at the end of a trioxyethylene linker was studied. Five different coumarins were studied thereof. In addition, the length of the polyoxyethylene linker was shortened with one of the coumarin.

The lanthanide complexes formed from these new ligands were investigated and characterized by different techniques used in coordination chemistry and photophysics. The stability of the lanthanide complexes was analyzed by complexometry based on spectrophotometric measurements. In addition, NMR spectroscopy, Mass Spectrometry and luminescence based experiments were carried out to assess the predominant formation of the desired species in solution. The luminescence of the complexes as a function of the pH value of the aqueous solution was also probed.

A particular emphasis on the photophysical properties of the complexes was undertaken. The excitation and emission spectra were measured by spectrofluorimetry. In some cases, the emission intensity was used to probe the presence of analytes such as the salt concentration. In other cases, the quantum yields and lifetimes were more convenient probing quantities. The quantum yields were measured either relative to the parent dpa standard quantum yield, or by an absolute method with an integrating sphere. Time resolved emission spectra were also measured, thus giving access to observed lifetimes. Furthermore, by measuring the time resolved emission at low temperature the phosphorescence spectra of the triplet state of the ligands in gadolinium complexes were observed. In the case of the dpa-polyoxyethylene-coumarin system developed in this thesis, time resolved

spectroscopy was also extended to the determination of the sensitization pathways of the studied europium complexes. The europium complexes enable the determination of intrinsic quantum yields and radiative lifetimes and therefore give access to the sensitization efficiency. With these various techniques, important results were found.

Concerning the replacement of a carboxylate by phosphoryl functional groups, the major outcomes are about the pH sensitivity of the luminescence. The optimal luminescence can be tuned from acidic with the diethoxyphosphoryl ligand up to basic with the monoethoxyphosphoryl ligand. This series then complements the optimal luminescence of the dpa complexes under neutral conditions. This behavior can be correlated with the pK_a values of the ligands and therefore, with the nature of the phosphoryl. Besides, the phosphorylated complexes demonstrated improved stabilities relative to the dicarboxylate analog, as already observed in the literature. The replacement by diethoxyphosphoryl was also shown to increase the quantum yield of the terbium complex, achieving a quite high value of 40 %. Even if the diethoxyphosphoryl picolinic acid ligand is a more efficient sensitizer than the monoethoxyphosphorylated ligand, monoethoxyphosphoryl picolinic acid based lanthanide complexes are more interesting for two reasons. First, the sensitivity of the monoethoxyphosphoryl moiety, which is yet to be explored, could be attractive for biological applications, for example, for probing pH and salt concentrations. In addition, the phosphorus is a stereocenter that could generate chiral ligands. This could be a nice perspective for future works on this structure.

The most extended part of this thesis deals with the dpa-polyoxyethylene-coumarin architecture. The major results of this study were probably to prove that lanthanide ions can be sensitized by the distant coumarin, and that in solution, the sensitization efficiency is independent on the length of the polyoxyethylene linker, at least from one –CH$_2$CH$_2$O– unit, up to three. The double sensitization of lanthanide ions either via the coumarin only or via a mixed pathway involving the dpa chromophore as well as the coumarin chromophore was shown to yield a sensitization efficiency that depends on the excitation wavelength. The investigation of the sensitization pathway, which was demonstrated to occur from the singlet excited state of the coumarin in frozen solution at 77 K, with limited resources was also a remarkable achievement of this work. Furthermore, the fact that the sensitization pathway is similar for all the investigated coumarins is noteworthy. This suggests that minor derivatizations on a same family of chromophores may not alter sensitization pathways but only energy transfer rates due to different excited state locations and due to additions of deactivating or quenching pathways.

Additional experiments in solution and at room temperature would be required to undeniably establish that the sensitization pathway from the coumarin moiety occurs through its singlet excited state under these conditions. A faster time resolution (picoseconds or femtosecond pulsed excitations) and/or transient absorption spectroscopy (particularly triplet-triplet, T-T, absorptions) could conclude this topic.

The collected results of Chapters 3-5 constitute a broad overview of the pros-and-cons of the dpa-polyoxyethylene-coumarin architecture for investigating the sensitization of lanthanide ions. Its versatility and potential applicability for a wide range of terminal chromophores could allow a systematic investigation of chromophores as sensitizers. The five coumarins and three length of the polyoxyethylene linker form a small library of ligands with the same design. The expansion of this library could be worthwhile. It would for instance be attractive to study a terminal chromophore with a triplet pathway and compare it with the singlet pathway of the coumarins. Chromophores that are sensitive to the pH or to an analyte could also yield complexes with desirable probing abilities. Concerning the other moieties of the ligand design, the nature of the linker could be improved or at least, other types of linkers could be tested. The limiting factor here is probably the water solubility of the ligands and of the resulting lanthanide complexes. Finally, other coordination sites might also be tested, and particularly those forming 1:1 complexes. Self quenching phenomena were indeed highlighted in Chapter 4.

From a color point of view, the incomplete energy transfer from a terminal fluorophore is interesting because it enables having multimodal emissions from a single molecular system. These types of structures are known in the literature and can even form white luminescent complexes. They also enable tuning the emission color by simply changing the excitation wavelength. In this work, the coumarin provides a blue emission and the europium ion a red emission. Under short wave UV, the europium emission is efficient and gives a red color with a very small blue contribution. On the other hand, under long wave UV, the coumarin emission has a stronger component compared to the red emission of the europium ion and looks from magenta to lavender depending on the ratio of red/blue. This type of complexes could also be attractive for bioimaging because they combine a fluorescent emission from the coumarin, with a long lived luminescent emission from the lanthanide ion, which can be discriminated by time resolved microscopy.

This study pointed out several important limitations of luminescent lanthanide complexes with uncoordinated sensitizers that are often not clearly addressed in the literature. The most obvious issue involves the flexibility of the linker and therefore,

the diffusion of the antenna in solution relative to the lanthanide ion. This behavior is important since it can preclude any improvement of the energy transfer rate by shortening the average distance to the lanthanide ion. Another problem of the tris complexes is the possibility that the introduction of more than one chromophore per lanthanide ion decreases the quantum yield due to self-quenching phenomena that can compete with the energy transfer rate.

The optimization of the sensitizer is of course an important perspective should this system be investigated further. However, variations of the linker could be more appealing. If water solubility could be a problem for short linkers or rigid linkers, this could be overcome by grafting a solubilizing moiety in addition to the linker, either on the linker, or on the distant antenna. Thereby, small unsaturated linkers could be imagined in order to increase the rigidity and to vary the stereochemistry (cis-trans or meta-ortho-para positions). Chiral linkers could also be envisaged thus forming chiral ligands. Sugars might for instance be possible linkers. Finally, "functional linkers" that can be cleaved or altered chemically, biologically or photochemically could provide sensitive luminescent probes. Similar strategies might also be undertaken on the distant chromophore.

The work done in the chemnistry part is a necessary step towards more complex structures. It enables defining the limitations of the investigated architectures by pointing at issues that were not straightforward at early stages of the study.

Chapter 6 opened the color science part of this thesis. Nevertheless, an important fraction of this chapter still relies on chemistry and photophysics. It then acts as a bridge at the interface of chemistry and color science. In this chapter, red luminescent and green luminescent inks were formulated from trisdipicolinate europium and terbium complexes. The complexes acted as luminescent dyes. The ink set was completed by a commercial blue luminescent ink. The luminescent inks were printed with an ink-jet printer on non-fluorescent papers and their photophysical properties were first analyzed under different conditions. The main result is that the dpa based luminescent inks are unaffected by concentration and by the superposition on each other and on the blue luminescent ink. Consequently, their application for color reproduction is ideal. In a second step, the inks were printed as luminescent halftones. Luminescent full color images were obtained by relying on a spectral prediction model and by using gamut mapping and precomputed color separation tables. The gamut of the luminescent inks was found to be large and give vivid accurate luminescent colors under a 254 nm UV excitation lamp with a UV-bandpass filter.

As perspectives in relation to this this particular application of luminescent lanthanide complexes, three different ways could be explored. The first one is of course to find a blue emitting compound suitable for ink-jet printing. Organic dyes could be tested, with the limitation of water solubility and inertness towards lanthanide complexes. Alternatively, inorganic nanophosphors could be derivatized to be water soluble. Should this possibility be considered, europium(II) phosphors would certainly be appealing. Other materials that are not water soluble could also be incorporated in nanoparticles such as silica nanoparticles, which can be functionalized to be water soluble. The second perspective deals with using other complexes than the dpa complexes, or using other lanthanide ions together with europium and terbium. The utilization of other complexes would be, for instance, to have complexes absorbing at higher wavelengths that can luminesce under a long wave UV lamp. Security features based on the joint utilization of two sets of luminescent inks, one of which is active only under short wave UV, while the other is also active under long wave UV could even be imagined. On the other hand, using other lanthanide ions would enable modulating the spectral fingerprint of the luminescence, which would provide further security features. The last perspective is to print separately the ligands and the metal ions to form the complexes on paper. The quality of the print will not be as good as with the already formed complexes because of registration issues and because of the difficulty to have a homogeneous mixing of the ligand and metal ion on paper. Nevertheless, this technique could introduce interesting perspectives for security features based on preprinted patterns that could be revealed by printed on top of it the correct ligand or the desired metal ion. Such an approach was tested with dpa and with the ligand investigated in Chapter 4, but precipitation issues occurred with the dpa-POE-coumarin ligand at the high concentration used here. Further investigations would be required to yield a functional application.

Here again, the work performed on the synthesized luminescent inks sets the base for future developments. The proof of principle was beyond expectations though and produced accurate vivid luminescent images. Without the model and the color management workflow, building more complex systems would not make sense, since accurate colors would not be ensured.

Up top now, the color was directly generated by luminescence. It was therefore a property of the luminescent material. Nevertheless, this color can be altered by attenuation of the emitted light with a colored material, i.e., a material that absorbs in the visible part of the spectrum. Chapter 8 follows this path for reproducing colors by attenuating a white luminescent emission with classical color halftones.

To model this attenuation, a new spectral prediction model was developed. The bases of this model are explained in Chapter 7.

The new spectral prediction model assumes that the average optical pathlength of light in the colorants of a halftone is proportional to the surface coverages of each colorant, and therefore, that the transmittance of a halftone is the product of the transmittances of the colorants raised as exponents by their surface. This spectral prediction model for transmittances and its application in reflection mode represent a possible alternative to state of the art models, and particularly to the Yule-Nielsen modified spectral Neugebauer model. The model is simpler because of the absence of the n-factor. It is yet as accurate for moderate and high frequency halftones.

Based on this new spectral prediction model, a backlighting model was developed. The backlight was a uniform white emissive luminescent layer formed by red, green-yellow and blue luminescent inks printed with offset on one side of a transmissive substrate and illuminated by UV light at 365 nm. The luminescent backlit colors are formed by the transmission of the luminescent backlight through the transmissive substrate and through color halftones printed on the other side of the substrate. The backlighting model describes how to combine luminescence with classical color halftones. The emission spectra of the backlit color halftones are modeled by a simple multiplicative filter-like approach. The prediction accuracy of the backlighting model is good. The limitation is the homogeneity of the white luminescent layer, which displayed variations of the emission spectrum across the page.

The gamut of the luminescent backlit colors is not very large both in terms of lightness and chroma. As a result, the images reproduced with this system are not contrasted and quite dull. To overcome the limited lightness range, the emission of the luminescent backlighting layer was attenuated by printing a UV-absorbing black halftone image on top of the luminescent layer. This additional halftone blocks part of the UV excitation light source and locally attenuates the luminescent white backlight. The resulting gamut was larger in the dark tones. However, its chroma is still limited. The obtained luminescent backlit images look yet much better than the same image without the UV-absorbing black halftone on top of the luminescent layer.

Finally, examples of security features taking advantage of the luminescent backlighting technique were presented. The first example involves the appearance of patterns embedded in the luminescent backlight and hence appearing in the

luminescent backlit images but invisible under normal light. The second example takes advantage of the fact that some luminescent backlit colors can be reproduced by different combinations of classical halftones and UV-absorbing halftones to induce color differences in the color halftones in specific regions that can form visible patterns in the halftoned color images. Under luminescent backlighting, the color differences disappear and thus no pattern is visible (i.e., the patterns are concealed).

Strong security features can be created from this technique. They are still fairly simple to authenticate since they can be visually checked by looking at the luminescent backlit image under UV light. The approach presented in this thesis demonstrates that luminescent backlighting is achievable. As future works, the simple white luminescent layer could be replaced by full color images. The modeling of the transmittances of the color halftones depending on the amount of luminescent ink printed on the verso side would be the major challenge of this more sophisticated luminescent backlighting method. The attenuation of the luminescent layers by any classical color halftone, thus enabling to form color images on top of the luminescent layer, could also be valuable, since it introduces even more possibilities of reproducing colors.

Relative to the state of the art, luminescent backlighting is quite unique. It is a different way to reproduce colors and avoids some of the problems that could be encountered in comparable techniques where the luminescent layer is printed or incorporated on the same side as the halftoned color image.

In the future, one may use the inks developed in Chapter 6 to print the luminescent layer instead of using offset printing. This would enable expanding the utilization of the luminescent layer by offering the possibility to easily print any luminescent halftone on the verso side. Concerning the color halftones, the classical inks could also be replaced by more absorbing ones in order to improve the chroma of the luminescent backlit colors.

It is noteworthy that such perspectives can be considered because of the success of the color reproduction workflow previously developed by others for classical inks in reflectance, and because of its correct adaptation in this work to luminescent prints and to the luminescent backlighting approach.

The color science part of this thesis aimed at finding new ways to reproduce colors by relying on luminescence. During this exploration, a new spectral prediction model was discovered. Both Chapter 6 and Chapter 8, which deal with color reproduction, present techniques that are appealing, not only from a color

point of view, but also for document security. Besides the potential refinements of the luminescent materials and of the inks that are dear to chemists, the engineering of new security features and color reproduction methods requires knowing how inks can be printed and how color images can be generated (i.e., what can be done with them). From a global point of view, the major achievement of this thesis is then certainly its multidisciplinary aspect. Even though the thesis was submitted to the chemistry doctoral school, a large part of the work deals with color and computer sciences related topics. The connecting thread was luminescence which is present in almost every chapter.

Luminescence is a quite fascinating and beautiful phenomenon, which enables producing display devices, efficient light sources, and many other products and applications. In those applications, lanthanide ions are firmly established. They are indeed unique emitters with amazing color characteristics.

The present thesis presented and investigated new lanthanide complexes, some of which possess uncommon properties. It highlighted that certain simple statements often claimed as well-established are not always true because of the different dynamic phenomena that can complicate the photophysical properties of the lanthanide complexes. In addition to these fundamental studies, this work applied standard europium and terbium complexes to the particular case of luminescent inks. It tested these inks in view of their utilization for color reproduction of full color images and rationalized the properties of the inks by carrying out photophysical measurements, which seems a novel approach in the field. Finally, this thesis also reported a new spectral prediction model for the prediction of transmittances and reflectances and a new way to reproduce colors by means of luminescence and color halftones using backlighting.

In each of these domains, things of beauty were created. Therefore, I would like to conclude with the first sentence from Endymion, a poem by John Keats first published in 1818:

"*A thing of beauty is a joy for ever:*
Its loveliness increases; it will never
Pass into nothingness; but still will keep
A bower quiet for us, and a sleep
Full of sweet dreams, and health, and quiet breathing."

Appendices

Appendix A: General procedures

The solvents were purified by a non-hazardous procedure by passing them onto activated alumina columns (Innovative Technology Inc. system). The chemicals were ordered from Fluka and Aldrich and used without further purification. ESI-MS spectra were obtained on a Finningan SSQ 710C spectrometer using 10^{-5}-10^{-4} M solutions in acetonitrile/H_2O/acetic acid (50/50/1) or MeOH, a capillary temperature of 200 °C and an acceleration potential equal to 4.5 keV. The instrument was calibrated using horse myoglobin standard and analyses were conducted in positive mode with a 4.6 keV ion spray voltage. Mass spectrometry experiments were performed by Dr Laure Ménin, and elemental analyses by Dr. E. Solari, at the École Polytechnique Fédérale de Lausanne. ^{1}H NMR and HSQC NMR spectroscopy were performed on a Bruker Avance DRX 400 spectrometer and ^{13}C NMR spectroscopy on a Bruker AV 600 MHz or on a Bruker Avance DRX 400 spectrometer. All NMR spectra were measured at 25°C, using deuterated solvents as internal standards. Chemical shifts are given in ppm relative to TMS. J values are given with a ± 0.5 Hz precision.

Appendix B: Synthesis of the 6ppa ligands

6-diethoxyphosphoryl picolinic acid (Hdeppa) was synthesized according to a known procedure[14] with ethylpicolinate as a starting material. The pure pale solid was obtained in 34 % yield from the starting material. The HPLC analysis showed the presence of one compound with a retention time of 21.6 minutes. ^{1}H NMR (400 MHz, D_2O) δ ppm 8.17 (m, 1 H), 8.07 (m, 2 H), 4.15 (m, 4 H), 1.24 (m, 6 H). ^{13}C NMR (126 MHz, D_2O) δ ppm 167.7 (s, $\underline{C}$OOH), 150.0 (d, J=152.0 Hz, $\underline{C}_{pyr6}$-P), 149.0 (d, J=53.5 Hz, $\underline{C}_{pyr2}$-C), 139.7 (d, J=12.0 Hz, $\underline{C}H_{pyr4}$), 132.1 (d, J=25.0 Hz, $\underline{C}H_{pyr5}$), 128.8 (d, J=3.5 Hz, $\underline{C}H_{pyr3}$), 65.8 (d, J=5.5 Hz, O-$\underline{C}H_2$-C), 16.9 (d, J=5.5 Hz, C-$\underline{C}H_3$). ^{31}P NMR (162 MHz, D_2O) δ ppm 12.5 (s). Anal. Calcd for $C_{10}H_{14}NO_5P$: 46.34% C, 5.44% H, 5.40% N; found: 46.62% C, 5.47% H, 5.35% N.

6-monoethoxyphosphoryl picolinic acid (H$_2$meppa) was obtained from Hdeppa. To a solution of 6-diethoxyphosphoryl picolinic acid (1.3 mmol, 337 mg) in water (32.5 ml), sodium hydroxide 0.1 M (1.3 mmol, 13 ml), was added at room temperature. After stirring 1 hour, another equivalent of sodium hydroxide 0.1 M (1.3 mmol, 13 ml) was added. The reaction was completed after 1.5 h as shown by ^{31}P NMR spectroscopy. The aqueous phase was washed three times with CH_2Cl_2 (3 x 60 ml) and acidified by HCl 0.1 M down to pH 1.5. No precipitation was observed. After evaporation of the solvent under reduced pressure, the precipitation of salts was performed by addition of MeOH (2 ml). Evaporation of the filtrate under reduced pressure and further precipitation of salts were repeated 3 times to afford H$_2$meppa as brownish transparent oil (233 mg, 78 %). The HPLC analysis showed the presence of one compound with a retention time of 8.0 minutes. ^{1}H NMR (400 MHz, D_2O) δ ppm 8.44 (m, 1 H), 8.32 (m, 1 H), 8.17 (m, 1 H), 3.89 (m, 2 H), 1.14 (t, J=7.0 Hz, 3 H). ^{13}C NMR (126 MHz, D_2O) δ ppm 163.9 (s, $\underline{C}$OOH), 153.0 (d, J=178.7 Hz, $\underline{C}_{pyr6}$-P), 146.6 (d, J=8.0 Hz, $\underline{C}_{pyr2}$-C), 143.1 (d, J=9.0 Hz, $\underline{C}H_{pyr4}$), 131.3 (d, J=13.0 Hz, $\underline{C}H_{pyr5}$), 127.8 (s, $\underline{C}H_{pyr3}$), 65.1 (O-$\underline{C}H_2$-C), 14.7 (s, C-$\underline{C}H_3$). ^{31}P NMR (162 MHz, D_2O) δ ppm 9.20 (s). Anal. Calcd for $C_8H_{10}NO_5P \cdot 2$ HCl: 31.60% C, 3.98% H, 4.61% N; found: 31.52% C, 3.56% H, 4.26% N.

6-dihydroxyphosphoryl picolinic acid (H$_3$dhppa) was synthesized from 6-monoethoxyphosphoryl picolinic acid. H$_2$meppa (0.65mmol, 150 mg) was dissolved in water (5 ml), and an excess of sodium hydroxide 5 M (10 mmol, 2 ml) was added. The solution was refluxed for 6 h. The solvent was then progressively evaporated to push the equilibrium towards the formation of the desired product.

The procedure was repeated once more until completion of the reaction as shown by ^{31}P NMR spectroscopy. The crude product was dissolved in water (25 ml) and the aqueous phase was washed three times with CH_2Cl_2 (3 x 25 ml). The aqueous phase was then acidified with HCl 0.1 M down to pH 1.5 without any precipitation of the product. After evaporation of the solvent under reduced pressure, the precipitation of salts was performed in MeOH similarly to H_2meppa and gave H_3dhppa as a pale brownish hygroscopic powder (86 mg, 63 %). The HPLC analysis showed the presence of one compound with a retention time of 1.1 minute. ^{1}H NMR (400 MHz, D_2O) δ ppm 7.80-7.72 (m). ^{13}C NMR (126 MHz, D_2O) δ ppm 163.7 (s, $\underline{C}$OOH), 152.9 (d, J=178.5 Hz, $\underline{C}_{pyr6}$-P), 146.6 (d, J=9.0 Hz, $\underline{C}_{pyr2}$-C), 145.3 (d, J=9.5 Hz, $\underline{C}H_{pyr4}$), 131.5 (d, J=13.0 Hz, $\underline{C}H_{pyr5}$), 128.0 (s, $\underline{C}H_{pyr3}$). ^{31}P NMR (162 MHz, D_2O) δ ppm 6.90 (s). Anal. Calcd for $C_6H_6NO_5P \cdot 0.25$ NaCl $\cdot 1.1$ MeOH: 31.02% C, 3.45% H, 5.10% N; found: 31.09% C, 3.34% H, 5.17% N.

Appendix C: Synthesis of the dp3Cy ligands

The dp3Cy ligands were synthesized according to the following procedure, except for dp3C1 which was synthesized according to a previous procedure. Its synthesis from the new method should however certainly be successful. The old procedure can be found in the reference[98].

The tosylated trioxyethylene glycol monomethyl ether were synthesised according to the procedure in the supplementary materials of Kohmoto and al.[99]

General procedure for the synthesis of 4-hydroxycoumarins

4-hydroxycoumarins were synthesised according to Jung et al.[58] The corresponding 4-substituted 2-hydroxyacetophenone (50 mmol) was dissolved with diethyl carbonate (75 mmol) in toluene (25 ml). The solution was added dropwise under inert atmosphere and at room temperature to a vigorously stirred suspension of sodium hydride (60% w/w moistened with oil, 250 mmol) in toluene (125 ml). After complete addition, the reaction was heated up to 105°C for 3 hours. The solvent was then evaporated. Water (100 ml) was added to the residual solid to quench the excess of sodium hydride. The solution was concentrated under vacuum to remove the remaining toluene and acidified with concentrated hydrochloric acid down to pH 1 to form a precipitate that can be filtered out, washed with water and dried in vacuo. Recrystallisation from ethanol can be performed to obtain higher purity 4-hydroxycoumarins if needed.

Non commercial 2-hydroxyacetophenones like 4-chloro-2-hydroxyacetophenone can be synthesised through a Fries rearrangement of the 3-substituted acetoxybenzene, for the 4-chloro-2-hydroxyacetophenone, 3-chloroacetoxybenzene, obtained from 3-chlorophenol, was reacted with AlCl$_3$.[100]

Synthesis of 7-hydroxycoumarins

7-hydroxy-4-methoxycoumarin (C2) was synthesised from 4-hydroxy-7-methoxycoumarin (C3) (1 g, 5.20 mmol) by demethylation of the 7-methoxy group with hydroiodic acid (75 ml) in a 1/1 (v/v) acetic acid/acetic anhydride solution (total 60 ml) under reflux (120°C) for 3h30. The obtained 4,7-dihydroxycoumarin (471 mg, 51 %) was then remethylated selectively in position 4 by heating in

methanol (0.1 M solution, 16 ml) with concentrated sulfuric acid (1.25 ml acid / mmol dihydroxycoumarin) for 1 hour and a half. 7-hydroxy-4-methoxycoumarin (C2) is obtained as a slightly pinkish white powder (163 mg, 54 % from 4,7-dihydroxycoumarin)

Synthesis of the POEMEated coumarins

Coumarins were coupled to a polyoxyethylene chain by attacking tosylated triethylene glycol monomethyl ether (1.2 eq) in DMF (0.3 M in coumarin) with an excess of K_2CO_3 (22 eq) at 75°C for 48 hours. The solvent was then evaporated, the residual slurry dissolved in dichloromethane, washed three times with half saturated NH_4Cl aqueous solution, dried with Na_2SO_4, and the solvent evaporated in vacuo. Purification by silica gel chromatography with ethyl acetate 100% as eluent gave the pure desired product as a solid after evaporation of the solvent. In the case of mp3C2 and mp3C3, the oily residue obtained after washing with aqueous NH_4Cl was solidified by adding a small amount of diethyl ether and sonicating at 40°C. The white solid was filtrated, rinsed with diethyl ether and further dried to yield pure mp3Cy.

Table 19. Yields of the synthesis of the POEMEated coumarins

Products	Yields
mp3C1	100%
mp3C2	100%
mp3C3	100%
mp3C4	50%
mp3C5	42%

The resulting yields are in agreement with the ability of the substituent to lower the nucleophilicity of the coupling hydroxyl group on the coumarin. Hence, an electron withdrawing group in position 7, like a chlorine (C5), diminishes the yield compared to the unsubstituted 4-hydroxycoumarin (C4). On the other hand, an electron donating group like a methoxy increases the yield up to a quantitative coupling.

Coupling of POEated coumarins with chelidamic acid

POEMEated coumarins were demethylated at the end of the POE side chain by reacting them with trimethylsilyl iodide (TMSI, 1.2 eq) in acetonitrile (0.15 M in POEMEated coumarin). TMSI was added dropwise in the warm solution (at 75°C) and further stirred 2 hours at 75°C. The solvent was then evaporated, the residue dissolved in dichloromethane (DCM) and the solution washed with $Na_2S_2O_3$ (0.09 M, 20 mmol $Na_2S_2O_3$ / mmol TMSI). The aqueous phase was then further extracted with DCM (2 times) and the collected organic layers dried over Na_2SO_4, filtered and evaporated under reduced pressure to yield the crude product used without purification in the next step.

Mitsunobu reaction with resin supported TPP

Diethylchelidamate (Et$_2$chelida) was dissolved in DCM (0.06 M in Et$_2$chelida) with the POEated coumarin (1.5 eq) and resin supported triphenylphosphine (PS-TPP, 1.5 eq). The dispersion was cooled down to 0°C and diisopropylazodicarboxylate (DIAD, 1.5 eq) was then added dropwise to the cold stirred solution. The reaction was then allowed to warm at room temperature and stirred for 5 hours. The solution was then filtered to remove the TPP resin. The resin was washed with DCM (50 mL) and the filtrate was washed with aqueous HCl 1M (50 mL) once and three times with H_2O (3 × 50 mL). The organic layer was dried with Na_2SO_4, filtered and evaporated under reduced pressure to yield on oil composed of the coupled desired product together with residual uncoupled POEated coumarin. The excess of POE containing coumarin is removed in the next step. The crude product was then used without further purification in the final step.

Deprotection of the carboxylic acid by hydrolysis of the diethyl ester moiety

The diesters groups of the POE coupled coumarin are removed by hydrolysis with aqueous NaOH in EtOH. The diethyl ester is first dissolved in ethanol (0.08 M) and aqueous NaOH (2.2 eq, 0.5 M in NaOH) is added dropwise to the stirred solution at room temperature. A precipitate gently appears after the NaOH addition. The reaction mixture is further stirred for 30 minutes. The product is then isolated as the sodium dicarboxylate salt.

The pure sodium dicarboxylate salt is obtained by recrystallisation of the precipitate in ethanol with a minimum amount of water followed by filtration. The

filtered solid is washed with cold ethanol and collected as a wet powder. The powder is then dried in vacuo to obtain the desired ligand. It is characterised by ^{1}H-NMR and ^{13}C-NMR in D_2O and by elemental analysis.

Characterisations of the compounds

^{1}H-NMR of the coumarins in DMSO-d6

C2: ^{1}H NMR δ: 10.57 (s, 1 H), 7.63 (d, J = 8.5 Hz, 1 H), 6.80 (dd, J_1 = 8.5 Hz, J_2 = 2.0 Hz, 1 H), 6.71 (d, J = 2.0 Hz, 1 H), 5.69 (s, 1 H), 3.98 (s, 3 H)

C3: ^{1}H NMR δ: 7.73 (d, J = 8.5 Hz, 1 H), 6.94 (m, 2 H), 5.43 (s, 1 H), 3.86 (s, 3 H)

C4: ^{1}H NMR δ: 7.84 (dd, J_1 = 8.0 Hz, J_2 = 1.5 Hz, 1 H), 7.66 (td, J_1 = 8.0 Hz, J_2 = 1.5 Hz, 1 H), 7.37 (m, 2 H), 5.62 (s, 1 H)

C5: ^{1}H NMR δ: 7.83 (d, J = 8.5 Hz, 1 H), 7.58 (d, J = 2.0 Hz, 1 H d1 = 20 sec.), 7.42 (dd, J_1 = 8.5 Hz, J_2 = 2.0 Hz ,1 H), 5.65 (s, 1 H)

^{1}H-NMR and ESI-MS of the POEMEated coumarins

mp3C1: ^{1}H NMR (CDCl$_3$, 400 MHz) δ= 7.48 (d, J = 9.0 Hz, 1 H), 6.88 (dd, J_1 = 9.0 Hz, J_2 = 2.5 Hz, 1 H), 6.82 (d, J = 2.5 Hz, 1 H), 6.13 (d, J = 1.0 Hz, 1 H), 4.18 (m, 2 H), 3.89 (m, 2 H), 3.74 (m, 2 H), 3.67 (m, 4 H), 3.55 (m, 2 H), 3.37 (s, 3 H), 2.39 (d, J = 1.0 Hz, 3 H).

mp3C2: ^{1}H NMR (DMSO-d6, 400 MHz) δ: 7.70 (d, J = 9.0 Hz, 1 H), 7.02 (d, J = 2.5 Hz, 1 H), 6.97 (dd, J_1 = 9.0 Hz, J_2 = 2.5 Hz, 1 H), 5.77 (s, 1 H), 4.22 (m, 2 H), 4.00 (s, 3 H), 3.78 (m, 2 H), 3.61 (m, 2 H), 3.55 (m, 2 H), 3.52 (m, 2 H), 3.43 (m, 2 H), 3.24 (s, 3 H). ESI-MS $C_{17}H_{23}O_7^+$, calcd. 339.144 m/z, found 339.141 m/z

mp3C3: ^{1}H NMR (DMSO-d6, 400 MHz) δ: 7.71 (d, J = 9.0 Hz, 1 H), 7.01 (d, J = 2.5 Hz, 1 H), 6.97 (dd, J_1 = 9.0 Hz, J_2 = 2.5 Hz, 1 H), 5.78 (s, 1 H), 4.34 (m, 2 H), 3.86 (m, 5 H), 3.65 (m, 2 H), 3.55 (m, 4 H), 3.43 (m, 2 H), 3.24 (s, 3 H). ESI-MS $C_{17}H_{23}O_7^+$, calcd. 339.144 m/z, found 339.143 m/z

mp3C4: ^{1}H NMR (DMSO-d6, 400 MHz) δ: 7.82 (dd, J_1 = 8.0 Hz, J_2 = 1.5 Hz, 1 H), 7.68 (td, J_1 = 7.5 Hz, J_2 = 1.5 Hz, 1 H), 7.40 (m, 2 H), 5.95 (s, 1 H), 4.37 (m, 2 H), 3.88 (m, 2 H), 3.65 (m, 2 H), 3.55 (m, 4 H), 3.42 (m, 2 H), 3.23 (s, 3 H). ESI-MS $C_{16}H_{21}O_6^+$, calcd. 309.134 m/z, found 309.137 m/z

mp3C5: ^{1}H NMR (DMSO-d6, 400 MHz) δ: 7.81 (d, J = 8.5 Hz, 1 H), 7.62 (d, J = 2.0 Hz, 1 H), 7.46 (dd, J_1 = 8.5 Hz, J_2 = 2.0 Hz, 1 H), 5.98 (s, 1 H), 4.37 (m,

2 H), 3.87 (m, 2 H), 3.65 (m, 2 H), 3.56 (m, 2 H), 3.53 (m, 2 H), 3.42 (m, 2 H), 3.23 (s, 3 H). ESI-MS $C_{15}H_{20}ClO_6^+$, calcd. 343.095 m/z, found 343.093 m/z

^{1}H-NMR and ^{13}C-NMR of the final products in D_2O

H$_2$dp3C1

^{1}H NMR (400 MHz, D_2O) δ= 7.43 (s, 2 H), 7.36 (m, 1 H), 6.78 (m, 1 H), 6.70 (m, 1 H), 6.02 (m, 1 H), 4.27 (d, J = 1.0 Hz, 2 H), 4.16 (m, 2 H), 3.97 (m, 2 H), 3.93 (m, 2 H), 3.84 (m, 4 H), 2.20 (s, 3 H)

Na$_2$dp3C2

^{1}H NMR (400 MHz, D_2O) δ 7.48 (d, 1 H, J = 8.5 Hz), 7.20 (s, 2 H), 6.80 (m, 2 H), 5.43 (s, 1 H), 4.18 (m, 2 H), 4.00 (m, 2 H), 3.85 (m, 5 H), 3.80 (m, 2 H), 3.74 (m, 2 H), 3.67 (m, 2 H).

^{13}C NMR (101 MHz, D_2O) δ 171.9 (C$_{carboxylate}$), 168.0 (^{4Coum}C$_{ar}$-O), 166.6 (^{4pyr}C$_{ar}$-O), 166.0 (^{7Coum}C$_{ar}$-O), 161.7 (^{2Coum}C$_{ar}$=O), 154.2 ($^{(2+6)pyr}$C$_{ar}$), 153.6 ($^{(8-1)-bridgeCoum}$C$_{ar}$), 124.0 (^{5Coum}C$_{ar}$-H), 112.8 (^{6Coum}C$_{ar}$-H), 111.1 ($^{(3+5)pyr}$C$_{ar}$-H), 108.3 ($^{(4-5)-bridgeCoum}$C$_{ar}$), 100.7 (^{8Coum}C$_{ar}$-H), 86.3 (^{3Coum}C$_{ar}$-H), 69.9 (OCH$_2$-C-H$_2$), 69.8 (OCH$_2$-C-H$_2$), 68.7 (OCH$_2$-C-H$_2$), 68.6 (OCH$_2$-C-H$_2$), 67.4 (OCH$_2$-C-H$_2$), 67.3 (OCH$_2$-C-H$_2$), 56.6 (O-C-H$_3$).

Na$_2$dp3C3

1H NMR (400 MHz, D_2O) δ 7.27 (d, J=9.0 Hz, 1 H), 7.05 (s, 2 H), 6.49 (dd, J=2.5, 9.0 Hz, 1 H), 6.33 (d, J=2.5 Hz, 1 H), 5.32 (s, 1 H), 4.12 (m, 2 H), 3.99 (m, 2 H), 3.87 (m, 2 H), 3.79 (m, 2 H), 3.74 (m, 2 H), 3.69 (m, 2 H), 3.62 (s, 3 H).

^{13}C NMR (101 MHz, D_2O) δ 171.8 (C$_{carboxylate}$), 167.1 (^{4Coum}C$_{ar}$-O), 166.5 (^{4pyr}C$_{ar}$-O), 165.9 (^{7Coum}C$_{ar}$-O), 162.7 (^{2Coum}C$_{ar}$=O), 154.1 ($^{(2+6)pyr}$C$_{ar}$), 153.8 ($^{(8-1)-bridgeCoum}$C$_{ar}$), 124.0 (^{6Coum}C$_{ar}$-H), 112.5 (^{5Coum}C$_{ar}$-H), 110.9 ($^{(3+5)pyr}$C$_{ar}$-H), 108.0 ($^{(4-5)-bridgeCoum}$C$_{ar}$), 99.9 (^{8Coum}C$_{ar}$-H), 86.9 (^{3Coum}C$_{ar}$-H), 70.2 (OCH$_2$-C-H$_2$), 69.9 (OCH$_2$-C-H$_2$), 68.7 (OCH$_2$-C-H$_2$), 68.5 (OCH$_2$-C-H$_2$), 68.2 (OCH$_2$-C-H$_2$), 67.3 (OCH$_2$-C-H$_2$), 55.7 (O-C-H$_3$).

Na$_2$dp3C4

^{1}H NMR (400 MHz, D_2O) δ 7.91 (m, 1 H), 7.62 (m, 1 H), 7.40 (m, 2 H), 7.33 (m, 2 H), 5.91 (m, 1 H), 4.49 (m, 2 H), 4.26 (m, 2 H), 4.12 (m, 2 H), 4.01 (m, 2 H), 3.94 (m, 2 H), 3.89 (m, 2 H).

^{13}C NMR (101 MHz, D_2O) δ 172.0 (C$_{carboxylate}$), 166.8 (^{4Coum}C$_{ar}$-O), 166.1 (^{4pyr}C$_{ar}$-O), 166.0 (^{2Coum}C$_{ar}$=O), 154.3 ($^{(2+6)pyr}$C$_{ar}$), 152.0 ($^{(8-1)-bridgeCoum}$C$_{ar}$), 133.0 (^{7Coum}C$_{ar}$-

H), 124.6 ($^{6Coum}C_{ar}$-H), 122.8 ($^{5Coum}C_{ar}$-H), 116.4 ($^{8Coum}C_{ar}$-H), 114.6 ($^{(4-5)\text{-}bridgeCoum}C_{ar}$),111.0 ($^{(3+5)pyr}C_{ar}$-H), 89.4 ($^{3Coum}C_{ar}$-H), 70.1 (OCH$_2$-C-H$_2$), 69.8 (OCH$_2$-C-H$_2$), 68.6 (2x OCH$_2$-C-H$_2$), 68.2 (OCH$_2$-C-H$_2$), 67.3 (OCH$_2$-C-H$_2$).

Na$_2$dp3C5

^{1}H NMR (400 MHz, D$_2$O) δ 7.45 (m, 1 H), 7.08 (m, 2 H), 7.01 (m, 2 H), 5.56 (s, 1 H), 4.22 (m, 2 H), 4.04 (m, 2 H), 3.92 (m, 2 H), 3.82 (m, 2 H), 3.76 (m, 2 H), 3.72 (m, 2 H).

^{13}C NMR (101 MHz, D$_2$O) δ 171.7 (C$_{carboxylate}$), 166.0 ($^{4Coum}C_{ar}$-O), 165.9 ($^{4pyr}C_{ar}$-O), 165.3 ($^{2Coum}C_{ar}$=O), 154.1 ($^{(2+6)pyr}C_{ar}$), 152.0 ($^{(8-1)\text{-}bridgeCoum}C_{ar}$), 138.1 ($^{7Coum}C_{ar}$-Cl), 124.9 ($^{5Coum}C_{ar}$-H), 124.1 ($^{6Coum}C_{ar}$-H), 116.4 ($^{8Coum}C_{ar}$-H), 113.2 ($^{(4-5)\text{-}bridgeCoum}C_{ar}$), 110.9 ($^{(3+5)pyr}C_{ar}$-H), 89.4 ($^{3Coum}C_{ar}$-H), 70.2 (OCH$_2$-C-H$_2$), 70.0 (OCH$_2$-C-H$_2$), 68.9 (OCH$_2$-C-H$_2$), 68.7 (OCH$_2$-C-H$_2$), 68.2 (OCH$_2$-C-H$_2$), 67.4 (OCH$_2$-C-H$_2$).

Elemental analysis of the final products

H$_2$dp3C1

C$_{23}$H$_{23}$NO$_{10}$ 1.6 H$_2$O (502.26): calcd. C 55.00, H 5.26, N 2.79; found C 55.07, H 5.23, N 3.04

Na$_2$dp3C2

Na$_2$C$_{23}$H$_{21}$NO$_{11}$ · 2 NaOH (613.40): calcd. C 45.04, H 3.78, N 2.28; found C 45.05, H 3.87, N 2.15

Na$_2$dp3C3

Na$_2$C$_{23}$H$_{21}$NO$_{11}$ · 2.3 NaOH (625.40): calcd. C 44.17, H 3.76, N 2.24; found C 44.19, H 3.62, N 2.52

Na$_2$dp3C4

Na$_2$C$_{22}$H$_{19}$NO$_{10}$ · 0.85 NaOH · 0.25 CH$_3$CH$_2$OH (548.89): calcd. C 49.24, H 3.92, N 2.55; found C 49.24, H 3.97, N 2.48

Na$_2$dp3C5

Na$_2$C$_{22}$H$_{18}$ClNO$_{10}$ · 0.4 CH$_3$CH$_2$OH (556.25): calcd. C 49.23, H 3.70, N 2.52; found C 49.30, H 3.68, N 2.30

Appendix D: Synthesis of the dpxC1 ligands

The shortening of the POE side chain was carried out by using shorter tosylated oligooxyethylene monomethyl ethers prepared according to the same procedure as the parent trioxyethylene linker. The rest of the synthesis is exactly the same as the synthesis of the dp3Cy ligands.

Characterisations of the compounds

^{1}H-NMR and ^{13}C-NMR of the final products in D_2O

Na$_2$dp2C1

^{1}H NMR (400 MHz, D$_2$O) δ 7.45 (d, 1 H, *J* = 9.0 Hz), 7.30 (s, 2 H), 6.88 (d, 1 H, *J* = 2.5 Hz), 6.82 (dd, 1 H, *J* = 9.0, 2.5 Hz), 6.10 (s, 1 H), 4.33 (m, 2 H), 4.22 (m, 2 H), 3.99 (m, 4 H), 2.32 (s, 3 H).

^{13}C NMR (HSQC) δ 126.1 (^{5Coum}C$_{ar}$-H), 113.9 (^{6Coum}C$_{ar}$-H), 111.2 ($^{(3+5)pyr}$C$_{ar}$-H), 110.2 (^{8Coum}C$_{ar}$-H), 101.7 (^{3Coum}C$_{ar}$-H), 68.8 (OCH$_2$-C-H$_2$), 68.6 (OCH$_2$-C-H$_2$), 67.6 (OCH$_2$-C-H$_2$), 67.4 (OCH$_2$-C-H$_2$), 17.9 (^{4Coum}C$_{ar}$-C-H$_3$).

Na$_2$dp1C1

^{1}H NMR (400 MHz, D$_2$O) δ 7.57 (d, 1 H, *J* = 9.0 Hz), 7.47 (s, 2 H), 6.94 (d, 1 H, *J* = 9.0 Hz), 6.90 (s, 1 H), 6.11 (s, 1 H), 4.53 (m, 2 H), 4.48 (m, 2 H), 2.34 (s, 3 H).

^{13}C NMR (HSQC) δ 125.9 (^{5Coum}C$_{ar}$-H), 113.1 (^{6Coum}C$_{ar}$-H), 111.4 ($^{(3+5)pyr}$C$_{ar}$-H), 110.3 (^{8Coum}C$_{ar}$-H), 101.8 (^{3Coum}C$_{ar}$-H), 67.0 (OCH$_2$-C-H$_2$), 66.8 (OCH$_2$-C-H$_2$), 18.0 (^{4Coum}C$_{ar}$-C-H$_3$).

Elemental analysis of the final products

Na$_2$dp2C1

Na$_2$C$_{21}$H$_{17}$NO$_9$ · 2.0 NaOH (553.34): calcd. C 45.58, H 3.46, N 2.53; found C 45.56, H 3.20, N 2.77

Na$_2$dp1C1

Na$_2$C$_{19}$H$_{13}$NO$_8$ · 2.0 H$_2$O (465.33): calcd. C 49.04, H 3.68, N 3.01; found C 49.02, H 3.69, N 2.94

Appendix E: Experimental part

The analytical grade solvents and chemicals were used without further purification. The aqueous solutions were prepared from doubly distilled water. The lanthanide solutions were prepared from the corresponding perchlorate salt and were titrated by complexometry using a standardized Na_2H_2EDTA solution in urotropine-buffered medium and with xylenol orange as indicator.

Spectrophotometric measurements

The UV-Vis absorption spectra were measured on a Perkin-Elmer Lambda 900 spectrophotometer or on a Perkin-Elmer Cary 1E spectrophotometer using 1 cm pathlength quartz cells or 0.2 cm pathlength quartz cells. The spectrophotometric titrations were performed with a J&M diode array spectrometer (Tidas series) connected to an external computer, or with one of the Perkin-Elmer spectrophotometers in 1 cm pathlength quartz cells. All titrations with the Tidas spectrometer were performed in a thermostated (25.0°C) glass-jacketed vessel and in a 0.1 M solution in KCl. In a typical ligand titration experiment as a function of pH, 25 ml of a $3 \cdot 10^{-5}$ M ligand solution was titrated with a standardized 0.1 M NaOH solution. The pH of the solution was continually measured with a freshly calibrated 3.0 M KCl electrode to ensure the pH value after base addition was stable. A UV-Vis spectrum using a Hellma optrode (optical pathlength of 1 cm) connected to the Tidas spectrometer and immersed in the thermostated vessel was then recorded once the pH value was stable. The procedure was repeated to measure the absorption each 0.2-0.4 pH unit. Since the titrations were performed with a base addition, the solutions were previously acidified with HCl until the absorption spectra do not change anymore (pH 1–2).

The factor analysis and mathematical treatment of the spectrophotometric data were performed with the SPECFIT program.

NMR measurements

The titrations of the ligands with Lu^{3+} were performed by addition of 2 µl of a 0.0825 M $Lu(ClO_4)_3$ solution in D_2O to 0.5 ml of a $3 \cdot 10^{-3}$ M solution of the ligand

in D_2O (0.11 equivalent of Lu^{3+} per addition). The ^1H and ^{31}P NMR spectra were recorded on a Bruker Avance DRX 400 spectrometer.

Luminescence measurements

The room temperature excitation and emission spectra were recorded on a Fluorolog 3-22 spectrofluorimeter from Jobin-Yvon or on a Perkin Elmer LS50B spectrofluorimeter in phosphorescence mode with a zero delay. The titration experiments were performed either on a Fluorolog 3-22 or on a Perkin Elmer LS50B in phosphorescence mode by integrating the intensity at 615 nm and monitoring the variation upon addition of aliquots containing 1/15 europium equivalent to a 0.1 M Tris buffered aqueous solution (pH 7.4) with a 0.3 mM concentration of ligand. The excitation and emission spectra, as well as the titration experiments were measured in 1 cm or 0.2 cm pathlength quartz cells.

Time-resolved measurements were performed either with a Fluorolog 3-22 or with a Hamamatsu photonic multichannel analyser C8808 detector after excitation of the samples by an Ekspla NT 342/3/UV pulsed laser. The wavelength of the laser can be tuned from the UVC up to the NIR. In a typical experiment, the excitation wavelength was set at 320 nm and gave a 6 ns pulse of 0.53 ± 0.04 cm^2 with a typical energy of 5 mJ at a frequency of 20 Hz. The resulting emissions were collected with an optical fibre and analysed on a Hamamatsu photonic multichannel analyser C8808 detector.

The low temperature measurements were performed at 77 K in quartz Suprasil® capillaries with 10 % glycerol added to the Tris-buffered aqueous solutions, and measured either with a Fluorolog 3-22 or with a Hamamatsu photonic multichannel analyser C8808 detector.

The quantum yields were determined in an integrating sphere by measuring the ratio of the emitted corrected intensity over the absorbed corrected intensity. Empty capillaries have been used as a blank. A 75 W Xenon light source with a monochromator was used as a light source. The emissions from the integrating sphere were collected with an optical fibre and analysed on a Hamamatsu photonic multichannel analyser C8808 detector. The correction function of the setup was calculated with a calibrated standards Deuterium and Halogen light sources as reference irradiances. Alternatively, the quantum yields were measured comparatively to europium or terbium trisdipicolinate aqueous solutions in Tris-

HCl 0.1 M at pH 7.4, which respectively exhibit a 24 % or 22 % quantum yield.[14] All concentrations were set at $1 \cdot 10^{-4}$ M, including the concentration of the reference trisdipicolinate complexes. The excitation wavelength was chosen where the absorption spectra of the reference and of the sample cross to ensure an identical amount of absorbed quanta.

All emission spectra were measured in photon counts and corrected for the instrumental function. The luminescence evolution of the europium complexes was performed by variation of the pH similarly to the titration of the ligands but in a 1:3 europium/ligand solution.

Relative spectral radiant emittances

The luminescent backlit emittances were measured on an optical table with a Maya2000 Pro back-thinned CCD spectrophotometer from Ocean Optics. The light source was a Camag UV lamp set on 254 nm (an 8W uncoated mercury lamp filtered through a Schott UV11 bandpass filter). The excitation light source was facing the luminescent image at 30° and the resulting emission was recorded with the Maya 2000 Pro spectrophotometer at 10°. The captured emission spectra were corrected to account for the wavelength non-linearity of the detector and to yield relative radiometric units. The correction was performed using a calibrated DHL-2000-BAL lamp from Ocean Optics.
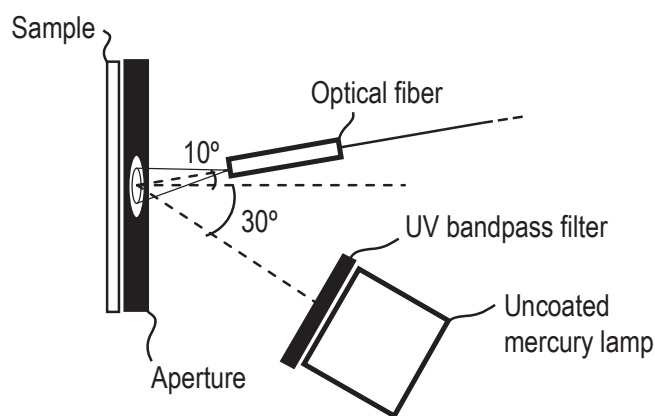
Figure 81. Setup used for measuring relative spectral radiant emittances of luminescent samples excited under 254 nm UV light
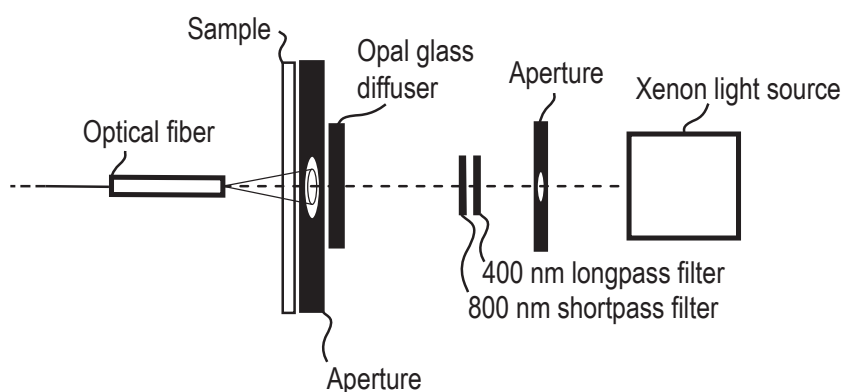
Transmittance measurements

The transmittances were measured on an optical table with a Maya2000 Pro back-thinned CCD spectrophotometer from Ocean Optics. The light source was a 75W Xenon light source filtered through a longpass filter with a cutoff wavelength at 400 nm and a shortpass filter with a cutoff wavelength at 800 nm. This light source was diffused on an opal glass placed in front of a 1 cm diameter illumination window, and a 600 μm optical fiber was used to collect the transmitted light. The viewing cone of the fiber was checked to be centered on the sample illumination window when the sample is placed in between the light source and the optical fiber (back illumination). The dark response of the detector was subtracted from each spectrum and was recorded each five measurements in order to take into account the heating of the CCD once illuminated, while the reference spectrum for measuring the transmittance spectra was the filtered Xe light source diffused through the opal glass, which was also recorded each five measurements in order to take into account the variations of the intensity of the light source that might occur.

Figure 82. Setup for measuring transmittances with a visible light source

Luminescent backlit relative spectral radiant emittances

The luminescent backlit emittances were measured using the same apparatus as the transmittances. The light source was replaced with a 9W mercury lamp (with a broad peak at 366 nm), and with a 365 nm bandpass filter (Schott UV11 filter). Because the luminescent layer emits diffusely, there is no need for an opal glass diffuser in front of the illuminated sample. The excitation light source was facing at 0° the luminescent layer located on the verso side of the unprinted substrate and the

232

resulting emission was recorded with the Maya 2000 Pro spectrophotometer on the recto side of the unprinted substrate at 0°. The captured emission spectra were corrected to account for the wavelength non-linearity of the detector and to yield relative radiometric units. The correction was performed using a calibrated DHL-2000-BAL lamp from Ocean Optics.
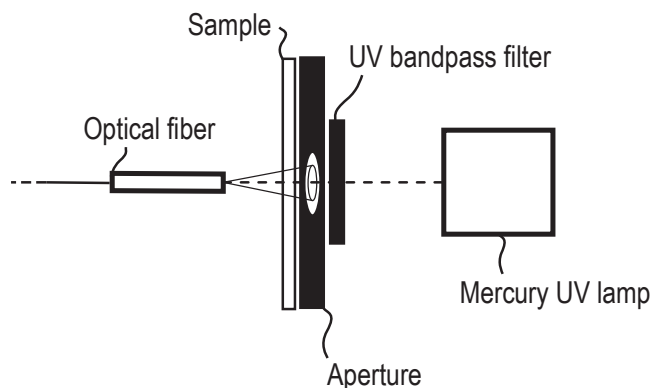
Figure 83. Setup for measuring luminescent backlit samples

Calibration and test of the spectral prediction models

In a typical calibration procedure of a spectral prediction model, the 36 variations of the 25 %, 50 %, and 75 % surface coverages of the three inks are measured in addition to the eight colorants. These measurements are used to obtain the twelve ink spreading curves by fitting the ink surface coverages depending on the twelve superposition conditions and by minimizing the difference between the predicted spectra according to the spectral prediction model and the measured spectra.

Once the ink spreading curves are calibrated, the model is tested. First, the 125 color samples formed by the 0 %, 25 %, 50 %, 75 % and 100 % surface coverages variations of the three inks are measured. The measured spectra are then converted to CIE-XYZ colors and then to CIELAB colors. The 125 color samples are then predicted according to the spectral prediction model by finding the effective surface coverages of the inks using the ink-spreading curves, by using Demichel's equations to obtain the corresponding surface coverages of the colorants that are needed in the spectral prediction models. The predicted spectra are then converted to CIE-XYZ and CIELAB colors. Finally, the prediction accuracy of the model is determined by computing the ΔE_{94} color difference between the measured and predicted CIELAB colors for the 125 tested colors.

Appendix F: Complexation, equilibria and stability constants

Without any acid-base considerations, the equilibrium between the free ligand L^{n-}, the aqua complex of the lanthanide ion $[Ln(H_2O)_9]^{3+}$ and the metal-ligand complexes $[LnL_x]^{3-x \cdot n}$ can be expressed as follows in Equation 39:

$$[Ln(H_2O)_9]^{3+} + x\, L^{n-} \leftrightarrows [Ln(H_2O)_{(9-m \cdot x)}L_x]^{(3-x \cdot n)} + m \cdot x\, H_2O \qquad (40)$$
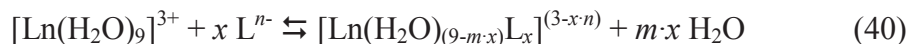
$$K = \frac{a\left([Ln(H_2O)_{(9-m \cdot x)}L_x]^{(3-x \cdot n)}\right) \cdot a\left(H_2O\right)^{m \cdot x}}{a\left([Ln(H_2O)_9]^{3+}\right) \cdot a\left(L^{n-}\right)^x} \qquad (41)$$

The equilibrium constant K is expressed here from the activities $a(i)$ of the compound i involved in the chemical equilibrium. The activity is a dimensionless quantity. From a thermodynamic point of view, it is expressed by Equation 41 as a deviation from the standard chemical potential $\mu_i^{\ominus}$ of the compound i.

$$a(i) = \exp\left(\frac{\mu_i - \mu_i^{\ominus}}{R \cdot T}\right) \qquad (42)$$

The chemical potential is the variation of the molar free enthalpy as a function of the variation of the number of compound i at constant temperature and pressure. The activity is a function of the concentration c_i of the compound i normalized by a standard concentration (usually, $c^{\ominus} = 1\,M$). The proportionality coefficient called activity coefficient γ_i defines the deviation from an ideal solution.

$$a(i) = \gamma_i \cdot \frac{c_i}{c^{\ominus}} \qquad (43)$$

For diluted solutions, the activity coefficient $\gamma_i = 1$, so that activities are replaced by normalized concentrations. The normalization by the standard concentration only cancels the dimension of the concentrations. In practice, the normalization is often omitted, the expression of the chemical equilibrium in Equation 40 thus becomes Equation 43 when using the bracket notation for concentrations. Nevertheless, the
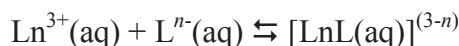
equilibrium constant K has to remain dimensionless, even though the notation suggests a dimension.
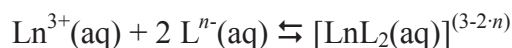
$$K = \frac{\left[[Ln(H_2O)_{(9-m\cdot x)}L_x]^{(3-x\cdot n)} \right] \cdot \left[H_2O \right]^{m\cdot x}}{\left[[Ln(H_2O)_9]^{3+} \right] \cdot \left[L^{n-} \right]^x} \tag{44}$$

In this thesis, the same notation as in Equation 43 is used.

The stoichiometry of the $[Ln(H_2O)_{(9-m\cdot x)}L_x]^{(3-x\cdot n)}$ complex depends on the number of coordination sites on the ligand L^{n-} and its steric hindrance. For example, a tridentate ligand (that is commonly encountered with lanthanide ions) releases three water molecule per ligand ($m = 3$). Since the coordination number of lanthanide ions is nine, three ligands are required to fill the coordination sphere ($x = 3$). Nevertheless, the formation of intermediate still hydrated complexes is expected. Therefore, the tridentate ligand may also form bis- and mono-coordinated ligand complexes in addition to the nonhydrated tris complex. The constants of those equilibria are usually expressed as β values. If we simplify the notation by writing the aqua complex as a free lanthanide ion in aqueous solution Ln^{3+}(aq) thus getting rid of the water molecules in the equilibria (the concentration of water in water can anyway be set constant at 55.56 M), it yields the following Equations 44-47:

$$Ln^{3+}(aq) + L^{n-}(aq) \leftrightarrows [LnL(aq)]^{(3-n)}$$

$$\beta_1 = \frac{\left[[LnL]^{(3-n)} \right]}{\left[Ln^{3+} \right] \cdot \left[L^{n-} \right]} \tag{45}$$

$$Ln^{3+}(aq) + 2\,L^{n-}(aq) \leftrightarrows [LnL_2(aq)]^{(3-2\cdot n)}$$

$$\beta_2 = \frac{\left[[LnL_2]^{(3-2\cdot n)} \right]}{\left[Ln^{3+} \right] \cdot \left[L^{n-} \right]^2} \tag{46}$$

$$Ln^{3+}(aq) + 3\,L^{n-}(aq) \leftrightarrows [LnL_3(aq)]^{(3-3\cdot n)}$$
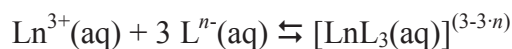
$$\beta_3 = \frac{\left[[LnL_3]^{(3-3\cdot n)} \right]}{\left[Ln^{3+} \right] \cdot \left[L^{n-} \right]^3} \tag{47}$$

$$Ln^{3+}(aq) + x\ L^{n-}(aq) \leftrightarows [LnL_3(aq)]^{(3-x \cdot n)}$$
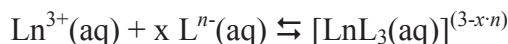
$$\beta_x = \frac{\left[[LnL_x]^{(3-x \cdot n)} \right]}{\left[Ln^{3+} \right] \cdot \left[L^{n-} \right]^x} \tag{48}$$

The β values can also be expressed as equilibrium constants K_x for the successive complexations shown hereafter in Equation 48-50:

$$Ln^{3+}(aq) + L^{n-}(aq) \leftrightarows [LnL(aq)]^{(3-n)}$$

$$K_1 = \frac{\left[[LnL]^{(3-n)} \right]}{\left[Ln^{3+} \right] \cdot \left[L^{n-} \right]} = \beta_1 \tag{49}$$

$$[LnL(aq)^{(3-n)}] + L^{n-}(aq) \leftrightarows [LnL_2(aq)]^{(3-2 \cdot n)}$$
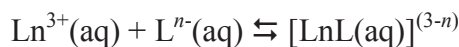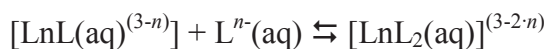
$$K_2 = \frac{\left[[LnL_2]^{(3-2 \cdot n)} \right]}{\left[[LnL]^{(3-n)} \right] \cdot \left[L^{n-} \right]} = \frac{\beta_2}{K_1} \tag{50}$$

$$[LnL_2(aq)^{(3-2 \cdot n)}] + L^{n-}(aq) \leftrightarows [LnL_3(aq)]^{(3-3 \cdot n)}$$
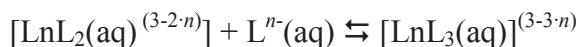
$$K_3 = \frac{\left[[LnL_3]^{(3-3 \cdot n)} \right]}{\left[[LnL_2]^{(3-2 \cdot n)} \right] \cdot \left[L^{n-} \right]} = \frac{\beta_3}{K_1 \cdot K_2} \tag{51}$$

Hence, the β values are the product of the successive equilibrium constants ($\beta_1 = K_1$, $\beta_2 = K_1 \cdot K_2$, $\beta_3 = K_1 \cdot K_2 \cdot K_3$). Those β stability constants are usually expressed as $\log\beta$ values. The $\log\beta_x$ are then the sum of the logarithmic successive equilibrium constants.

Appendix G: Supplementary luminescent color images

Figure 84. Setup used to shoot pictures of luminescent color images
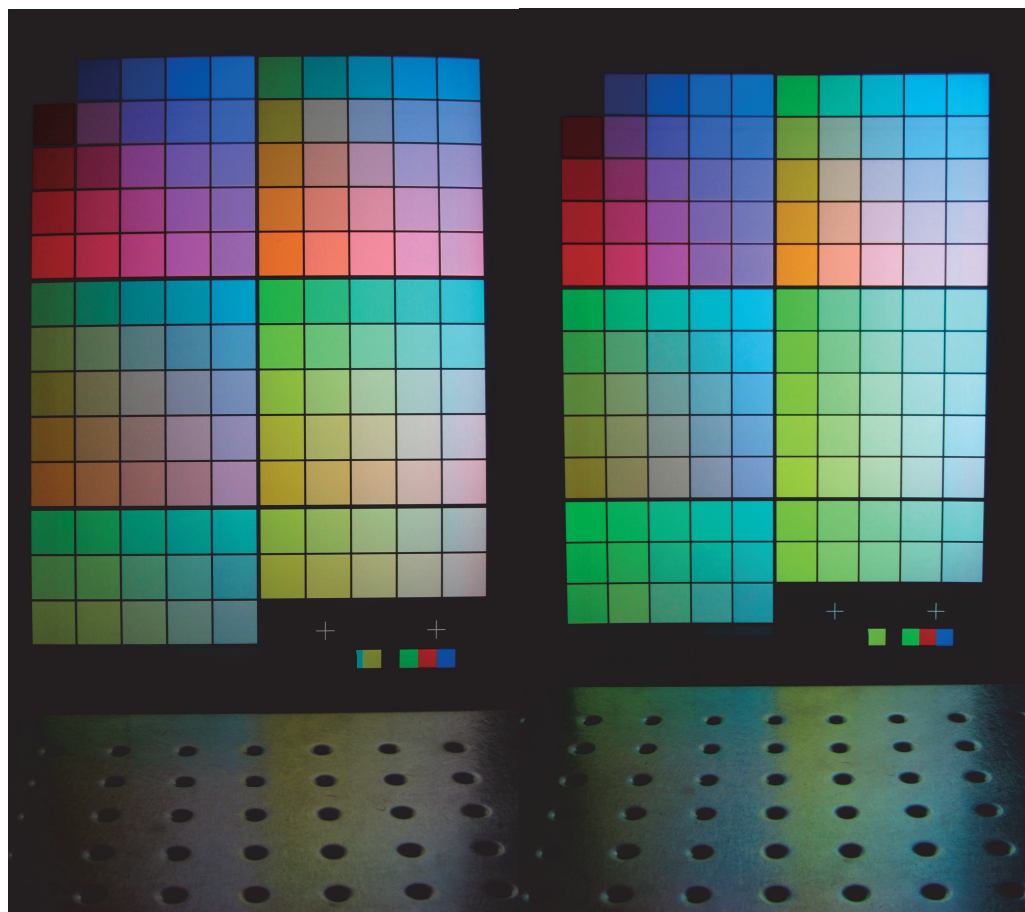
Figure 85. Photographs of the 125 luminescent color samples used to calibrate and test the spectral prediction model printed on the Canson paper (left) and on the Hahnemühle paper (right)

Figure 86. Photographs of the fruits, ski and orchestra luminescent images printed on the Canson paper (left) and on the Hahnemühle paper (right)

Figure 87. Photographs of luminescent images (the Balmoral Hotel in Edinburgh and of the coast of the Isle of Skye in Scotland) printed on the Canson paper (left) and on the Hahnemühle paper (right)

Figure 88. Photographs of luminescent images (a sunset, a Ferrari and a black and white picture) printed on the Canson paper (left) and on the Hahnemühle paper (right)
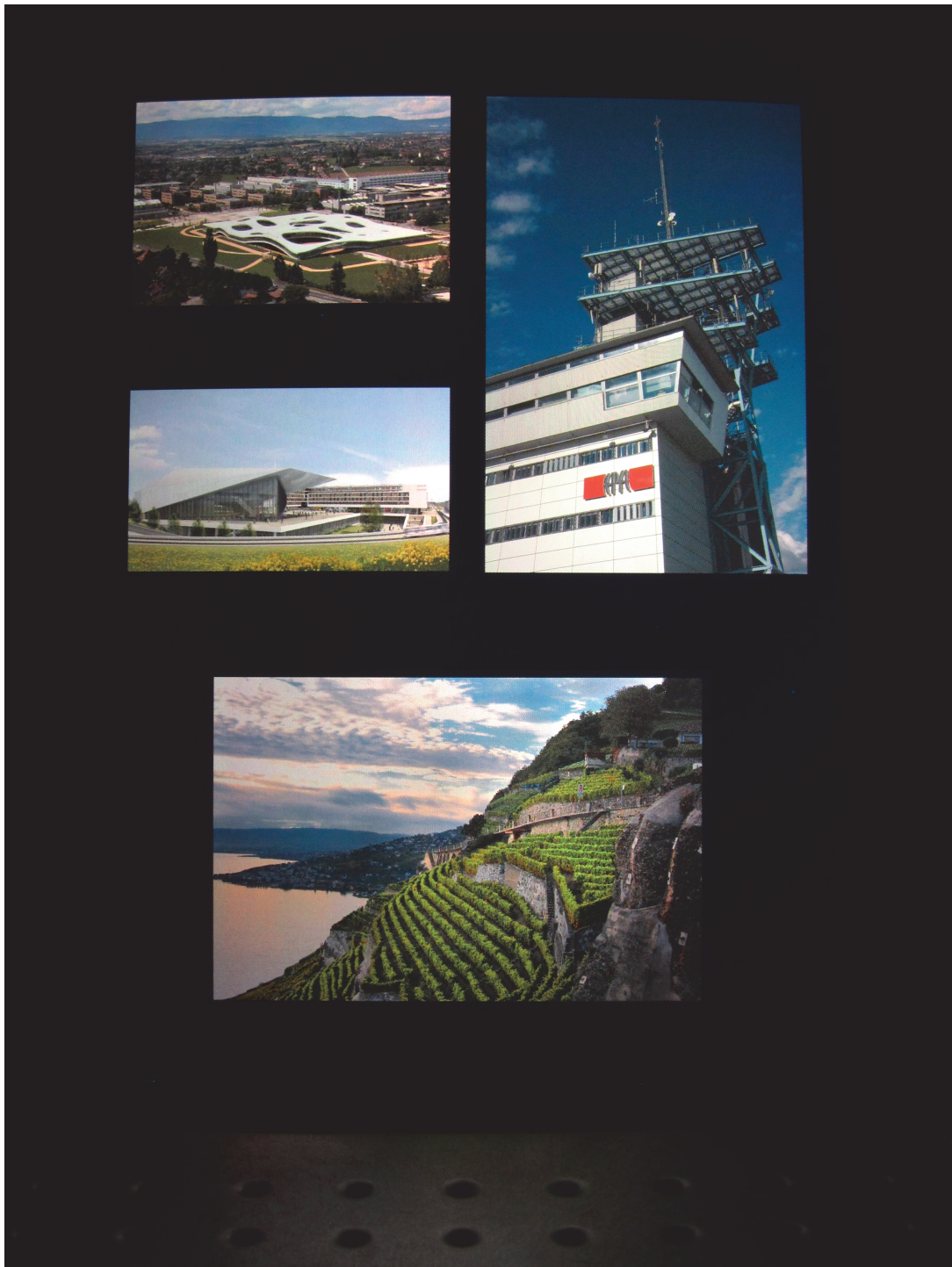
Figure 89. Photographs of luminescent color images (EPFL pictures and Lavaux wineyards) printed on the Canson paper

References

References

1. S. Cotton. *Lanthanide and actinide chemistry*. John Wiley & Sons Ltd, Chichester, UK, 2006.

2. C.-H. Huang. *Rare earth coordination chemistry : fundamentals and applications*. John Wiley& Sons, Singapore ; Hoboken, NJ, 2010.

3. M. D. Seymour and Q. Fernando. Effect of Ionic-Strength on Equilibrium-Constants - Use of a Pre-Programmed or Programmable Pocket Calculator in Laboratory. *J Chem Educ*, **1977**, *54* (4), 225-227.

4. J. Andres and A. S. Chauvin, (2012) Lanthanide: Luminescence Applications in *The Rare Earth Elements: Fundamentals and Applications*, ed. D. A. Atwood. Chichester, UK: John Wiley & Sons Ltd, pp. 135-152.

5. J. Andres and A. S. Chauvin, (2012) Lanthanide: Luminescence in *The Rare Earth Elements: Fundamentals and Applications*, ed. D. A. Atwood. Chichester, UK: John Wiley & Sons Ltd, pp. 111-133.

6. P. Hänninen and H. Härmä. *Lanthanide luminescence : photophysical, analytical and biological aspects*. Springer, Heidelberg, 2011.

7. B. Valeur. *Molecular fluorescence : principles and applications*. Wiley-VCH, Weinheim ; New York, 2002.

8. T. Forster. 10th Spiers Memorial Lecture - Transfer Mechanisms of Electronic Excitation. *Discuss Faraday Soc*, **1959**, (27), 7-17.

9. D. L. Dexter. A Theory of Sensitized Luminescence in Solids. *J Chem Phys*, **1953**, *21* (5), 836-850.

10. M. Kleinerman. Energy Migration in Lanthanide Chelates. *J Chem Phys*, **1969**, *51* (6), 2370-&.

11. R. M. Supkowski and W. D. Horrocks. On the determination of the number of water molecules, q, coordinated to europium(III) ions in solution from luminescence decay lifetimes. *Inorg Chim Acta*, **2002**, *340*, 44-48.

12. M. H. V. Werts, R. T. F. Jukes and J. W. Verhoeven. The emission spectrum and the radiative lifetime of Eu3+ in luminescent lanthanide complexes. *Phys Chem Chem Phys*, **2002**, *4* (9), 1542-1548.

13. D. L. Rosen, C. Sharpless and L. B. McGown. Bacterial spore detection and determination by use of terbium dipicolinate photoluminescence. *Anal Chem*, **1997**, *69* (6), 1082-1085.

14. A. S. Chauvin, F. Gumy, D. Imbert and J. C. G. Bunzli. Europium and terbium tris(dipicolinates) as secondary standards for quantum yield determination. *Spectrosc Lett*, **2004**, *37* (5), 517-532.

15.   A. L. Gassner, C. Duhot, J. C. G. Bunzli and A. S. Chauvin. Remarkable tuning of the photophysical properties of bifunctional lanthanide tris(dipicolinates) and its consequence on the design of bioprobes. *Inorg Chem*, **2008**, *47* (17), 7802-7812.

16.   L. VanMeervelt, K. Binnemans, K. VanHerck and C. GorllerWalrand. X-ray crystal structure analysis of the terbium dipicolinate complex Na-3[Tb(C7H3NO4)(3)].NaClO4.6H(2)O. *B Soc Chim Belg*, **1997**, *106* (1), 25-27.

17.   P. A. Brayshaw, J. M. Harrowfield and A. N. Sobolev. A Strongly Luminescent Organic-Solvent-Soluble Salt of the Tris(Dipicolinato)Europium(Iii) Trianion. *Acta Crystallogr C*, **1995**, *51*, 1799-1802.

18.   D. P. Glover-Fischer, D. H. Metcalf, T. A. Hopkins, V. J. Pugh, S. J. Chisdes, J. Kankare and F. S. Richardson. Excited-state enantiomer interconversion kinetics probed by time-resolved chiroptical luminescence spectroscopy. The solvent and temperature dependence of Lambda-Eu(dpa)(3)(3-)reversible arrow Delta-Eu(dpa)(3)(3-) enantiomer interconversion rates in solution. *Inorg Chem*, **1998**, *37* (12), 3026-3033.

19.   C. N. Reilley and B. W. Good. Structure-Independent Method for Dissecting Contact and Dipolar Nuclear Magnetic-Resonance Shifts in Lanthanide Complexes and Its Use in Structure Determination. *Anal Chem*, **1975**, *47* (13), 2110-2116.

20.   H. Donato and R. B. Martin. Dipolar Shifts and Structure in Aqueous-Solutions of 3-1 Lanthanide Complexes of 2,6-Dipicolinate. *J Am Chem Soc*, **1972**, *94* (12), 4129-&.

21.   I. Grenthe. Stability Relationships among Rare Earth Dipicolinates. *J Am Chem Soc*, **1961**, *83* (2), 360-&.

22.   I. Grenthe. Thermodynamic Properties of Rare Earth Complexes .2. Free Energy, Enthalpy and Entropy Changes for Formation of Rare Earth Diglycolate and Dipicolinate Complexes at 25.00 Degrees C. *Acta Chem Scand*, **1963**, *17* (9), 2487-&.

23.   A. Aebischer, F. Gumy and J. C. G. Bunzli. Intrinsic quantum yields and radiative lifetimes of lanthanide tris(dipicolinates). *Phys Chem Chem Phys*, **2009**, *11* (9), 1346-1353.

24.   M. Latva, H. Takalo, V. M. Mukkala, C. Matachescu, J. C. Rodriguez-Ubis and J. Kankare. Correlation between the lowest triplet state energy level of the ligand and lanthanide(III) luminescence quantum yield. *J Lumin*, **1997**, *75* (2), 149-169.

25.   E. Brunet, O. Juanes, R. Sedano and J. C. Rodriguez-Ubis. Lanthanide complexes of polycarboxylate-bearing dipyrazolylpyridine ligands with

near-unity luminescence quantum yields: the effect of pyridine substitution. *Photoch Photobio Sci*, **2002**, *1* (8), 613-618.

26.   K. Lunstroot, P. Nockemann, K. Van Hecke, L. Van Meervelt, C. Gorller-Walrand, K. Binnemans and K. Driesen. Visible and Near-Infrared Emission by Samarium(III)-Containing Ionic Liquid Mixtures. *Inorg Chem*, **2009**, *48* (7), 3018-3026.

27.   A. D'Aleo, L. Toupet, S. Rigaut, C. Andraud and O. Maury. Guanidinium as powerful cation for the design of lanthanate tris-dipicolinate crystalline materials: Synthesis, structure and photophysical properties. *Opt Mater*, **2008**, *30* (11), 1682-1688.

28.   G. L. Hilmes, N. Coruh and J. P. Riehl. Quantitative Aspects of Pfeiffer Effect Optical-Activity in Aqueous Dysprosium(Iii) Complexes with 2,6-Pyridinedicarboxylic Acid. *Inorg Chem*, **1988**, *27* (7), 1136-1139.

29.   C. Andraud and O. Maury. Lanthanide Complexes for Nonlinear Optics: From Fundamental Aspects to Applications. *Eur J Inorg Chem*, **2009**, (29-30), 4357-4371.

30.   A. D'Aleo, A. Picot, P. L. Baldeck, C. Andraud and O. Maury. Design of Dipicolinic Acid Ligands for the Two-Photon Sensitized Luminescence of Europium Complexes with Optimized Cross-Sections. *Inorg Chem*, **2008**, *47* (22), 10269-10279.

31.   E. Deiters, B. Song, A. S. Chauvin, C. D. B. Vandevyver and J. C. G. Bunzli. Effect of the length of polyoxyethylene substituents on luminescent bimetallic lanthanide bioprobes. *New J Chem*, **2008**, *32* (7), 1140-1152.

32.   V. Fernandez-Moreira, B. Song, V. Sivagnanam, A. S. Chauvin, C. D. B. Vandevyver, M. Gijs, I. Hemmila, H. A. Lehr and J. C. G. Bunzli. Bioconjugated lanthanide luminescent helicates as multilabels for lab-on-a-chip detection of cancer biomarkers. *Analyst*, **2010**, *135* (1), 42-52.

33.   I. M. Clarkson, A. Beeby, J. I. Bruce, L. J. Govenlock, M. P. Lowe, C. E. Mathieu, D. Parker and K. Senanayake. Experimental assessment of the efficacy of sensitised emission in water from a europium ion, following intramolecular excitation by a phenanthridinyl group. *New J Chem*, **2000**, *24* (6), 377-386.

34.   H. Tadokoro, Y. Chatani, T. Yoshihara, S. Tahara and S. Murahashi. Structural Studies on Polyethers, [-(Ch-2)M-O-]N .2. Molecular Structure of Polyethylene Oxide. *Makromolekul Chem*, **1964**, *73*, 109-127.

35.   P. G. de Gennes. Polymers at an Interface - a Simplified View. *Adv Colloid Interfac*, **1987**, *27* (3-4), 189-209.

36.   Z. E. Chamas, X. M. Guo, J. L. Canet, A. Gautier, D. Boyer and R. Mahiou. Clicked dipicolinic antennae for lanthanide luminescent probes. *Dalton T*, **2010**, *39* (30), 7091-7097.

37.   G. Bernardinelli, C. Piguet and A. F. Williams. The 1st Self-Assembled Dinuclear Triple-Helical Lanthanide Complex - Synthesis and Structure. *Angewandte Chemie-International Edition in English*, **1992**, *31* (12), 1622-1624.

38.   A. S. Chauvin, S. Comby, B. Song, C. D. B. Vandevyver and J. C. G. Bunzli. A versatile ditopic ligand system for sensitizing the luminescence of bimetallic lanthanide bio-imaging probes. *Chem-Eur J*, **2008**, *14* (6), 1726-1739.

39.   C. D. B. Vandevyver, A. S. Chauvin, S. Comby and J. C. G. Bunzli. Luminescent lanthanide bimetallic triple-stranded helicates as potential cellular imaging probes. *Chem Commun*, **2007**, (17), 1716-1718.

40.   A. S. Chauvin, S. Comby, B. Song, C. D. B. Vandevyver, F. Thomas and J. C. G. Bunzli. A polyoxyethylene-substituted bimetallic europium helicate for luminescent staining of living cells. *Chem-Eur J*, **2007**, *13* (34), 9515-9526.

41.   A. S. Chauvin, (2012) Lanthanide: Luminescence Bioprobes in *The Rare Earth Elements: Fundamentals and Applications*, ed. D. A. Atwood. Chichester, UK: John Wiley & Sons Ltd, pp. 535-559.

42.   N. M. Shavaleev, S. V. Eliseeva, R. Scopelliti and J. C. G. Bunzli. Designing Simple Tridentate Ligands for Highly Luminescent Europium Complexes. *Chem-Eur J*, **2009**, *15* (41), 10790-10802.

43.   P. Taborsky, I. Svobodova, P. Lubal, Z. Hnatejko, S. Lis and P. Hermann. Formation and dissociation kinetics of Eu(III) complexes with H(5)do3ap and similar dota-like ligands. *Polyhedron*, **2007**, *26* (15), 4119-4130.

44.   I. Lukes, J. Kotek, P. Vojtisek and P. Hermann. Complexes of tetraazacycles bearing methylphosphinic/phosphonic acid pendant arms with copper(II), zinc(II) and lanthanides(III). A comparison with their acetic acid analogues. *Coordin Chem Rev*, **2001**, *216*, 287-312.

45.   N. N. Katia, A. Lecointre, M. Regueiro-Figueroa, C. Platas-Iglesias and L. J. Charbonniere. Nonmacrocyclic Luminescent Lanthanide Complexes Stable in Biological Media. *Inorg Chem*, **2011**, *50* (5), 1689-1697.

46.   S. Comby, D. Imbert, A. S. Chauvin, J. C. G. Bunzli, L. J. Charbonniere and R. F. Ziessel. Influence of anionic functions on the coordination and photophysical properties of lanthanide(III) complexes with tridentate bipyridines. *Inorg Chem*, **2004**, *43* (23), 7369-7379.

47.   Z. Kotkova, G. A. Pereira, K. Djanashvili, J. Kotek, J. Rudovsky, P. Hermann, L. V. Elst, R. N. Muller, C. F. G. C. Geraldes, I. Lukes and J. A. Peters. Lanthanide(III) Complexes of Phosphorus Acid Analogues of H(4)DOTA as Model Compounds for the Evaluation of the Second-Sphere Hydration. *Eur J Inorg Chem*, **2009**, (1), 119-136.

48. A. S. Chauvin, S. Comby, M. Baud, C. De Piano, C. Duhot and J. C. G. Bunzli. Luminescent Lanthanide Helicates Self-Assembled from Ditopic Ligands Bearing Phosphonic Acid or Phosphoester Units. *Inorg Chem*, **2009**, *48* (22), 10687-10696.

49. J. C. G. Bunzli, A. S. Chauvin, H. K. Kim, E. Deiters and S. V. Eliseeva. Lanthanide luminescence efficiency in eight- and nine-coordinate complexes: Role of the radiative lifetime. *Coordin Chem Rev*, **2010**, *254* (21-22), 2623-2633.

50. P. G. Tarassoff and N. Filipescu. Coumarinium-Europium Energy-Transfer - Efficient Triplet Migration between 2 Cations. *J Chem Soc Chem Comm*, **1975**, (6), 208-209.

51. C. Féau, E. Klein, P. Kerth and L. Lebeau. Synthesis and properties of europium complexes derived from coumarin-derivatized azamacrocycles. *Synthetic Met*, **2009**, *159* (5-6), 528-536.

52. S. G. Roh, N. S. Baek, K. S. Hong and H. K. Kim. Synthesis and photophysical properties of luminescent lanthanide complexes based on coumarin-3-carboxylic acid for advanced photonic applications. *B Kor Chem Soc*, **2004**, *25* (3), 343-344.

53. M. T. Alonso, E. Brunet, O. Juanes and J. C. Rodriguez-Ubis. Synthesis and photochemical properties of new coumarin-derived ionophores and their alkaline-earth and lanthanide complexes. *J Photoch Photobio A*, **2002**, *147* (2), 113-125.

54. M. T. Alonso, E. Brunet, C. Hernandez and J. C. Rodriguezubis. Synthesis and Complexation Properties of 3-Aroylcoumarin Crown-Ethers - a New Class of Photoactive Macrocycles. *Tetrahedron Lett*, **1993**, *34* (46), 7465-7468.

55. J. C. Rodriguez-Ubis, M. T. Alonso, O. Juanes and E. Brunet. Luminescent cryptands. 3-aroylcoumarin macrobicyclic complexes of europium(III) and terbium(III): the effect of coumarin substitution. *Luminescence*, **2000**, *15* (6), 331-340.

56. B. D. Wagner. The Use of Coumarins as Environmentally-Sensitive Fluorescent Probes of Heterogeneous Inclusion Systems. *Molecules*, **2009**, *14* (1), 210-237.

57. P. R. Hammond, A. N. Fletcher, R. A. Henry and R. L. Atkins. Search for Efficient, near Uv Lasing Dyes .1. Substituent Effects on Bicyclic Dyes. *Appl Phys*, **1975**, *8* (4), 311-314.

58. J. C. Jung, Y. J. Jung and O. S. Park. A convenient one-pot synthesis of 4-hydroxycoumarin, 4-hydroxythiocoumarin, and 4-hydroxyquinolin-2(1H)-one. *Synthetic Commun*, **2001**, *31* (8), 1195-1200.

59.   C. Féau, E. Klein, C. Dosche, P. Kerth and L. Lebeau. Synthesis and characterization of coumarin-based europium complexes and luminescence measurements in aqueous media. *Org Biomol Chem*, **2009**, *7* (24), 5259-5270.

60.   E. Pershagen, J. Nordholm and K. E. Borbas. Luminescent Lanthanide Complexes with Analyte-Triggered Antenna Formation. *J Am Chem Soc*, **2012**, *134* (24), 9832-9835.

61.   M. Li and P. R. Selvin. Luminescent Polyaminocarboxylate Chelates of Terbium and Europium - the Effect of Chelate Structure. *J Am Chem Soc*, **1995**, *117* (31), 8132-8138.

62.   P. R. Selvin, J. Jancarik, M. Li and L. W. Hung. Crystal structure and spectroscopic characterization of a luminescent europium chelate. *Inorg Chem*, **1996**, *35* (3), 700-705.

63.   G. Vereb, E. Jares-Erijman, P. R. Selvin and T. M. Jovin. Temporally and spectrally resolved imaging microscopy of lanthanide chelates. *Biophys J*, **1998**, *74* (5), 2210-2222.

64.   J. Y. Chen and P. R. Selvin. Synthesis of 7-amino-4-trifluoromethyl-2-(1H)-quinolinone and its use as an antenna molecule for luminescent europium polyaminocarboxylates chelates. *J Photoch Photobio A*, **2000**, *135* (1), 27-32.

65.   G. Wyszecki and W. S. Stiles. *Colour science : concepts and methods, quantitative data and formulae*. Wiley, New York ; Chichester, 1982.

66.   R. M. Boynton. *Human color vision*. Optical Society of America, Washington, DC, 1992.

67.   T. Smith and J. Guild. The C.I.E. colorimetric Standards and their use. *Trans. Opt. Soc.*, **1931**, *33* (3), 73-134.

68.   H. S. Fairman, M. H. Brill and H. Hemmendinger. How the CIE 1931 color-matching functions were derived from Wright-Guild data. *Color Res Appl*, **1997**, *22* (1), 11-23.

69.   D. L. MacAdam. Visual sensitivities to color differences in daylight. *J Opt Soc Am*, **1942**, *32* (5), 247-274.

70.   J. Morovic. *Color gamut mapping*. John Wiley & Sons, Chichester, England ; Hoboken, NJ, 2008.

71.   H. E. J. Neugebauer. Die theoretischen Grundlagen des Mehrfarbendruckes. *Zietschrift für Wissenschaftliche Photographie, Photophysik und Photochemie*, **1937**, *36* (4), 73-89.

72.   J. A. C. Yule and W. J. Nielsen. The penetration of light into paper and its effect on halftone reproduction. *TAGA Proceedings*, **1951**, *4*, 66-75.

73. R. D. Hersch and F. Crete. *Improving the Yule-Nielsen modified spectral Neugebauer model by dot surface coverages depending on the ink superposition conditions*. 2005.

74. J. A. S. Viggiano. The color of halftone tints. *Proc. TAGA*, **1985**, 647-661.

75. M. Hebert and R. D. Hersch. Analyzing halftone dot blurring by extended spectral prediction models. *J Opt Soc Am A*, **2010**, *27* (1), 6-12.

76. M. Hebert and R. D. Hersch. Yule-Nielsen based recto-verso color halftone transmittance prediction model. *Appl Optics*, **2011**, *50* (4), 519-525.

77. R. D. Hersch, P. Donze and S. Chosson. Color images visible under UV light. *Acm T Graphic*, **2007**, *26* (3).

78. F. Bernardini, J. Mittleman, H. Rushmeier, C. Silva and G. Taubin. The ball-pivoting algorithm for surface reconstruction. *Ieee T Vis Comput Gr*, **1999**, *5* (4), 349-359.

79. G. J. Braun and M. D. Fairchild. Image lightness rescaling using sigmoidal contrast enhancement functions. *J. Electron. Imaging*, **1999**, *8* (4), 380-393.

80. J. Morovic and M. R. Luo. The fundamentals of gamut mapping: A survey. *J Imaging Sci Techn*, **2001**, *45* (3), 283-290.

81. R. L. Van Renesse. *Optical document security*. Artech House, Boston, Mass. ; London, 2004.

82. B. A. Lent, G. G. Deng and J. F. Ezpeleta, 1997. A Jet Ink Composition. International Appl. PCT WO 97/10307, filed 11.09.1996.

83. J. D. Auslander and W. Berson, 1996. Bar Codes Using Luminescent Invisible Inks. U.S. Pat. 5542971, filed 1.12.1994.

84. I. Guilford Jones and Y. Dingxue, 2002. Compositions and Methods for Luminescence Lifetime Comparison. U.S. Pat. 6402986, filed 16.07.1999.

85. V. Aboutanos, T. Tiller, C. Reinhard and S. Rascagnères, 2010. Secure Document Comprising Luminescent Chelates. U.S. Pat. Appl. 0307376, filed 11.05.2010.

86. W. J. Coyle and J. C. Smith, 2010. Methods and ink compositions for invisibly printed security images having multiple authentication features. U.S. Pat. 7821675, filed Apr. 5, 2004.

87. R. D. Franz. Comparisons of pKa and log P values of some carboxylic and phosphonic acids: Synthesis and measurement. *Aaps Pharmsci*, **2001**, *3* (2).

88. A. D'Aleo, A. Picot, A. Beeby, J. A. G. Williams, B. Le Guennic, C. Andraud and O. Maury. Efficient Sensitization of Europlum, Ytterbium, and Neodymium Functionalized Tris-Dipicolinate Lanthanide Complexes through Tunable Charge-Transfer Excited States. *Inorg Chem*, **2008**, *47* (22), 10258-10268.

89.   T. K. Trout, J. M. Bellama, R. A. Faltynek, E. J. Parks and F. E. Brinckman. Effect of pH on the Emission Properties of Aqueous Tris(2,6-Dipicolinato)Terbium(III) Complexes. *Inorg Chim Acta*, **1989**, *155* (1), 13-15.

90.   D. S. Mcclure. Triplet-Singlet Transitions in Organic Molecules - Lifetime Measurements of the Triplet State. *J Chem Phys*, **1949**, *17* (10), 905-913.

91.   P. Klán and J. Wirz. *Photochemistry of organic compounds : from concepts to practice*. Wiley, Oxford, 2009.

92.   L. N. Puntus, K. A. Lyssenko, I. S. Pekareva and J. C. G. Bunzli. Intermolecular Interactions as Actors in Energy-Transfer Processes in Lanthanide Complexes with 2,2'-Bipyridine. *J Phys Chem B*, **2009**, *113* (27), 9265-9277.

93.   L. N. Puntus, V. F. Zolin, V. A. Kudryashova, V. I. Tsaryuk, J. Legendziewicz, P. Gawryszewska and R. Szostak. Charge transfer bands in the Eu3+ luminescence excitation spectra of isomeric europium pyridine-dicarboxylates. *Phys Solid State+*, **2002**, *44* (8), 1440-1444.

94.   F. R. Clapper and J. A. C. Yule. The Effect of Multiple Internal Reflections on the Densities of Half-Tone Prints on Paper. *J Opt Soc Am*, **1953**, *43* (7), 600-603.

95.   M. Hebert, R. D. Hersch and L. Simonot. Spectral prediction model for piles of nonscattering sheets. *J Opt Soc Am A*, **2008**, *25* (8), 2066-2077.

96.   D. T. Delpy, M. Cope, P. Vanderzee, S. Arridge, S. Wray and J. Wyatt. Estimation of Optical Pathlength through Tissue from Direct Time of Flight Measurement. *Phys Med Biol*, **1988**, *33* (12), 1433-1442.

97.   R. Balasubramanian and E. Dalal. *A method for quantifying the color gamut of an output device*. San Jose, CA, 1997.

98.   J. Andres and A. S. Chauvin. Europium Complexes of Tris(dipicolinato) Derivatives Coupled to Methylumbelliferone: A Double Sensitization. *Eur J Inorg Chem*, **2010**, (18), 2700-2713.

99.   S. Kohmoto, E. Mori and K. Kishikawa. Room-temperature discotic nematic liquid crystals over a wide temperature range: Alkali-metal-ion-induced phase transition from discotic nematic to columnar phases. *J Am Chem Soc*, **2007**, *129* (44), 13364.

100.   J. I. Luengo and J. D. Elliott, 2002. Endothelin receptor antagonists. U.S. Pat. 6353116, filed Dec. 14, 1999.

Curriculum Vitæ

Julien ANDRES

Chemin des Crêts 4, 1084 Carrouge (Switzerland)   Mobile: +41 79 417 90 07
Born 15th April 1984, Swiss, Single   Email: julien.andres@gmail.com

Education

- **Since 2008   PhD in Chemistry at EPFL**
- **2003 – 2008   Master in Molecular and Biological Chemistry at EPFL**

Experience

- **Since 2008   PhD at EPFL (supervisors: Dr. MER A.-S. Chauvin, Pr. R. D. Hersch)**
  - Synthesizing and characterizing organic ligands for luminescent lanthanide complexes;
  - Using luminescent compounds as luminescent inks for color reproduction and document security.
  - Developing spectral prediction models for color reproduction with luminescent inks and classical inks (cyan, magenta and yellow) printed in offset and/or ink-jet;
  - Taught general chemistry to 1st year undergraduate students in medicine, pharmacy and biology and introductory laboratory chemistry to 1st year undergraduate students in pharmacy and biology;
  - Received a reward for a particularly proficient teaching activity;
  - Wrote four publications (three in chemistry and one in color science), a patent application and two chapters of a book on rare-earth elements.

- **2008   Internship at the Laboratory of Catalytic and Organic Synthesis at EPFL**
  - Investigated a new catalytic method of cyclization that resulted in a publication.

- **2007   Master Project at the Photochemical Dynamic Group at EPFL**
  - Found invisible luminescent compounds suitable for ink-jet printing of accurate luminescent color images.

Scientific skills

Chemistry

- Qualified in organic synthesis and coordination chemistry, and particularly of water soluble and luminescent compounds;
- Trained with complexometry, spectrophotometry, NMR spectroscopy and to work with lasers;
- Proficient with the photophysical characterization of luminescent materials, and particularly of luminescent lanthanide complexes, quantum yield and lifetime analysis, spectrofluorimetry and phosphorescence measurements.

Color Science

- Experienced in radiometry and colorimetry of luminescent materials;
- Educated in color reproduction, spectral color prediction models (developed with Matlab) and optical document security.

Language skills

- French: native
- English: fluent
- German: conversational

Activities

- **Since 2010**   Photography
- **Since 2009**   Golf course authorization
- **2000- 2011**   Regional basketball referee at the "Association Vaudoise de Basketball".

Publications

J. Andres, R. D. Hersch. Color Reproduction with Luminescent Backlit Transmissive Colors. *Color Research and Application*, **2012**, submitted full paper article.

J. Andres, A.-S. Chauvin. Energy Transfer in Coumarin-Sensitised Lanthanide Luminescence: Investigation of the Nature of the Sensitiser and its Distance to the Lanthanide Ion. *Physical Chemistry Chemical Physics*, **2012**, full paper article under revision.

J. Andres, A.-S. Chauvin. (2012) Lanthanides: Luminescence in *The Rare Earth Elements: Fundamentals and Applications*, edited by D. A. Atwood. Chichester, UK: John Wiley & Sons Ltd, pp.111-133.

J. Andres, A.-S. Chauvin (2012) Lanthanides: Luminescence Applications in *The Rare Earth Elements: Fundamentals and Applications*, edited by D. A. Atwood. Chichester, UK: John Wiley & Sons Ltd, pp.135-152.

R. D. Hersch, J. Andres. Synthesis of authenticable halftone images with non-luminescent halftones illuminated by a luminescent emissive layer. US Patent Application, submitted Jan. 10, 2012.

J. Andres, A.-S. Chauvin. 6-Phosphoryl Picolinic Acids as Europium and Terbium Sensitizers. *Inorganic Chemistry*, **2011**, 50(20), 10082-10090.

J. Andres, A.-S. Chauvin. Europium Complexes of Tris(dipicolinato) Derivatives Coupled to Methylumbelliferone: A Double Sensitization. *European Journal of Inorganic Chemistry*, **2010**, 2010(18), 2700-2713.

F. De Simone, J. Andrès, R. Torosantucci, Jérôme Waser. Catalytic Formal Homo-Nazarov Cyclization. *Organic Letters*, **2009**, 11(4), 1023-1026.

Oral presentations

J. Andres, A.-S. Chauvin. *Printing luminescent lanthanide complexes for color reproduction with invisible inks*. 8th International Conference on f-elements, 2012, Udine, Italy.

J. Andres, A.-S. Chauvin. *Design of water soluble lanthanide complexes with a double sensitization ability*. COST action CM1006, European f-element Network, 2012, Tarragona, Spain.

Poster presentations

J. Andres, A.-S. Chauvin. *Double sensitization of europium III coordinated to dipicolinate derivatives with para-polyoxyethylene-coumarins.* Swiss Chemical Society Fall meeting, 2011, Ecole Polytechnique Fédérale de Lausanne, Switzerland.

J. Andres, A.-S. Chauvin. *Diethoxy, monoethoxy and dihydroxy 6-phosphoryl picolinic acid as luminescent lanthanide sensitizers*. 7th International Conference on f-elements, 2009, Cologne, Germany.